POLITECHNIKA
GDAŃSKA
WYDZIAŁ FIZYKI TECHNICZNEJ
I MATEMATYKI STOSOWANEJ

WYDZIAŁ FIZYKI TECHNICZNEJ
I MATEMATYKI STOSOWANEJ

Imię i nazwisko autora rozprawy: Karolina Górnicka
Dyscyplina naukowa: Inżynieria Materiałowa

ROZPRAWA DOKTORSKA

Tytuł rozprawy w języku polskim:
„Badanie właściwości nadprzewodzących wybranych układów międzymetalicznych”

Tytuł rozprawy w języku angielskim:
“Superconductivity in the selected intermetallic systems”

Promotor *podpis*
prof. dr hab. inż. Tomasz Klimczuk

Gdańsk, rok 2021

ROZPRAWA DOKTORSKA

Badanie właściwości nadprzewodzących wybranych układów międzymetalicznych

mgr inż. Karolina Górnicka

Promotor: prof. dr hab. inż. Tomasz Klimczuk

„Praca wykonana przy wsparciu grantu
Narodowego Centrum Nauki –
OPUS (UMO-2017/27/B/ST5/03044)”

„Praca wykonana przy wsparciu grantu
Ministerstwa Nauki i Szkolnictwa Wyższego –
Diamentowy Grant (0205/DIA/2017/46)”

…………………………..

Spis treści

Wykaz ważniejszych skrótów i oznaczeń

T	Temperatura
T_c	Temperatura przejścia do stanu nadprzewodnictwa
M	Magnetyzacja
μ_0	Przenikalność magnetyczna próżni
H	Natężenie pola magnetycznego
χ	Podatność magnetyczna
ρ	Oporność właściwa
RRR	Stosunek oporności próbki w temperaturze pokojowej do oporności resztkowej (ang. *Residual Resistivity Ratio*)
Θ_D	Temperatura Debye'a
R	Stała gazowa
ZFC	Tryb pomiaru magnetyzacji próbki w funkcji temperatury, gdy pole magnetyczne było włączane po schłodzeniu próbki (ang. *Zero Field Cooling*)
FC	Tryb pomiaru magnetyzacji próbki w funkcji temperatury, gdy pole magnetyczne było włączane przed schłodzeniem próbki (ang. *Field Cooling*)
PPMS	System pomiarowy Physical Properties Measurement System firmy Quantum Design
λ_{ep}	Sprzężenie electron-fonon
$\mu_0H_{c1}(0)$	Dolne pole krytyczne
$\mu_0H_{c2}(0)$	Górne pole krytyczne
ξ_{GL}	Długość koherencji
λ_{GL}	Głębokość wnikania
κ_{GL}	Parametr Ginzburga – Landaua
γ	Współczynnik Sommerfelda

Streszczenie

Niniejsza rozprawa doktorska dotyczy badania właściwości nadprzewodzących w wybranych układach międzymetalicznych. Zakres przeprowadzonych badań eksperymentalnych obejmuje syntezę związków w formie poli- oraz monokrystalicznej, badania strukturalne metodą proszkowej dyfrakcji rentgenowskiej oraz pomiary właściwości fizycznych (podatność magnetyczna, ciepło właściwe oraz opór elektryczny). Przedstawioną pracę stanowi zbiór 7 publikacji naukowych opublikowanych w czasopismach: *Superconductor Science and Technology* (IF 3.067, 100 pkt MNiSW 2019), *Physical Review B* (IF 3.736, 140 pkt MNiSW 2019), *Journal of Alloys and Compounds* (IF 4.65, 100 pkt MNiSW 2019), *Chemistry of Materials* (IF 9.567, 200 pkt MNiSW 2019) oraz *Advanced Functional Materials* (IF 16.836, 200 pkt MNiSW 2019). W ramach doktoratu opracowano metodę syntezy oraz opisano właściwości stanu nadprzewodzącego dla związków międzymetalicznych zawierających metal alkaliczny lit ($LiPd_2Ge$, $LiGa_2Ir$ oraz LiBi), a także związków międzymetalicznych zawierających wybrany metal z rodziny platynowców ($CeIr_3$, $ThIr_3$, $CaRh_2$, $NbIr_2B_2$ oraz $TaIr_2B_2$). Na podstawie przeprowadzonych badań określono typ nadprzewodnictwa (I-go lub II-go rodzaju) oraz wyznaczono wartości parametrów fizycznych opisujących stan nadprzewodzący: temperaturę krytyczną (T_c), sprzężenie elektron-fonon (λ_{ep}), dolne pole krytyczne ($\mu_0H_{c1}(0)$), górne pole krytyczne ($\mu_0H_{c2}(0)$), długość koherencji (ξ_{GL}), głębokość wnikania (λ_{GL}), parametr Ginzburga-Landaua ($\kappa_{GL} = \lambda_{GL}/\xi_{GL}$) oraz znormalizowaną wielkość skoku ciepła właściwego ($\Delta C/\gamma T_c$). W przedstawionej rozprawie opisano osiem związków wykazujących zjawisko nadprzewodnictwa, w tym cztery nowe nadprzewodniki odkryte przez autorkę pracy.

Słowa kluczowe

Nadprzewodnictwo, związki międzymetaliczne, proszkowa dyfrakcja rentgenowska, badania eksperymentalne, związki typu Heuslera, fazy Lavesa, nadprzewodniki niecentrosymetryczne

Abstract

The doctoral dissertation concerns the study of superconducting properties in selected intermetallic systems. The scope of the conducted experimental research includes the synthesis of poly- and monocrystalline compounds, powder x-ray diffraction studies and measurements of physical properties (magnetic susceptibility, heat capacity and electrical resistivity). The presented thesis consists of 7 scientific articles published in the following journals: *Superconductor Science and Technology* (IF 3.067, 100 pkt MNiSW 2019), *Physical Review B* (IF 3.736, 140 pkt MNiSW 2019), *Journal of Alloys and Compounds* (IF 4.65, 100 pkt MNiSW 2019), *Chemistry of Materials* (IF 9.567, 200 pkt MNiSW 2019) and *Advanced Functional Materials* (IF 16.836, 200 pkt MNiSW 2019). During the Ph.D. studies, the synthesis method and the properties of the superconducting state for intermetallic compounds containing lithium ($LiPd_2Ge$, $LiGa_2Ir$ and LiBi) and the selected metal from the platinum-group element ($CeIr_3$, $ThIr_3$, $CaRh_2$, $NbIr_2B_2$ and $TaIr_2B_2$) have been described. Based on the research studies, the type of superconductivity (type-I or type-II) was determined and the physical parameters describing the superconducting state were determined: critical temperature (T_c), electron-fonon coupling (λ_{ep}), lower critical field ($\mu_0H_{c1}(0)$), upper critical field ($\mu_0H_{c2}(0)$), coherence length (ξ_{GL}), penetration depth (λ_{GL}), Ginzburg-Landau parameter ($\kappa_{GL} = \lambda_{GL}/\xi_{GL}$) and renormalized specific heat jump ($\Delta C/\gamma T_c$). In the presented dissertation eight superconducting compounds have been described, including four new superconductors discovered by the author of the thesis.

Key words

Superconductivity, intermetallic compounds, powder x-ray diffraction, experimental studies, Heusler-type compounds, Laves phase, noncentrosymmetric superconductors

1. Wstęp

Nadprzewodnictwo uznawane jest za jedno z najważniejszych i najbardziej fascynujących zjawisk w dziedzinie fizyki materii skondensowanej. Zaobserwowane po raz pierwszy przez Heike Kamerlingh-Onnesa w 1911 roku, polega na zaniku oporu elektrycznego w materiale schłodzonym poniżej odpowiedniej temperatury, zwanej temperaturą krytyczną (T_c). W konsekwencji nadprzewodnik może przewodzić prąd elektryczny bez strat. Zerowa rezystancja nie jest jedynym zjawiskiem charakteryzującym stan nadprzewodzący. Drugą ważną cechą materiału nadprzewodzącego jest diamagnetyzm polegający na niemożności wniknięcia zewnętrznego pola magnetycznego, o natężeniu mniejszym od granicznego, do wnętrza materiału, ograniczając się do jego cienkiej warstwy przypowierzchniowej. Wykorzystanie tych dwóch właściwości (zerowy opór i idealny diamagnetyzm) w wielu dziedzinach nauki stanowi niezwykle ważne wyzwanie intelektualne o ogromnym potencjale zastosowań technologicznych [1,2].

Pomimo ponad stuletniej historii, nadprzewodnictwo w dalszym ciągu wzbudza duże zainteresowanie zarówno w środowisku naukowym, jak i gospodarczym. Odkrywane są nadprzewodniki z coraz wyższymi temperaturami krytycznymi [3,4], a także materiały o własnościach innych niż znane wcześniej tj. nadprzewodniki niekonwencjonalne [5,6]. Obecnie nadprzewodniki znajdują zastosowanie w NMR i MRI, czyli tomografii z zastosowaniem elektromagnesów nadprzewodnikowych do badań jądrowego rezonansu magnetycznego w medycynie. Nadprzewodniki są również wykorzystywane w akceleratorach cząstek elementarnych [3].

Głównym celem niniejszej rozprawy doktorskiej jest opisanie stanu nadprzewodzącego, w oparciu o teorie mikroskopowe nadprzewodnictwa indukowanego oddziaływaniem elektronów z siecią krystaliczną, w wybranych związkach międzymetalicznych. Znaczna liczba zsyntetyzowanych nadprzewodników, z szerokim spektrum przebadanych oraz opisanych własności, jest uzupełnieniem stanu obecnej wiedzy w zakresie objętym pracą doktorską. Szczególny nacisk został położony na opisanie mechanizmu funkcjonującego w nowych nadprzewodnikach odkrytych przez autorkę pracy ($LiPd_2Ge$, $LiGa_2Ir$, $NbIr_2B_2$ oraz $TaIr_2B_2$). Przedstawioną pracę stanowi zbiór 7 publikacji opublikowanych w czasopismach naukowych znajdujących się w bazie Journal Citation Reports (JCR). Część pierwsza pracy doktorskiej jest wprowadzeniem teoretycznym i zawiera również wybrane informacje o badanych nadprzewodnikach. W części drugiej przedstawione zostały artykuły poprzedzone krótkim opisem.

Zakres przeprowadzonych badań obejmował syntezę oraz badania właściwości strukturalnych i fizycznych związków $CeIr_3$ (A1), $ThIr_3$ (A2), $CaRh_2$ (A3), $LiPd_2Ge$ (A4), $LiGa_2Ir$ (A5), LiBi (A6) oraz $NbIr_2B_2$ i $TaIr_2B_2$ (A7). Dla materiałów A1, A2 oraz A4-A7, we współpracy z grupą dr. hab. inż. Bartłomieja Wiendlochy, prof. AGH, przeprowadzone zostały obliczenia numeryczne własności elektronowych i fononowych, co pozwoliło na pełniejsze zrozumienie właściwości badanych związków.

2. Część teoretyczna

Niniejszy rozdział został poświęcony opisowi zagadnień teoretycznych związanych z tematyką pracy doktorskiej. W pierwszej części krótko scharakteryzowano zjawisko nadprzewodnictwa i opisano najważniejsze parametry charakteryzujące materiały nadprzewodzące. Drugą część rozdziału stanowi przegląd literatury umożliwiający pogląd na obecny stan wiedzy badanych związków.

2.1 Charakterystyczne właściwości nadprzewodników

2.1.1 Rezystywność

Wiele związków i stopów międzymetalicznych po oziębieniu poniżej charakterystycznej dla danego materiału, tzw. temperatury krytycznej (T_c) wykazuje właściwości nadprzewodzące. Podstawową cechą tego stanu jest zerowa rezystywność. Przykładowy wykres oporności właściwej w funkcji temperatury dla niecentrosymetrycznego nadprzewodnika Re_6Hf [7] przedstawiono na Rys.2.1. Opór właściwy materiału w stanie normalnym można opisać formułą Blocha-Grüneisena: $\rho(T) = \rho_0 + 4AT\left(\frac{T}{\Theta_D}\right)^4 \int_0^{\frac{T}{\Theta_D}} \frac{x^5dx}{(e^x-1)(1-e^{-x})}$, gdzie ρ_0 jest oporem resztkowym związanym z rozpraszaniem elektronów na domieszkach, a Θ_D jest temperaturą Debye. Poniżej temperatury krytycznej T_c = 5.96 K obserwuje się spadek oporności do zera (wstawka Rys.2.1), przy czym zanik oporu jest bardzo szybki tzn. następuje w bardzo wąskim przedziale temperatur.

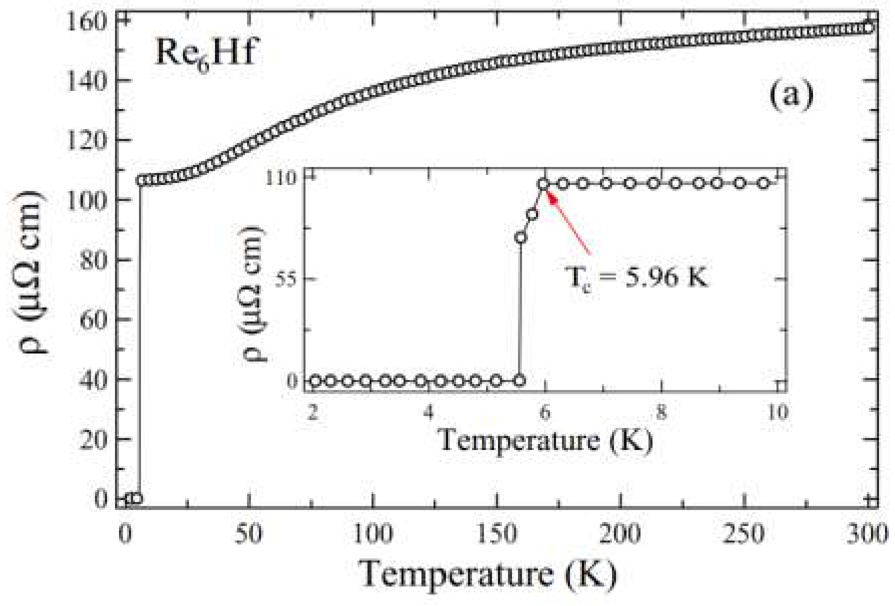

Rys.2.1. Zależność oporności właściwej od temperatury dla nadprzewodnika Re_6Hf. Wstawka przedstawia przejście do stanu nadprzewodzącego w T_c = 5.96 K [7].

2.1.2 Parametry krytyczne nadprzewodnika

Niemierzalnie małą wartość oporu elektrycznego nadprzewodnika można zaobserwować tylko w przypadku, gdy materiał znajduje się w odpowiednich warunkach. Jak wspomniano wcześniej, nadprzewodnictwo obserwowane jest tylko poniżej pewnej, krytycznej temperatury, różnej dla różnych związków. Drugim istotnym parametrem jest natężenie zewnętrznego pola magnetycznego. Nadprzewodnik traci właściwości nadprzewodzące w dostatecznie silnym, zewnętrznym polu magnetycznym (zwanym polem krytycznym), nawet gdy znajduje się w temperaturze mniejszej od T_c [2,8,9]. Wartość pola krytycznego (H_c) jest zależna od temperatury, zmniejszając się monotonicznie z jej wzrostem, aż do wartości zerowej w $T=T_c$. Relację między H_c, a temperaturą opisuje w przybliżeniu wzór (2.1):

$$H_c(T) = H_c(0)\left[1 - \left(\frac{T}{T_C}\right)^2\right], \tag{2.1}$$

gdzie $H_c(0)$ jest wartością pola krytycznego w 0 K. Warto zaznaczyć, że opisanie przedstawionej zależności przez parabolę, jest wynikiem czysto doświadczalnym i nie ma znaczenia podstawowego. W rzeczywistości krzywe eksperymentalne często nie są idealnymi parabolami i do ich opisu należy posłużyć się wyrażeniem wielomianowym [8].

Trzecim i ostatnim parametrem krytycznym stanu nadprzewodzącego jest gęstość prądu J płynącego przez materiał nadprzewodnika. Jeżeli J przekroczy wartość krytyczną (J_c), to materiał również utraci właściwości nadprzewodzące, pomimo zachowania natężenia pola magnetycznego i temperatury poniżej ich wartości krytycznych ($H < H_c$ oraz $T < T_c$) [2,8,9].

Stan nadprzewodnictwa jest więc charakteryzowany funkcją trzech parametrów krytycznych: temperatury (T_c), natężenia pola magnetycznego (H_c) oraz gęstości prądu (J_c). Na Rys 2.2 przedstawiona została powierzchnia krytyczna nadprzewodnika oddzielająca dwa stany materiału: stan nadprzewodnictwa oraz stan normalny.

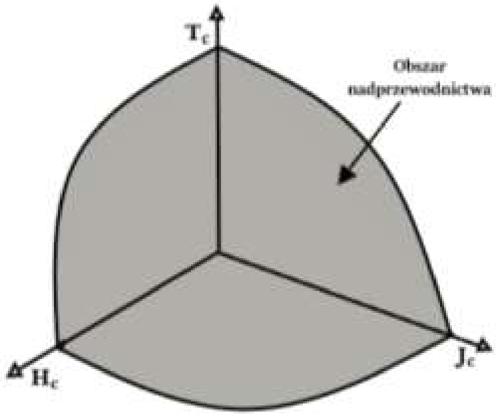

Rys.2.2. Powierzchnia J-H-T wyznaczona przez trzy parametry krytyczne

2.1.3 Zjawisko Meissnera-Ochsenfelda

Fundamentalną właściwością materiałów nadprzewodzących oziębionych poniżej temperatury T_c jest wypychanie pola magnetycznego ze swego wnętrza. Efekt ten polega na powstawaniu prądów ekranujących, płynących w cienkiej warstwie przypowierzchniowej, które to generują pole o takiej samej wartości jak pole zewnętrzne, lecz przeciwnie do niego skierowane. W efekcie nadprzewodnik zachowuje się jak idealny diamagnetyk, tzn. indukcja magnetyczna (*B*) wewnątrz nadprzewodnika wynosi zero [2,8–11]. Efekt ten zwany zjawiskiem Meissnera-Ochsenfelda został zilustrowany na Rys.2.3.

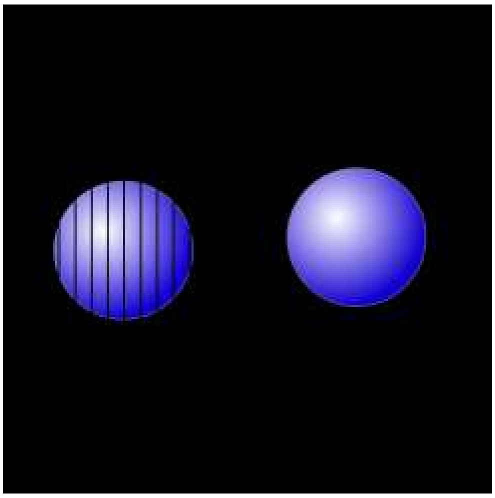

Rys.2.3. Zjawisko Meissnera-Ochsenfelda, po lewej stronie nadprzewodnik w stanie normalnym ($T>T_c$), po prawej w stanie nadprzewodzącym ($T<T_c$) [12].

2.1.4 Nadprzewodniki I i II-go rodzaju

Ze względu na odmienne zachowanie materiałów nadprzewodzących w zewnętrznym polu magnetycznym, wyróżnia się dwie klasy nadprzewodników: pierwszego i drugiego rodzaju [2,8].

Nadprzewodniki I-go rodzaju, znajdujące się w temperaturze poniżej T_c oraz w zewnętrznym polu magnetycznym, wykazują idealny diamagnetyzm, a gdy przyłożone pole osiągnie i przekroczy krytyczną wartość (H_c), wówczas materiał przechodzi do stanu normalnego [2,8]. Rys.2.4. przedstawia zależność namagnesowania w funkcji zewnętrznego pola magnetycznego dla idealnej próbki nadprzewodnika I-go rodzaju.

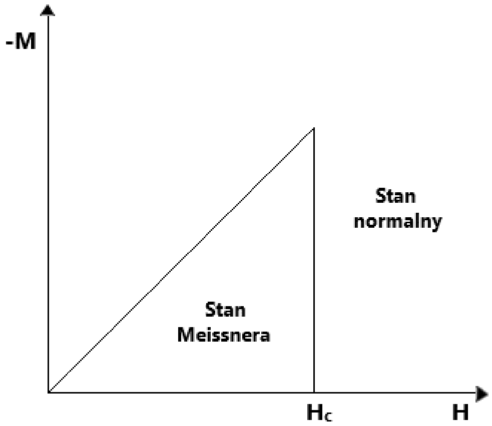

Rys.2.4. Zależność namagnesowania od przyłożonego pola magnetycznego dla idealnej próbki nadprzewodnika I-go rodzaju.

Dużą rolę przy przejściu nadprzewodnika I-go rodzaju do stanu normalnego pod wpływem zewnętrznego pola magnetycznego odgrywają efekty odmagnesowujące. Jedynie dla próbek w postaci cienkich, długich prętów ustawionych zgodnie z kierunkiem pola, efekty te są nieistotne. W konsekwencji w próbkach nadprzewodnika o skończonych rozmiarach współistnieją dwie fazy: nadprzewodząca oraz normalna. Stan, w którym obie fazy występują w postaci sąsiadujących ze sobą obszarów (domen), nazywa się stanem pośrednim [2,8]. Reakcja na przyłożone pole magnetyczne dla nadprzewodnika o niezerowym współczynniku odmagnesowania została przedstawiona schematycznie na Rys.2.5. Zakres pól, dla jakich pojawia się stan pośredni, zależy od rozmiarów i kształtu badanej próbki, a także jej orientacji względem kierunku zewnętrznego pola magnetycznego.

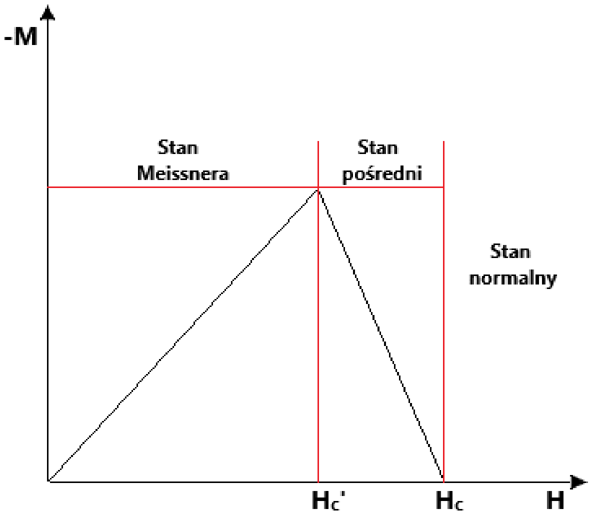

Rys.2.5. Zależność namagnesowania od przyłożonego pola magnetycznego dla nadprzewodnika I-go rodzaju o niezerowym współczynniku odmagnesowania.

Łatwo zauważyć, że przejście ze stanu nadprzewodnictwa do stanu normalnego ulega rozmyciu i rozciąga się na pewien przedział natężenia pola magnetycznego, powyżej pola H_c'. Wraz z jego wzrostem obszary nadprzewodzące zajmują coraz mniejszą objętość, znikając całkowicie po osiągnięciu wartości krytycznej pola (H_c). Warto wspomnieć, że tak długo jak istnieją domeny nadprzewodzące, tak długo próbka wykazuje zerowy opór elektryczny [2,8].

Dla próbki o kształcie elipsoidy obrotowej wewnętrzne natężenie pola magnetycznego (H_w) jest równe [8]:

$$H_w = H_z - NM, \tag{2.2}$$

gdzie H_z jest polem zewnętrznym, M jest namagnesowaniem, a N współczynnikiem demagnetyzacji. Ponieważ w stanie idealnego diamagnetyzmu namagnesowanie nadprzewodnika jest równe $M = -H_w$, otrzymujemy:

$$M(N-1) = H_z, \tag{2.3}$$

Następnie, korzystając z zależności $\chi = M/H_z$ i wykonując proste przekształcenia, dostajemy wyrażenie na zależność podatności magnetycznej od współczynnika demagnetyzacji:

$$\chi_{sc} = \left(\frac{1}{1-N}\right), \tag{2.4}$$

gdzie χ_{sc} jest podatnością magnetyczną w stanie nadprzewodzącym.

Przez wiele lat sądzono, że istnieje tylko jedna klasa nadprzewodników, a anomalie obserwowane dla nadprzewodzących stopów czy zanieczyszczonych metali, przypisywano wpływom domieszek. Jednakże w 1957 roku A. Abrikosow opublikował pracę [13], w której wskazał możliwość istnienia nowej kategorii nadprzewodników o nieco innych właściwościach, niż dotychczas znano. Okazało się, że obserwowane w wielu materiałach nadprzewodzących anomalie nie sprowadzają się do wpływu zanieczyszczeń, a stanowią samoistną własność nowej klasy nadprzewodników, które nazwano nadprzewodnikami II-go rodzaju [8].

Materiały będące nadprzewodnikami drugiego rodzaju charakteryzują się inną reakcją na przyłożone pole magnetyczne niż nadprzewodniki pierwszego rodzaju. Jeżeli natężenie pola jest mniejsze od pewnej krytycznej wartości (H_{c1}), nazywanej w tym przypadku dolnym (pierwszym) polem krytycznym, to nadprzewodnik II-rodzaju zachowuje się jak nadprzewodnik I-rodzaju, a więc wykazuje idealny diamagnetyzm (stan Meissnera). Po przekroczeniu wartości H_{c1}, przy powierzchni próbki, a następnie w całej jej objętości pojawiają się nici strumienia magnetycznego, zwane worteksami lub wirami. Gęstość wirów wzrasta wraz ze wzrostem zewnętrznego pola magnetycznego, a po osiągnięciu wartości górnego pola krytycznego (H_{c2}), sąsiednie wiry nachodzą na siebie, co prowadzi do przejścia materiału w stan normalny [2,8–10]. Strukturę między dwoma polami krytycznymi H_{c1} oraz H_{c2}, nazywa się stanem mieszanym. Rys.2.6. ilustruje namagnesowanie nadprzewodnika II-go rodzaju.

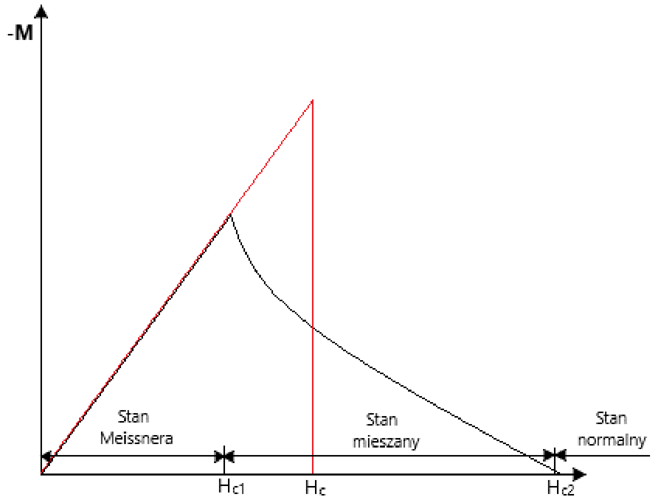

Rys.2.6. Zależność namagnesowania od przyłożonego pola magnetycznego dla nadprzewodnika II-go rodzaju. Linia czerwona na wykresie reprezentuje pole krytyczne dla nadprzewodnika I-go rodzaju o takiej samej temperaturze przejścia.

Dla nadprzewodników II-go rodzaju definiuje się również termodynamiczne pole krytyczne (H_c), przy którym wartość energii swobodnej dla stanu całkowicie nadprzewodzącego jest równa energii swobodnej dla stanu normalnego [2,8]. Obrazowo H_c jest równe (w przybliżeniu) polu krytycznemu dla nadprzewodnika I-go rodzaju o takiej samej temperaturze przejścia (czerwona linia na Rys.2.6.). Wzór 2.5 przedstawia jakościową relację między H_c, H_{c1} oraz H_{c2}:

$$H_c \sim \sqrt{H_{c1}H_{c2}}. \tag{2.5}$$

2.1.5 Ciepło właściwe w stanie nadprzewodzącym

Pomiary ciepła właściwego znacznie rozszerzyły wiedzę o nadprzewodzących materiałach. Precyzyjne doświadczenia wykazały, że w temperaturach niższych od T_c, przyczynek do ciepła właściwego związany z elektronami przewodnictwa ($C_{el.}$) zależy ekspotencjalnie od temperatury (wzór 2.6):

$$C_{el} = a exp\left(\frac{-\Delta_0}{k_B T}\right), \tag{2.6}$$

gdzie *a* oraz Δ_0 to pewne stałe. Tego typu wykładnicza zależność świadczy o wzbudzaniu elektronów do wyższego stanu energetycznego, oddzielonego od ich stanu podstawowego „odstępem energetycznym”, a więc wskazuje na istnienie przerwy energetycznej w widmie energetycznym elektronów przewodnictwa w stanie nadprzewodzącym [2,8,10]. Na Rys.2.7. przestawiono zależność ciepła elektronowego w funkcji T/T_c dla nadprzewodnika Re_6Hf. Powyżej temperatury krytycznej zależność C_{el} od T jest liniowa, tak jak w typowym metalu.

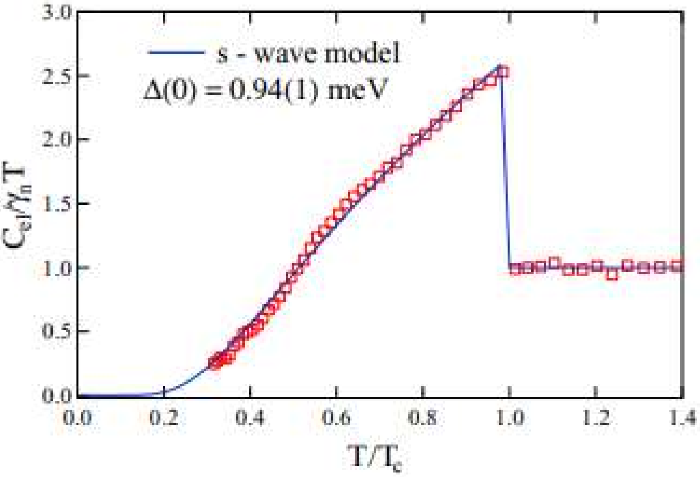

Rys.2.7. Zależność $C_{el}/\gamma_n T$ w funkcji T/T_c dla nadprzewodnika Re_6Hf [7].

2.1.6 Głębokość wnikania pola magnetycznego

Zadowalający opis nadprzewodnictwa przyniosła hipoteza zaproponowana przez braci Heinza oraz Fritza Londonów [14], która w oparciu o klasyczną elektrodynamikę (równania Maxwella i prawo Ohma), wyjaśniła zjawisko Meissnera oraz zakładała istnienie charakterystycznej głębokości wnikania. Otrzymany model przewiduje, że pole magnetyczne wnika do nadprzewodnika jedynie na pewną niewielką głębokość, zanikając ekspotencjalnie przy wzrastającej odległości od powierzchni próbki (wzór 2.7):

$$B(x) = Bexp(\frac{-x}{\lambda_L}), \tag{2.7}$$

gdzie *B(x)* jest indukcją magnetyczną na głębokości x wewnątrz materiału, a λ_L jest londonowską głębokością wnikania. Parametr λ_L, zdefiniowany wzorem 2.8, określa głębokość wnikania indukcji pola magnetycznego do wnętrza nadprzewodnika (na tej głębokości pole zmniejsza się e-krotnie względem wartości na powierzchni) [2,8,14]:

$$\lambda_L = \sqrt{\frac{m_e}{\mu_0 n_s e^2}}, \tag{2.8}$$

gdzie m_e - masa elektronu, μ_0 - przenikalność magnetyczna próżni, n_s - koncentracja nadprzewodzących elektronów oraz *e* – ładunek elektronu. Parametr ten o wymiarze długości jest charakterystyczny dla danego nadprzewodnika i odgrywa istotną rolę w określeniu jego własności.

2.1.7 Najważniejsze wyniki fenomenologicznej teorii Ginzburga-Landaua (G-L)

W latach pięćdziesiątych XX wieku została przedstawiona kolejna teoria, która w sposób pełniejszy opisywała zjawiska zachodzące w materiałach nadprzewodnikowych. Hipoteza, zaproponowana przed dwóch rosyjskich uczonych L. Landaua oraz W. Ginzburga [15], powstała na bazie ogólnej teorii przejść fazowych drugiego rodzaju. Pomimo tego, że teoria nie opisywała zjawiska nadprzewodnictwa na poziomie mikroskopowym, Ginzburg i Landau otrzymali doskonałe wyniki pokazujące związek pomiędzy makroskopowymi parametrami (dolnym i górnym polem krytycznym), a parametrami mikroskopowymi (głębokość wnikania pola magnetycznego do nadprzewodnika oraz długość koherencji) [2,8,10].

Bazując na teorii G-L otrzymano temperaturową zależność londonowskiej głębokości wnikania (λ) (wzór 2.9). W odróżnieniu od teorii Londonów, teoria G-L dopuszcza przestrzenną niejednorodność gęstości elektronów:

$$\lambda(T) = \sqrt{\frac{2b}{\mu_0 a(T_c - T)} \frac{m_e}{2e^2}}, \tag{2.9}$$

gdzie *a* i *b* to współczynniki spełniające warunek: *a* > 0, *b* > 0. Zależność λ_{GL} od temperatury jest więc funkcją potęgową $\left(1 - \frac{T}{T_c}\right)^{-1/2}$.

Kolejnym istotnym rezultatem wynikającym z teorii G-L jest wyznaczenie drugiego podstawowego parametru o wymiarze długości charakteryzującego nadprzewodnik – długości koherencji ξ. Przedstawioną wielkość można zdefiniować jako długość, na której gęstość elektronów nadprzewodzących maleje do zera. Ponieważ zdefiniowana wzorem 2.9 głębokość wnikania zależy od temperatury, a długość koherencji powinna mieć taką samą temperaturową zależność, zatem parametr ξ zależy od temperatury w następujący sposób [2,8,10]:

$$\xi(T)=\left(\frac{\hbar^2}{4m_e a(T_c-T)}\right)^{1/2}. \tag{2.10}$$

Zależność ξ od temperatury w modelu G-L jest więc również funkcją potęgową $\left(1-\frac{T}{T_c}\right)^{-1/2}$.

Jedynym stałym, niezależnym od temperatury parametrem jest parametr Ginzburga-Landaua ϰ, będący stosunkiem przedstawionych powyżej wielkości:

$$\varkappa=\frac{\lambda}{\xi}=\frac{m_e}{e\hbar}\sqrt{\frac{4b}{\mu_0}}. \tag{2.11}$$

Wykorzystując założenia wynikające z teorii Ginzburga-Landaua, można również oszacować górne i dolne pole krytyczne. Dolne pole krytyczne wyraża się wzorem:

$$H_{c1}=\frac{\Phi_0}{4\pi\mu_0\lambda^2}\ln\varkappa, \tag{2.12}$$

natomiast górne pole krytyczne w teorii G-L wyraża się za pomocą ϰ oraz termodynamicznego pola krytycznego $H_c(T)$:

$$H_{c2}=\sqrt{2}\varkappa H_c=\Phi_0\frac{1}{\mu_0 2\pi\xi^2}. \tag{2.13}$$

Rezultatem powyższego równania jest to, że stan mieszany może pojawiać się w polu większym od H_c tylko wtedy, gdy parametr ϰ jest większy od $1/\sqrt{2}$ – co jest zgodne z wynikami otrzymanymi eksperymentalnie. Na tej podstawie można stwierdzić, że [2,8–10]:

- jeżeli ϰ < $1/\sqrt{2}$, badany materiał jest nadprzewodnikiem pierwszego rodzaju (λ<<ξ),
- jeżeli ϰ > $1/\sqrt{2}$, badany materiał jest nadprzewodnikiem drugiego rodzaju (λ>>ξ).

Przedstawione powyżej parametry, powiązane są ze sobą następującą zależnościami:

$$H_c(T)\lambda(T)\xi(T)=\frac{\hbar}{2e\mu_0\sqrt{2}}=\frac{\Phi_0}{2\sqrt{2}\pi\mu_0}, \tag{2.14}$$

oraz

$$H_{c1}H_{c2}=H_c^2\ln\varkappa. \tag{2.15}$$

2.1.8 Najważniejsze wyniki teorii BCS

Właściwości mikroskopowe nadprzewodników opisuje teoria zaproponowana przez Johna Bardeena, Leona Coopera oraz Roberta Schrieffera, nazwana w literaturze teorią BCS [16,17]. Podstawą tej teorii jest założenie, że w stanie nadprzewodzącym pomiędzy nośnikami ładunku pojawia się oddziaływanie przyciągające, co prowadzi do utworzenia stanu związanego dwóch elektronów. Utworzenie pary Coopera jest możliwe za pośrednictwem drgań sieci krystalicznej (fononów). W uproszczeniu, poruszający się elektron, obdarzony ładunkiem ujemnym, deformuje strukturę dodatnio naładowanych rdzeni atomowych, co powoduje polaryzację sieci tzn. zagęszczenie dodatnich ładunków. W konsekwencji, drugi elektron o przeciwnym spinie i przeciwnie skierowanym wektorze falowym, może być przyciągany w stronę takich obszarów, co będzie źródłem sprzężenia między elektronami. Powstała w ten sposób para charakteryzuje się mniejszą energią w porównaniu do sumarycznej energii dwóch prawie swobodnych elektronów [2,8–10]. Przedstawiona teoria jest podstawą do zrozumienia i opisu mechanizmu nadprzewodnictwa w nadprzewodnikach konwencjonalnych.

W ramach teorii BCS otrzymano wyrażenie na długość koherencji, ξ_0, interpretowaną jako średnią odległość między elektronami tworzącymi parę Coopera (rozmiar przestrzenny pary):

$$\xi_0 = \frac{\hbar v_F}{\Delta} \tag{2.16}$$

gdzie v_F jest prędkością Fermiego. Jak widać ze wzoru (2.16), istnieje związek między długością koherencji, a szerokością przerwy energetycznej. Zaniedbując elastyczne rozpraszanie elektronów, powyższa wielkość jest powiązana z długością koherencji w teorii G-L wyrażeniem $\xi \sim 0.74\xi_0$ [18]. Dla przedstawionej sytuacji (ang. *clean limit*), współczynnik rozpraszania jest niski, a zatem elektrony mają długą średnią drogę swobodną (l_e) pomiędzy kolejnymi zderzeniami ($l_e >> \xi_0$). Jednakże, kiedy współczynnik rozpraszania będzie wysoki (ang. *dirty limit*), $l_e << \xi_0$, wtedy ξ będzie związana z ξ_0 relacją $\xi \propto \sqrt{\xi_0 l_e}$.

Z teorii BCS wyprowadzono także wyrażenie na temperaturę krytyczną (2.17):

$$T_c = 1.14\frac{\hbar\omega_D}{k_B}\exp(-\frac{1}{N(E_F)V}) \tag{2.17}$$

gdzie ω_D jest częstością Debye'a i z temperaturą Debye'a wiąże się relacją: $\hbar\omega_D/k_B = \Theta_D$, $N(E_F)$ jest gęstością stanów elektronowych na poziomie Fermiego dla jednego kierunku spinu, a V jest potencjałem parującym. Iloczyn $N(E_F)V$ równy jest wielkości λ_{ep} – bezwymiarowej stałej sprzężenia elektron-fonon. Parametr λ_{ep} pomaga sklasyfikować badany materiał jako nadprzewodnik słabo lub silnie sprzężony. Brak jest powszechnie akceptowanego kryterium stopnia sprzężenia i najczęściej przyjmuje się, że dla słabo sprzężonych nadprzewodników $\lambda_{ep} < 0.5$. Użyteczną zależność opisującą temperaturę krytyczną przejścia do stanu nadprzewodzącego podał McMillan (2.18) [19]:

$$T_c = \left(\frac{\Theta_D}{1.45}\right)\exp\left[-\frac{1.04(1+\lambda_{ep})}{\lambda_{ep}-\mu^*(1+0.62\,\lambda_{ep})}\right], \tag{2.18}$$

gdzie μ^* jest parametrem o wartościach z przedziału 0.1 – 0.15, wynikającym z siły odpychania Coulomba. Powyższy wzór umożliwia oszacowanie λ_{ep} wykorzystując łatwo mierzalne parametry (T_c oraz Θ_D).

Jednym z ważniejszych równań otrzymanych z teorii BCS jest relacja wiążąca wartość szerokości przerwy energetycznej $\Delta(0)$ z temperaturą krytyczną (2.19):

$$2\Delta(0) = 3.52k_BT_c. \tag{2.19}$$

2.2 Przegląd literaturowy badanych związków

2.2.1 $CeIr_3$ oraz $ThIr_3$

Pierwsze doniesienia literaturowe o dwuskładnikowych związkach $CeIr_3$ oraz $ThIr_3$ pochodzą z lat sześćdziesiątych ubiegłego wieku [20]. T.H. Geballe i in. opublikowali pracę, w której postulowali występowanie nadprzewodnictwa w temperaturach krytycznych wynoszących odpowiednio T_c = 3.34 K oraz T_c = 4.71 K dla $CeIr_3$ oraz $ThIr_3$. Należy podkreślić, że w powyższej pracy podano jedynie temperatury krytyczne i nie wyznaczono żadnych innych parametrów charakteryzujących stan nadprzewodnictwa. Jon Ce^{3+} jest magnetyczny, tym samym większość związków, w których zawarty jest Ce wykazuje właściwości antyferromagnetyczne lub ferromagnetyczne w niskich temperaturach. Ponieważ magnetyzm ma tendencję do zaburzania nadprzewodnictwa, występowanie tego zjawiska w związku z Ce jest niezwykle rzadką i interesującą osobliwością.

Struktura krystaliczna związku $CeIr_3$ określona została w pracach [21,22]. Sologub i in., zaproponowali, że $CeIr_3$ krystalizuje w trygonalnej strukturze krystalicznej (*R-3m* No.166) i należy do serii związków stanowiących szereg homologiczny $R_{2m+n}T_{4m+5n}$, gdzie *m* oraz *n* odpowiadają kolejno liczbie warstw (bloków) typu $MgCu_2$ oraz typu $CaCu_5$. Rys.2.8. przedstawia strukturę $CeIr_3$ zaczerpniętą z publikacji [22]. Jeśli *m* oraz *n* są równe 1, wówczas struktura krystaliczna jest typu $PuNi_3$, tym samym charakterystyczne warstwy ułożone są naprzemiennie. Wzajemne ułożenie poszczególnych warstw może znacząco wpływać na występowanie nadprzewodnictwa, mieszanej walencyjności czy też uporządkowania magnetycznego.

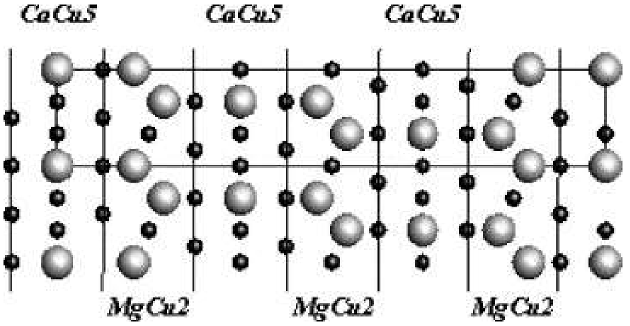

Rys.2.8. Struktura związku $CeIr_3$ w rzucie na płaszczyznę ac. Na rysunku zaznaczono ułożenie poszczególnych warstw typu $CaCu_5$ oraz $MgCu_2$ [22].

Co ciekawe, w literaturze nie pojawia się informacja o danych krystalograficznych dla $ThIr_3$ [20,23]. Związek nie znajduje się również w bazie materiałowej ICSD.

W 2018 roku ukazała się praca Y.J.Sato i in. [24] dotycząca właściwości nadprzewodzących związku $CeIr_3$. W publikacji [24] przedstawione zostały wyniki badań właściwości elektrycznych, cieplnych oraz magnetycznych (Rys.2.9), wykonane na monokryształach $CeIr_3$ otrzymanych metodą Czochralskiego. Autorzy pracy [24] sugerują, że $CeIr_3$ jest konwencjonalnym nadprzewodnikiem II-go rodzaju z T_c = 3.0 – 3.4 K (w zależności od pomiaru, z którego wyznaczona została temperatura krytyczna).

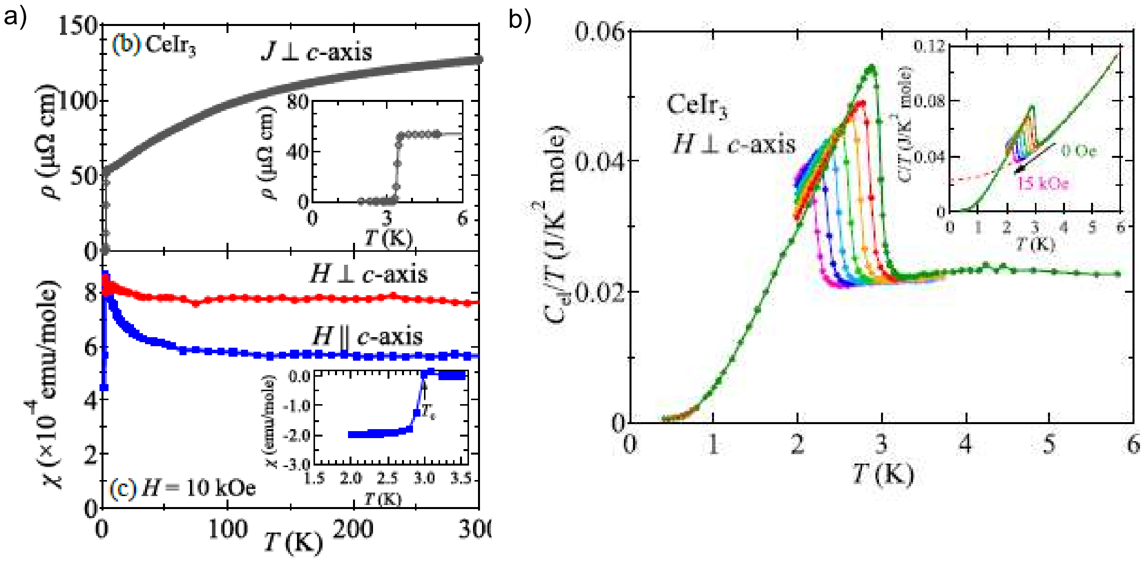

Rys.2.9.a) zależność oporności elektrycznej i podatności magnetycznej od temperatury; c) zależność C_{el}/T od temperatury dla monokryształu związku CeIr$_3$ [24].

Górny panel Rys.2.9(a) przedstawia temperaturową zależność oporności właściwej. W wysokich temperaturach autorzy zauważają tendencję oporu elektrycznego do nasycania. W niskich temperaturach obserwowany jest gwałtowny spadek *ρ(T)* do zera, świadczący o przejściu materiału do stanu nadprzewodzącego. Podatność magnetyczna w funkcji temperatury dla pola magnetycznego przyłożonego prostopadle do osi *c* oraz równolegle do osi *c*, przedstawiona została na panelu dolnym Rys.2.9(a). Zdaniem autorów [24], niemalże niezależna od temperatury podatność magnetyczna w wysokich temperaturach (T > 100 K) wskazuje na paramagnetyzm Pauli'ego. Wstawka przedstawia $\chi(T)$ w pobliżu temperatury krytycznej, gdzie obserwowane jest przejście materiału do stanu Meissnera. Objętościowy charakter nadprzewodnictwa w CeIr$_3$ potwierdzono badaniami ciepła właściwego, co zostało przedstawione na Rys.2.9(b). Szacowany, znormalizowany skok ciepła właściwego otrzymany przez autorów [24] wynosi $\Delta C/\gamma T_c = 1.39$.

Dla związku ThIr$_3$, do roku 2019, w literaturze można znaleźć jedynie informację o temperaturze krytycznej ($T_c = 4.71$ K) [20].

2.2.2 $CaRh_2$

Chociaż informacje o występowaniu stanu nadprzewodzącego w związku $CaRh_2$ pojawiły się ponad 60 lat temu [25], do 2019 roku jedynym znanym parametrem charakteryzującym nadprzewodnik była temperatura krytyczna wyznaczona eksperymentalnie przez B.T. Matthiasa [25] ($T_c = 6.4$ K). W publikacji [25] brak jest jakichkolwiek informacji na temat syntezy, metody pomiaru temperatury przejścia, innych parametrów stanu nadprzewodzącego.

Struktura krystaliczna związku $CaRh_2$ określona została przez E.A. Wooda oraz V.B. Comptona w 1957 roku [26]. $CaRh_2$ krystalizuje w strukturze regularnej (*Fd-3m* No. 227) typu Lavesa. Warto nadmienić, że ze względu na typ struktury, rodzinę Lavesa można podzielić na trzy grupy: fazę heksagonalną (*C14*) typu $MgZn_2$, fazę regularną (*C15*) typu $MgCu_2$ oraz fazę heksagonalną (*C36*) typu $MgNi_2$. W związkach, o ogólnym wzorze AB_2, większy atom *A* znajduje się w środku wielościanu zbudowanego z 16 atomów, natomiast mniejszy atom *B* mieści się w środku dwudziestościanów. Wielościany koordynacyjne zbudowane są zarówno z atomów *A* jak i *B*, co przedstawia Rys.2.10. Struktura regularna, w której krystalizuje $CaRh_2$, przedstawiona jest na Rys.2.10(a). Liczba koordynacyjna wynosi 12 dla atomu Rh (Rys. 2.10(b)) oraz 16 dla atomu Ca (Rys.2.10(c)).

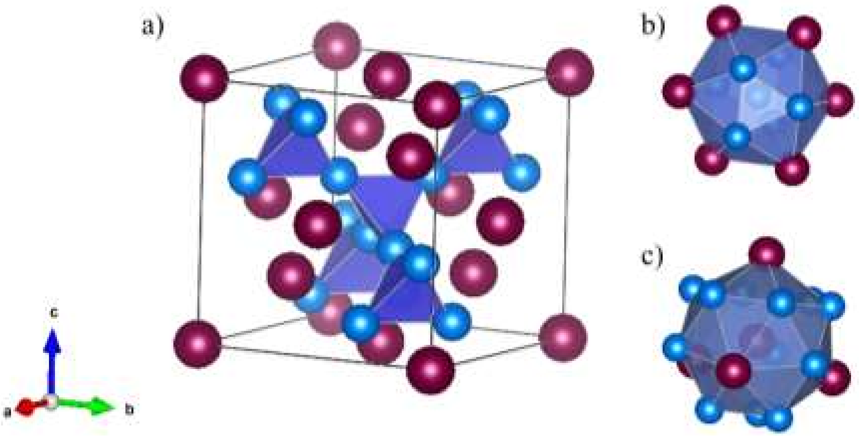

Rys.2.10. a) struktura regularna fazy Lavesa z wyróżnionymi tetraedrami; b) wielościan koordynacyjny otaczający atom Rh; c) wielościan typu Franka-Kaspera otaczający atom Ca. Rysunek wykonany w programie VESTA.

W 2015 roku, N. Haldolaarachchige i in. [27] scharakteryzowali właściwości fizyczne izoelektronowego odpowiednika związku $CaRh_2$, tj. $CaIr_2$. W ref. [27] autorzy przedstawili wyniki analizy strukturalnej, pomiarów magnetycznych, cieplnych oraz elektrycznych. Rys.2.11 prezentuje dyfraktogram rentgenowski oraz wyniki badań właściwości elektrycznych oraz magnetycznych uzyskane przez autorów pracy [27]. $CaIr_2$ również krystalizuje w strukturze regularnej typu Lavesa (*Fd-3m* No. 227).

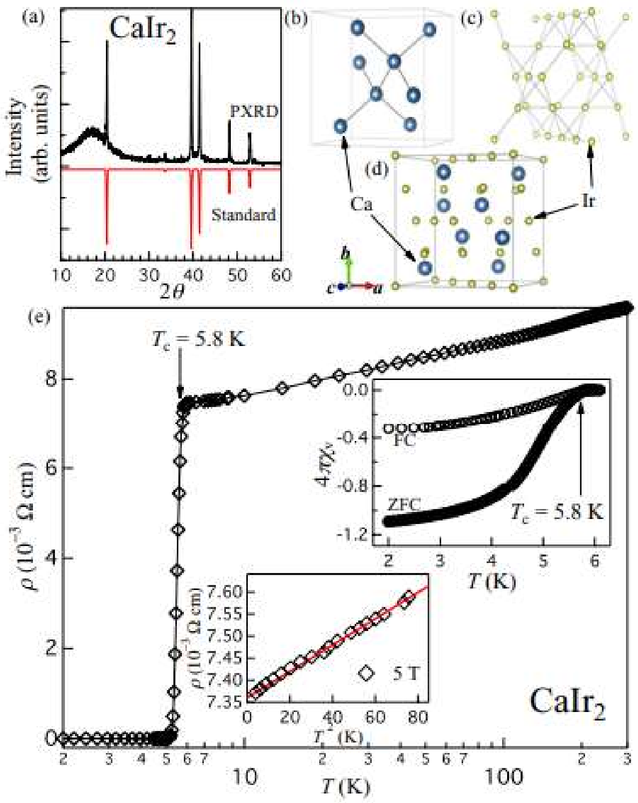

Rys.2.11. a) Dyfraktogram rentgenowski uzyskany dla związku CaIr$_2$; b-d) struktura regularna typu Lavesa wraz z wyróżnionymi podsieciami; e) oporność właściwa w funkcji temperatury. Wstawki przedstawiają zależność ρ od T^2 (dolna wstawka) oraz objętościową podatność magnetyczną w funkcji temperatury (wstawka górna) [27].

Spadek oporności do zera oraz przejście do stanu Meissnera wskazują na pojawienie się nadprzewodnictwa z T_c = 5.8 K. Na podstawie usyskanych wyników, między innymi dość niskiej wartości znormalizowanego skoku ciepła właściwego ($\Delta C/\gamma T_c$=0.89), autorzy [27] postulują, że CaIr$_2$ jest słabo sprzężonym nadprzewodnikiem II-rodzaju.

Obliczenia teoretyczne własności elektronowych i fononowych dla CaRh$_2$ zostały przedstawione przez G. P. Srivastava i in. [28] w 2017 roku. Obliczona struktura pasmowa, gęstość stanów elektronowych DOS(E) oraz krzywe dyspersji fononów dla związku CaRh$_2$ pokazano na Rys.2.12. Uzyskane wyniki sugerują, że dominujący wkład do DOS(E) w okolicy poziomu energii Fermiego mają stany elektronowe pochodzące od elektronów 4*d* atomu Rh. Potwierdza to wcześniejsze przypuszczenia, że w badanym materiale nadprzewodnictwo związane jest z atomami metalu przejściowego, podczas gdy rolą Ca jest stabilizowanie struktury. Obliczone krzywe dyspersji fononów, przedstawione na Rys.2.12(b) pokazują, że wszystkie mody fononowe mają dodatnie częstotliwości, co świadczy o stabilność związku CaRh$_2$ w regularnej strukturze typu MgCu$_2$. Widać również, że gałęzie wypełniają pełen zakres częstotliwości, nie pozostawiając przerwy między kolejnymi krzywymi dyspersji fononów. W szczególności, mody akustyczne oraz mody optyczne o niskiej częstotliwości charakteryzują się dość dużą dyspersją.

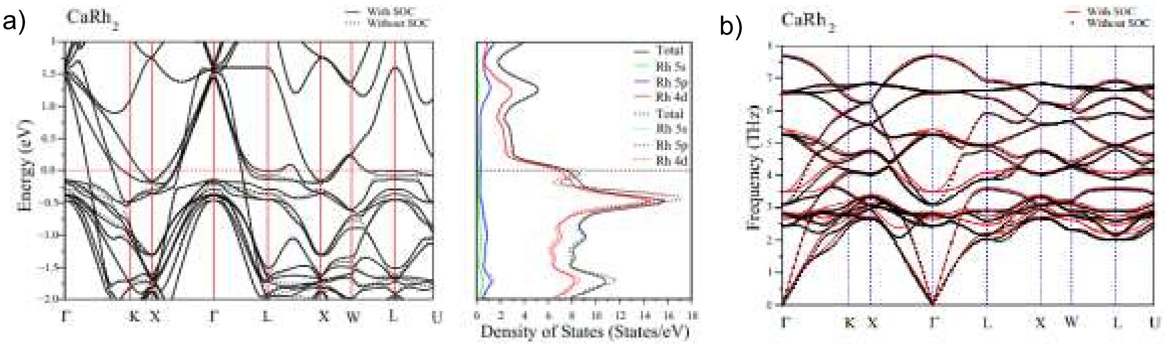

Rys.2.12. a) Obliczona struktura pasmowa oraz gęstość stanów elektronowych dla $CaRh_2$; b) Obliczone krzywe dyspersji fononów [28].

2.2.3 $LiPd_2Ge$ oraz $LiGa_2Ir$

Liczącą ponad 100 lat rodzinę związków typu Heuslera tworzą materiały o szerokiej gamie różnorodnych własności fizykochemicznych, które mogą znaleźć zastosowanie w obszarach spintroniki, fotowoltaiki, a także źródłach odnawialnych [29,30]. Pełne Heuslery, o stechiometrii X_2YZ, krystalizują w układzie regularnym ściennie centrowanym (*Fm-3m* No. 225), gdzie X jest najczęściej atomem metalu przejściowego grup 9-11, a Y oraz Z to metal przejściowy grupy 3-5, ziemi rzadkiej lub metal z bloku *p*. Struktura pełnego Heuslera przedstawiona została na Rys.2.13. Kolorem czerwonym oznaczone zostały atomy X obsadzające pozycję 8*c* (¼, ¼, ¼). Wbudowują się one w centrum komórki elementarnej tworząc sześcian. Atomy Y oraz Z, które obsadzają pozycje 4*a* (0,0,0) oraz 4*b* (½, ½, ½), oznaczono kolorem niebieskim i zielonym.

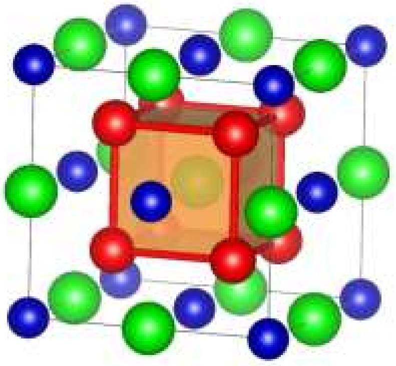

Rys.2.13. Struktura krystaliczna związków typu Heuslera Rysunek wykonany w programie VESTA.

Właściwości fizyczne faz Heuslera są silnie zależne od składu chemicznego oraz ilości elektronów walencyjnych (ang. *valence electron count* (VEC)) [30,31]. Dla ponad 70% Heuslerów wykazujących nadprzewodnictwo VEC = 27 lub 28 [31,32], co odpowiada 6.5 oraz 6.75 elektronom na atom. Odpowiada to wartościom leżącym idealnie w trzecim maksimum zależności temperatury krytycznej od ilości elektronów walencyjnych na atom (VEC/at.) [33]. Powyższa zależność została zaproponowana w latach 60-tych przez Matthiasa [33] i dość dobrze sprawdza się dla czystych metali [33], związków A15 [34] oraz pełnych Heuslerów [31]. Należy podkreślić, że do 2018 roku, dla wszystkich nadprzewodników typu Heuslera VEC było większe od 25, co odpowiada 6.25 el./at.

Pierwsze doniesienia literaturowe dotyczące związku $LiPd_2Ge$ pojawiły się na początku lat 70-tych. C.J. Kistrup oraz H.U. Schuster [35] opublikowali pracę, w której przedstawili dane krystalograficzne dla kilkunastu związków typu Heuslera na bazie Li, w tym również dla $LiPd_2Ge$. Wyznaczona przez autorów stała sieci krystalicznej $LiPd_2Ge$ wynosi a = 6.01Å.

W 2019 roku ukazała się praca autorstwa S. Ayhana oraz G.K. Balcia [36] zawierająca obliczenia teoretyczne dla serii związków LiX_2Ge (X: Rh, Cu, Ni, Pd). Rys.2.14. przedstawia strukturę pasmową, a także całkowitą oraz parcjalną gęstość stanów elektronowych (DOS(E)) dla związku $LiPd_2Ge$. W pobliżu poziomu energii Fermiego dominujący wkład do DOS(E) pochodzi od elektronów stanu 4*d* metalu przejściowego. Zgodnie z przeprowadzonymi obliczeniami $LiPd_2Ge$ powinien wykazywać charakter metaliczny, na co wskazuje brak przerwy energetycznej. Wartość DOS na poziomie energii Fermiego wynosi 0.99 stanów/eV. Liczba elektronów walencyjnych dla powyższego związku wynosi 25, co daje 6.25 elektronów na atom – wartość leżącą na początku trzeciego maksimum zależności T_c od VEC/at. [33].

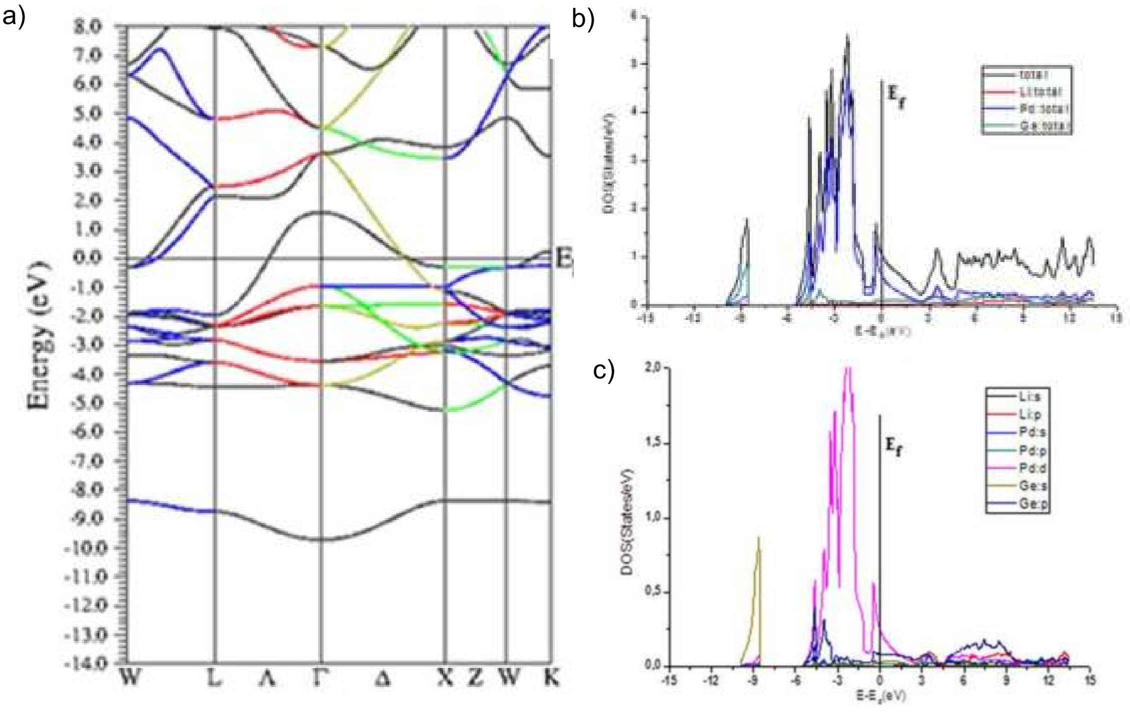

Rys.2.14. a) Obliczona struktura pasmowa; b) całkowita gęstość stanów elektronowych; c) częściowa gęstość stanów elektronowych dla związku $LiPd_2Ge$ [36].

Struktura drugiego z badanych związków, $LiGa_2Ir$, po raz pierwszy została opisana w publikacji A. Czybulki i in. [37]. W pracy z 1990 roku [37] przedstawiono dane krystalograficzne dla związków typu Heuslera zawierających Li, metal platynowca oraz Al, Ga lub In. Wyznaczona eksperymentalnie stała sieci dla $LiGa_2Ir$ wynosi a = 6.0 Å [37].

Obliczenia struktury elektronowej dla związków A_2MX oraz AMX_2 (A: Li; M:Rh, Pd, Ir, Pt; X:Al, Ga, In) przedstawione zostały przez L. Drews-Nicolai oraz G. Hohlneicher [38]. Struktura pasmowa oraz całkowita gęstość stanów elektronowych (DOS(E)) dla $LiGa_2Ir$ zostały pokazane na Rys.2.15.

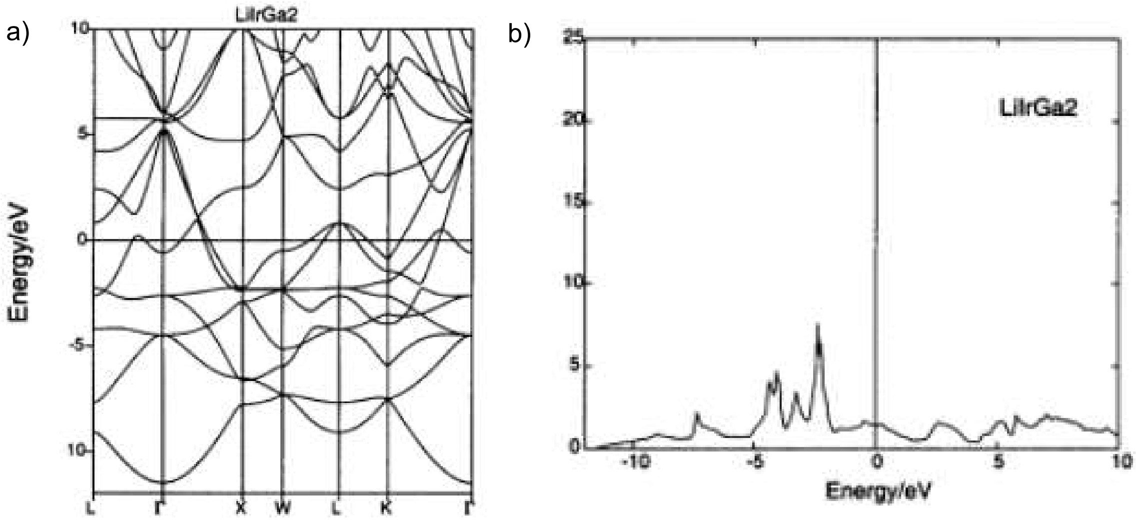

Rys.2.15. a) Obliczona struktura pasmowa; b) całkowita gęstość stanów elektronowych dla związku $LiGa_2Ir$ [38].

Otrzymane przez autorów [38] wyniki wskazują, że $LiGa_2Ir$ powinien być metalem z dominującym wkładem do DOS(E) pochodzącym od elektronów stanu *d* atomu Irydu. Do 2021 nie pojawiły się dane eksperymentalne opisujące właściwości fizyczne $LiGa_2Ir$.

W 2019 roku E.M. Carnicom i in. opublikowali pracę, w której opisali właściwości fizyczne $LiGa_2Rh$, w tym występowanie stanu nadprzewodzącego w T_c = 2.4 K [39]. Rys. 2.16 prezentuje wyniki z pomiaru ciepła właściwego. Główny panel przedstawia zależność C_p/T w funkcji temperatury (główny panel) i w funkcji T^2 (wstawka). Uzyskany znormalizowany skok ciepła właściwego ($\Delta C/\gamma T_c$=1.48) świadczy o objętościowym charakterze nadprzewodnictwa w $LiGa_2Rh$, jak również o dobrej jakości badanej próbki. Zdaniem autorów [39] $LiGa_2Rh$ jest słabo sprzężonym (λ_{ep} = 0.52) konwencjonalnym nadprzewodnikiem II-go rodzaju.

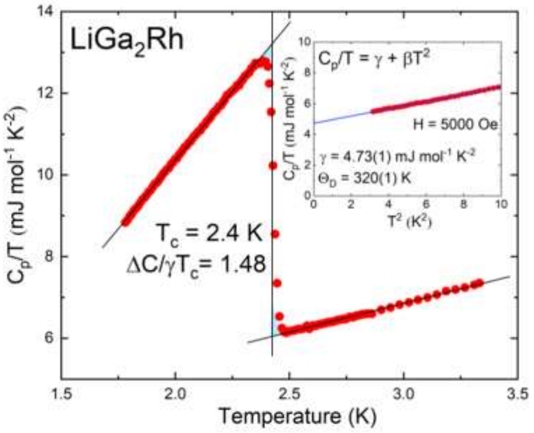

Rys.2.16. Zależność C_p/T w funkcji temperatury dla związku $LiGa_2Rh$. Wstawka: C_p/T w funkcji T^2 [39].

Liczba elektronów walencyjnych dla związku $LiGa_2Rh$ wynosi 16, co daje 4 elektrony na atom – wartość leżącą na początku drugiego maksimum zależności T_c od VEC/at. [33]. Według wiedzy autorki niniejszego doktoratu, jest to pierwszy związek typu Heuslera, w którym zaobserwowano nadprzewodnictwo dla VEC < 25.

2.2.4 LiBi

Pierwsze doniesienia literaturowe na temat związku LiBi pojawiają się w pracy [40] z 1935 roku, w której E.Zintl oraz G. Brauer przedstawili informacje dotyczące struktury krystalicznej. LiBi krystalizuje w strukturze tetragonalnej (*P4/mmm* No. 123), a stałe sieci przedstawione w ref. [40] wynoszą a = 3.361Å oraz c = 4.247Å.

17 lat później pojawiła się informacja o występowaniu stanu nadprzewodzącego w T_c = 2.49 K [42]. Doniesienie to zostało potwierdzone w 1970 roku przez T. Sambongi [41], który badał zmianę T_c pod wpływem ciśnienia dla związków Li^6Bi oraz $Li^{nat}Bi$. Wykres zależności T_c od ciśnienia (P) przedstawiono na Rys.2.17. Wyznaczona w warunkach normalnych temperatura przejścia do stanu nadprzewodzącego wynosi 2.455 K dla $Li^{nat}Bi$ oraz 2.47 K dla Li_6Bi. Otrzymana wartość jest w znakomitej zgodności z T_c zmierzoną przez N. I. Alekseevskii [42]. Według T. Sambongi zmiana T_c pod wpływem zewnętrznego ciśnienia wynosi -2.9×10^{-5} K/bar i nie zależy od masy izotopowej Li. Do 2020 roku jedynymi określonym parametrami charakteryzującym nadprzewodnik LiBi były temperatura krytyczna i jej zmiana pod wpływem ciśnienia.

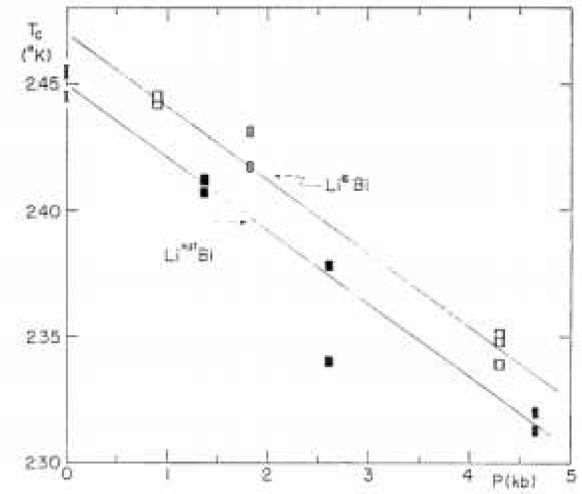

Rys.2.17. Zależność T_c od ciśnienia zewnętrznego dla związków Li^6Bi oraz $Li^{nat}Bi$ [41].

W 2014 roku zostały opisane właściwości nadprzewodzące izoelektronowego odpowiednika LiBi – NaBi. W pracy [43] przedstawione zostały wyniki eksperymentalne badań właściwości elektrycznych, magnetycznych oraz cieplnych dla monokryształu NaBi. Określona wartość temperatury krytycznej wynosi 2.15 K i jest nieznacznie niższa niż dla analogu z Li. Zdaniem autorów NaBi jest umiarkowanie sprzężonym nadprzewodnikiem II-go rodzaju ($\Delta C/\gamma T_c$=0.78, λ_{ep} = 0.62).

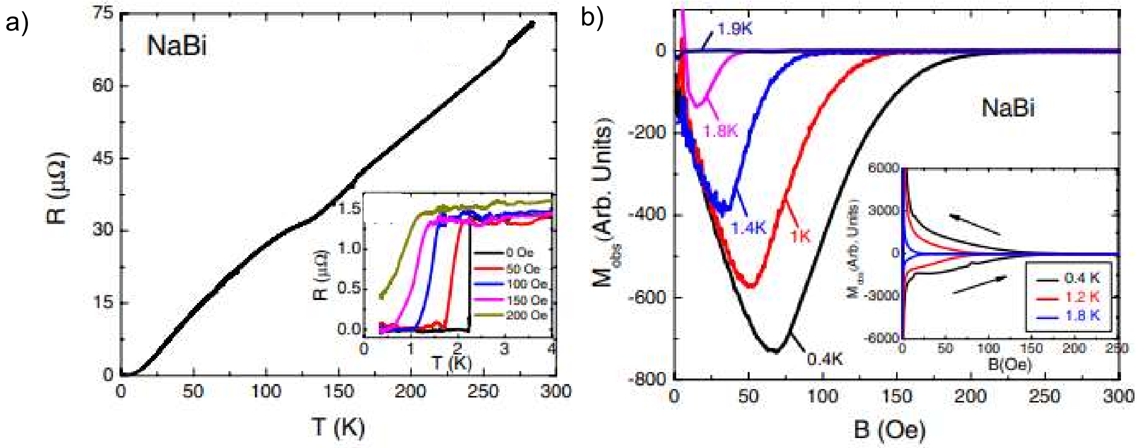

Rys.2.18. a) Temperaturowa zależność oporu. Wstawka: przejście do stanu nadprzewodzącego w zerowym i niezerowym polu magnetycznym; b) zależność namagnesowania od pola magnetycznego dla NaBi w stanie nadprzewodzącym. Wstawka: pętla histerezy zmierzona w trzech temperaturach [43].

Rys.2.18 (a) przedstawia wyniki pomiaru oporu elektrycznego (*R*) uzyskane przez S.K. Kushwaha i in. [43]. Uzyskana wartość RRR (wartość oporu w temperaturze 300 K/wartość oporu w 4.2 K) ~ 50 i świadczy o dobrej jakości mierzonej próbki. Wstawka przedstawia zależność *R* od *T* w pobliżu temperatury przejścia do stanu nadprzewodzącego. Wraz ze wzrostem przyłożonego pola magnetycznego, T_c przesuwa się w stronę niższych wartości, co jest zgodne z oczekiwaniami. Panel (b) prezentuje zależność namagnesowania (*M*) od zewnętrznego pola magnetycznego (*B*) zmierzoną w pięciu temperaturach (poniżej T_c). Zdaniem autorów [43] uzyskane krzywe *M*(*B*) potwierdzają nadprzewodnictwo II-go rodzaju z wartością dolnego pola krytycznego, w 0.4 K, H_{c1} = 30±10 Oe.

2.2.5 $NbIr_2B_2$ oraz $TaIr_2B_2$

$NbIr_2B_2$ oraz $TaIr_2B_2$ są nowymi związkami międzymetalicznymi krystalizującymi w nieznanej wcześniej strukturze krystalicznej (*Cc* No.9), a zatem w literaturze brak jest informacji o badanych w niniejszej pracy związkach. Należy również podkreślić, że do 2020 roku nie opisano ani jednego potrójnego borku w układach Nb-Ir-B oraz Ta-Ir-B.

W 2018 roku E.M. Carnicom i in. [44] opublikowali pracę, w której raportowano występowanie nadprzewodnictwa w dwóch nowych związkach boru: $NbRh_2B_2$ (T_c = 7.6(1) K) oraz $TaRh_2B_2$ (T_c = 5.8(1) K). Oba materiały krystalizują w układzie trygonalnym (*P3₁* No.144). Najważniejszymi cechami struktury *P3₁* jest jej chiralność oraz brak środka symetrii [44], co może znacząco wpływać na charakter występującego nadprzewodnictwa. Rys.2.19 przedstawia wyniki zaczerpnięte z publikacji [44]. Panel (a) prezentuje temperaturową zależność oporności elektrycznej (ρ) dla $NbRh_2B_2$. W niskich temperaturach zaobserwowano gwałtowny spadek oporności do zera, świadczący o przejściu materiału do stanu nadprzewodzącego. We wstawce przedstawiono wpływ zewnętrznego pola magnetycznego na temperaturę krytyczną. Warto podkreślić, że spadek ρ do zera jest także obserwowany dla maksymalnej wartości przyłożonego pola magnetycznego ($\mu_0 H$ = 14 T). Panel (b) pokazuje zależność $\mu_0 H_{c2}$ od temperatury dla obu związków. Wyznaczone wartości górnego pola krytycznego wynoszą 11.7(4) T dla $TaRh_2B_2$ oraz 18.0(4) T dla $NbRh_2B_2$. W obu przypadkach $\mu_0 H_{c2}(0)$ przekracza tzw. limit Pauli'ego ($\mu_0 H^{Pauli} = 1.85 T_c$), który wynosi odpowiednio 10.7(2) T dla związku z Ta oraz 14.1(2) T dla analogu z Nb. Większa od oczekiwanej dla konwencjonalnego (BCS) nadprzewodnika wartość górnego pola krytycznego była wcześniej obserwowana dla materiałów, w których nie występuje środek symetrii (np. $CePt_3Si$ [45]) i może świadczyć o niekonwencjonalnym charakterze zjawiska nadprzewodnictwa w potrójnych związkach $NbRh_2B_2$ i $TaRh_2B_2$.

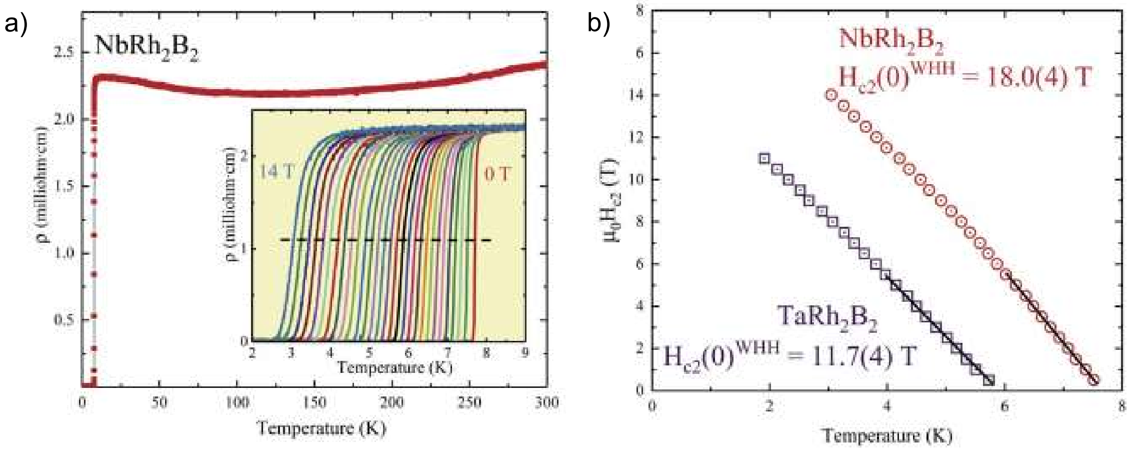

Rys.2.19. a) Temperaturowa zależność oporności elektrycznej dla $NbRh_2B_2$. Wstawka: przejście do stanu nadprzewodzącego w zerowym i niezerowym polu magnetycznym; b) zależność górnego pola krytycznego od temperatury dla dwóch związków [44].

Wykorzystując technikę spektrometrii relaksacji/rotacji mionów (μSR), D.A. Mayoh i in. [46] wykazali, że $TaRh_2B_2$ jest nadprzewodnikiem II-go rodzaju z dwoma nadprzewodzącymi przerwami energetycznymi (tzw. multigap superconductor), co może przekładać się na obserwowaną dużą wartość górnego pola krytycznego.

3. Cel pracy

Celem niniejszej pracy jest opisanie stanu nadprzewodzącego, w oparciu o teorie mikroskopowe nadprzewodnictwa indukowanego oddziaływaniem elektronów z siecią krystaliczną, w wybranych związkach międzymetalicznych. W pracy postawiono siedem hipotez badawczych będących uzupełnieniem stanu obecnej wiedzy w zakresie objętym pracą doktorską:

1. W międzymetalicznym związku $CeIr_3$ można spodziewać się występowania silnych korelacji elektronowych i innych egzotycznych właściwości fizycznych, jak np. mieszana lub pośrednia walencyjność (ang. *mixed/intermediate valency*), co w konsekwencji może wpływać na stan nadprzewodzący.
2. Związek $ThIr_3$ jest pierwszym przedstawicielem szeregu homologicznego $R_{2m+n}T_{4m+5n}$ (n=m=1) zawierającym pierwiastek aktynowca, w którym stan nadprzewodzący charakteryzuje się silniejszym sprzężeniem elektron-fonon niż w izoelektronowych odpowiednikach $LaIr_3$ oraz $CeIr_3$.
3. Postulowana dla związku rodziny faz Lavesa $CaRh_2$ temperatura przejścia do stanu nadprzewodzącego powinna być niższa niż dla $CaIr_2$.
4. Ponieważ znane są $LiPd_2X$, gdzie X = Ge i Sn, powinien występować również związek typu Heuslera dla X = Si, tj. $LiPd_2Si$. Co więcej, biorąc pod uwagę liczbę elektronów walencyjnych VEC = 25, materiały te powinny wykazywać metaliczny charakter przewodnictwa i być może również nadprzewodnictwo.
5. Ponieważ w niedawno opisanym związku typu Heuslera $LiGa_2Rh$ odkryto zjawisko nadprzewodnictwa, izoelektronowy $LiGa_2Ir$ podobnie powinien być nadprzewodnikiem, a postulowana temperatura krytyczna będzie wyższa niż dla $LiGa_2Rh$.
6. LiBi jest nadprzewodnikiem I-go rodzaju, w którym za nadprzewodnictwo odpowiadają kwadratowe sieci bizmutu,
7. Istnieją izoelektronowe odpowiedniki potrójnych związków $(Nb,Ta)Rh_2B_2$ z irydem, które wykazują właściwości nadprzewodzące.

Każda z hipotez była analizowana, a następnie weryfikowana poprzez badania eksperymentalne obejmujące syntezę oraz pomiary właściwości fizycznych. Na pełniejsze zrozumienie otrzymanych wyników pozwoliły obliczenia numeryczne własności elektronowych i fononowych wykonane przez grupę dr. hab. inż. Bartłomieja Wiendlochy. Uzyskane efekty zostały przedstawione w publikacjach naukowych wchodzących w skład niniejszej pracy doktorskiej.

Zakres przeprowadzonych badań eksperymentalnych obejmował syntezę związków w formie poli- oraz monokrystalicznej (LiBi), badania strukturalne prowadzone metodą proszkowej dyfrakcji rentgenowskiej oraz pomiary właściwości fizycznych (podatność magnetyczna, ciepło właściwe oraz opór elektryczny). Syntezę związków polikrystalicznych przeprowadzono metodą reakcji w fazie stałej lub topienia w łuku elektrycznym, natomiast materiał monokrystaliczny otrzymano metodą wzrostu z fazy ciekłej. Badania strukturalne obejmowały pomiary proszkową dyfrakcją rentgenowską przy użyciu dyfraktometru Bruker D2

Phaser. Analizę otrzymanych dyfraktogramów (metoda LeBaila lub Rietvelda) przeprowadzono przy użyciu oprogramowania *Topas* oraz *Fullprof Suite*. Wszystkie pomiary właściwości fizycznych przeprowadzono wykorzystując system pomiarowy *PPMS* (*Physical Property Measurement System, Quantum Design*) w zakresie temperatur 0.3 – 300 K oraz w polu magnetycznym do 9 T.

4. Wykaz artykułów wraz z ich opisem

W niniejszym rozdziale przedstawiono publikacje naukowe wchodzące w skład rozprawy doktorskiej. Artykuły opatrzone są uzasadnieniem podjęcia danego problemu badawczego, wskazaniem konkretnej hipotezy badawczej, krótkim opisem otrzymanych rezultatów, ze szczególnym uwzględnieniem wyników badań eksperymentalnych uzyskanych przez autorkę rozprawy, oraz załączoną oryginalną wersją artykułu opublikowanego w czasopiśmie (lub wysłanego do recenzji).

A1. **K. Górnicka**, E. M. Carnicom, S. Gołąb, M. Łapiński, B. Wiendlocha, W. Xie, D. Kaczorowski, R. J. Cava, T. Klimczuk,
$CeIr_3$: Superconductivity in a phase based on Tetragonally Close Packed (TCP) clusters
Superconductor Science and Technology 32 (2019) 025008 (13pp),

A2. **K. Górnicka**, Das D., Gutowska S., Wiendlocha B., Winiarski M., Klimczuk T., Kaczorowski D.
Iridium 5d -electron driven superconductivity in $ThIr_3$
Physical Review B -Vol. 100,iss. 21 (2019), s.214514,

A3. **K. Górnicka**, R. J. Cava, T. Klimczuk,
The electronic characterization of the cubic Laves-phase superconductor $CaRh_2$
Journal of Alloys and Compounds 793 (2019) 393e399,

A4. **K. Górnicka**, Kuderowicz G., Carnicom E., Kutorasiński K., Wiendlocha B., Cava R., Klimczuk T.
Soft-mode enhanced type-I superconductivity in $LiPd_2Ge$
Physical Review B -Vol. 102,iss. 2 (2020), s.1-13,

A5. **K. Górnicka**, G. Juderowicz, M.J. Winiarski, B. Wiendlocha, T. Klimczuk,
Superconductivity in $LiGa_2Ir$ Heusler type compound with VEC = 16
przesłane do Scientific Reports

A6. **K. Górnicka**, Gutowska S., Winiarski M., Wiendlocha B., Xie W., Cava R., Klimczuk T.
Superconductivity on a Bi Square Net in LiBi
Chemistry of Material -Vol. 32,iss. 7 (2020), s.3150-3159,

A7. **K. Górnicka**, X. Gui, B. Wiendlocha, L.T. Nguyen, W. Xie, R.J. Cava, T. Klimczuk
$NbIr_2B_2$ and $TaIr_2B_2$ – New Low Symmetry Noncentrosymmetric Superconductors with Strong Spin-Orbit Coupling;
Advanced Functional Materials 2021, 31, 2007960

4.1 (A1) $CeIr_3$: superconductivity in a phase based on tetragonally close packed clusters

4.1.1 Cel badawczy

Blisko pół wieku temu, Ted Geballe i inni w ref. [20] podali temperatury przejścia do stanu nadprzewodzącego dla podwójnych związków należących do rodziny $R_{2m+n}T_{4m+5n}$: $LaRh_3$, $LaIr_3$, YIr_3, YRh_3, $LuIr_3$ oraz $CeIr_3$. Ponieważ wewnętrzny magnetyzm najczęściej prowadzi do rozrywania par Coopera, istotną kwestią pozostaje opis mechanizmu nadprzewodnictwa w związku zawierającym cer.

Należy jednak pamiętać, że znane są związki międzymetaliczne, w których obserwowane jest współistnienie nadprzewodnictwa i ferromagnetyzmu, np. związki na bazie uranu UGe_2, UIr, URhGe oraz UCoGe [47–50]. Co najciekawsze, elektrony pochodzące z powłoki 5*f* atomów uranu, odpowiedzialne są zarówno za uporządkowanie ferromagnetyczne, jak i za pojawienie się zjawiska nadprzewodnictwa. Przykładem związku o takich unikalnych właściwościach jest także antyferromagnetyczny dwuskładnikowy związek ciężkofermionowy - $CeIn_3$ dla którego temperatura Néela T_N = 10 K (p = 0 GPa), T_c = 200 mK (p = 2.6 GPa) [51].

Niezwykle ważnym aspektem w nadprzewodnikach zawierających Ce jest wartościowość tego jonu. Szczegółowe badania właściwości fizycznych $CeIr_3$ są niezbędne do weryfikacji **hipotezy 1**, która zakłada występowanie mieszanej walencyjności jonu Ce.

Związek $CeIr_3$ w postaci monokrystalicznej został w 2018 roku zbadany przez autorów ref. [24]. Badania zaprezentowane w artykule A1 dla polikrystalicznego $CeIr_3$ rozszerzają wyniki pomiarów otrzymanego przez Y.J Sato [24] dla monokrystalicznego odpowiednika.

Celem badań opisanych w publikacji A1 było wyznaczenie parametrów charakteryzujących stan nadprzewodzący i normalny w $CeIr_3$, szczegółowy opis struktury krystalicznej oraz określenie walencyjności jonu Ce. Badania eksperymentalne obejmowały proszkową dyfrakcję rentgenowską, rentgenowską analizę strukturalną monokryształów (prof. Weiwei Xie), spektroskopię fotoelektronów w zakresie promieniowania X (XPS) (dr inż. Marcin Łapiński), pomiary transportowe, cieplne oraz magnetyczne. Szczegółowe badania właściwości fizycznych zostały uzupełnione obliczeniami struktury elektronowej (mgr inż. Sylwia Gołąb, dr hab. inż. Bartłomiej Wiendlocha).

4.1.2 Opis rezultatów

Synteza polikrystalicznej próbki $CeIr_3$ została przeprowadzona metodą topienia w piecu łukowym w atmosferze argonu o bardzo wysokiej czystości (5N), w połączeniu z późniejszym wygrzewaniem w temperaturze 1370℃ przez 12 godzin w warunkach wysokiej próżni (p = 10^{-6} Torr). Tak otrzymaną próbkę utarto, sprasowano i ponownie wygrzewano w temperaturze 1400℃ przez 36 godzin w wysokiej próżni.

Badania strukturalne metodą proszkowej dyfrakcji rentgenowskiej potwierdziły, że $CeIr_3$ krystalizuje w strukturze trygonalnej (*R-3m* No.166). Jak wspomniano w rozdziale 2.2.1, Sologub i in. [22], zaproponowali, że $CeIr_3$ należy do serii związków stanowiących szereg homologiczny $R_{2m+n}T_{4m+5n}$, gdzie *m* oraz *n* odpowiadają kolejno liczbie warstw (bloków) typu $MgCu_2$ oraz typu $CaCu_5$. Przeprowadzona przez nas szczegółowa analiza struktury krystalograficznej pokazuje, że jeden z bloków odpowiada strukturze $MgZn_2$, a nie jak dotychczas sądzono regularnej strukturze $MgCu_2$, która posiada inną symetrię niż romboedryczna struktura *R-3m*. Strukturę $CeIr_3$ można rozpatrzeć jako naprzemienne warstwy związków $CeIr_2$ oraz $CeIr_5$ krystalizujące odpowiednio w strukturach typu $MgZn_2$ oraz $CaCu_5$.

Wykonane w pierwszej kolejności niskotemperaturowe badania podatności magnetycznej, potwierdziły przejście ze stanu normalnego w stan nadprzewodzący w T_c = 2.5 K. Krzywe namagnesowania w funkcji zewnętrznego pola magnetycznego pozwoliły na wyznaczenie wartości dolnego pola krytycznego ($\mu_0 H_{c1}(0)$ = 17.3 mT). Pełna pętla namagnesowania, wykonana w T = 2 K, potwierdziła nadprzewodnictwo II-go rodzaju w $CeIr_3$. Badania własności transportowych oraz cieplnych potwierdziły występowanie przejścia do stanu nadprzewodzącego. Na temperaturowej zależności oporności elektrycznej zaobserwowano spadek do zera w temperaturze krytycznej T_c = 2.75 K, która przesuwa się w stronę niższych wartości wraz ze wzrostem przykładanego pola magnetycznego. Uzyskane dane pozwoliły na określenie górnego pola krytycznego ($\mu_0 H_{c2}(0)$ = 3.5 T). Oszacowana wartość jest niższa od oczekiwanej dla teorii BCS ($\mu_0 H^{Pauli}(0) = 1.85 T_c$ = 4.6 T).

Na objętościowy charakter nadprzewodnictwa w badanym związku wskazuje skok ciepła właściwego obserwowany w pobliżu temperatury krytycznej (T_c = 2.46 K). Oszacowany znormalizowany skok ciepła właściwego wynosi $\Delta C/\gamma T_c$ = 1.24 i jest nieznacznie niższy od wartości wynikającej z teorii BCS ($\Delta C/\gamma T_c$ = 1.43). Wykorzystując wzory przedstawione w części teoretycznej wyznaczono: parametr sprzężenia elektron-fonon (λ_{ep} = 0.65), długość koherencji (ξ_{GL} = 97 Å), głębokość wnikania (λ_{GL} = 1640 Å) oraz parametr Ginzburga-Landaua ($\kappa_{GL} = 17$). Przedstawione w publikacji A1 wyniki wskazują, że $CeIr_3$ jest umiarkowanie sprzężonym nadprzewodnikiem II-go rodzaju.

Wyliczona wartość objętości komórki elementarnej $CeIr_3$ zdecydowanie odbiega od liniowego trendu (V vs r_{RE}) obserwowanego dla innych związków rodziny $REIr_3$ (RE = La, Pr, Nd, Gd oraz Ce), dla których walencyjność jonu ziemi rzadkiej wynosi +3. Wyraźne odchylenie od liniowości sugeruje, że walencyjność Ce w $CeIr_3$ nie wynosi +3, jak dla pozostałych lantanowców. Powyższe stwierdzenie zostało potwierdzone eksperymentalnie przy użyciu metody badania XPS. Dla trójwartościowego Ce główne linie fotoemisyjne pochodzą od stanów elektronowych $3d^9 4f^1$, natomiast na widmie XPS obserwuje się również maksima pochodzące od stanów $3d^9 4f^0$, co sugeruje mieszaną wartościowość jonu Ce w $CeIr_3$.

Mieszaną walencyjność jonu Ce potwierdza również analiza podatności magnetycznej zmierzonej w zakresie temperatur 3 - 300 K (stan normalny). Podatność magnetyczna wykazuje wiele cech charakterystycznych dla związków międzymetalicznych zawierających Ce z pośrednią walencyjnością tj. nieznaczna wartość χ i jej słaba zależność od temperatury powyżej

50 K. Wyraźny wzrost $\chi(T)$ obserwowany w niskich temperaturach można przypisać obecności niewielkiej ilości zanieczyszczeń magnetycznych. Mogą to być tlenki ceru i/lub nieskompensowane jony Ce^{+3} znajdujące się między ziarnami krystalicznymi lub na powierzchni badanego materiału.

Obliczenia numeryczne własności elektronowych potwierdzają pośrednią walencyjność jonu Ce, a także pokazują że dominujący wkład do DOS(E) w okolicy poziomu energii Fermiego mają stany elektronowe pochodzące od elektronów 5*d* atomu Ir.

4.1.3 Treść artykułu A1

4.1.3 Treść artykułu A1

Tytuł: $CeIr_3$: superconductivity in a phase based on tetragonally close packed clusters

Autorzy: Karolina Górnicka, Elizabeth M. Carnicom, Sylwia Gołąb, Marcin Łapiński, Bartłomiej Wiendlocha, Weiwei Xie, Dariusz Kaczorowski, Robert J. Cava, Tomasz Klimczuk

Czasopismo: Supercond. Sci. Technol. 32 (2019) 025008 (13pp)

Impact factor: 3.067 (2019)

Liczba punktów ministerialnych MNiSW: 100 pkt

DOI: 10.1088/1361-6668/aaf48f

Mój udział polegał na syntezie próbki polikrystalicznej, przeprowadzeniu badań strukturalnych metodą proszkowej dyfrakcji rentgenowskiej wraz z analizą LeBaila otrzymanego dyfraktogramu, pomiarach właściwości magnetycznych, cieplnych, elektrycznych wraz z analizą wyników, udziale w dyskusji otrzymanych rezultatów, wyznaczeniu parametrów charakteryzujących stan normalny i nadprzewodzący, przygotowaniu rysunków oraz tekstu manuskryptu części eksperymentalnej obejmującej wyniki wyżej wymienionych pomiarów. Pełniłam rolę autora korespondencyjnego oraz przygotowałam odpowiedzi na recenzje. Kierowałam również projektem naukowym (Diamentowy Grant, MNiSW) obejmującym badania opisane w pracy.

Karolina Górnicka
mgr inż. Karolina Górnicka

„Republished with permission of IOP Publishing, from $CeIr_3$: superconductivity in a phase based on tetragonally close packed clusters Karolina Górnicka, Elizabeth M. Carnicom, Sylwia Gołąb, Marcin Łapiński, Bartłomiej Wiendlocha, Weiwei Xie, Dariusz Kaczorowski, Robert J. Cava, Tomasz Klimczuk, Supercond. Sci. Technol. 32 (2019) 025008 (13pp); permission conveyed through Copyright Clearance Center, Inc.”

IOP Publishing
Superconductor Science and Technology
Supercond. Sci. Technol. **32** (2019) 025008 (13pp)
https://doi.org/10.1088/1361-6668/aaf48f

CeIr$_3$: superconductivity in a phase based on tetragonally close packed clusters

Karolina Górnicka[1], Elizabeth M Carnicom[2], Sylwia Gołąb[3], Marcin Łapiński[1], Bartłomiej Wiendlocha[3], Weiwei Xie[4], Dariusz Kaczorowski[5], Robert J Cava[2] and Tomasz Klimczuk[1]

[1] Faculty of Applied Physics and Mathematics, Gdansk University of Technology, ul. Narutowicza 11/12, 80-233 Gdańsk, Poland
[2] Department of Chemistry, Princeton University, Princeton, NJ 08544, United States of America
[3] Faculty of Physics and Applied Computer Science, AGH University of Science and Technology, Aleja Mickiewicza 30, 30-059 Kraków, Poland
[4] Department of Chemistry, Louisiana State University, Baton Rouge, LA 70803, United States of America
[5] Institute of Low Temperature and Structure Research, Polish Academy of Sciences, PO Box 1410, 50-950 Wrocław, Poland

E-mail: karolina.gornicka@pg.edu.pl

Received 30 August 2018, revised 12 November 2018
Accepted for publication 28 November 2018
Published 10 January 2019

Abstract

We present the crystallographic analysis, superconducting and spectroscopic characterization, and theoretical modeling of CeIr$_3$. Lattice parameters $a = 5.2945(1)$ Å and $c = 26.219(1)$ Å are found for the R-3m symmetry crystal structure, which are close to the literature values. CeIr$_3$ is a moderate type-II superconductor ($\kappa_{GL} = 17$, $\lambda_{e-p} = 0.65$) below 2.5 K. Ce ions exhibit a strongly intermediate valence character as evidenced by x-ray photoelectron spectroscopy. The normal state magnetic susceptibility is weakly temperature dependent and follows the inter-configuration fluctuation model with a singlet Ce$-4f^0$ ground state. Theoretical calculations support a non-magnetic ground state of the system and reveal that Ir$-5d$ states are dominant at the Fermi level.

Keywords: superconductivity, intermetallic compounds, crystal structure

(Some figures may appear in colour only in the online journal)

1. Introduction

For several years, superconductivity emerging on the verge of electronic instability, e.g. of a magnetic nature, has attracted much attention owing to its possible unconventional character. In this context, materials bearing *d*- and *f*-electrons are particularly interesting, since their electronic properties are often dominated by strong spin–orbit coupling (SOC). Recently, within the family of Ce-based heavy fermion superconductors [1, 2], the most intensively studied compounds have been those from a homologous series Ce$_nT_m$In$_{3n+2m}$, where T = Co, Rh, Ir, Pd or Pt, forming with tetragonal crystal structures built of n layers of CeIn$_3$ (AuCu$_3$ type) and m layers of TIn$_2$ (HgTe$_2$ type).

A related homologous series [3] is $RE_{2m+n}T_{4m+5n}$, where m and n represent the number of MgCu$_2$- and CaCu$_5$-type blocks, respectively. In this formula, *RE* stands for an early rare earth metal (La–Gd) and T is a transition metal: Ir or Rh. In contrast to Ce$_nT_m$In$_{3n+2m}$, this series has not been intensively studied and only a few compounds with the stoichiometry RET_3 ($m = 1$, $n = 1$) and RE_2T_7 ($m = 1$, $n = 2$) have been reported [4, 5]. This is likely caused by a difficult synthesis process. Although a binary compound in this group, CeIr$_3$, was reported as a superconductor more than 50 years ago [5], details on its superconducting state were reported only recently [6]. Here, we describe the synthesis and characterization of polycrystalline CeIr$_3$ by means of dc magnetization, electrical resistivity and heat capacity measurements. In addition, in

0953-2048/19/025008+13$33.00

order to examine the valence of Ce ions, an x-ray photoelectron spectroscopy (XPS) study was performed. The experimental data are supplemented by electronic structure calculations.

2. Experimental

Polycrystalline samples of nominal composition $CeIr_3$, $Ce_{1.03}Ir_3$ and $Ce_{1.05}Ir_3$ were synthesized by arc-melting cerium (4N) and iridium (3N5) in an arc furnace (MAM-1 Edmund Buhler GmbH) on a water-cooled copper hearth using a tungsten electrode under a high purity argon atmosphere. A piece of zirconium was used as an oxygen getter. First, a button of Ir was prepared by arc-melting iridium powder alone. The Ir ingot was then melted with Ce pieces with 3% excess to compensate for the expected loss of Ce. After the initial melt, the sample button was turned and re-melted four to five times to improve homogeneity. Mass loss during the synthesis was lower than 1%, and the sample button formed was uniform, hard and silvery gray in color. The samples obtained were then wrapped in tantalum foil and annealed at 1370 °C for 12 h under high vacuum (10^{-5} Torr). Subsequently, the resulting material was ground well, pressed into a pellet using a hydraulic press and then heated under high vacuum to 1400 °C and held at this temperature for 36 h.

The crystal structure of $CeIr_3$ was confirmed using a Bruker Apex II x-ray single crystal diffractometer with Mo Kα1 radiation ($\lambda = 0.710\,73$ Å). The room temperature intensity data were collected for a crystal taken from the nominally $Ce_{1.03}Ir_3$ sample, over a full sphere of reciprocal space with 0.5° scans in ω, 10 s per frame of exposure time, and a 2θ ranging from 4° to 75°. The SAINT program [7] was used to both extract intensities and to correct for polarization and Lorentz effects and the XPREP program [8] was used to perform face-indexed numerical absorption corrections. Twinning of the unit cell was tested using the Cell_Now program. The crystal structure of $CeIr_3$ was solved using direct methods and refined by full-matrix least-squares on F^2 with the SHELXTL package [9].

The structure and phase purity of the samples at room temperature was evaluated by powder x-ray diffraction (pXRD) on a Bruker D8 Advance Eco diffractometer (Cu Kα), equipped with a LynxEye-XE detector. X-ray analysis was performed on well-ground powder of the $CeIr_3$ sample. XPS was performed using an Argus (Omicron Nano-Technology) x-ray photoelectron spectrometer. The photoelectrons were excited by a Mg-Kα x-ray source operated at 15 keV and 300 W. The XPS measurement was performed at room temperature under ultra-high vacuum conditions, at pressures below 1.1×10^{-8} mbar. It is known that cerium on surfaces tends to exist as Ce^{3+} rather than Ce^{4+} [10]. To avoid this potential issue, the $CeIr_3$ sample was sputter-cleaned by Ar ions *in situ* (FDG 150 ion source mounted in the analytic chamber) before the XPS measurement. Data analysis was performed with the CASA XPS software package using a Shirley background subtraction and least-square Gaussian–Lorentzian curve fitting algorithm. The spectra obtained were calibrated to give a binding energy of 285.00 eV for C 1 s.

Magnetization measurements were carried out using a Quantum Design Dynacool Physical Property Measurement System (PPMS) with a vibrating sample magnetometer function. Both zero-field-cooled (ZFC) and field-cooled (FC) data were collected from 1.7 to 3 K under an applied field of 20 Oe. The magnetization was also measured at various temperatures in the superconducting state as a function of applied field. ZFC magnetic susceptibility was measured from 3 to 300 K under 1 kOe field. Resistivity and heat capacity measurements were performed on a PPMS Evercool II. Temperature- and magnetic field-dependent electrical transport measurements were made using a standard four-probe technique. For these experiments, 37 μm diameter platinum wire leads were spark-welded to the sample surface. The two-τ time-relaxation method was used to measure the specific heat in magnetic fields up to 2 T.

Electronic structure calculations were performed using the full-potential linearized augmented plane-wave method with local orbitals (LAPW + LO) and the Perdew–Burke–Ernzerhof generalized gradient approximation (GGA) exchange-correlation potential, as implemented in the WIEN2k package [11]. To account for the possible strong Coulomb interaction effect due to the presence of the *4f*-electrons of cerium, the GGA+U [12] method was used. We determined the magnitude of the U-parameter for the $4f$ states of Ce with the help of the impurity method [13]. As a result, $U = 6$ eV was obtained, which agrees with the typically used value of the effective $U_{eff} = U - J = 5$ eV, as J is on the order of 1 eV [14]. This value of the effective $U_{eff} = 5$ eV was then used in our studies. We also performed additional calculations using the onsite-exact-exchange hybrid Fock approximation [15], with the standard value of the parameter $\alpha = 0.25$ (see, [15]), and both methods gave similar results. The self-interaction correction double-counting correction method was used, as the around-mean field (AMF) method predicted quite large magnetic moments on Ce atoms (0.5–1 μ_B), which were not observed in our experiment. The unit cell volume was optimized in the calculations, but the experimental parameters changed only slightly: a by about 0.6% and c by about 1.1%, which did not significantly affect the calculated electronic structure of this compound. To clarify the effect of Coulomb interactions, both GGA and GGA+U methods were employed, with SOC included in each case.

3. Results and discussion

The single crystal diffraction experiments confirmed the crystal structure [4] of $CeIr_3$, which forms in the space group R-3m (No. 166), where $a = 5.304(4)$ Å and $c = 26.273(20)$ Å. Crystallographic data and the refined positions for a crystal obtained from the nominal $Ce_{1.03}Ir_3$ composition are gathered in tables 1 and 2, respectively. It should be noted that the refined stoichiometry of the single crystal studied was $Ce_{0.96(2)}Ir_3$ (from the sample also used for all physical

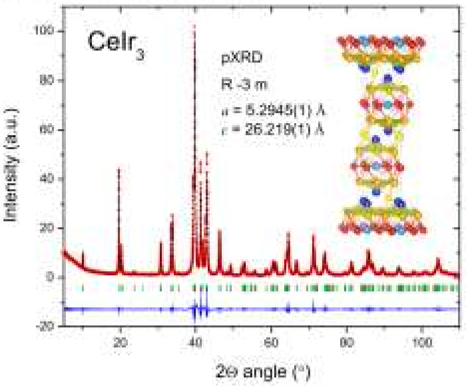

Figure 1. Powder x-ray diffraction pattern (red points) together with the LeBail refinement profile (black solid line) for $\mathrm{CeIr_3}$. The green vertical bars indicate the expected Bragg peak positions. The blue curve is the difference between experimental and model results.

Table 1. Crystallographic data for $\mathrm{CeIr_3}$ at 175(2) K.

$\mathrm{CeIr_3}$	
F.W. (g mol^{-1});	716.72
Space group; Z	R-3m (No.166); 9
Lattice parameters	$a = 5.280$ (4) Å $c = 26.166$ (20) Å
Volume (Å^3)	640 (1)
Absorption correction	Numerical
Θ range (deg)	2.335 to 33.058
hkl ranges	$-8 \leqslant h, k \leqslant 8$ $-39 \leqslant l \leqslant 39$
No. reflections; R_{int}	3239; 0.1041
No. independent reflections	347
No. parameters	18
R_1; wR_2 (all I)	0.0558; 0.1185
Goodness of fit	1.000
Diffraction peak and hole (e$^-$ Å^{-3})	5.150; −4.140

measurements)—within two standard deviations of the ideal 1:3 composition, which is thus taken as the formula of the compound. The space group and lattice parameters obtained were taken as the starting point for the LeBail fit of the pXRD pattern shown in figure 1. The fit is excellent and there is no impurity phase observed in the pXRD pattern of the sample whose properties were studied. The estimated lattice parameters from the LeBail fit ($a = 5.2945(1)$ Å, $c = 26.219(1)$ Å) are in very good agreement with the single crystal diffraction results as well as with those reported in the literature [3, 4, 6, 16].

An expanded view of the unit cell and the atomic coordination polyhedra for $\mathrm{CeIr_3}$ are shown in figure 2. It has previously been proposed that $\mathrm{CeIr_3}$ can be considered as a stacking of cubic $\mathrm{MgCu_2}$-type and $\mathrm{CaCu_5}$-type layers [3] but the cubic $\mathrm{MgCu_2}$-type and rhombohedral $\mathrm{CeIr_3}$ structures have different symmetry. Considering the similar polyhedral environments in both cubic and hexagonal Laves phases, we rather describe $\mathrm{CeIr_3}$ as a combination of stacking hexagonal $\mathrm{MgZn_2}$-type and $\mathrm{CaCu_5}$-type layers (figure 2).

The polyhedral environments for all atomic sites in $\mathrm{CeIr_3}$ are Frank−Kasper polyhedral [17]. One Ce site is surrounded by a 16-vertex polyhedron consisting of Ir atoms and the other Ce site is centered within a truncated tetrahedron of 12 Ir atoms. The Ir sites are coordinated by distorted icosahedra of six Ce and six Ir atoms, three Ce and nine Ir atoms, and five Ce and seven Ir atoms. Such Frank−Kasper polyhedra are signature building blocks of tetrahedrally close packed (tcp) solids. Typical examples of tcp solids include the cubic $\mathrm{MgCu_2}$-type and hexagonal $\mathrm{MgZn_2}$-type Laves phases, $\mathrm{CaCu_5}$-type compounds, and α-Mn. We argue that in this context $\mathrm{CeIr_3}$ can best be seen as consisting of stacked layers of $\mathrm{CeIr_2}$ in a hexagonal $\mathrm{MgZn_2}$-type structure and $\mathrm{CaCu_5}$-type $\mathrm{CeIr_5}$. These structure types, consisting of densely packed tetrahedral clusters, are known to be good hosts for superconductivity.

For the purposes of the electronic structure calculations, which will be discussed further, a primitive cell must be considered, and so we also present an alternative description of the structure of $\mathrm{CeIr_3}$. The primitive cell of $\mathrm{CeIr_3}$ contains three formula units. There are two non-equivalent positions of Ce and three of Ir. In the crystal structure shown schematically in the inset of figure 1 one can distinguish a metallic plane consisting of Ir(18*h*) and a plane consisting of hexagons of Ir(6*c*) centered at Ce(3*a*)—they are Kagome-like 2D sublattices that are also found in the $\mathrm{CeIr_5}$ structure. The latter plane is situated in the middle between two metallic planes such that each Ir(6*c*) has six nearest neighbors Ir(18*h*) and form with them two nearly non-distorted tetrahedra (Ir(18*h*)–Ir(18*h*) with a distance equal to 2.64 Å and Ir(18*h*)–Ir(6*c*) −2.66 Å). Ce(6*c*) has six in-plane nearest neighbors Ir(18*h*) and Ir(18*h*) has four another Ir(18*h*) nearest neighbors.

The remaining atoms Ir(3*b*) and Ce(6*c*) form a layer that is similar to Ir(6*c*)–Ce(3*a*) plane: Ir(3*b*) are situated between the two metallic planes, just like Ir(6*c*), and form a tetrahedron-like structure with Ir(18*h*) (Ir(18*h*)–Ir(3*b*) distance is equal to 2.68 Å, so it is only 0.04 Å bigger than the Ir(18*h*)–Ir(18*h*) distance). The Ce(6*c*) atoms are moved from the in-plane position closer to the metallic plane, such that they are above the center of a hexagon, consisting of its 6 nearest neighbors Ir(18*h*).

Figure 3 presents the unit cell volume (V) versus covalent radius of the rare earth metal (RE) for 6 $RE\mathrm{Ir_3}$ compounds: $\mathrm{LaIr_3}$ [18], $\mathrm{CeIr_3}$ [3, 4, 6], $\mathrm{PrIr_3}$ [19], $\mathrm{NdIr_3}$ [4] and $\mathrm{GdIr_3}$ [4]. $RE\mathrm{Ir_3}$ compounds for rare earths heavier than Gd have not been reported. As expected, the volume increases monotonically with an increase in the covalent radius of the RE^{+3} metal. The trend is linear, except for Ce, for which the unit cell volume is much smaller and comparable with the unit cell volume of $\mathrm{GdIr_3}$. This clearly suggests that the Ce oxidation state in $\mathrm{CeIr_3}$ is not purely +3, but intermediate between +3 and +4.

Figure 4 presents the results of the XPS investigations of the Ce 3*d* core level spectrum recorded for the sputter-cleaned $\mathrm{CeIr_3}$ sample. Due to spin–orbit interactions there are two Ce

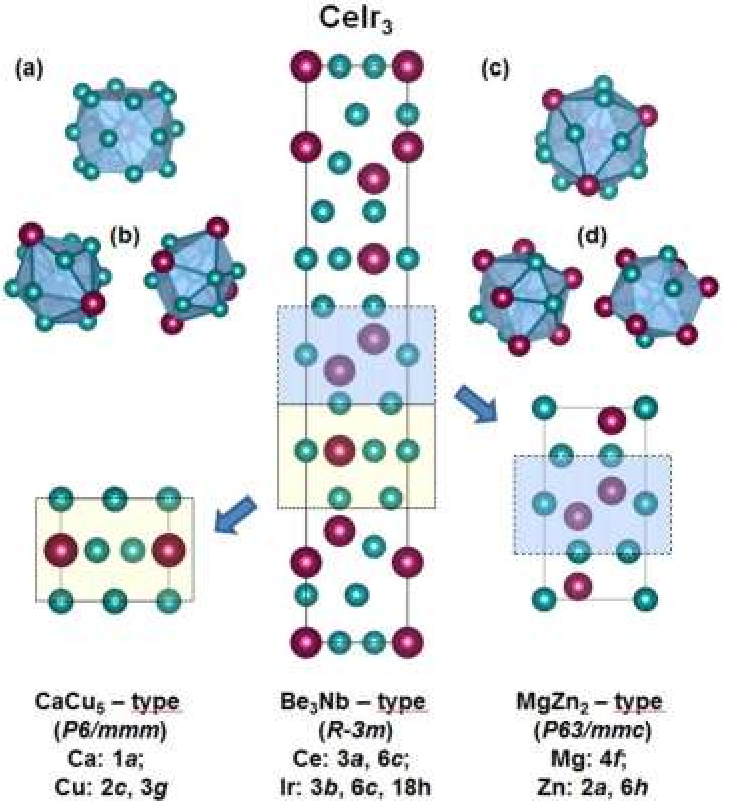

Figure 2. Crystal structure of CeIr$_3$, with polyhedral and slab layers emphasized. (a) 16-vertex polyhedron with a Ce atom center in CaCu$_5$-type CeIr$_5$, (b) distorted icosahedra with Ir atom centers in CaCu$_5$-type CeIr$_5$, (c) 12 vertex polyhedron with Ce atom center in MgZn$_2$-type CeIr$_2$, (d) distorted icosahedra with Ir atom centers in MgZn$_2$-type CeIr$_2$.

Table 2. Refined atomic coordinates and equivalent isotropic displacement parameters of CeIr$_3$ (U_{eq} is defined as one-third of the trace of the orthogonalized U_{ij} tensor (Å^2)).

Atom	Wyck.	Occ.	x	y	z	U_{eq}
Ce1	3*a*	1	0	0	0	0.0052(10)
Ce2	6*c*	1	0	0	0.1395(1)	0.0066(7)
Ir1	3*b*	1	0	0	½	0.0087(7)
Ir2	6*c*	1	0	0	0.3334(1)	0.0094(6)
Ir3	18 *h*	1	0.5007(2)	0.4993(2)	0.0824(1)	0.0071(4)

$3d$ photoemission lines, attributed to the $3d_{5/2}$ and $3d_{3/2}$ components. The splitting in energy between the $3d_{5/2}$ and $3d_{3/2}$ lines is 18.6 eV, while the peaks' intensity ratio $3d_{5/2}/3d_{3/2}$ is 3/2 [20–22]. The recorded spectrum was deconvoluted into six peaks, grouped into three doublets corresponding to the $3d^9 4f^0$, $3d^9 4f^1$ and $3d^9 4f^2$ states. The doublet with peaks at 915.5 and 896.9 eV is attributed to the $3d^9 4f^0$ state, the doublet at 904.6 and 886.0 eV is attributed to the $3d^9 4f^1$ state, while the peaks at 900.3 and 881.7 eV are attributed to the $3d^9 4f^2$ state of Ce [10, 20–27]. It is well known that the main photoemission lines originating from trivalent cerium are $3d^9 4f^1$, while the presence of $3d^9 4f^0$ peaks indicates that the valence of cerium is larger than 3+ [20, 21]. Following [28, 29], the mean occupation of the Ce ion ground state can be estimated by comparing the intensity of the latter peak to the sum of intensities of all the

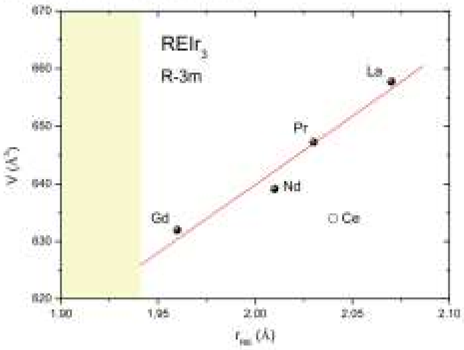

Figure 3. Unit cell volume (V) versus covalent radius for REIr$_3$ compounds, where RE is a heavy rare earth metal (La, Ce, Pr, Nd and Gd). The unit cell volume values were taken from [4–6, 18, 19]:.

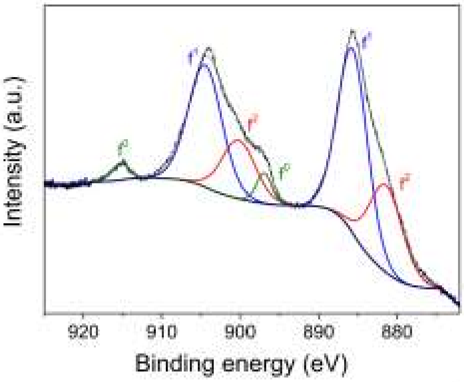

Figure 4. XPS Ce 3d spectrum of a sputter-cleaned CeIr$_3$ sample. f^0 f^1 and f^2 refer to spectral characteristics resulting from electron occupancy in the f orbitals.

components to the Ce 3d spectrum. In the case of CeIr$_3$, the ratio $I\,(f^0)/[I\,(f^0)+I\,(f^1)+I\,(f^2)]$ leads to the effective occupancy of the 4f^0 level to be 0.95 at room temperature. In turn, on the basis of the Gunnarsson and Schonhammer theory [28, 29], the hybridization energy can be determined from the ratio $I\,(f^2)/[I\,(f^0)+I\,(f^1)+I\,(f^2)]$ that yields for CeIr$_3$ a value of 200 meV. Both the reduced occupancy of the 4f state at 300 K and the large strength of the hybridization between the Ce 4f electrons and conduction electrons (mostly the 5d electrons of Ir, see below), manifest the strongly intermediate valence character of the Ce ions in this material.

The inset of figure 5 shows the normal state magnetic susceptibility data taken over the range 3–300 K in an applied magnetic field of 0.1 T. Above about 50 K, $\chi(T)$ is weakly temperature dependent and its magnitude is small, with a small increase on approaching room temperature. These features are typical for Ce-based intermetallics with valence fluctuations. The pronounced tail seen at low temperatures can be attributed to the presence in the specimen studied of a small amount of magnetic impurities. These could be cerium oxides and/or uncompensated Ce^{+3} ions located on the sample surface or between crystalline grains, as is often observed in intermediate valence materials. Accordingly, the experimental $\chi(T)$ data can be described by the formula

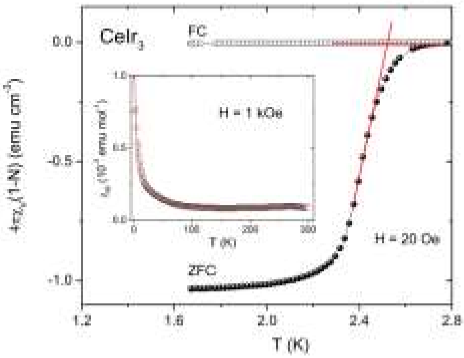

Figure 5. Main panel: zero-field-cooled (ZFC) and field-cooled (FC) temperature-dependent volume magnetic susceptibility $\chi_V(T)$ measurements performed under a small applied magnetic field of 20 Oe. Inset shows normal state magnetic susceptibility versus temperature data over the range 3–300 K in a field of 1000 Oe. Details of the fit (solid line) are explained in the text.

$$\chi(T)=\chi_{\mathrm{ICF}}(T)+\chi_{\mathrm{imp}}(T)+\chi_0, \tag{1}$$

where $\chi_{\mathrm{ICF}}(T)$ is the susceptibility given by the inter-configuration fluctuation model (ICF) of intermediate valency [30], $\chi_{\mathrm{imp}}(T)$ is the Curie–Weiss impurity contribution, assumed to have the form $\chi_{\mathrm{imp}}(T)=C_{\mathrm{imp}}/(T-\theta_{\mathrm{imp}})$, and χ_0 represents temperature independent contributions, e.g. core-electron diamagnetism, conduction-electron paramagnetism and Van Vleck paramagnetism. In the scope of the ICF model the susceptibility of a Ce-based compound with a non-magnetic 4f^0 ground state configuration and a magnetic 4f^1 excited state configuration is represented by

$$\chi_{\mathrm{ICF}}(T)=\frac{N\mu_{\mathrm{eff}}^2[1-\nu(T)]}{3k_{\mathrm{B}}(T+T_{sf})}, \tag{2}$$

where N and k_{B} are the Avogadro's number and the Boltzmann constant, respectively, $\mu_{\mathrm{eff}}=2.54\ \mu_{\mathrm{B}}$ is the effective magnetic moment of the exited 4f^1 state, T_{sf} is the spin fluctuation temperature and the factor $1-\nu(T)$ stands for an effective thermal population of the excited state, where

$$\nu(T)=\frac{1}{1+6\exp[-E_{\mathrm{ex}}/k_{\mathrm{B}}(T+T_{sf})]} \tag{3}$$

with E_{ex} being an energy gap between the ground and excited states.

The least-squares fit of the experimental data to equation (3) yielded the following parameters: $T_{sf}=223$ K, $E_{\mathrm{ex}}=260$ meV, $C_{\mathrm{imp}}=0.004$ emu K mol^{-1}, $\chi_{\mathrm{imp}}=-3$ K

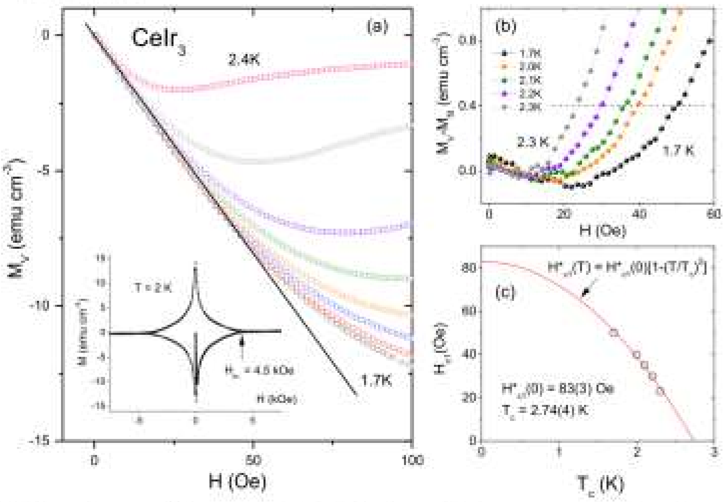

Figure 6. (a) The field-dependent magnetization curves $M_V(H)$ for CeIr$_3$ taken at different temperatures. The inset shows the magnetization hysteresis loop at 2 K. (b) M_V–M_{fit} plotted as a function of applied magnetic field and (c) the H^*_{c1} values with the corresponding temperatures.

and $\chi_0 = 5.5 \times 10^{-5}$ emu mol^{-1}. The calculated $\chi(T)$ is represented in the inset of figure 5 by a solid line. The large magnitude of E_{ex} clearly indicates that the excited $4f^1$ configuration in CeIr$_3$ is quite distant from the non-magnetic $4f^0$ ground state. In consequence, the effective population of the magnetic $4f^1$ level, which is zero at zero Kelvin, hardly changes with increasing temperature reaching a value of only 0.02 at 300 K. This finding naturally explains a Pauli-like character of $\chi(T)$ below room temperature.

Attributing the low temperature tail in $\chi(T)$ to stable Ce^{+3} ions only, the impurity concentration ($n = C_{imp}/C_{Ce3+}$ where $C_{Ce3+} = \mu_{eff}^2/8$) is estimated to be only 0.5 at% Ce^{+3} ions per mol, i.e. well below the detection limit of standard x-ray diffraction.

The magnetic characterization of the superconducting properties of CeIr$_3$ is shown in the main panel of figure 5. Both ZFC and FC temperature-dependent volume magnetic susceptibility measurements, $\chi_v = dM/dH$ where M is the magnetization and H is the applied field, were performed under an applied magnetic field of 20 Oe. The bifurcation of the ZFC and FC magnetic susceptibilities indicates the transition into the superconducting state, which is in agreement with reported data [5, 6, 16, 31]. It can be seen that for the ZFC signal, the transition is slightly broadened and reaches saturation at lower temperature. When corrected for the demagnetization effect, $N = 0.52$ (estimated from the M (H) fit discussed in the following section), at the lowest temperature $T = 1.67$ K, the diamagnetic signal exceeds the expected $\chi_V = -1/4\pi(1-N)$ value, indicating a full Meissner state. The FC signal is much weaker, likely caused by strong flux pinning in our CeIr$_3$ sample. The superconducting critical temperature (T_c) was estimated as the intersection between two lines: the first one is an extrapolation of the normal state χ_V to lower temperature and the second is the steepest slope line of the superconducting signal [32]. The T_c for CeIr$_3$ is 2.5 K and is slightly lower than reported in the literature [5, 6, 16, 31]. Defining the critical temperature as the onset of the transition to the superconducting state $T_{c\ onset}$ is about 2.7 K. It is worth noting that a sample with nominal composition CeIr$_3$ did not show superconductivity, and that two-step superconductivity is observed for nominal Ce$_{1.05}$Ir$_3$. This suggests that superconductivity in this system is very sensitive to the chemical composition.

In figure 6(a), the field-dependent magnetization curves $M_V(H)$ for CeIr$_3$ measured at different temperatures are shown. Assuming that a linear response to an applied magnetic field indicates a full Meissner effect, the demagnetization factor $N = 0.52$ was obtained. The N value is consistent with the sample shape with respect to the magnetic field. The inset shows the full magnetization versus applied magnetic field loop collected in the superconducting state at 2 K. It is evident that CeIr$_3$ exhibits conventional type-II superconductivity. The irreversible field (H_{irr}) estimated from the plotted curve is 4.5 kOe at 2 K and for fields $H > H_{irr}$, vortices are unpinned. The linear fit (M_{fit}) to the initial slope in magnetization curves was used to construct the M_V–M_{fit} and plotted as a function of the applied magnetic field (see figure 6(b)). The field where there is the first deviation from a linear response of the magnetization curve (black dashed line) is the lower critical field, H_{c1}, at each temperature. At $T = 1.7$ K, H^*_{c1} is 50 Oe and decreases monotonically with an increase in temperature, to 23 Oe at $T = 2.3$ K. The H^*_{c1}

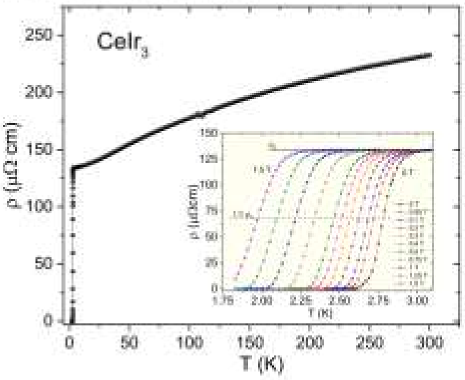

Figure 7. The temperature dependence of the electrical resistivity for CeIr$_3$ between 1.85 and 300 K in zero magnetic field. Inset: the magnetic field-dependent resistivity of CeIr$_3$ in the vicinity of the superconducting transition.

values with the corresponding temperatures are shown in figure 6(c). As expected, H^*_{c1} varies as a function of T^2 in accordance with Ginzburg–Landau (GL) theory:

$$H^*_{c1}(T) = H^*_{c1}(0)\left[1 - \left(\frac{T}{T_c}\right)^2\right], \tag{4}$$

where $H^*_{c1}(0)$ is the lower critical field at 0 K and T_c is the superconducting critical temperature. The quadratic equation fits the data well and, for CeIr$_3$, H^*_{c1} at 0 K is estimated to be 83(3) Oe. Correcting for the demagnetization factor ($N = 0.52$), the lower critical field at 0 K is calculated to be $H_{c1}(0) = 173$ Oe (17.3 mT). This value is larger than that reported for the CeIr$_3$ single crystal ($H_{c1}(0) = 51$ Oe) [6].

The temperature dependence of the electrical resistivity for CeIr$_3$ between 1.85 and 300 K in zero magnetic field is presented in the main panel of figure 7. The overall $\rho(T)$ behavior is typical of intermetallic compounds [18, 33, 34]—at low temperatures a residual resistivity (ρ_0) is observed and the high temperature data show tendency towards saturation that would be expected as the charge carrier mean-free path becomes comparable to the interatomic distances [35–37]. Similar behavior has been reported for other Ir-based superconductors e.g. CaIr$_2$ [38] , LaIr$_3$ [18], TaIr$_2$Ge$_2$ [33] and La$_7$Ir$_3$ [39]. The other plausible scenario assumes *s–d* Mott scattering [40–42]. The residual resistivity ratio (ρ(300 K)/ρ (10 K) = 1.7) is found to be rather small, which suggests that the resistivity is dominated by disorder in the polycrystalline sample. At low temperatures, the resistivity of CeIr$_3$ indicates a superconducting transition at 2.75 K, where T_c is taken as 50% of the resistivity drop. The slightly higher critical temperature value obtained in the resistivity measurement is likely due to the influence of surface superconductivity emerging in each cross-sectional area of the sample. The inset of figure 7 shows the magnetic field-dependent resistivity of CeIr$_3$ around the transition. As expected, the superconducting transition becomes broader and the T_c shifts to lower temperature as the applied magnetic field is increased. These data were used to extract the upper critical field ($\mu_0 H_{c2}$), taken as the midpoint of the resistivity transition at each applied field. The upper critical field $\mu_0 H_{c2}(T)$ of CeIr$_3$ is presented in figure 9 and will be discussed further.

In order to characterize the thermodynamic transition, specific heat measurements were conducted on a flat polished sample. Figure 8(a) presents a closer view of the transition temperature under zero magnetic field. The sharp anomaly displayed in the specific heat data confirms bulk superconductivity in CeIr$_3$. In order to extract the superconducting transition temperature and the value of the specific heat jump, we used a linear approximation of the data just above and below the transition. The corresponding graphical equal-area construction (entropy conserving) with the vertical line located at the transition temperature $T_c = 2.46$ K is shown by solid blue lines in figure 8(a) and is slightly lower than the value obtained from resistivity data (as described above) and comparable with the T_c estimated from the magnetic susceptibility measurement. The specific heat jump is found to be about $\Delta C/T_c =$ 31.2 mJ mol^{-1} K^{-2}. In part (b) of the same figure, the normal state specific heat of CeIr$_3$ is presented under a magnetic field of $\mu_0 H = 2$ T. The data plotted as C_p/T versus T^2 can be fitted using the formula $C_p/T = \gamma + \beta T$ [2], where γT and βT [3] are the electronic specific heat coefficient and phonon contribution, respectively. A linear least-squares fit yields the Sommerfeld coefficient $\gamma = 25.1$ (3) mJ mol^{-1} K^{-2} and $\beta = 2.72(6)$ mJ;mol^{-1} K^{-4}. In a simple Debye model for the phonon contribution, the β coefficient is related to the Debye temperature Θ_D through

$$\Theta_D = \left(\frac{12\pi^4}{5\beta} nR\right)^{1/3}, \tag{5}$$

where $R = 8.314$ J mol^{-1} K^{-1} and $n = 4$ for CeIr$_3$. The calculated Debye temperature is 142(1) K, which is very close to the value obtained for CeIr$_3$ single crystals [6]. The specific heat anomaly observed at the superconducting transition is usually normalized as $\Delta C/\gamma T_c$. Using the value of $\Delta C/T_c = 31.2$ mJ mol^{-1} K^{-2} and $\gamma = 25.1(3)$ mJ mol^{-1} K^{-2}, we obtained $\Delta C/\gamma T_c = 1.24$. The calculated value is slightly lower than the BCS value of 1.43, suggesting that CeIr$_3$ is a weakly coupled superconductor, however the value is very close to that for LaIr$_3$ [18] ($\Delta C/\gamma T_c = 1.22$).

Knowing the Debye temperature, the electron–phonon coupling constant, λ_{e-p}, can be estimated from the inverted McMillan equation [43]

$$\lambda_{e-p} = \frac{1.04 + \mu^* \ln(\Theta_D/1.45T_c)}{(1 - 0.62\mu^*)\ln(\Theta_D/1.45T_c) - 1.04}, \tag{6}$$

where μ^* is the repulsive screened Coulomb constant, typically taken as $\mu^* = 0.13$ for many intermetallic superconductors [6, 33, 44–46]. Using the Debye temperature $\Theta_D = 142(1)$ K and $T_c = 2.46$ K (from the specific heat measurements), we obtain $\lambda_{e-p} = 0.65$, which suggests weak

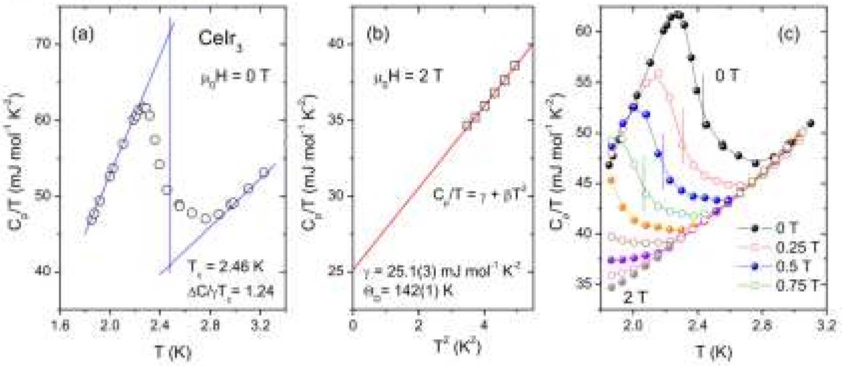

Figure 8. (a) The specific heat anomaly in zero magnetic field. (b) C_p/T versus T^2 plot under a $\mu_0 H = 2$ T magnetic field. The red solid line represents the linear fit of the data. (c) C_p/T versus T under various applied magnetic fields.

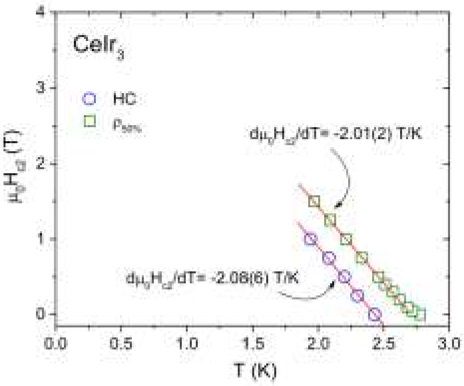

Figure 9. The temperature dependence of the upper critical field of CeIr$_3$, determined from heat capacity (blue circles) and electrical resistivity (green squares) measurements.

electron–phonon coupling behavior. In addition, for non-interacting particles, the electronic specific heat coefficient is proportional to the density of states at the Fermi energy $N(E_F)$. Using the relation

$$N\ (E_F) = \frac{3\gamma}{\pi^2 k_B^2 (1 + \lambda_{e\text{-}p})}, \tag{7}$$

where k_B is the Boltzmann constant, $N(E_F)$ is calculated to be 6.5 states eV^{-1} per formula unit for CeIr$_3$.

Figure 8(c) shows the specific heat data plotted as C_p/T versus T in various magnetic fields. The vertical solid lines present the midpoints of the superconducting transitions for each applied field from 0 to 2 T. With increasing magnetic field, the size of the specific heat jump becomes smaller and shifts to lower temperatures. Using the transition temperature estimated at different magnetic fields, we can calculate the upper critical field $\mu_0 H_{c2}(T)$. Determination of the upper critical field $\mu_0 H_{c2}$ via resistivity (green squares) and heat capacity (blue circles) measurements is shown in figure 9. For a single-band type-II BCS superconductor, the orbital upper critical field at 0 K can be estimated from the Werthamer–Helfand–Hohenberg expression [47, 48]

$$\mu_0 H_{c2}(0) = -AT_c \frac{d\mu_0 H_{c2}}{dT}\bigg|_{T=T_c}, \tag{8}$$

where A is the purity factor given by 0.693 for the dirty and 0.73 for the clean limit. Although the data points are shifted, the $d\mu_0 H_{c2}/dT$ slope determined from the $\rho(T)$ data and $C_p(T)$ data are almost identical $d\mu_0 H_{c2}/dT = -2.01(2)$ T/K and $-2.08(6)$ T/K, respectively. Taking $T_c = 2.46$ K, for CeIr$_3$ we estimate $\mu_0 H_{c2}(0) = 3.5$ T in the dirty limit and $\mu_0 H_{c2}(0) = 3.7$ T in the clean limit. The value of the upper critical field is smaller than the Pauli limiting field for weak electron–phonon coupling within the BCS theory [49, 50] $H_{c2}^{p}(0) = 1.85\, T_c$ which for $T_c = 2.46$ K gives $H_{c2}^{p}(0) = 4.6$ T for CeIr$_3$.

Assuming that the upper critical field is purely orbital, the superconducting coherence length is calculated to be $\xi_{GL} = 97$ Å, using the GL formula [51] $H_{c2} = \Phi_0/2\pi\xi_{GL}^2$ where $\Phi_0 = hc/2e$ is the quantum flux. Similarly, from the relation

$$H_{c1} = \frac{\Phi_0}{4\pi\lambda_{GL}^2} \ln \frac{\lambda_{GL}}{\xi_{GL}}, \tag{9}$$

we find the superconducting penetration depth $\lambda_{GL} = 1640$ Å for CeIr$_3$. The GL parameter $\kappa_{GL} = \lambda_{GL}/\xi_{GL}$ can then be estimated as $\kappa_{GL} = 17$, supporting the type-II nature of the superconductivity. Finally, the thermodynamic critical field can be obtained from κ_{GL}, H_{c1} and H_{c2} using the formula

$$H_{c1} H_{c2} = H_c^2 \ln \kappa_{GL} \tag{10}$$

yielding $\mu_0 H_c = 147$ mT. A summary of all the measured and calculated superconducting parameters determined here for CeIr$_3$ are gathered in table 3.

In the calculations, the electronic structure for CeIr$_3$ is compared to that of LaIr$_3$ [18], which is an isostructural superconductor with an unoccupied La 4f shell. The densities

Table 3. Experimental superconducting and normal state parameters of $CeIr_3$

Parameter	Unit	Value
T_c	K	2.46
$\mu_0 H_{c2}(0)$	T	3.5
$\mu_0 H_{c1}(0)$	mT	17.3
$\mu_0 H_c$	mT	147
λ_{e-p}	—	0.65
$\xi_{GL}(0)$	Å	97
$\lambda_{GL}(0)$	Å	1640
κ	—	17
γ	mJ mol^{-1} K^{-2}	25.1(3)
β	mJ mol^{-1} K^{-4}	2.72(6)
Θ_D	K	142(1)
RRR	—	1.7
$\Delta C_p/\gamma T_c$	—	1.24
DOS(E_F)	eV f.u.$^{-1}$	6.5

of states (DOSs) of $CeIr_3$ calculated without (labeled as no U) and with (labeled as +U) electron–electron interactions, together with the DOS of $LaIr_3$ are presented in figure 10. The partial DOSs are shown in figure 11, and the Fermi surface (FS) and electronic dispersion relations of $CeIr_3$ are shown in figure 12. The values of the DOS at the Fermi level (E_F) and the occupancy of electronic orbitals are presented in tables 4 and 5 for $CeIr_3$ and $LaIr_3$, respectively, while the calculated Sommerfeld coefficients and the electron–phonon coupling parameters are given in table 6.

Cerium atoms ([Xe]$4f^1 5d^1 6s^2$) contribute four, while iridium ([Xe]$5d^7 6s^2$) atoms contribute nine valence electrons to the electronic system. Our spin-polarized calculations converged to a non-magnetic state, for both types of calculations: with U and without U. This is seen in the DOS of $CeIr_3$ in figure 10, where the spin-up and spin-down parts are practically the same. The main valence band block (from -10 eV to E_F) consists mainly of Ir 5*d* states, with a small fraction of *d*-states of Ce and 6*s*-states of Ir, with the latter in the lower energy part. 4*f* electronic states of Ce form a large DOS peak, seen above the Fermi level, where also smaller contributions from unoccupied 5*d* states of Ce and Ir are visible.

Evidently, the inclusion of Coulomb repulsion (calculations including U) shifts the 4*f*-states further above the Fermi level, which strongly reduces the calculated occupancy of the 4*f*-orbitals of Ce. Total and partial densities of states at the Fermi level are collected in table 4. The dominating contribution to DOS(E_F) comes from 5*d* states of Ir atoms, as also can be deduced from figure 11. Among the Ir atoms, the largest partial DOS(E_F) is found on Ir(6*c*) atoms, which form the Kagome-like 2D lattice with Ce(3*a*) in the crystal structure. However, since there are three times more Ir(18*h*), in comparison with Ir(6*c*), the total contribution from the Ir(18*h*) sublattice to the density of states at the Fermi level is the largest one. The overall domination of Ir 5*d* states at the FS strongly suggests that the superconductivity of $CeIr_3$ is mediated by the *d*-states of Ir atoms. This situation is similar to what was previously found for $LaIr_3$ (which has $T_c = 3.32$ K, slightly larger than that of $CeIr_3$), for which the *d*-states of Ir were concluded to be the most important for superconductivity [18]. By comparing the densities of states of these two systems, plotted in figures 10(b) and (c), one can see that the overall shape of the DOS function of $CeIr_3$ below the Fermi level is similar to the one of $LaIr_3$, which means that states from Ir are hybridized with Ce/La in a similar way. Thus, the main difference between these systems comes from the additional valence electron provided by the cerium atom. As a consequence, the Fermi level is shifted to higher energies, towards the DOS minimum seen just above E_F, making the DOS(E_F) value smaller in $CeIr_3$. This is correlated with its smaller superconducting critical temperature (2.46 K in $CeIr_3$ compared to 3.32 K in $LaIr_3$).

Table 4 also includes the orbital occupation numbers, computed by integrating the angular momentum decomposed partial densities of states inside the atomic spheres ($R_{Ce} = 2.9$ a_B, $R_{Ir} = 2.48$ a_B, a_B is the Bohr radius). Due to hybridization, we observe an *s*–*p* transfer of electronic states for all of the atoms, and importantly, strong reduction of the 4*f* orbital occupation, to about 0.2. These results, together with the DOS and dispersion relation plots, show rather strong hybridization of the Ce 4*f* states, giving rise to the itinerant picture of the 4*f* electrons in that material. Qualitatively, such a low occupation of the 4*f* shell confirms that Ce ions in $CeIr_3$ are closer to the Ce^{4+} ($4f^0$) configuration, than to the magnetic Ce^{3+} ($4f^1$) state, in agreement with experimental findings. Concerning the valence state of the Ce atoms, our DFT 4*f* occupation would correspond to 20% of Ce^{3+} and 80% of Ce^{4+} valence states, giving the average valence of 3.2. This is not far from the value of 3.38, suggested in [16] as well as from 3.30, assumed to be the highest possible valence for the $4f_0$ state in an intermetallic compound [53].

To complete the discussion of the electronic band structure, figure 12 presents the electronic dispersion relations and FS of $CeIr_3$. As our calculation resulted in a non-magnetic ground state, only one spin direction is presented. In the GGA calculations, four bands cross the Fermi level, building up four pieces of the FS. When U is included, one piece consisting of a small Γ-centered pocket (figure 12(a)), associated with the band colored in red in figure 12(i), disappears. The hole-like piece of the FS (figure 12(b)) consists of a Γ-centered pocket and six pockets around the T-point, which become disconnected once the Coulomb repulsion is turned on (figure 12(f)). This piece of the FS is built up from the band plotted in blue in figures 12(i) and (j). The third piece of the FS (figure 12(c)) is cylinder-like in shape, with the symmetry axis around the trigonal direction, which becomes more pronounced when the U repulsion is included. This quasi-2D behavior of this part of the FS may be connected to the sequence of metallic Ir layers perpendicular to the trigonal axis. The associated band (plotted in purple in figures 12(i) and (j)) is almost linear in in-plane directions (T–C–C′–T). The last, electron-like piece of the FS (figures 12(d) and (h)) consists of six small pockets around the *L*-points, which are associated with the orange band in figures 12(i) and (j), and cross E_F at two non-high symmetry points in the Y–L direction. In conclusion, the FS is rather complex, $CeIr_3$ is a

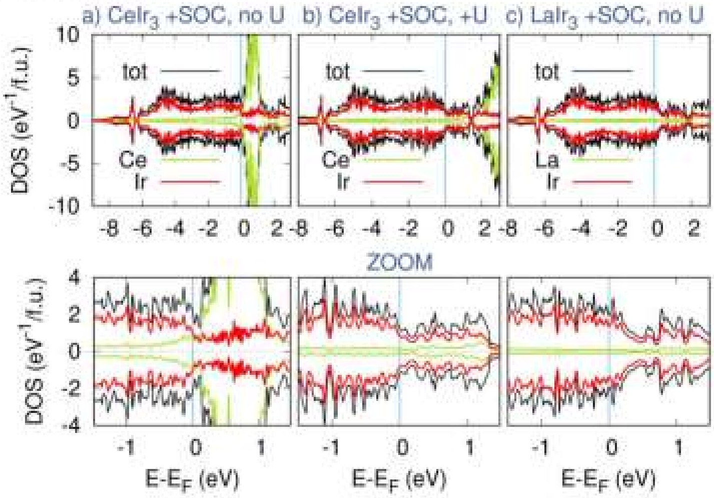

Figure 10. Density of states of CeIr$_3$ compound calculated with SOC and (a) without U, (b) with $U_{\mathrm{eff}} = 5$ eV and (c) density of states of LaIr$_3$. The main valence band is shown at the top while the DOS in the vicinity of Fermi level is shown at the bottom.

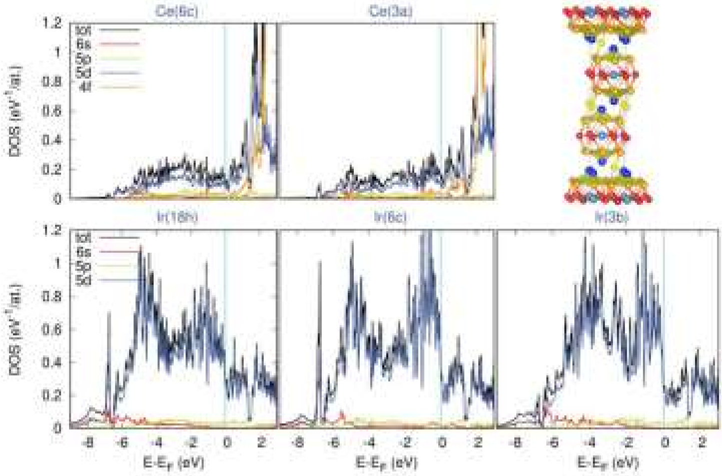

Figure 11. Partial density of states of CeIr$_3$ coming from all five non-equivalent atoms, calculated with $U_{\mathrm{eff}} = 5$ eV and SOC and the crystal structure of CeIr$_3$:Ce(6c) and Ce(3a) are marked with dark and light blue balls, while the Ir(18h), Ir(6c) and Ir(3b) atoms are marked by orange, red and yellow balls respectively.

multi-band superconductor, and in large areas of reciprocal space, a steep and quasi-linear character of the dispersion is observed, which is responsible for a relatively small total density of states in this compound. It is worth noting that the FS of the sister compound LaIr$_3$ (see [18]) consists of three analogous parts, however due to its different Fermi level position, only the cylinder-like part (here presented in figures 12(c) and (g)) looks similar.

Finally, we compare the theoretical density of states with the heat capacity measurements. The GGA+U value of the Sommerfeld coefficient $\gamma_{\mathrm{GGA+U}} = 5.7$ mJ mol^{-1}K^{-2} (shown in table 6) is much smaller than the experimental one,

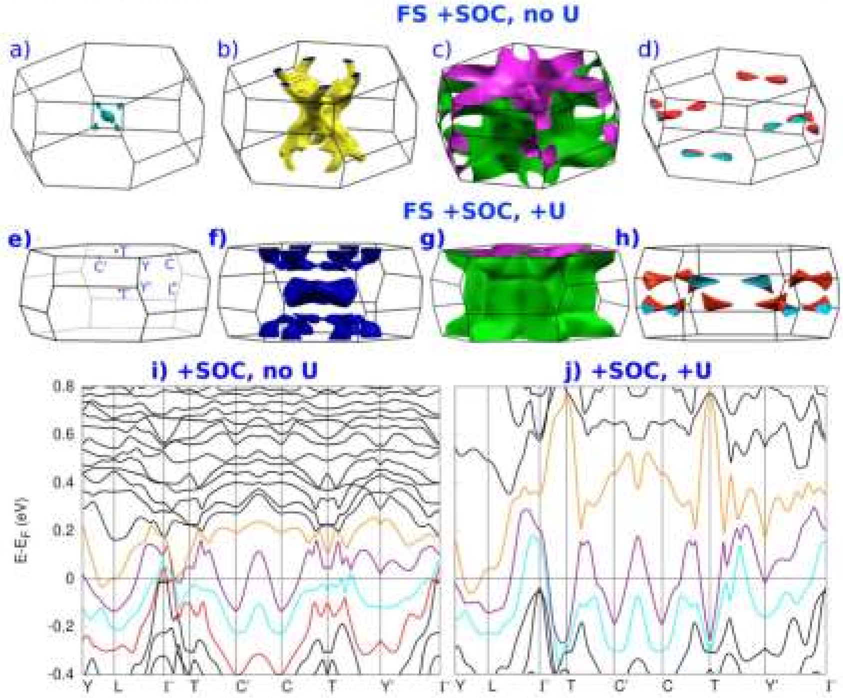

Figure 12. The Fermi surface of CeIr$_3$ calculated (a)–(d) without U; (f)–(h) with $U_{\mathrm{eff}} = 5$ eV; the same for the electronic structure (i) and (j). Panel (e) shows the location of the high-symmetry points. The Fermi surface was plotted using XCrysDen [52].

Table 4. Orbital filling and partial density of states at the Fermi level (in eV^{-1} per atom units) of CeIr$_3$.

	CeIr$_3$ GGA+SOC					CeIr$_3$ GGA+SOC+U				
	Ce(6*c*)	Ce(3*a*)	Ir(18*h*)	Ir(6*c*)	Ir(3*b*)	Ce(6*c*)	Ce(3*a*)	Ir(18*h*)	Ir(6*c*)	Ir(3*b*)
	(Per atom)					(Per atom)				
Valence *Q*	4	4	9	9	9	4	4	9	9	9
Q (*e*)	2.69	2.50	7.52	7.48	7.48	2.08	1.85	7.67	7.67	7.69
Q *s*-states	0.18	0.15	0.55	0.52	0.54	0.19	0.15	0.55	0.52	0.54
Q *p*-states	0.33	0.31	0.42	0.38	0.39	0.33	0.31	0.43	0.39	0.40
Q *d*-states	1.11	0.98	6.48	6.50	6.48	1.32	1.16	6.62	6.68	6.69
Q *f*-states	1.04	1.05				0.21	0.20			
DOS(E_F)	1.21	2.22	0.72	0.93	0.61	0.22	0.28	0.59	0.74	0.52

$\gamma_{\mathrm{expt}} = 25$ mJ mol^{-1} K^{-2}. This difference cannot be explained by the renormalization due to the electron–phonon interaction only, since that would require having very large $\lambda_{\mathrm{e-p}}$ value, $\lambda_{\mathrm{e-p}} = \gamma_{\mathrm{expt}}/\gamma_{\mathrm{calc}} - 1 = 3.4$, which strongly disagrees with the value obtained using the experimental T_c and the McMillan formula ($\lambda_{\mathrm{e-p}} = 0.65$). This suggests the presence of an additional renormalization of the electronic specific heat due to electronic interactions, treated in our GGA+U calculations in an approximate way. It is also possible that the SIC method used to deal with correlated *f* electrons leads to too strong reduction of the presence of 4*f* states near the Fermi level. In calculations without *U* the DOS(E_F) is larger, equal to 4.38 eV^{-1} per f.u, which leads to a larger $\gamma_{\mathrm{calc}} = 10.2$ (mJ mol^{-1} K^{-2}) and $\lambda_{\mathrm{e-p}} = 1.5$, so still twice as large as expected from the McMillan formula. Calculations done using the AMF double-counting method [15] resulted in a γ_{calc} much closer to the experimental value, however, as mentioned above, this method predicted an erroneous magnetic ground state of the system. This reflects the fact that density functional calculations usually face problems with cerium compounds.

Table 5. Orbital filling and partial density of states at the Fermi level (in eV^{-1} per atom units) of $LaIr_3$.

	$LaIr_3$ GGA + SOC				
	La(6*c*)	La(3*a*)	Ir(18*h*)	Ir(6*c*)	Ir(3*b*)
			(Per atom)		
Valence *Q*	3	3	9	9	9
Q (*e*)	1.17	1.05	7.51	7.46	7.50
Q *s*-states	0.08	0.07	0.55	0.52	0.55
Q *p*-states	0.32	0.31	0.40	0.37	0.37
Q *d*-states	0.61	0.53	6.49	6.51	6.51
Q *f*-states	0.15	0.14			
DOS(E_F)	0.16	0.20	0.94	1.29	1.27

Table 6. Density of states at the Fermi level, Sommerfeld coefficient and electron–phonon coupling constant calculated from heat capacity data as $\lambda_{e-p} = \gamma_{expt}/\gamma_{calc} - 1$, and by using the experimental T_c and inverted McMillan formula (with $\mu^* = 0.13$).

	$CeIr_3$ GGA+SOC	$CeIr_3$ GGA +SOC+U	$LaIr_3$ GGA+SOC
DOS(E_F)	4.31	2.42	3.9
γ_{calc}	10.16	5.71	9.2
γ_{expt}	25.1		11.5
$\lambda_{e-p} = \gamma_{expt}/\gamma_{calc} - 1$	1.47	3.4	0.25
λ (T_c)	0.63		0.55

For the case of $LaIr_3$, on the other hand, the computed 'bare' value of the Sommerfeld coefficient $\gamma_{calc} = 9.2$ (mJ mol^{-1} K^{-2}) is very close to the experimental $\gamma_{expt} = 11.5$ (mJ mol^{-1} K^{-2}) [18] leaving room only for a small renormalization parameter $\lambda_{e-p} = 0.25$. This is smaller than expected from the magnitude of T_c ($\lambda_{e-p} = 0.55$), however the disagreement is not as substantial as for the Ce-containing case.

4. Conclusion

In summary, we have synthesized and studied the physical properties of polycrystalline $CeIr_3$. Single crystal diffraction and a LeBail refinement of the pXRD data confirm the rhombohedral structure in centrosymmetric space group R-3m (No. 166) with lattice cell parameters $a = 5.2945(1)$ Å, $c = 26.219(1)$ Å (at room temperature) in agreement with the literature. The calculated unit cell volume for $CeIr_3$ does not follow the trend expected for rare earth based compounds and suggests that the Ce oxidation state in $CeIr_3$ is not +3. This was proven through our room temperature XPS and magnetic susceptibility studies. The normal state magnetic susceptibility was fitted by using the ICF model of intermediate valency.

Temperature-dependent magnetic susceptibility, resistivity and heat capacity measurements confirm bulk superconductivity with $T_c = 2.46$ K. Analysis of the specific heat data reveal that $CeIr_3$ is a moderately correlated superconductor ($\lambda_{e-p} = 0.65$). Detailed analysis of field-dependent magnetization allowed us to estimate the lower critical field at $T = 0$ K (17.3 mT). Resistivity and heat capacity measurements, performed under various magnetic fields and below T_c, give the upper critical field at 0 K of about 3.5 T, which is below the Pauli limit for $CeIr_3$ $H_{c2}^{P}(0) = 4.6$ T. Our values are close to the superconducting parameters refined by Sato *et al* on a $CeIr_3$ crystal obtained by the Czochralski method [6].

Our band structure calculations confirm the non-magnetic ground state of this compound, with a small occupation of the Ce 4*f* shell. The computed FS indicates a multi-band character for this compound, with the dominating contribution to DOS(E_F) coming from 5*d* states of Ir atoms. The overall domination of Iridium 5*d* states at the FS strongly suggests that $CeIr_3$ is indeed an Ir 5*d*-band superconductor and that 5*d* electrons play the dominant role in the superconductivity; a similar situation is observed [16] for $CeRu_2$ and $LaIr_3$. On the other hand, the enhanced Sommerfeld coefficient γ_{expt} of $CeIr_3$ compared to that of $LaIr_3$, and the disagreement between the computed and measured γ values show that the hybridized 4*f* electronic states of Ce in $CeIr_3$ have a subtle impact on the physical properties

Acknowledgments

This work was supported by the Ministry of Science and Higher Education (Poland) under project DI2016 020 546 ('Diamentowy Grant'). Research performed at the AGH-UST was supported by the National Science Center (Poland), project No. 2017/26/E/ST3/00 119. The materials synthesis and powder x-ray diffraction work at Princeton University was supported by the US Department of Energy, Division of Basic Energy Sciences, grant DE-FG02-98ER45706.

ORCID iDs

Elizabeth M Carnicom https://orcid.org/0000-0001-7895-5147
Bartlomiej Wiendlocha https://orcid.org/0000-0001-9536-7216
Tomasz Klimczuk https://orcid.org/0000-0002-7089-4631

References

[1] Steglich F *et al* 1979 Superconductivity in the presence of strong Pauli paramagnetism: $CeCu_2Si_2$ *Phys. Rev. Lett.* **43** 1892–6
[2] Weng Z F, Smidman M, Jiao L, Lu X and Yuan H Q 2016 Multiple quantum phase transitions and superconductivity in Ce-based heavy fermions *Rep. Prog. Phys.* **79** 094503
[3] Sologub O, Salamakha P, Gonçalves A P, Ipser H and Almeida M 2004 Crystal structure of the $CeIr_3$ compound *J. Alloys Compd.* **373** L5–7
[4] Blazina Z, Mohanty R C and Raman A 1989 *Intermediate Phases in Some Rare-Earth-Metal-Iridium Systems* (Baton Rouge, LA: Southern Univ.)
[5] Geballe T H *et al* 1965 Superconductivity in binary alloy systems of the rare earths and of thorium with Pt-group metals *Phys. Rev.* **137** A119–27

[6] Sato Y J *et al* 2018 Superconducting properties of CeIr$_3$ single crystal *J. Phys. Soc. Japan* **87** 053704

[7] Sheldrick G M 2012 SAINT program (Madison, WI: Bruker AXS Inc.)

[8] Sheldrick G M 2015 Crystal structure refinement with SHELXL *Acta Crystallogr.* C **71** 3–8

[9] Sheldrick G M 2008 A short history of SHELX *Acta Crystallogr.* A **64** 112–22

[10] Krill G, Kappler J P, Meyer A, Abadli L and Ravet M F 1981 Surface and bulk properties of cerium atoms in several cerium intermetallic compounds: XPS and X-ray absorption measurements *J. Phys. F: Met. Phys.* **11** 1713

[11] Blaha P, Schwarz K, Madsen G K H, Kvasnicka D and Luitz J 2001 *WIEN2K, an Augmented Plane Wave + Local Orbitals Program for Calculating Crystal Properties* (Vienna: Technische Universität Wien)

[12] Anisimov V I, Aryasetiawan F and Lichtenstein A I 1997 First-principles calculations of the electronic structure and spectra of strongly correlated systems: the LDA + U method *J. Phys.: Condens. Matter* **9** 767

[13] Anisimov V I and Gunnarsson O 1991 Density-functional calculation of effective Coulomb interactions in metals *Phys. Rev.* B **43** 7570–4

[14] Dong R, Wan X, Dai X and Savrasov S Y 2014 Orbital-dependent electronic masses in Ce heavy-fermion materials studied via Gutzwiller density-functional theory *Phys. Rev.* B **89** 165122

[15] Novák P, Kuneš J, Chaput L and Pickett W E Exact exchange for correlated electrons *Phys. Status Solidi* b **243** 563–72

[16] Hakimi M and Huber J G 1985 The valence of Ce in CeRu$_2$ and CeIr$_3$ thru superconductivity *Physica* B +C **135** 434–7

[17] Frank F C and Kasper J S 1958 Complex alloy structures regarded as sphere packings: I. Definitions and basic principles *Acta Crystallogr.* **11** 184–90

[18] Haldolaarachchige N *et al* 2017 Ir d-band derived superconductivity in the lanthanum–iridium system LaIr$_3$ *J. Phys.: Condens. Matter* **29** 475602

[19] Górnicka K in preparation

[20] Kaczorowski D and Ślebarski A 2010 Kondo lattice behavior and magnetic ordering in CeRh$_3$Si *Phys. Rev.* B **81** 214411

[21] Kaczorowski D *et al* 2010 Magnetic properties and electronic structures of intermediate valence systems CeRhSi$_2$ and Ce$_2$Rh$_3$Si$_5$ *J. Phys.: Condens. Matter* **22** 215601

[22] Pikul A P *et al* 2010 Giant crystal-electric-field effect and complex magnetic behavior in single-crystalline CeRh$_3$Si$_2$ *Phys. Rev.* B **81** 174408

[23] Krawczyk M, Holdynski M, Lisowski W, Sobczak J W and Jablonski A 2015 Electron inelastic mean free paths in cerium dioxide *Appl. Surf. Sci.* **341** 196–202

[24] Qiu L, Liu F, Zhao L, Ma Y and Yao J 2006 Comparative XPS study of surface reduction for nanocrystalline and microcrystalline ceria powder *Appl. Surf. Sci.* **252** 4931–5

[25] Chowdhury S and Lin K-S 2012 Characterization and surface reactivity analyses of ceria nanorod catalyst for methanol interaction *Mater. Chem. Phys.* **133** 163–9

[26] Paparazzo E, Ingo G M and Zacchetti N 1991 X-ray induced reduction effects at CeO$_2$ surfaces: an x-ray photoelectron spectroscopy study *J. Vac. Sci. Technol.* A **9** 1416–20

[27] Ohno Y 1993 Core-electron spectra and electronic structure of CeNbS$_3$ *Phys. Rev.* B **48** 5515–24

[28] Fuggle J C *et al* 1983 Electronic structure of Ce and its intermetallic compounds *Phys. Rev.* B **27** 7330–41

[29] Gunnarsson O and Schönhammer K 1983 Electron spectroscopies for Ce compounds in the impurity model *Phys. Rev.* B **28** 4315–41

[30] Sales B C and Wohlleben D K 1975 Susceptibility of interconfiguration-fluctuation compounds *Phys. Rev. Lett.* **35** 1240–4

[31] Huber J G 1990 Probing d-band superconductivity in XIr$_3$ compounds *Physica* B **163** 219–23

[32] Klimczuk T and Cava R J 2004 Carbon isotope effect in superconducting MgCNi$_3$ *Phys. Rev.* B **70** 212514

[33] Srivichitranond L C *et al* 2017 Superconductivity in a new intermetallic structure type based on endohedral Ta@Ir$_7$Ge$_4$ clusters *Phys. Rev.* B **95** 174521

[34] Strychalska-Nowak J *et al* 2017 Fermi-liquid behavior of binary intermetallic compounds Y$_3$M (M = Co, Ni, Rh, Pd, Ir, Pt) *Mater. Res. Express* **4** 066501

[35] Wiesmann H *et al* 1977 Simple model for characterizing the electrical resistivity in A15 superconductors *Phys. Rev. Lett.* **38** 782–5

[36] Hussey || N E, Takenaka K and Takagi H 2004 Universality of the Mott–Ioffe–Regel limit in metals *Phil. Mag.* **84** 2847–64

[37] Calandra M and Gunnarsson O 2002 Electrical resistivity at large temperatures: saturation and lack thereof *Phys. Rev.* B **66** 205105

[38] Haldolaarachchige N, Gibson Q, Schoop L M, Luo H and Cava R J 2015 Characterization of the heavy metal pyrochlore lattice superconductor CaIr$_2$ *J. Phys.: Condens. Matter* **27** 185701

[39] Barker J A T *et al* 2015 Unconventional superconductivity in La$_7$Ir$_3$ revealed by muon spin relaxation: introducing a new family of noncentrosymmetric superconductor that breaks time-reversal symmetry *Phys. Rev. Lett.* **115** 267001

[40] Mott N F 1972 The electrical resistivity of liquid transition metals *Phil. Mag. J. Theor. Exp. Appl. Phys.* **26** 1249–61

[41] Mott N F 1964 Electrons in transition metals *Adv. Phys.* **13** 325–422

[42] Nagel S R 1978 Thermoelectric power and resistivity in a metallic glass *Phys. Rev. Lett.* **41** 990–3

[43] McMillan W L 1968 Transition temperature of strong-coupled superconductors *Phys. Rev.* **167** 331–44

[44] Verchenko V Y, Tsirlin A A, Zubtsovskiy A O and Shevelkov A V 2016 Strong electron–phonon coupling in the intermetallic superconductor Mo$_8$Ga$_{41}$ *Phys. Rev.* B **93** 064501

[45] Singh D, Hillier A D, Thamizhavel A and Singh R P 2016 Superconducting properties of the noncentrosymmetric superconductor Re$_6$Hf *Phys. Rev.* B **94** 054515

[46] Carnicom E M *et al* 2018 TaRh$_2$B$_2$ and NbRh$_2$B$_2$: superconductors with a chiral noncentrosymmetric crystal structure *Sci. Adv.* **4** eaar7969

[47] Werthamer N R, Helfand E and Hohenberg P C 1966 Temperature and purity dependence of the superconducting critical field, H$_{c2}$: III. Electron spin and spin–orbit effects *Phys. Rev.* **147** 295–302

[48] Helfand E and Werthamer N R 1966 Temperature and purity dependence of the superconducting critical field, H$_{c2}$: II *Phys. Rev.* **147** 288–94

[49] Chandrasekhar B S 1962 *Appl. Phys. Lett.* **1** 7

[50] Clogston A M 1962 Upper limit for the critical field in hard superconductors *Phys. Rev. Lett.* **9** 266–7

[51] Tinkham M 1996 *Introduction to Superconductivity* (New York: McGraw-Hill)

[52] Kokalj A 2003 Computer graphics and graphical user interfaces as tools in simulations of matter at the atomic scale *Comput. Mater. Sci.* **28** 155

[53] Gschneidner K A, Eyring L and Hufner S 1987 *Handbook on the Physics and Chemistry of Rare Earths* vol 10 (Amsterdam: Elsevier Science)

Source material's DOI: https://doi.org/10.1088/1361-6668/aaf48f

4.2 (A2) Iridium 5*d*-electron driven superconductivity in $ThIr_3$

4.2.1 Cel badawczy

Ted Geballe w pracy [20] poświęconej badaniom nadprzewodnictwa w podwójnych związkach międzymetalicznych, podał między innymi temperaturę krytyczną dla $ThIr_3$ (T_c = 4.71 K) [20]. Określona T_c jest wyraźnie wyższa niż dla związku $CeIr_3$, który został opisany w artykule A1. Wyniki przedstawione w publikacji A2 są kontynuacją badań nad związkami bogatymi w Ir. **Hipoteza 2** zakłada, że $ThIr_3$ krystalizuje w tej samej strukturze co jego izoelektronowe odpowiedniki $LaIr_3$ oraz $CeIr_3$, a więc jest pierwszym przedstawicielem szeregu homologicznego $R_{2m+n}T_{4m+5n}$ (n=m=1) zawierającym pierwiastek aktynowca. Jon Th^{+4} jest niemagnetyczny, zatem wiele związków międzymetalicznych, które tworzy wykazuje właściwości nadprzewodzące.

W związku z tym, że atom Th charakteryzuje się większą liczbą masową niż atom Ce, zasadnym było pytanie, w jakim stopniu silniejsze oddziaływanie elektron-fonon będzie wpływać na właściwości nadprzewodzące związku $ThIr_3$.

Celem badań opisanych w publikacji A2 było określenie struktury krystalicznej związku $ThIr_3$ oraz wyznaczenie parametrów charakteryzujących stan nadprzewodzący i normalny. Badania eksperymentalne obejmowały proszkową dyfrakcję rentgenowską, pomiary elektryczne, cieplne oraz magnetyczne. Wyniki badań zostały uzupełnione obliczeniami struktury elektronowej (Sylwia Gutowska, dr Bartłomiej Wiendlocha).

4.2.2 Opis rezultatów

Th jest pierwiastkiem promieniotwórczym, zatem synteza $ThIr_3$ została przeprowadzona w Instytucie Niskich Temperatur i Badań Strukturalnych PAN we Wrocławiu. Polikrystaliczną próbkę otrzymano metodą topienia w piecu łukowym w atmosferze argonu o bardzo wysokiej czystości, bez późniejszego wygrzewania.

Na podstawie badań strukturalnych oraz analizy Rietvelda uzyskanego dyfraktogramu rentgenowskiego wykazano, że $ThIr_3$ krystalizuje w strukturze trygonalnej (R-$3m$ No.166), potwierdzając tym samym postawioną hipotezę 2 zakładającą, że $ThIr_3$ jest pierwszym przedstawicielem szeregu homologicznego $R_{2m+n}T_{4m+5n}$ (n=m=1) zawierającym pierwiastek aktynowca. Przeprowadzona analiza Rietvelda pozwoliła również po raz pierwszy na wyznaczenie stałych sieci oraz pozycji atomów w komórce elementarnej.

Pomiary właściwości magnetycznych jednoznacznie wskazują na przejście materiału do stanu nadprzewodzącego w T_c = 4.5 K (temperatura wyznaczona z temperaturowej zależności podatności magnetycznej). Otrzymana temperatura krytyczna jest nieznacznie niższa od wartości raportowanej w pracy T. Geballe (T_c = 4.71 K) [20]. Analiza zachowania badanego materiału w zewnętrznym polu magnetycznym, a także otrzymany kształt krzywych namagnesowania w funkcji przyłożonego pola magnetycznego, pozwoliły na sklasyfikowanie $ThIr_3$ jako nadprzewodnika II-go rodzaju. Wyznaczona wartość dolnego pola krytycznego wynosi $H_{c1}(0)$ = 60 Oe i jest niższa od wartości uzyskanych dla $LaIr_3$ ($H_{c1}(0)$ = 110 Oe [52]) oraz $CeIr_3$ ($H_{c1}(0)$ = 173 Oe).

Badania oporu elektrycznego oraz ciepła właściwego potwierdziły stan nadprzewodzący w $ThIr_3$. Pomiary oporności elektrycznej w zerowym oraz niezerowym polu magnetycznym pozwoliły na wyznaczenie górnego pola krytycznego ($H_{c2}(0)$ = 47 kOe), które jest prawie dwa razy mniejsze od limitu Pauli'ego ($H^{Pauli}(0) = 1.85T_c \times 10\ 000 = 82$ kOe). Objętościowy charakter nadprzewodnictwa potwierdza skok ciepła właściwego w T_c = 4.41 K, a znormalizowana wartość skoku ciepła właściwego wynosi $\Delta C/\gamma T_c$ = 1.6 i jest większa od wartości określonej w teorii BCS dla słabo sprzężonych nadprzewodników. Oszacowana z pomiarów cieplnych temperatura przejścia do stanu nadprzewodzącego jest w świetnej zgodności z wartościami uzyskanymi z badań magnetycznych i elektrycznych. Wykorzystując wzory przedstawione w części teoretycznej wyznaczono: długość koherencji (ξ_{GL} = 83 Å), głębokość wnikania (λ_{GL} = 3150 Å) oraz parametr Ginzburga-Landaua ($\kappa_{GL} = 38$).

Parametr sprzężenia elektron-fonon, wyliczony ze wzoru McMillana, wynosi λ_{ep} = 0.74. Porównując wartości λ_{ep} *oraz* $\Delta C/\gamma T_c$ z wielkościami uzyskanymi dla $LaIr_3$ (λ_{ep} = 0.57, $\Delta C/\gamma T_c$ = 1.22) oraz $CeIr_3$ (λ_{ep} = 0.65, $\Delta C/\gamma T_c$ = 1.24) można stwierdzić, że w związku $ThIr_3$ oddziaływanie elektron-fonon jest najsilniejsze.

Przeprowadzone obliczenia struktury elektronowej pokazują, że dominujący wkład do DOS(E) w okolicy poziomu energii Fermiego mają stany elektronowe pochodzące od elektronów 5*d* atomu Ir, z niewielkim udziałem elektronów stanu 6*d* Th.

4.2.3 Treść artykułu A2

4.2.3 Treść artykułu A2

Tytuł: Iridium 5*d*-electron driven superconductivity in $ThIr_3$

Autorzy: Karolina Górnicka, Debarchan Das, Sylwia Gutowska, Bartłomiej Wiendlocha, Michał J. Winiarski, Tomasz Klimczuk, Dariusz Kaczorowski

Czasopismo: PHYSICAL REVIEW B 100, 214514 (2019)

Impact factor: 3.575 (2019/2020)

Liczba punktów ministerialnych MNiSW: 140 pkt

DOI: 10.1103/PhysRevB.100.214514

Mój udział polegał na przeprowadzeniu badań strukturalnych metodą proszkowej dyfrakcji rentgenowskiej, częściowych pomiarach właściwości magnetycznych, cieplnych oraz elektrycznych, analizie otrzymanych wyników, udziale w dyskusji uzyskanych rezultatów, wyznaczeniu parametrów charakteryzujących stan normalny i nadprzewodzący, przygotowaniu rysunków oraz tekstu manuskryptu części eksperymentalnej. Brałam udział w przygotowaniu odpowiedzi na recenzje. Kierowałam również projektem naukowym (Diamentowy Grant, MNiSW) obejmującym badania opisane w pracy.

Karolina Górnicka

mgr inż. Karolina Górnicka

***The original source: Physical Review B** 100, 214514*

PHYSICAL REVIEW B **100**, 214514 (2019)

Iridium 5*d*-electron driven superconductivity in $\mathrm{ThIr_3}$

Karolina Górnicka,[1] Debarchan Das,[2] Sylwia Gutowska,[3] Bartłomiej Wiendlocha,[3] Michał J. Winiarski,[1]
Tomasz Klimczuk,[1] and Dariusz Kaczorowski[2,*]
[1]*Faculty of Applied Physics and Mathematics, Gdansk University of Technology, ul. Narutowicza 11/12, 80–233 Gdańsk, Poland*
[2]*Institute of Low Temperature and Structure Research, Polish Academy of Sciences, P.O.Box 1410, 50-590 Wrocław 2, Poland*
[3]*Faculty of Physics and Applied Computer Science, AGH University of Science and Technology,*
Aleja Mickiewicza 30, 30–059 Kraków, Poland

(Received 24 April 2019; revised manuscript received 12 October 2019; published 24 December 2019)

A polycrystalline sample of superconducting $\mathrm{ThIr_3}$ was obtained by arc-melting Th and Ir metals. Powder x-ray diffraction revealed that the compound crystalizes in a rhombohedral crystal structure (*R-3m*, s.g. #166) with the lattice parameters: $a = 5.3394(1)$ Å and $c = 26.4228(8)$ Å. Normal and superconducting states were studied by magnetic susceptibility, electrical resistivity, and heat capacity measurements. The results showed that $\mathrm{ThIr_3}$ is a type-II superconductor (Ginzburg-Landau parameter $\kappa = 38$) with the critical temperature $T_c = 4.41$ K. The heat capacity data yielded the Sommerfeld coefficient $\gamma = 17.6\,\mathrm{mJ/(mol\,K^2)}$ and the Debye temperature $\Theta_D = 169$ K. The ratio $\Delta C/(\gamma T_c) = 1.6$, where ΔC stands for the specific heat jump at T_c, and the electron-phonon coupling constant $\lambda_{e-p} = 0.74$ suggest that $\mathrm{ThIr_3}$ is a moderate-strength superconductor. The experimental studies were supplemented by band structure calculations, which indicated that the superconductivity in $\mathrm{ThIr_3}$ is governed mainly by 5*d* states of iridium. The significantly smaller band-structure value of Sommerfeld coefficient as well as the experimentally observed quadratic temperature dependence of resistivity and enhanced magnetic susceptibility suggest the presence of electronic interactions in the system, which compete with superconductivity.

DOI: 10.1103/PhysRevB.100.214514

I. INTRODUCTION

Since the discovery of superconductivity over a century ago, the investigation of superconductors is still one of the most attractive topics in the condensed matter physics. Despite the fact that several distinct superconducting families have been found and studied thoroughly in the hope of understanding various Cooper pairing mechanisms, new findings still emerge even from simple, binary intermetallic systems. In this respect, materials bearing *d* and *f* electrons are particularly intriguing, since their electronic properties are often dominated by strong spin-orbit coupling [1]. Recently, a homologous series $\mathrm{RE}_{2m+n}T_{4m+5n}$, where RE is a light lanthanide metal, and T is a transition metal, Ir or Rh has attracted a lot of attention [2–8]. The latter compounds constitute an important class of materials exhibiting a variety of physical phenomena, like superconductivity and different types of magnetic ordering [5–12]. $\mathrm{RE}_{2m+n}T_{4m+5n}$ compounds crystallize with a centrosymmetric rhombohedral structure (space group *R-3m*) of the $\mathrm{PuNi_3}$-type, build of m $\mathrm{MgCu_2}$-type blocks and n $\mathrm{CaCu_5}$-type blocks. Amidst $m = n = 1$ representatives, superconductivity was found in $\mathrm{LaIr_3}$ and $\mathrm{CeIr_3}$ below T_c of 3.5 K and 2.5 K, respectively [5–7]. In the latter compound, Ce ions exhibit a strongly intermediate valence character. In turn, in $\mathrm{NdIr_3}$ a ferromagnetic ground state was observed with the Curie temperature $T_C = 10.6$ K [8].

Recently, we succeeded in synthesizing the actinoid-bearing representative of the $\mathrm{RE}_{2m+n}T_{4m+5n}$ family, viz. $\mathrm{ThIr_3}$, which was briefly communicated by Geballe *et al.* [9] to be a superconductor with $T_c = 4.71$ K. Though the latter report was published over 50 years ago, to the best of our knowledge, no detailed studies have been performed as yet, aimed at determining the superconducting parameters of that compound.

In this paper, we report on the preparation of polycrystalline sample of $\mathrm{ThIr_3}$ and our exhaustive investigation of its electronic properties by means of dc magnetization, electrical resistivity, and heat capacity measurements. The experimental data are supplemented by the results of electronic band structure calculations.

II. EXPERIMENTAL AND CALCULATION DETAILS

Polycrystalline sample of $\mathrm{ThIr_3}$ was prepared by arc-melting stoichiometric mixture of pure elements (purity: Th-99.7 wt.%, Ir - 99.9 wt.%) under high-purity argon atmosphere using an arc furnace installed inside a Braun glove-box with controlled oxygen and moisture contents. To promote homogeneity, the button was turned over and remelted several times. Final mass loss was less than 1%. The product was stable against air and moisture, hard, and grey in color.

The crystal structure and phase purity of the sample was checked at room temperature by powder x-ray diffraction (PXRD) using a PANalytical diffractometer equipped with Cu $K\alpha$ radiation. The data were analyzed by the Rietveld method implemented in the FULLPROF package

---

[*] Corresponding author: d.kaczorowski@intibs.pl

[13]. The crystal structure was drawn using the VESTA software [14].

A Quantum Design Dynacool Physical Property Measurement System (PPMS) with a vibrating sample magnetometer and a Quantum Design Magnetic Property Measurement System (MPMS-XL) were used to measure the magnetic properties of the sample. The temperature dependences of the zero-field-cooled (ZFC) and field-cooled (FC) magnetic susceptibility (defined as dM/dH, where M is the magnetization and H is the applied field strength) were measured in an external magnetic field of 20 Oe. Furthermore, the magnetic field variations of the ZFC magnetization were measured at various temperatures in the superconducting state. In addition, the temperature dependence of dM/dH was determined in the normal state at temperatures up to 400 K in a magnetic field of 5 kOe. Electrical resistivity and heat capacity measurements were carried out in the temperature interval 0.4–300 K using a Quantum Design PPMS platform equipped with a Helium-3 refrigerator. Temperature- and magnetic-field-dependent electrical transport measurements were made using a standard four-probe technique, in which Pt wires were attached to the polished sample using conductive silver epoxy Epotek H20E. For the heat capacity measurements, a standard relaxation technique was used. The data were collected in zero magnetic field and magnetic fields up to 60 kOe.

Electronic structure calculations were undertaken to study the origin of electronic states building the Fermi surface of $ThIr_3$, to investigate the behavior of $5f$ states of Th and to calculate the band-structure values of the Sommerfeld coefficient and the Pauli paramagnetic susceptibility. We used the QUANTUM ESPRESSO package [15,16], based on pseudopotential and plane-waves methods, with Rappe-Rabe-Kaxiras-Joannopoulos ultrasoft pseudopotentials and the Perdew-Burke-Ernzerhof generalized gradient approximation for the exchange-correlation potential [17]. Wave function and charge density cutoff energies were set to 60 and 600 Ry, respectively. The lattice parameters and the atomic positions were optimized using the Broyden-Fletcher-Goldfarb-Shanno algorithm implemented in the QUANTUM ESPRESSO package. The theoretical values of the rhombohedral lattice parameters a and c were found slightly smaller than the experimental ones, namely by −0.28% and −0.75%, respectively. To investigate the relativistic effects, two types of calculations were performed: scalar-relativistic and fully-relativistic with spin orbit coupling (SOC) effect considered for both Th and Ir atoms.

III. RESULTS AND DISCUSSION

A. Crystal structure

The PXRD pattern of $ThIr_3$ together with its Rietveld fitting profile and the Bragg positions are shown in Fig. 1. The data indicated the rather good quality of the sample examined, although a small amount of ThO_2 (less than 1% wt.) was detected as an impurity. An anisotropic broadening of reflections was observed, with the $(00l)$ reflections being noticeably broader than expected. An anisotropic strain model was introduced in the refinement, which led to a significant increase of the fit quality (χ^2 reduced from 11 to 6.5).

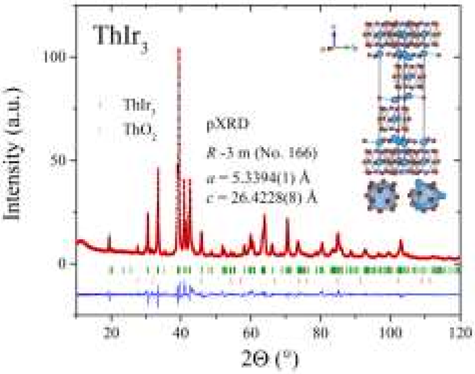

FIG. 1. Powder x-ray diffraction pattern (PXRD) (red points) together with the LeBail refinement profile (black solid line) for $ThIr_3$. The green and orange vertical bars indicate the expected Bragg peak positions for $ThIr_3$ and ThO_2 impurity, respectively. The amount of the impurity phase is 1.3(1) wt.%., i.e., 3.9(3) mol%.The blue curve is the difference between the experimental and model results. The inset shows the crystal structure of $ThIr_3$ together with Frank-Kasper polyhedrals with Th atom in the center.

The crystallographic and refinement parameters are listed in Table I. The calculations indicated that the compound crystallizes with a rhombohedral crystal structure (space group *R-3m*, No.166) of the $PuNi_3$ type with the lattice parameters: $a = 5.3394(1)$ Å and $c = 26.4228(8)$ Å. The refined values are larger than those reported for RE-based $REIr_3$ compounds, i.e., $a = 5.32$ Å and $c = 26.34$ Å for $LaIr_3$ [5], and $a = 5.2945(1)$ Å and $c = 26.219(1)$ Å for $CeIr_3$ [7].

The crystallographic unit cell of $ThIr_3$ is shown in the inset to Fig. 1. It contains three nonequivalent positions of Ir atoms and two of Th atoms. Atomic environment of each of the sites is a Frank-Kasper polyhedron [18]. In one of its positions, Th

TABLE I. Crystallographic data for $ThIr_3$. The reliability factors provided are conventional Rietveld R factors (corrected for background contribution) calculated only for points with the Bragg contribution. B_{iso} stands for equivalent isotropic displacement parameters. Numbers in parentheses are statistical uncertainties of the least significant digits and are not corrected for the presence of possible experimental errors.

Space group	*R-3m* (#166)		Reliability factors	
a (Å)	5.3394(1)		R_p (%)	15.4
c (Å)	26.4228(8)		R_{wp} (%)	15.5
V (Å^3)	653.09		R_{exp} (%)	6.09
Density (g/cm^3)	18.5		χ^2	6.51
Atom (position):	x	y	Z	B_{iso} (Å^2)
Th1 (3a)	0	0	0	0.85(7)
Th2 (6c)	0	0	0.1396(1)	1.56(6)
Ir1 (3b)	0	0	$\frac{1}{2}$	0.87(8)
Ir2 (6c)	0	0	$\frac{1}{3}$	0.50(6)
Ir3 (18h)	0.4995(2)	0.5005(2)	0.0829	0.75(3)

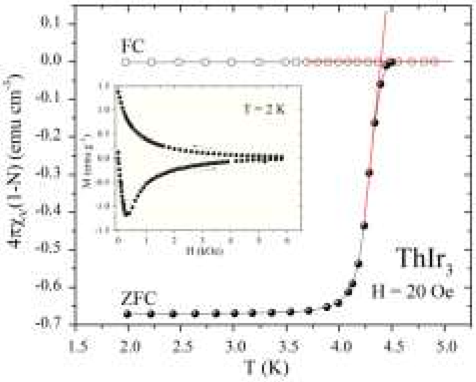

FIG. 2. Temperature dependences of the zero-field-cooled (ZFC) and field-cooled (FC) volume magnetic susceptibility measured in a magnetic field of 20 Oe. The raw data were corrected for the demagnetization factor, as described in the main text. The red straight lines illustrate derivation of the critical temperature. The inset shows the isothermal magnetization versus applied magnetic field measured at 2 K with increasing and decreasing field, as indicated by the arrows.

is coordinated by 16 Ir atoms, and in the other one by 12 Ir atoms forming truncated tetrahedrons.

One can distinguish three types of layers in the crystal structure of ThIr$_3$, namely the plane consisting of Th(3*a*) and Ir(6*c*) atoms [with distances Th(3*a*)-Ir(6*c*) = Ir(6*c*)-Ir(6*c*) = 3.08 Å], the plane of Ir(18*h*) atoms [with Ir(18*h*)-Ir(18*h*) distance of 2.67 Å) and a sandwich made of three planes of Th(6*c*), Ir(3*b*), and Th(3*a*) atoms [with Th(3*a*)-Ir(3*b*) distance equal to 3.17 Å]. The observed anisotropic PXRD peak broadening can likely be attributed to the presence of some disorder in the layer stacking sequence.

The nearest neighbors in the ThIr$_3$ unit cell are Ir(18*h*) atoms with Ir(18*h*) atoms and Ir(18*h*) atoms with Ir(6*c*) atoms located at the same distance of 2.67 Å. A slightly larger distance (2.71 Å) is between Ir(3*b*) and Ir(18*h*) atoms. As can be inferred from Fig. 1, two types of polyhedra with Ir(18*h*) atoms in the corners are formed, one is centered at Ir(6*c*) atom and the other one is centered at Ir(3*b*) atom. In turn, Th(3*a*) atom has six Ir(6*c*) atoms as its nearest neighbors located at a distance of 3.08 Å. Similarly, Th(6*c*) atom has six Ir(18*h*) atoms as the nearest neighbors with Th(6*c*)-Ir(18*h*) distance equal to 3.06 Å. In both cases Ir atoms are organized into hexagons, in-plane and out-of-plane, for the Th(3*a*) and Th(6*c*) environment, respectively (see Fig. 1).

B. Superconducting properties

The main panel of Fig. 2 shows the low-temperature magnetic susceptibility (χ) of ThIr$_3$ measured in a small applied field of 20 Oe in the ZFC and FC regimes. Strong diamagnetic signal observed in the ZFC data corroborates the superconducting ground state, reported in Ref. [9]. The superconducting critical temperature, estimated as an intersection between the line set by the steepest slope of the superconducting signal and the line obtained by extrapolation of the normal state magnetic susceptibility to lower temperatures [19], equals $T_c = 4.41$ K. In turn, defining T_c as an onset of diamagnetic ZFC susceptibility yields a value of 4.5 K, which is closer to the literature data ($T_c = 4.71$ K [9,20]). At 2 K, the diamagnetic susceptibility corrected for the demagnetization factor $N = 0.55$ [obtained from the $M(H)$ fit discussed next] amounts to about $-0.7 \times (1/4\pi)$. In contrast to the ZFC data, the FC diamagnetic susceptibility measured in the superconducting state is very small. This finding implies a substantial pinning effect, likely at grain boundaries in the polycrystalline sample studied. The inset to Fig. 2 presents the magnetic field dependence of the magnetization measured in the superconducting state of ThIr$_3$ with increasing and decreasing the magnetic field strength. It is apparent from the figure that the compound exhibits a conventional type-II superconductivity. Above T_c, ThIr$_3$ is a Pauli-type paramagnet with the total magnetic susceptibility of about 40×10^{-5} emu/mol (not shown).

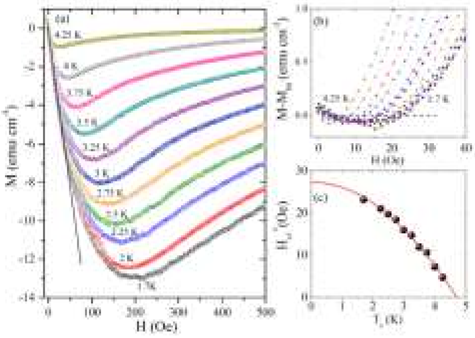

FIG. 3. (a) Magnetic field dependences of the magnetization of ThIr$_3$ taken at several different temperatures in the superconducting state upon cooling the sample in zero field. The straight line emphasizes a linear behavior of the isotherm taken at 1.7 K. (b) Analysis of the magnetization isotherms from panel (a), as described in the main text. (c) Temperature variation of the lower critical field derived from panel (b) The red line represents the fit of Eq. (1) to the experimental data.

In order to determine the lower critical field of ThIr$_3$, the magnetization was measured as a function of magnetic field at several temperatures below the superconducting transition temperature T_c [see Fig. 3(a)]. For each temperature, the experimental data obtained in small magnetic fields were fitted using the proportionality $M_{\mathrm{fit}} = -pH$, appropriate for a full shielding effect. Comparing the value of prefactor p derived from the isotherm taken at $T = 1.7$ K with the ideal diamagnetism quantified as $\frac{-1}{4\pi}$, the demagnetization factor $N = 0.55$ was found, fairly consistent with shape of the sample used in the magnetic measurements. In the next step, from the plot of the difference $M - M_{\mathrm{fit}}$ versus H [see Fig. 3(b)], the values of the lower critical field were extracted for each temperature (note the black dashed line), as displayed in Fig. 3(c). The

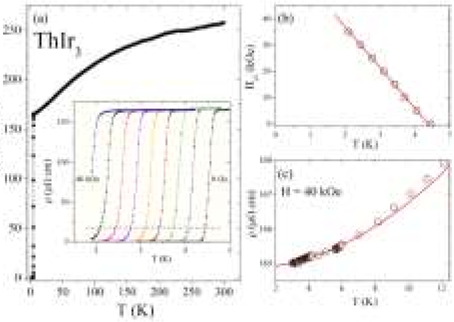

FIG. 4. (a) Temperature dependence of the electrical resistivity of ThIr$_3$ measured in zero magnetic field. The inset shows the low-temperature resistivity data taken in several different magnetic fields: 0, 5, 10, 15, 20, 25, 30, 35, and 40 kOe (consecutive curves from right to left). The horizontal dashed line illustrates the criterion used for deriving the critical temperature. (b) Temperature dependence of the upper critical field, determined from the electrical resistivity data. The solid straight line represents the initial slope of the upper critical field curve. (c) Low-temperature electrical resistivity of ThIr$_3$ measured in a field of 40 kOe. The solid red line emphasizes a Fermi liquid behavior.

so-obtained data points were analyzed with the expression:

$$H_{c1}(T) = H_{c1}(0)\left[1 - \left(\frac{T}{T_c}\right)^2\right], \qquad (1)$$

which yielded the parameters and $T_c = 4.65(3)$ K and $H_{c1}(0) = 27(1)$ Oe. Correcting the latter value for the demagnetization effect, the lower critical field $H_{c1}(0) = 60$ Oe was determined. Remarkably, the critical temperature obtained from this analysis is very close to T_c derived from the magnetic susceptibility measurements, as well as the values derived from the electrical resistivity and heat capacity data (see below), thus proving the correctness of the approach applied.

The superconducting transition for ThIr$_3$ was further characterized through temperature and magnetic field dependent measurements of the electrical resistivity. As can be inferred from the main panel of Fig. 4(a), the normal-state resistivity reveals metallic behavior ($d\rho/dT > 0$), although the residual resistivity ratio RRR $= \rho(300\text{ K})/\rho(5\text{ K}) = 1.6$ is rather small. The latter feature can be attributed to polycrystalline nature of the sample investigated that probably contained many macroscopic defects. The observed strongly curvilinear character of $\rho(T)$ may originate from sizable contribution of Mott-type interband scattering processes to the electrical conduction in ThIr$_3$ [21–23]. The onset of the superconducting state manifests itself as a sharp drop in the resistivity down to zero. The critical temperature defined as a 90% decrease of the resistivity with respect to its normal state value amounts to $T_c = 4.4$ K, in good agreement with the magnetic susceptibility data. In applied magnetic fields, the width of the superconducting transition slightly increases and T_c systematically shifts to lower temperature with increasing the field strength [see the inset to Fig. 4(a)]. Applying the same criterion as for the zero-field $\rho(T)$ data, one can derive the temperature variation of the upper critical field ($\mu_0 H_{c2}$), shown in Fig. 4(b).

According to the Werthamer-Helfand-Hohenberg approach [24,25], the orbital upper critical field at 0 K in a single-band type-II Bardeen-Cooper-Schrieffer (BCS) superconductor can be estimated from the formula

$$H_{c2}(0) = -AT_c \left.\frac{dH_{c2}}{dT}\right|_{T=T_c}, \qquad (2)$$

where A is the purity factor given by 0.693 for the dirty and 0.73 for the clean limit. For ThIr$_3$ one finds $dH_{c2}/dT = -15.4(1)$ kOe/K [note the red straight line in Fig. 4(b)], which implies $H_{c2}(0) = 47$ and 49 kOe in the dirty and clean limit scenario, respectively. The obtained values are distinctly smaller than the Pauli limiting field $H_{c2}^{p}(0) = 1.85T_c = 82$ kOe, calculated for ThIr$_3$ assuming weak electron-phonon coupling.

Then, if one assumes the upper critical field to be purely orbital, the coherence length can be derived from the Ginzburg-Landau formula $H_{c2} = \Phi_0/2\pi\xi_{\mathrm{GL}}^2$, where $\Phi_0 = hc/2e$ is the quantum flux. This way, we found for ThIr$_3$ the value $\xi_{\mathrm{GL}} = 83$ Å within the dirty limit scenario. In the next step, from the relation

$$H_{c1} = \frac{\Phi_0}{4\pi\lambda_{\mathrm{GL}}^2} ln \frac{\lambda_{\mathrm{GL}}}{\xi_{\mathrm{GL}}}, \qquad (3)$$

where we estimated the superconducting penetration depth $\lambda_{\mathrm{GL}} = 3150$ Å. The so-obtained parameters yielded the Ginzburg-Landau parameter $\kappa_{\mathrm{GL}} = \lambda_{\mathrm{GL}}/\xi_{\mathrm{GL}} = 38$ corroborating that ThIr$_3$ is a type-II superconductor. Finally, from the relationship

$$H_{c1}H_{c2} = H_c^2 ln\kappa_{\mathrm{GL}}, \qquad (4)$$

one can determine the thermodynamic critical field in the studied compound to be $H_c = 884$ Oe.

Figure 4(c) displays $\rho(T)$ of ThIr$_3$ measured in applied magnetic field of 40 kOe. These data, representing the electrical resistivity in the normal state, can be approximated by the function

$$\rho(T) = \rho_0 + AT^2, \qquad (5)$$

where the first term is the residual resistivity due to crystal defects and the second one accounts for electron-electron scattering processes [26,27]. The least-squares fitting of Eq. (5) to the experimental data in the range 3–7 K yielded the parameters: $\rho_0 = 164.86(1)\ \mu\Omega$ cm and $A = 0.01854(3)\ \mu\Omega\,\mathrm{cm/K^2}$.

The results of low-temperature heat capacity measurements are summarized in Fig. 5. The zero-field raw data displayed in panels (a) and (c) were corrected for the impurity contribution due to 1% wt. of ThO$_2$, based on the specific heat data of the latter material, reported by Magnani *et al.* [28]. The pronounced sharp anomaly in $C/T(T)$ confirms bulk nature of the superconductivity in ThIr$_3$. From the equal entropy construction shown in Fig. 5(a), which reflects the expected entropy balance between the normal state and the superconducting state at the superconducting phase transition, one finds the critical temperature $T_c = 4.41$ K, which is almost identical to those determined from the magnetic and resistivity

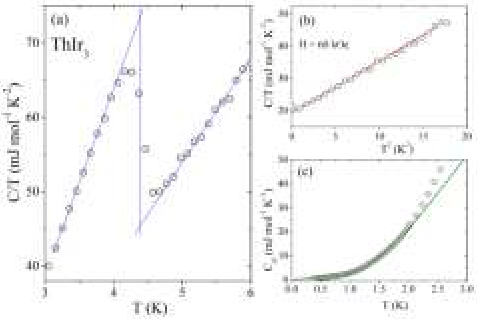

FIG. 5. (a) Temperature dependence of the specific heat over temperature ratio of ThIr$_3$ measured in zero magnetic field in the vicinity of the superconducting phase transition. The thin solid lines illustrate the equal entropy construction used to derive the critical temperature. (b) The specific heat over temperature ratio measured in a magnetic field of 6 T and plotted as a function of squared temperature. The red straight line represents the Debye fit discussed in the main text. (c) Low-temperature variation of the electronic contribution to the zero-field specific heat of ThIr$_3$. The solid red line is the BCS-type fit described in the text.

data. The so-determined specific heat jump at T_c is about $\Delta C = 124\,\mathrm{mJ/(molK)}$.

In an external magnetic field of 60 kOe, the superconductivity in ThIr$_3$ is entirely suppressed [see Fig. 3(c)], and thus the experimental data shown in Fig. 5(b) represents the normal state of the compound. From the standard Debye formula $C/T = \gamma_n + \beta T^2$, applied in the temperature range up to 4 K, one obtains the Sommerfeld coefficient $\gamma_n = 19.4(4)\,\mathrm{mJ/(mol\,K^2)}$ and the parameter $\beta = 1.59(5)\,\mathrm{mJ/(mol\,K^4)}$, which gives the Debye temperature $\Theta_D = 169(2)\,\mathrm{K}$ through the relationship

$$\Theta_D = \left(\frac{12\pi^4}{5\beta} nR\right)^{1/3}, \tag{6}$$

where $R = 8.314\,\mathrm{J/(mol\,K)}$ is the gas constant and $n = 4$ is the number of atoms per formula unit.

The dimensionless electron-phonon coupling constant, which is a measure of the strength of attractive interaction between electrons and phonons, can be estimated from the inverted McMillan equation [29]

$$\lambda_{e-p} = \frac{1.04 + \mu \ln(\Theta_D/1.45T_c)}{(1 - 0.62\mu)\ln(\Theta_D/1.45T_c) - 1.04}, \tag{7}$$

where μ^* is the repulsive screened Coulomb part, usually set to $\mu^* = 0.13$ for intermetallic superconductors [30,31]. In the case of ThIr$_3$, one obtains $\lambda_{e-p} = 0.74$ indicating a moderately coupled superconductor.

Figure 5(c) shows the electronic specific heat in the superconducting state up to 2 K, derived by subtracting the lattice βT^3 contribution from the $C(T)$ data. The solid red line in that figure represent a least-squares fitting to the experimental results of the function $C_{el}(T) = \gamma_{imp}T + B\exp(-\Delta/k_BT)$, which considers some contribution from a fraction of nonsuperconducting impurity phase (the first term) in addition to the standard fully gapped superconductivity (the exponential term, where k_B stands for the Boltzmann constant). The analysis yielded $\gamma_{imp} = 1.8\,\mathrm{mJ/(mol\,K^2)}$ and $\Delta = 0.50(5)\,\mathrm{meV}$. It is worthwhile noting that the so-obtained energy gap is somewhat smaller than the estimate $\Delta = 1.76\,k_B\,T_c = 0.67\,\mathrm{meV}$ provided by the BCS theory.

TABLE II. Superconducting and normal state parameters of ThIr$_3$, CeIr$_3$ [7], and LaIr$_3$ [5].

Parameter	Unit	ThIr$_3$	CeIr$_3$	LaIr$_3$
T_c	K	4.41	2.46	3.32
$H_{c2}(0)$	kOe	47	35	38.4
$H_{c1}(0)$	Oe	60	173	1102
H_c	Oe	884	1470	1750
λ_{e-p}	–	0.74	0.65	0.57
$\xi_{GL}(0)$	Å	83	92	92.59
$\lambda_{GL}(0)$	Å	3150	1640	960
κ	–	38	17	10.37
γ	mJ/(mol K^2)	17.6	25.1	11.5
β	mJ/(mol K^4)	1.59	2.72	–
Θ_D	K	169	142	366
RRR	–	1.6	1.7	–
$\Delta C/\gamma T_c$	–	1.6	1.24	1.22

By subtracting γ_{imp} from the Sommerfeld coefficient γ obtained in the normal state (see above) one can determine the intrinsic electronic specific heat coefficient in ThIr$_3$ to be $\gamma = 17.6\,\mathrm{mJ/(mol\,K^2)}$. Using this value and the afore-derived specific heat jump at T_c, another important superconducting parameter can be calculated namely the ratio $\Delta C/\gamma T_c = 1.6$. The obtained value is larger than the expected value of 1.43 for a weakly coupled BCS superconductor, thus supporting the finding from the McMillan approach (see above). All the superconducting and normal state parameters of ThIr$_3$ are gathered in Table II.

C. Electronic band structure

The density of states (DOS) in ThIr$_3$ calculated without and with inclusion of the spin-orbit coupling is presented in Fig. 6. In each case, the main contribution to DOS comes from Ir atoms, although Th atoms contribution is also significant, especially above the Fermi level. The overall shape of DOS is not strongly affected by SOC, however some important differences are seen near the Fermi level. As shown in detail in Fig. 7, $N(E_F)$ computed with SOC is considerably larger than that without SOC (3.46 and $2.45\,\mathrm{eV^{-1}/f.u.}$, respectively). The small peak, which appears in DOS in the full-relativistic calculations, originates from $5f$ states of the Th($3a$) atoms, as can be inferred from Fig. 8, where the partial DOS, decomposed over atomic orbitals, is plotted for each Th and Ir state (the partial densities at the Fermi level are listed in Table III). As expected, the main contributions to the overall atomic densities come from Ir-5d states and Th-6d states, while Th- $5f$ states contribute to the large DOS peak above E_F. The largest contribution to $N(E_F)$ comes from the Ir($6c$) and Th($3a$) atoms, which form together a layer in the crystal structure of ThIr$_3$ (see the inset to Fig. 1 and the discussion in

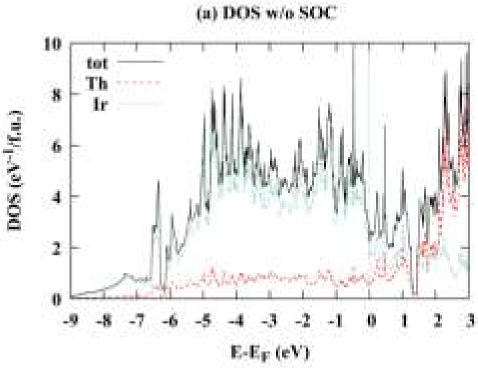

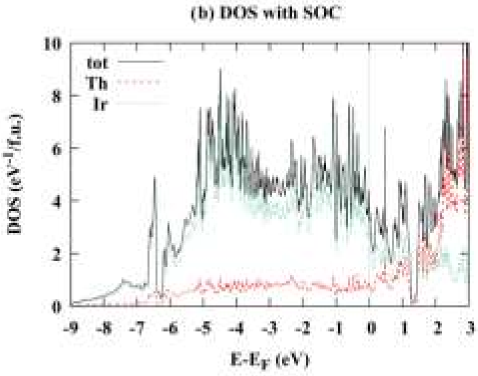

FIG. 6. Density of states in $ThIr_3$ calculated without (a) and with (b) spin-orbit coupling effect (solid black lines). The Th and Ir contributions (summed over all atomic positions) are marked by dashed red and dotted green lines, respectively.

Sec. III A).This effect is related to the spin-orbit interaction, as the SOC significantly increases DOS values for both types of atoms.

In Table III, one can find the electric charges derived by integrating partial DOS up to E_F. Iridium, with valence electron configuration $5d^7 6s^2$, and thorium, with valence configuration $6d^2 7s^2$, are expected to contribute nine and four electrons to the main valence band, respectively. For both elements, chemical bonding and hybridization effect may cause charge transfer from s to d states, and charge transfer from Ir atoms to Th atoms. Some electric charge is also transferred to Th-$5f$ orbitals, which are basically empty in elemental Th, yet are well known to exhibit much aptitude to hybridize with s and d states [32]. Depending on the experimental or computational technique, filling of the $5f$ orbital in crystalline Th atom was reported in the literature to span between 0.5 and 1.3. In the case of $ThIr_3$, the $5f$ orbital filling was estimated to be about 0.8 per atom. However, these states are of itinerant nature, with equal spin-up and spin-down occupation, hence no magnetic moment, associated with $5f$ electrons, is observed, in agreement with the experimental findings. Figure 8 shows valence charge density plots, where charge transfers are clearly visible.

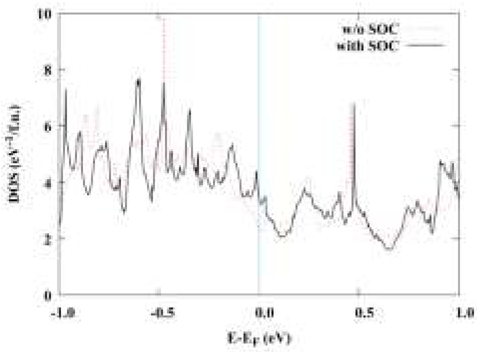

FIG. 7. Comparison of the scalar-relativistic and full-relativistic density of states in $ThIr_3$ near the Fermi level. The results computed without and with spin-orbit coupling effect are shown by dashed red and solid black lines, respectively.

Figure 9 displays the Fermi surface (FS) and the electronic dispersion relations in $ThIr_3$ calculated without SOC and with SOC (FS was visualized using the program XCRYSDEN [33]). Due to large number of bands (there are 93 valence electrons per unit cell), only the energy range in the vicinity of the Fermi level is shown. Bands crossing E_F are plotted with color lines. Their number is three in the scalar-relativistic case and four in the full-relativistic case. As can be inferred from the figures, SOC removes band degeneracy in high-symmetry points, see especially the T point and L-Γ direction, and significantly

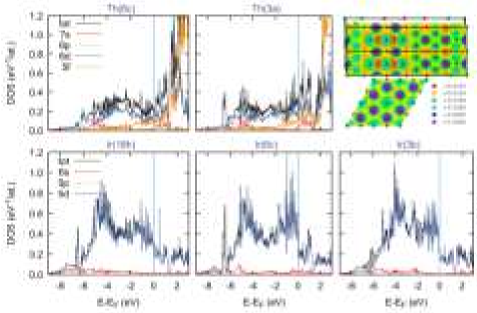

FIG. 8. Partial density of states in $ThIr_3$ calculated with spin-orbit coupling included. For each Th and Ir atom, the contributions from different orbitals are plotted with different colors. In the upper right corner, two valence electron charge density plots are shown. They are plotted in (010) and (001) planes of the conventional unit cell, respectively (on a logarithmic scale, in units of e/a_0^3). The Th and Ir atoms are marked with red and green balls, respectively. These plots show a metallic character of Ir clusters, an in-plane charge transfer between Th(3a) and its nearest neighbor Ir(6c) and an out-of-plane charge transfer between Th(6c) and Ir(18h) atoms.

TABLE III. Orbital filling in $ThIr_3$ calculated as an integral of DOS over energy, using DOS from scalar-relativistic and full-relativistic calculations. Partial DOS at the Fermi level contributed by each atom is also given (in eV^{-1}).

	w/o SOC					with SOC				
	Ir(3b)	Ir(6c)	Ir(18h)	Th(3a)	Th(6c)	Ir(3b)	Ir(6c)	Ir(18h)	Th(3a)	Th(6c)
No. of valence electrons	9	9	9	4	4	9	9	9	4	4
charge $Q(e)$	8.57	8.68	8.64	4.58	4.61	8.53	8.64	8.60	4.68	4.69
Q of s states	0.73	0.80	0.80	0.63	0.59	0.71	0.79	0.79	0.65	0.59
Q of p states	0.04	0.03	0.04	0.22	0.26	0.04	0.03	0.04	0.25	0.28
Q of d states	7.80	7.84	7.80	2.96	2.95	7.78	7.82	7.77	3.00	2.98
Q of f states				0.76	0.81				0.79	0.84
DOS at E_F	0.47	0.71	0.61	0.67	0.44	0.65	1.29	0.77	0.93	0.62
Total DOS at E_F	2.45 $(eV^{-1}/f.u.)$					3.46 $(eV^{-1}/f.u.)$				

influences overall shape of the FS sheets. All parts of FS have a three-dimensional character, except for the FS pockets plotted in panels (c) and (g), which are cylindrical-like in shape with the trigonal axis as their symmetry axis. This feature is a consequence of the presence of atomic layers perpendicular to the trigonal direction, and the largest contribution to that FS sheet comes from metallic layers of Ir(18h). It is worth noting that similar FS topology was found before in a sister compound $CeIr_3$ [7].

From the aforementioned value of DOS at the Fermi level, $N(E_F) = 3.46\,eV^{-1}/f.u.$, one can calculate the Sommerfeld coefficient to be $\gamma_{calc} = 8.155\,mJ/(mol\,K^2)$. This value is distinctly smaller than the experimental one $[\gamma = 17.6\,mJ/(mol\,K^2)]$, and the renormalization factor $\lambda = \gamma/\gamma_{calc} - 1 = 1.16$ is notably larger than the electron-phonon coupling parameter $\lambda_{e-p} = 0.74$ calculated from the McMillan equation (see above). However, if one assumes, that the electronic heat capacity is renormalized by the electron-phonon interaction only, $\lambda = 1.16$ would imply the superconducting critical temperature $T_{c,0} = 10.6\,K$, which is much higher than the experimental one. Such a discrepancy can be possibly attributed to substantial electron-electron interactions, identified in the low-temperature electrical resistivity data of $ThIr_3$ as the Fermi liquid behavior $\rho \propto AT^2$ with renormalized A coefficient (see above). In line with this hypothesis, a similar discrepancy is observed for the magnetic susceptibility values. The computed value of the Pauli paramagnetic susceptibility is $\chi_P = 11 \times 10^{-5}\,emu/mol$, thus it is

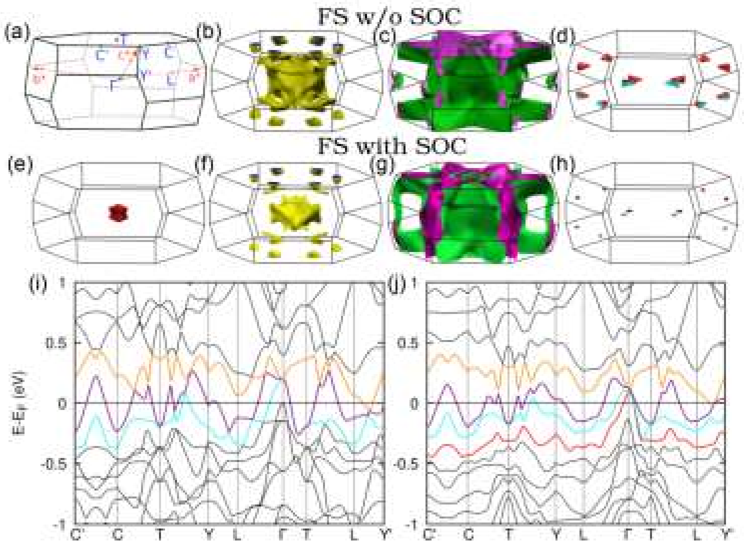

FIG. 9. (a) Brillouin zone used for calculation of the electronic structure of $ThIr_3$. The location of high symmetry points is indicated. (b)–(d) Fermi surface pockets calculated in scalar-relativistic approach. (e)–(h) Fermi surface calculated with spin-orbit coupling effect included. (i) Band structure in the vicinity of the Fermi level calculated without spin-orbit coupling. (j) Band structure computed in full-relativistic approach.

TABLE IV. Analysis of the electron-phonon interaction and the superconducting critical temperature of $ThIr_3$ assuming the presence of effective depairing electron-paramagnon interactions. $T_{c,0}$ is the critical temperature calculated assuming renormalization due to electron-phonon interaction, and $T_{c,\mathrm{eff}}$ is the effective critical temperature computed with addition of spin fluctuations effect. For the meaning of all the other symbols see the main text.

Parameter	Unit	Value
Θ_D	K	169
γ	mJ/(mol K^2)	17.6
γ_{calc}	mJ/(mol K^2)	8.155
$\lambda = \gamma/\gamma_{\mathrm{calc}} - 1$	–	1.158
$T_{c,0}(\mu^* = 0.13)$	K	10.63
λ_{e-p}	–	0.74
λ_{sf}	–	0.1
μ^*_{eff}	–	0.209
λ_{eff}	–	0.962
$T_{c,\mathrm{eff}}$	K	4.55
T_c	K	4.41

almost four times smaller than the experimental susceptibility $\chi = 40 \times 10^{-5}$ emu/mol. As the experimental susceptibility additionally contains negative diamagnetic contributions, the enhancement of the paramagnetic susceptibility is even larger, validating the picture of important electronic interactions in $ThIr_3$.

To try to quantify this effect, we may follow the route proposed for many *d*-band superconductors, like vanadium and its alloys [34–38], Mo_3Sb_7 [39], La_3Co [40] or Y_3Rh [41]. Assuming that the electronic correlations take mostly the form of spin fluctuations (electron-paramagnon interactions), characterized by the coupling constant λ_{sf}, one can compute the superconducting critical temperature from the modified McMillan's formula [29,39]:

$$T_{c,\mathrm{eff}} = \frac{\Theta_D}{1.45}\exp\left[\frac{-1.04(1+\lambda_{\mathrm{eff}})}{\lambda_{\mathrm{eff}} - \mu^*_{\mathrm{eff}}(1+0.62\lambda_{\mathrm{eff}})}\right], \qquad (9)$$

where $\lambda_{\mathrm{eff}} = \frac{\lambda_{e-p}}{1+\lambda_{sf}}$ represents the effective coupling parameter and $\mu^*_{\mathrm{eff}} = \frac{\mu^*+\lambda_{sf}}{1+\lambda_{sf}}$ is the effective Coulomb repulsion constant [39]. Assuming the presence of weak electron-paramagnon interactions with postulated $\lambda_{sf} = 0.10$, the electron-phonon coupling parameter and the Coulomb repulsion parameter become renormalized to $\lambda_{\mathrm{eff}} = 0.96$ and $\mu^*_{\mathrm{eff}} = 0.21$, yielding $T_{c,\mathrm{eff}} = 4.5$ K that is close to the experimental value. Also the renormalized Sommerfeld coefficient $\gamma = \gamma_{\mathrm{calc}}(1 + \lambda_{e-p} + \lambda_{sf})$ is now in a good agreement with the experimental value (see Table IV).

IV. CONCLUSIONS

The compound $ThIr_3$ crystallizes with a centrosymmetric rhombohedral unit cell of the $PuNi_3$-type, and can be considered as the first actinoid-based representative of the homologous series $RE_{2m+n}T_{4m+5n}$, where RE was restricted thus far to a light lanthanide element only, and T = Ir or Rh. The crystal structure is composed from alternating $MgCu_2$- and $CaCu_5$-type blocks. It contains three nonequivalent positions of Ir atoms and two of Th atoms. The characteristic feature is the presence of a layer formed by Ir(6*c*) and Th(3*a*) atoms with fairly short interatomic distance.

As its lanthanide counterparts $LaIr_3$ and $CeIr_3$, $ThIr_3$ becomes superconducting at low temperatures. The bulk nature of the superconducting state in this material is evident from the prominent anomalies at $T_c = 4.41$ K in its thermodynamic (magnetic susceptibility, heat capacity) and electrical transport characteristics. Our analysis of the experimental and theoretical data revealed that $ThIr_3$ is a *d* band, moderately coupled type-II superconductor with isotropic *s*-wave energy gap. The main role in the electronic properties of $ThIr_3$ is played by the 5*d* states of iridium with contribution from 6*d* states of thorium. Calculated occupation of 5*f* states of Th is comparable to that found in crystalline Th, although these are itinerant and nonmagnetic states. At low temperatures, the normal-state electrical conductivity in this material is mostly governed by electron-electron interactions with minor yet not negligible effective mass renormalization. The electronic interactions also additionally renormalize the electronic specific heat coefficient γ and the paramagnetic susceptibility, and their competition with the electron-phonon coupling effectively leads to lowering of the superconducting critical temperature. A consistent explanation of the magnitude of both γ and T_c was reached when a small electron-paramagnon interaction parameter $\lambda_{sf} = 0.1$ was assumed. It will be worth investigating other actinoid-based counterparts to examine possible interplay between superconductivity and magnetism in these systems.

ACKNOWLEDGMENTS

This work was partly supported by the Ministry of Science and Higher Education (Poland) under Project No. DI2016 020546 ("Diamentowy Grant"). Research performed at the AGH-UST was supported by the National Science Center (Poland), Project No. 2017/26/E/ST3/00119. S.G. was partly supported by the EU Project POWR.03.02.00-00-I004/16. M.J.W. was supported by the Foundation For Polish Science (FNP).

---

[1] K. H. J. Buschow, Rep. Prog. Phys. **40**, 1179 (1977).
[2] E. Parthé and R. Lemaire, Acta Crystallogr. B **31**, 1879 (1975).
[3] D. T. Cromer and A. C. Larson, Acta Crystallogr. **12**, 855 (1959).
[4] O. Sologub, P. Salamakha, A. P. Gonçalves, H. Ipser, and M. Almeida, J. Alloys Compd. **373**, L5 (2004).
[5] N. Haldolaarachchige, L. Schoop, M. A. Khan, W. Huang, H. Ji, Kalani Hettiarachchilage, and D. P. Young, J. Phys.: Condens. Matter **29**, 475602 (2017).
[6] Y. J. Sato, A. Nakamura, Y. Shimizu, A. Maurya, Y. Homma, D. Li, F. Honda, and D. Aoki, J. Phys. Soc. Jpn. **87**, 053704 (2018).

[7] K. Górnicka, E. M. Carnicom, S. Gołąb, M. Łapiński, B. Wiendlocha, W. Xie, D. Kaczorowski, R. J. Cava, and T. Klimczuk, Supercond. Sci. Technol. **32**, 025008 (2019).

[8] K. Górnicka, W. Xie, E. M. Carnicom, R. J. Cava, and T. Klimczuk, Phys. Rev. B **99**, 104430 (2019).

[9] T. H. Geballe, B. T. Matthias, V. B. Compton, E. Corenzwit, G. W. Hull, and L. D. Longinotti, Phys. Rev. **137**, A119 (1965).

[10] D. Gignoux, R. Lemaire, P. Molho, and F. Tasset, J. Magn. Magn. Mater. **15–18**, 289 (1980).

[11] S. B. Roy and P. Chaddah, Phys. Rev. B **55**, 11100 (1997).

[12] B. T. Matthias, H. Suhl, and E. Corenzwit, Phys. Rev. Lett. **1**, 449 (1958).

[13] J. Rodríguez-Carvajal, Phys. B **192**, 55 (1993).

[14] K. Momma and F. Izumi, J. Appl. Crystallogr. **44**, 1272 (2011).

[15] P. Giannozzi, S. Baroni, N. Bonini, M. Calandra, R. Car, C. Cavazzoni, D. Ceresoli, G. L. Chiarotti, M. Cococcioni, I. Dabo, A. Dal Corso, S. de Gironcoli, S. Fabris, G. Fratesi, R. Gebauer, U. Gerstmann, C. Gougoussis, A. Kokalj, M. Lazzeri, L. Martin-Samos, N. Marzari, F. Mauri, R. Mazzarello, S. Paolini, A. Pasquarello, L. Paulatto, C. Sbraccia, S. Scandolo, G. Sclauzero, A. P. Seitsonen, A. Smogunov, P. Umari, and R. M. Wentzcovitch, J. Phys.: Condens. Matter **21**, 395502 (2009).

[16] P. Giannozzi, O. Andreussi, T. Brumme, O. Bunau, M. Buongiorno Nardelli, M. Calandra, R. Car, C. Cavazzoni, D. Ceresoli, M. Cococcioni, N. Colonna, I. Carnimeo, A. Dal Corso, S. de Gironcoli, P. Delugas, R. A. DiStasio, A. Ferretti, A. Floris, G. Fratesi, G. Fugallo, R. Gebauer, U. Gerstmann, F. Giustino, T. Gorni, J. Jia, M. Kawamura, H.-Y. Ko, A. Kokalj, E. Küçükbenli, M. Lazzeri, M. Marsili, N. Marzari, F. Mauri, N. L. Nguyen, H.-V. Nguyen, A. Otero-de-la-Roza, L. Paulatto, S. Poncé, D. Rocca, R. Sabatini, B. Santra, M. Schlipf, A. P. Seitsonen, A. Smogunov, I. Timrov, T. Thonhauser, P. Umari, N. Vast, X. Wu, and S. Baroni, J. Phys.: Condens. Matter **29**, 465901 (2017).

[17] J. P. Perdew, K. Burke, and M. Ernzerhof, Phys. Rev. Lett. **77**, 3865 (1996).

[18] F. C. Frank and J. S. Kasper, Acta Crystallogr. **11**, 184 (1958).

[19] T. Klimczuk and R. J. Cava, Phys. Rev. B **70**, 212514 (2004).

[20] M. Hakimi and J. G. Huber, Physica B+C **135**, 434 (1985).

[21] J. Jensen and A. Mackintosh, *Rare Earth Magnetism: Structures and Excitations* (Clarendon Press, Oxford, 1991).

[22] V. I. Zaremba, D. Kaczorowski, G. P. Nychyporuk, U. C. Rodewald, and R. Pöttgen, Solid State Sci. **6**, 1301 (2004).

[23] V. Zaremba, Y. Galadzhun, B. Belan, A. Pikul, J. Stępień-Damm, and D. Kaczorowski, J. Alloys Compd. **316**, 64 (2001).

[24] N. R. Werthamer, E. Helfand, and P. C. Hohenberg, Phys. Rev. **147**, 295 (1966).

[25] E. Helfand and N. R. Werthamer, Phys. Rev. **147**, 288 (1966).

[26] N. F. Mott, Philos. Mag.: J. Theor. Exp. Appl. Phys. **26**, 1249 (1972).

[27] K. A. Gschneidner, L. Eyring, and G. H. Lander, *Handbook on the Physics and Chemistry of Rare Earths* (Elsevier, Amsterdam, 2002).

[28] N. Magnani, P. Santini, G. Amoretti, R. Caciuffo, P. Javorský, F. Wastin, J. Rebizant, and G. H. Lander, Phys. B Condens. Matter **359–361**, 1087 (2005).

[29] W. L. McMillan, Phys. Rev. **167**, 331 (1968).

[30] E. M. Carnicom, W. Xie, T. Klimczuk, J. Lin, K. Górnicka, Z. Sobczak, N. P. Ong, and R. J. Cava, Sci. Adv. **4**, eaar7969 (2018).

[31] L. C. Srivichitranond, E. M. Seibel, W. Xie, Z. Sobczak, T. Klimczuk, and R. J. Cava, Phys. Rev. B **95**, 174521 (2017).

[32] K. T. Moore and G. van der Laan, Rev. Mod. Phys. **81**, 235 (2009).

[33] A. Kokalj, Comput. Mater. Sci. **28**, 155 (2003).

[34] G. A. Gibson and R. Meservey, Phys. Rev. B **40**, 8705 (1989).

[35] H. Rietschel and H. Winter, Phys. Rev. Lett. **43**, 1256 (1979).

[36] M. Matin, L. S. Sharath Chandra, S. K. Pandey, M. K. Chattopadhyay, and S. B. Roy, Eur. Phys. J. B **87**, 131 (2014).

[37] A. H. MacDonald, Phys. Rev. B **24**, 1130 (1981).

[38] R. C. Zehder and H. Winter, J. Phys.: Condens. Matter **2**, 7479 (1990).

[39] B. Wiendlocha, J. Tobola, M. Sternik, S. Kaprzyk, K. Parlinski, and A. M. Oleś, Phys. Rev. B **78**, 060507(R) (2008).

[40] J. Strychalska, M. Roman, Z. Sobczak, B. Wiendlocha, M. J. Winiarski, F. Ronning, and T. Klimczuk, Phys. C **528**, 73 (2016).

[41] J. Strychalska-Nowak, B. Wiendlocha, K. Hołowacz, P. Reczek, Mateusz Podgórski, M. J. Winiarski, and T. Klimczuk, Mater. Res. Express **4**, 066501 (2017).

Source material's DOI: https://doi.org/10.1103/PhysRevB.100.214514

4.3 (A3) The electronic characterization of the cubic Laves-phase superconductor $CaRh_2$

4.3.1 Cel badawczy

Dyskusja na temat właściwości fizycznych faz Lavesa rozpoczęła się w latach 20-tych i 30-tych, kiedy opublikowana praca Lavesa zapewniła wgląd w niezwykłe cechy tej klasy materiałów [53–55] . W ostatnim czasie fazy Lavesa cieszą się szczególnym zainteresowaniem ze względu na ich właściwości fizyczne tj. uporządkowanie magnetyczne, przejścia strukturalne, wysoką anizotropię magnetokrystaliczną oraz dużą magnetostrykcję w temperaturze pokojowej [56–60]. Wśród rodziny Lavesa można również znaleźć związki wykazujące nadprzewodnictwo. Największą wartość temperatury krytycznej, osiągającą 10 K, odnotowano dla $V_2Hf_{0.5}Zr_{0.5}$ [61]. Dzisiaj, spośród ponad 1000 znanych faz Lavesa, ponad 60% stanowią związki oparte na metalach ziem rzadkich. Pomimo tak dużej liczby znanych i przebadanych materiałów, wciąż istnieją nierozwiązane problemy dotyczące parametrów kontrolujących stabilność faz Lavesa.

Motywacją do przeprowadzenia badań zawartych w pracy (A3) był brak szczegółowych danych eksperymentalnych nt. właściwości fizycznych nadprzewodnika $CaRh_2$. Jak podano w rozdziale 2.2.2, jedynym znanym parametrem charakteryzującym stan nadprzewodzący była temperatura krytyczna wynosząca T_c = 6.4 K. Charakterystyka eksperymentalna nadprzewodników, które występują zarówno w wersji z Ir jak i Rh jest ważna, ze względu na możliwość zbadania wpływu sprzężenia spin-orbita na właściwości nadprzewodzące. Kolejnym czynnikiem motywującym, było opracowanie skutecznej i szybkiej metody syntezy faz Lavesa z metalami ziem alkalicznych (Ca, Sr).

Celem badań opisanych w publikacji A3 było opracowanie skutecznej metody syntezy faz Lavesa z Ca oraz eksperymentalne wyznaczenie parametrów charakteryzujących stan nadprzewodzący i normalny. Badania eksperymentalne obejmowały proszkową dyfrakcję rentgenowską, pomiary elektryczne, cieplne oraz magnetyczne.

4.3.2 Opis rezultatów

Syntezę polikrystalicznej próbki $CaRh_2$ przeprowadzono metodą reakcji w fazie stałej. Ze względu na stosunkowo szybki proces utleniania metalicznego Ca w powietrzu, wszystkie czynności związane z otrzymaniem materiału zostały wykonane w komorze rękawicowej (ang. *glove box*). Czynnikami, które zdecydowały o sukcesie syntezy fazy Lavesa $CaRh_2$ były odpowiednio dobrana nadwyżka metalu ziemi alkalicznej oraz proces chłodzenia próbki podczas pierwszego wygrzewania. Metoda opisana w pracy A3 z powodzeniem została wykorzystana przez autorkę doktoratu do otrzymania innych faz Lavesa tj. $CaPt_2$, $SrIr_2$ oraz $SrRh_2$.

Niskotemperaturowe pomiary podatności magnetycznej potwierdziły występowanie stanu nadprzewodzącego w $CaRh_2$. Wyznaczona temperatura krytyczna, T_c = 5.16 K, jest zdecydowanie niższa od raportowanej w pracy Matthiasa (T_c = 6.4 K) i jednocześnie niższa niż raportowana dla $CaIr_2$ w ref. [27] T_c = 5.8 K Potwierdza to stawianą hipotezę, że zamiana Rh na

Ir w związkach międzymetalicznych krystalizujących w tej samej strukturze, a tym samym możliwe występowanie silniejszego efektu sprzężenia spin-orbita, prowadzi do wzrostu temperatury krytycznej.

Na podstawie wyników pomiarów magnetycznych wyznaczono dolne pole krytyczne ($H_{c1}(0)$ = 418 Oe). Oszacowana wartość jest porównywalna z wartościami uzyskanymi dla innych faz Lavesa tj. $CeRu_2$ ($H_{c1}(0)$ = 200-400 Oe [62]) oraz $CaIr_2$ ($H_{c1}(0)$ = 381 Oe [27]).

W celu wyznaczenia wszystkich parametrów charakteryzujących stan nadprzewodzący, wykonano pomiary ciepła właściwego oraz oporu elektrycznego. Na wykresie temperaturowej zależności oporności elektrycznej w zerowym polu magnetycznym widać gwałtowny spadek $\rho(T)$ do zera. Ze wzrostem przykładanego pola, T_c przesuwa się w stronę niższych wartości, co pozwoliło na wyznaczenie górnego pola krytycznego ($\mu_0H_{c2}(0)$ = 3.37 T). Oszacowany parametr jest prawie trzy razy mniejszy od limitu Pauli'ego ($\mu_0H^{Pauli}(0)$ = $1.85T_c$ = 9.5 T).

Niskotemperaturowe pomiary ciepła właściwego jednoznacznie wskazują na przejście II-go rodzaju w T_c = 5.13 K, potwierdzając objętościowy charakter nadprzewodnictwa w $CaRh_2$. Znormalizowana wartość skoku ciepła właściwego wynosi $\Delta C/\gamma T_c$ = 1.78 i jest zdecydowanie wyższa od wartości wynikającej z teorii BCS ($\Delta C/\gamma T_c$ = 1.43). Parametr sprzężenia elektron-fonon został wyznaczony zarówno ze wzoru McMillana (λ_{ep}=0.63), jak i równania Allena-Dynesa (λ_{ep}=0.89) dla silnie sprzężonych nadprzewodników [63]. Uzyskane wyniki sugerują, że badany związek jest umiarkowanie, bądź silnie sprzężonym nadprzewodnikiem II-go rodzaju.

Oprócz parametrów przedstawionych powyżej wyznaczono również: długość koherencji (ξ_{GL} = 98 Å), głębokość wnikania (λ_{GL} = 942 Å) oraz parametr Ginzburga-Landaua ($\kappa_{GL} = 9.5$).

4.3.3 Treść artykułu A3

4.3.3 Treść artykułu A3

Tytuł: The electronic characterization of the cubic Laves-phase superconductor CaRh$_2$

Autorzy: Karolina Górnicka, Robert J. Cava, Tomasz Klimczuk

Czasopismo: Journal of Alloys and Compounds 793 (2019) 393e399

Impact factor: 4.650 (2019)

Liczba punktów ministerialnych MNiSW: 100 pkt

DOI: 10.1016/j.jallcom.2019.04.199

Mój udział polegał na syntezie próbki polikrystalicznej, przeprowadzeniu badań strukturalnych metodą proszkowej dyfrakcji rentgenowskiej wraz z analizą LeBaila otrzymanego dyfraktogramu, pomiarach właściwości magnetycznych, cieplnych, elektrycznych wraz z analizą wyników, udziale w dyskusji otrzymanych rezultatów, wyznaczeniu parametrów charakteryzujących stan normalny i nadprzewodzący, przygotowaniu rysunków oraz tekstu manuskryptu. Pełniłam rolę autora korespondencyjnego oraz przygotowałam odpowiedzi na recenzje.

Karolina Górnicka

mgr inż. Karolina Górnicka

The original source: Journal of Alloys and Compounds *Volume 793, 15 July 2019, Pages 393-399*

Journal of Alloys and Compounds 793 (2019) 393–399

Contents lists available at ScienceDirect

Journal of Alloys and Compounds

journal homepage: http://www.elsevier.com/locate/jalcom

The electronic characterization of the cubic Laves-phase superconductor $CaRh_2$

Karolina Górnicka [a, *], Robert J. Cava [b], Tomasz Klimczuk [a]

[a] Faculty of Applied Physics and Mathematics, Gdańsk University of Technology, ul. Narutowicza 11/12, 80-233, Gdańsk, Poland
[b] Department of Chemistry, Princeton University, Princeton, NJ, 08544, USA

A R T I C L E I N F O

Article history:
Received 12 February 2019
Received in revised form
1 April 2019
Accepted 2 April 2019
Available online 21 April 2019

Keywords:
Superconductivity
Laves phase
Synthesis
Experimental characterization

A B S T R A C T

We present the synthesis and experimental characterization of the electronic properties of the cubic Laves phase superconductor $CaRh_2$. Its crystal structure was confirmed by powder X-ray diffraction and its ambient temperature lattice parameter ($a = 7.5326(6)$ Å) is in good agreement with the literature. Magnetization, resistivity and heat-capacity measurements indicate that $CaRh_2$ is a moderate-coupling type-II superconductor ($\lambda_{e-p} = 0.89$) with a transition temperature $T_c = 5.13$ K. A sharp discontinuity at T_c in the heat capacity shows that the normalized specific-heat jump is $\Delta C/\gamma T_c = 1.78$, which exceeds the value predicted by weak-coupling BCS theory (1.43).

1. Introduction

There are more than a thousand known binary compounds in the Laves phase family [1]. Many of them show interesting physical behavior such as long range magnetic ordering [2] large magnetocaloric effects [3] and superconductivity [4–7]. Laves phase compounds are also important in engineering applications, i.e. some can be used as a hydrogen storage system [8–13]. In this family there are also compounds characterized by low density, high melting temperature and high oxidation resistance - the properties required for high-temperature applications [14–17].

As expressed by Fritz Laves [18], depending on the crystal structure there are three different materials structures in this family, i.e. the fcc C15-type cubic structure (*Fd-3m*), the C14-type hexagonal structure ($P6_3/mmc$) and the C36-type dihexagonal structure ($P6_3/mmc$). Among them, the C15 one is considered to be favorable for superconductivity, with critical temperatures ranging from 0.07 K for $HfMo_2$ to above 10 K for $V_2Hf_{0.5}Zr_{0.5}$ [19,20]. Many of them were reported decades ago, with the superconductivity confirmed only by resistivity or magnetic measurements. Hence, detailed studies of the superconducting state in this important family is often missed.

B. T. Matthias and E. Corenzwit [4] studied the alkaline earth (*Ae*) metal based Laves phase compounds $AeRh_2$ and $AeIr_2$ and found superconductivity with the critical temperature of 6.4 K and 4–6.15 K for $CaRh_2$ and $CaIr_2$, respectively. The crystal structure of $CaRh_2$ and $CaIr_2$ was described by Wood et al. [21]. Recently, Haaldolaarachchige, et al. [6] studied the superconducting properties of $CaIr_2$, revealing $T_c = 5.8$ K from susceptibility, resistivity and specific heat measurements. Although theoretical work can be found, the detailed experimental characterization of $CaRh_2$ is still lacking in the literature [22,23].

In this paper, we report synthesis and for the first time experimental characterization of the electronic properties of the cubic Laves phase superconductor $CaRh_2$. We have used magnetization, resistivity and heat capacity measurements to probe the superconducting ground state.

2. Experimental details

The polycrystalline sample of $CaRh_2$ was prepared from elemental Ca-pieces (4 N; Alfa Aesar) and Rh-powder (3N8; Mennica-Metale, Poland) by a two-step solid state reaction method. An excess of calcium (25%) was added in order to compensate for the Ca loss due to evaporation. All the following manipulations were performed in a protective Ar-atmosphere in a glove box system (p(O2) < 0.5 ppm). The starting materials were added into an alumina crucible and then sealed inside an Ar-filled

---

[*] Corresponding author.
E-mail address: karolina.gornicka@pg.edu.pl (K. Górnicka).

https://doi.org/10.1016/j.jallcom.2019.04.199

quartz tube. The ampoule was heated to 870 °C, kept at that temperature for 12 h, and then slowly cooled (20 °C per hour) and held at 800 °C for 2 h. The as-prepared material was thoroughly reground and pressed into a pellet. Subsequently, the pellet was enclosed in an evacuated quartz tube, slowly heated to 800 °C and held for 12 h. No melting was observed and the resulting material was hard, dense and black in color. To avoid possible decomposition, the obtained material was kept inside the glove box until characterization.

The chemical composition of the sample was examined using an FEI Quanta 250 FEG scanning electron microscope (SEM) equipped with an Apollo-X SDD energy-dispersive spectrometer (EDS). The data were analyzed using the EDAX TEAM™ software. The purity and the crystal structure of the sample at room temperature was verified by powder X-ray diffraction (pXRD) using a PANalytical diffractometer equipped with Cu Kα radiation. The data were analyzed by the LeBail method using the FullProf package [24]. Magnetic susceptibility and magnetization measurements were performed using a Quantum Design Dynacool Physical Property Measurement System (PPMS) with a vibrating sample magnetometer (VSM) function in the temperature range of 1.7–6.5 K under various applied magnetic fields. Resistivity and heat capacity measurements were performed on a PPMS Evercool II system. The electrical resistivity was measured by a conventional four-probe method, in which small diameter Pt wires (50 μm) were attached to the previously polished sample using conductive epoxy (Epotek H20E). A sample with contacts was annealed at 110 °C for 30 min in a chamber furnace. Data were collected from 1.9 to 300 K under zero field and in magnetic fields up to 2.4 T. The specific heat data was measured using the two-τ time-relaxation method between 1.9 and 300 K at 0 T and in magnetic fields up to 3 T. The sample was attached to the measuring stage using Apiezon N grease to ensure good thermal contact.

3. Results

The $CaRh_2$ sample was first characterized at room temperature using an energy dispersive spectrometer (EDS) and the powder X-ray diffraction technique (pXRD). The EDS analysis revealed that the actual Ca:Rh ratio 2:1 is consistent with the nominal composition ($CaRh_2$) within experimental error, confirming the stoichiometry of the sample. The X-ray powder diffraction pattern of $CaRh_2$ is shown in Fig. 1. The pXRD confirmed a good quality sample with a small amount of impurity phase (denoted by asterisks). In a more detailed analysis of the data, the *Fd-3m* phase was refined with the LeBail method. The LeBail fit to the powder diffraction pattern, represented by the black solid line in Fig. 1, gave the lattice constant $a = 7.5326(6)$ Å. This value is in a very good agreement with the data published previously, by Wood et al. [21]. The results obtained confirm that $CaRh_2$ crystallizes in the cubic Laves-phase crystal structure, in which Ca atoms are arranged on the diamond structure sites, and Rh atoms generate tetrahedra. The Bragg positions and the difference plot between experimental and fitted data (blue line) are also shown in Fig. 1. An additional pXRD scan was performed on a pulverized sample exposed to air for 12 h. The obtained pattern confirms stability of $CaRh_2$ over that time period.

To characterize the superconducting transition of $CaRh_2$, zero-field-cooled (ZFC) and field-cooled (FC) dc magnetic susceptibility (defined as $\chi = dM/dH$ where M is the magnetization and H is the applied magnetic field) was measured in the temperature interval 2–6 K under an applied field of 10 Oe. The plot of the volume magnetic susceptibility (χ_V) versus temperature is shown in Fig. 2. The clear diamagnetic signal observed confirms the occurrence of superconductivity in this material. The superconducting transition temperature, T_c, was determined as the point at which the extrapolation of the normal-state magnetic susceptibility intersects with the steepest slope line of the superconducting signal [25] yielding $T_c = 5.16$ K. The conservatively-determined value thus obtained is slightly lower than reported in literature ($T_c = 6.4$ K) [4]. When corrected for the demagnetization factor, $N = 0.65$ (determined from the volume magnetization, $M_V(H)$, in applied fields below H_{c1} discussed in the following section), the zero-field-cooled dc susceptibility ($4\pi\chi_V$) approaches a value of −1 for $T < 4$ K indicating that the shielding volume fraction is 100%. Compared with the ZFC data, the much lower field-cooled (FC) diamagnetic signal is typically observed in polycrystalline samples.

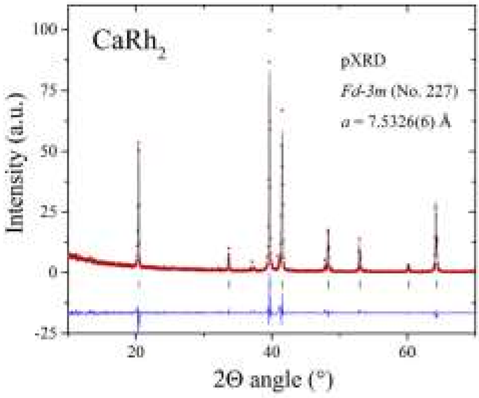

Fig. 1. Powder X-ray diffraction pattern of $CaRh_2$ (red points) together with the LeBail refinement profile (black solid line). The green vertical bars indicate the expected Bragg peak positions (space group *Fd-3m*). The blue curve is the difference between experimental and model results. . (For interpretation of the references to color in this figure legend, the reader is referred to the Web version of this article.)

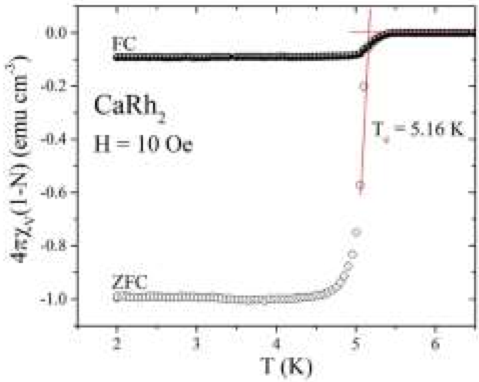

Fig. 2. Zero-field-cooled (ZFC) and field-cooled (FC) temperature-dependent volume magnetic susceptibility $\chi_V(T)$ measurements performed under a small applied magnetic field of 10 Oe.

To determine the lower critical field $H^*_{c1}(0)$, magnetization curves, $M_V(H)$, in low applied magnetic fields were measured for a range of temperatures ($1.7\ K \le T \le 4.25$ K) as shown in the inset of

Fig. 3. Assuming that the initial linear response to fields is perfectly diamagnetic, we obtain a demagnetization factor (N = 0.65) that is consistent with the sample's shape. The value of the lower critical field H^*_{c1} at each temperature is defined as the point of deviation from the full Meissner effect of the data curve. Above H^*_{c1}, magnetic flux begins to penetrate the sample and thus the magnetization starts to deviate from linearity. In order to precisely calculate this point, we follow the methodology described elsewhere [26,27]. The main panel of Fig. 3 presents the temperature variation of H^*_{c1}(T). As expected, the resulting values decrease monotonically with increasing temperature and can be described using the Ginzburg-Landau equation:

$$H^*_{c1}(T) = H^*_{c1}(0)\left[1 - \left(\frac{T}{T_c}\right)^2\right], \tag{1}$$

where $H^*_{c1}(0)$ is the lower critical field at 0 K and T_c is the superconducting critical temperature. The experimental data are well described with the above formula and a fit (red solid line) yields $H^*_{c1}(0) = 146(1)$ Oe. Correcting for the demagnetization factor (N = 0.65), the lower critical field at 0 K is calculated to be $H_{c1}(0) = 418$ Oe (41.8 mT). The value obtained is comparable with these reported for cubic Laves phases $CeRu_2$ ($H_{c1}(0) = 200–400$ Oe [7]) and $CaIr_2$ ($H_{c1}(0) = 381$ Oe [6]).

Further evidence of the superconductivity in $CaRh_2$ is given by the abrupt drop in resistivity, as summarized in Fig. 4. The main panel shows the electrical resistivity as a function of temperature for the range between 1.8 and 300 K in zero applied magnetic field. The ρ(T) data decrease with decreasing temperature, indicating metallic behavior (dρ/dT > 0). At higher temperatures the resistivity curve exhibits a tendency to saturate that suggests that some additional scattering processes, e.g. Mott interband scattering [28–30], determines the electrical resistivity of $CaRh_2$ and/or the charge carrier mean free path becomes comparable to the interatomic spacing (the Ioffe-Regel limit [31–33]). The residual resistivity ratio RRR is rather low and is found to be ρ(300)/ρ(10) = 4.3, which is typical for a metal in a polycrystalline form where grain boundaries conduct poorly. The red line through the experimental data represents a fit called a parallel resistor model (PRM) [31,34–36] that combines a Bloch-Grüneisen resistivity ρ_{GB} together with a parallel, temperature independent resistor ρ_{max}:

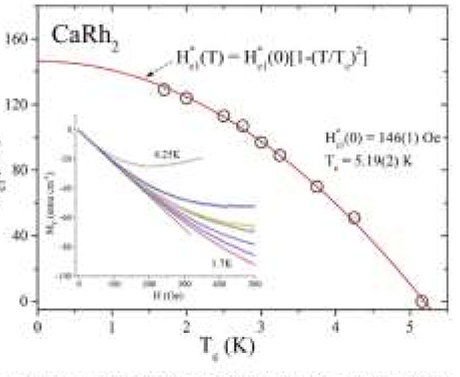

Fig. 3. The temperature dependence of the lower critical fields. The inset shows the field-dependent magnetization curves $M_V(H)$ for $CaRh_2$ taken at different temperatures.

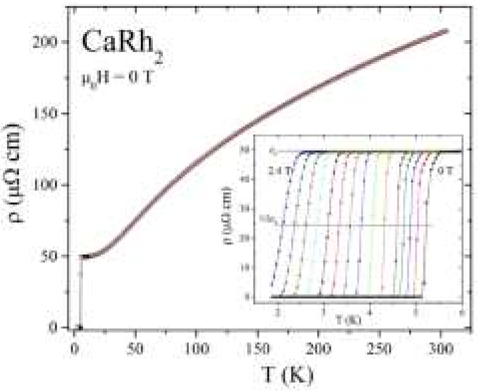

Fig. 4. Main panel: The temperature dependent resistivity for $CaRh_2$ over a wide temperature range. The inset presents the detail of the superconducting transition in the resistivity in zero field and in various applied fields.

$$\rho^{-1}(T) = \rho_{max}^{-1} + (\rho_0 + \rho_{BG})^{-1} \tag{2}$$

and

$$\rho_{GB} = 4R\Theta_R\left(\frac{T}{\Theta_R}\right)^5\int\frac{x^5}{[\exp(x)-1][1-\exp(-x)]}dx \tag{3}$$

where Θ_R is the Debye temperature obtained from fitting resistivity measurements and R is a material-dependent constant independent of T. The ρ(T) data above T_c are well described by this model, yielding the fit parameters $\rho_0 = 56.3(6)$ μΩ cm, $\rho_{max} = 424.7(8)$ μΩ cm and $\Theta_R = 158(1)$ K.

At low temperatures the electrical resistivity drops sharply to zero at $T_c = 5.2$ K, where, for resistivity data, T_c is defined by the temperature of the 50% drop of the ρ(T) data in zero magnetic field. The superconducting transition was measured in a variety of applied fields for the same sample, as shown in the inset of Fig. 4. As the magnetic field is increased, T_c shifts to lower temperature and the transition becomes slightly broader. Using the criterion of the 50% normal state resistivity point as the transition temperature, we determine the upper critical field $\mu_0H_{c2}(0)$ for $CaRh_2$ (see Fig. 5). It is evident from the graph that the data obtained varies linearly with temperature. Given that the influence of spin-orbit coupling for the $CaRh_2$ is rather weak, the data are fit with the following Ginzburg-Landau relation [37–39]:

$$\mu_0H_{c2}(T) = \mu_0H_{c2}(0)\frac{(1-t^2)}{(1+t^2)} \tag{4}$$

where $t = T/T_c$ and T_c is the transition temperature at zero magnetic field. The solid line in Fig. 5 presents the best fit of the experimental data by equation (4). The extrapolation yields $\mu_0H_{c2}(0) = 3.37$ T, which is slightly lower than the value obtained for $CaIr_2$ ($\mu_0H_{c2}(0) = 4$T [6]). The Pauli limiting field within the BCS theory for weak electron-phonon coupling [40,41] gives $H^P_{c2}(0) = 1.85\ T_c = 9.5$ T, which is almost three times larger than estimated upper critical field value for $CaRh_2$. Consequently, the coherence length, ξ_{GL}, can be estimated using the Ginzburg-Landau formula $H_{c2} = \Phi_0/2\pi\xi^2_{GL}$, where $\Phi_0 = hc/2e$ is the quantum flux. For

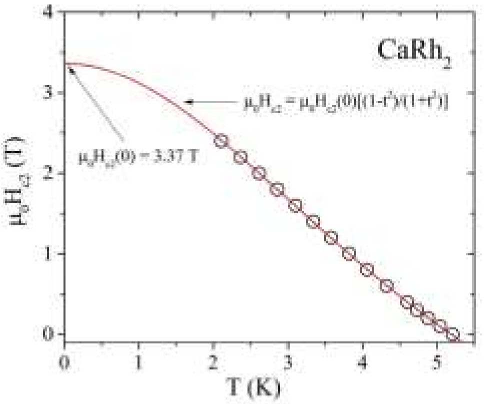

Fig. 5. The temperature dependence of the upper critical field of CaRh$_2$, determined from electrical resistivity measurements.

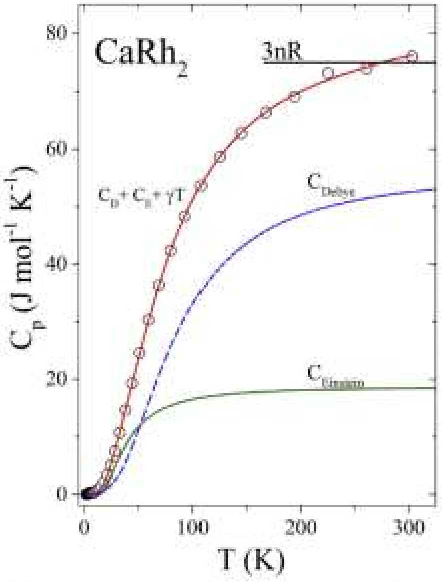

Fig. 6. The specific heat of CaRh$_2$ versus temperature in zero magnetic field with a fit to a combined model (red solid line) with 75% of the weight is Debye model (blue dashed line) and 25% is Einstein model (green solid line). (For interpretation of the references to color in this figure legend, the reader is referred to the Web version of this article.)

$\mu_0H_{C2}(0) = 3.37$ T, we obtained $\xi_{GL}(0) = 98$ Å.

The superconducting penetration depth $\lambda_{GL}(0)$ can then be obtained from $H_{C1}(0)$ and $\xi_{GL}(0)$ using the relation:

$$H_{c1} = \frac{\Phi_0}{4\pi\lambda_{GL}^2}\ln\frac{\lambda_{GL}}{\xi_{GL}}. \tag{5}$$

The value is found to be $\lambda_{GL}(0) = 942$ Å for CaRh$_2$. Moreover, the Ginzburg-Landau parameter$\kappa_{GL} = \lambda_{GL}/\xi_{GL} = 9.5 > 1/\sqrt{2}$, confirming that CaRh$_2$ is a type-II superconductor [37]. Finally, the thermodynamic critical field can be obtained from κ_{GL}, H_{c1} and H_{c2} using the formula

$$H_{c1}H_{c2} = H_c^2\ln\kappa_{GL} \tag{6}$$

yielding $\mu_0H_c = 250$ mT.

The characterization of the superconducting transition by specific heat measurements is shown in Fig. 6 and Fig. 7. The panel of Fig. 6 depicts the temperature dependence of the specific heat C_p of CaRh$_2$ from 1.9 K to 300 K in zero magnetic field. At high temperatures the heat capacity approaches the Dulong-Petit limit (3 nR = 74.8 J mol^{-1}K^{-1}, where n = 3 and R = 8.31 J mol^{-1}K^{-1} are the number of atoms per formula unit and the gas constant, respectively), which suggests that there are no magnetic degrees of freedom in this material. There is also no evidence for any anomalies that may correspond to a structural phase transition between base temperature and room temperature. The red solid line denotes a fit to a combined model: $C_p = \gamma T + (1-k)C_{Einstein} + kC_{Debye}$, where γ is the Sommerfeld coefficient and

$$C_{Einstein}(T) = 3nR\left(\frac{\Theta_E}{T}\right)^2 exp\left(\frac{\Theta_E}{T}\right)\left[exp\left(\frac{\Theta_E}{T}\right) - 1\right]^{-2} \tag{7}$$

$$C_{Debye}(T) = 9nR\left(\frac{T}{\Theta_D}\right)^3\int\frac{x^4\exp(x)}{[\exp(x)-1]^2}dx \tag{8}$$

The Debye temperature obtained from the fit is equal to $\Theta_D = 345(5)$ K, the Einstein temperature $\Theta_E = 122(3)$ K, $k = 0.75(2)$ of the weight belongs to the Debye heat capacity C_{Debye} (blue dashed line), 0.25 of the weight belongs to the Einstein heat capacity $C_{Einstein}$ (green solid line) and $\gamma = 16.9(5)$ mJ mol^{-1} K^{-2}.

The Fig. 7(a) presents C_p/T plotted as a function of temperature, characterizing the specific heat jump at the thermodynamic transition. The bulk nature of the superconductivity and the good quality of the sample are confirmed by a sharp, large anomaly at 5.13 K, which is consistent with the superconducting transition temperature determined by the magnetic and resistivity data. The specific heat jump at T_c, estimated by using the equal entropy construction (blue solid lines), is $\Delta C/T_c = 44$ mJ mol^{-1} K^{-2}.

The part (b) of the same figure shows the heat-capacity measurements under applied magnetic fields. The magnitude of the discontinuity and the transition temperature decrease as the strength of the applied magnetic field is increased. The width of the transition also becomes broader in higher magnetic fields.

Panel (c) of Fig. 7 shows the normal-state specific heat data plotted as C_p/T versus T^2 under an applied magnetic field of $\mu_0H = 3$ T. The experimental data can be fitted using the equation $C_p/T = \gamma + \beta T^2$, where the first and second terms are attributed to the electronic and lattice contributions to the heat capacity, respectively. The extrapolation gives $\gamma = 24.7(1)$ mJ mol^{-1} K^{-2} and $\beta = 0.175(7)$ mJ mol^{-1} K^{-4}. Furthermore, the Debye temperature Θ_D can be calculated using the relation

$$\Theta_D = \left(\frac{12\pi^4}{5\beta}nR\right)^{1/3} \tag{9}$$

where R = 8.31 J mol^{-1} K^{-1} and n = 3 for CaRh$_2$. The resulting value of Θ_D is 322(4), which is significantly larger than the Debye temperature for CaIr$_2$ ($\Theta_D = 160$ K [6]) and CeRu$_2$ ($\Theta_D = 173$ K [7]) and

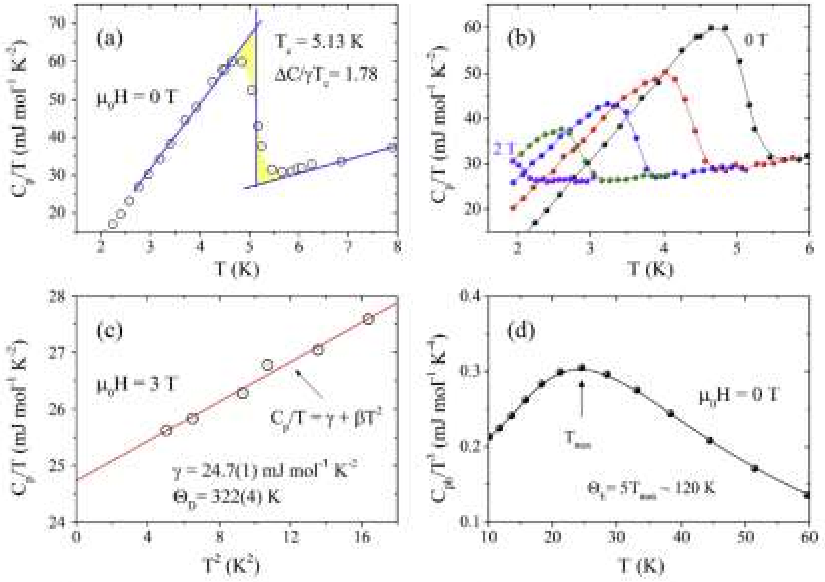

Fig. 7. Panel (a): the specific heat anomaly in zero magnetic field at low temperatures with $T_c = 5.13$ K. (b) The temperature dependence of the C_p/T in applied magnetic fields up to $\mu_0H = 2$ T. (c) C_p/T vs. T^2 measured at 3 T magnetic field. A red solid line represents a linear fit used to estimate the values of electronic and phonon specific heat coefficients. (d) The phonon contribution to heat capacity divided by T^3 versus T. (For interpretation of the references to color in this figure legend, the reader is referred to the Web version of this article.)

is close to the value obtained from the fit to the combined model. Having the estimated Debye temperature Θ_D, the electron-phonon constant λ_{e-p}, which gives the strength of the attractive interaction between the electron and phonon, can be calculated from the inverted McMillan formula [42]:

$$\lambda_{e-p} = \frac{1.04 + \mu^* ln(\Theta_D/1.45T_c)}{(1-0.62\,\mu^*)ln(\Theta_D/1.45T_c) - 1.04} \tag{10}$$

where μ^* is the Coulomb pseudopotential parameter, typically taken as $\mu^* = 0.13$ for many intermetallic superconductors [27,39,43,44]. Using $T_c = 5.13$ K and $\Theta_D = 322$ K, we obtained $\lambda_{e-p} = 0.63$, indicating that $CaRh_2$ is a moderate-coupling superconductor.

Fig. 7(d) displays the phonon contribution to heat capacity C_{ph} divided by T^3 versus temperature, where $C_{ph} = C_p - \gamma T$. The maximum temperature of C_{ph}/T^3 is equal to $T_{max} = \Theta_E/5$ and hence the Einstein temperature is $\Theta_E = 5 \times 24$ K $= 120$ K – in a perfect agreement with a whole temperature fit.

Using the specific heat jump value ($\Delta C/T_c = 44$ mJ mol^{-1} K^{-2}) and the Sommerfeld coefficient ($\gamma = 24.7(1)$ mJ mol^{-1}K^{-2}), another important superconducting parameter $\Delta C/\gamma T_c$ can be calculated. The normalized specific heat jump at T_c is equal to 1.78. The value exceeds the weak coupling superconductivity value predicted by the BCS theory (1.43) suggesting moderate or strong-coupling superconductivity in $CaRh_2$. Using the equation proposed by F. Marsiglio and J. P. Carbotte for strong-coupling superconductors [45]:

$$\frac{\Delta C_p}{\gamma T_c} = 1.43\left[1 + 53\left(\frac{T_c}{\omega_{ln}}\right)^2 \ln\left(\frac{\omega_{ln}}{3T_c}\right)\right], \tag{11}$$

the logarithmic averaged phonon frequency obtained $\omega_{ln} = 105$ K is smaller than calculated $\omega_{ln} = 120.2$ K or 140.8 K (with the spin-orbit coupling) [22]. Then from the Allen and Dynes equation for the strong-coupling superconductors [46]:

$$T_c = \left(\frac{\omega_{ln}}{1.2}\right)\exp\left[-\frac{1.04(1+\lambda_{e-p})}{\lambda_{e-p} - \mu^*(1+0.62\,\lambda_{e-p})}\right], \tag{12}$$

we estimated $\lambda_{e-p} = 0.89$, which is larger than derived from the inverted McMillan equation ($\lambda_{e-p} = 0.63$).

In addition, having calculated the Sommerfeld coefficient and electron-phonon coupling constant, the non-interacting density of states at the Fermi level $N(E_F)$ can be estimated from:

$$N(E_F) = \frac{3\gamma}{\pi^2 k_B^2 (1+\lambda_{e-p})}, \tag{13}$$

where k_B is the Boltzmann constant. The calculated $N(E_F) = 6.44$ states eV^{-1} per formula unit (f.u.) or 5.54 states eV^{-1} per f.u. for $\lambda_{e-p} = 0.63$ and 0.89, respectively. The superconducting and normal state parameters of $CaRh_2$ are gathered in Table 1.

Table 1
Superconducting and normal state parameters of $CaRh_2$ (this work) and $CaIr_2$ [6]. Parameters marked by an asterisk were derived from equations for strong coupling superconductors.

Parameter	Unit	$CaRh_2$	$CaIr_2$
T_c	K	5.13	5.8
$\mu_0H_{c2}(0)$	T	3.37	4.0
$\mu_0H_{c1}(0)$	mT	41.8	38.1
μ_0H_c	mT	250	600
λ_{e-p}	–	0.63 0.89*	0.79
$\xi_{GL}(0)$	Å	98	90.7
$\lambda_{GL}(0)$	Å	942	960
κ_{GL}	–	9.5	10.6
γ	$mJ\,mol^{-1}\,K^{-2}$	24.7(1)	8.4
β	$mJ\,mol^{-1}\,K^{-4}$	0.175(7)	–
Θ_D	K	322(4)	160
RRR	–	4.3	–
$\Delta C_p/\gamma T_c$	–	1.78	0.89
$N(E_F)$	$eV\,f.u.^{-1}$	6.44 5.54*	3.49

4. Summary

We have synthesized high quality polycrystalline $CaRh_2$ using a solid state reaction method. Powder XRD confirms the fcc C15 crystal structure type for this material, in the cubic Laves phase structure, with the refined lattice parameter $a = 7.5325(6)$ Å in agreement with reported by Wood et al. [21]. Heat capacity, magnetic susceptibility and resistivity measurements reveal superconductivity with $T_c = 5.13$ K. The $CaRh_2$ material tested was the purest in the Ca-Rh series prepared, and the T_c of the other synthesized samples was reproducible and near 5.1 K. This value is lower than reported by B. T. Matthias and E. Corenzwit (6.4 K) [4], but the omission of details from that report does not allow us to speculate about why the number they report for T_c is different from ours. The T_c for $CaRh_2$ is slightly lower than superconducting critical temperature of $CaIr_2$ (5.8 K) [6].

Comparison of the superconducting parameters for $CaRh_2$ and $CaIr_2$ (see Table 1), shows similar values of lower as well as upper critical fields, penetration depth, coherence length and the Ginzburg-Landau parameter. In contrast, the parameters revealed from the heat capacity measurements are different. The twice larger Debye temperature for $CaRh_2$ might be due to much lower molar mass of Rh (103 g/mol) versus Ir (192 g/mol). The Sommerfeld parameter, and hence the density of states at the E_F, is again larger for the Rh-based compound.

Recent theoretical studies on $CaRh_2$ and $CaIr_2$ Laves-phase materials show the importance of the SOC effect in this system. The *ab initio* pseudopotential results reveal that including the SOC makes the low-frequency phonon modes harder, and that the calculated critical temperature decreases from 9.08 K to 6.97 K as one proceeds from the Rh to the Ir material. A similar effect is observed for the electron-phonon coupling constant, which changes from 1.17 to 0.96. However, both T_c and λ_{e-p} are much higher than reported in this work. This discrepancy might be due to a different value of the logarithmically averaged phonon frequency ω_{ln} which is 105 K and 120 K from experiment and calculations, respectively. A comparable study of the Sr analogs $SrRh_2$ and $SrIr_2$ is in progress [47].

Acknowledgment

The research performed at the Gdansk University of Technology was supported by the National Science Centre (Poland) grant (UMO-2017/27/B/ST5/03044). The synthesis and thermodynamic characterization performed at Princeton was supported by the Department of Energy, Division of Basic Energy Sciences, grant DE-FG02-98ER45706.

References

[1] Karl A. Gschneidner Jr., Vitalij K. Pecharsky, Binary rare earth Laves phases — an overview, Z. für Kristallogr. - Cryst. Mater. 221 (2006), https://doi.org/10.1524/zkri.2006.221.5-7.375.
[2] Tian Gao, Ningning Qi, Yufeng Zhang, Tao Zhou, Magnetic properties and large magnetocaloric effect in Laves phase metallic compound, J. Phys. Conf. Ser. 568 (2014), 042006, https://doi.org/10.1088/1742-6596/568/4/042006.
[3] Niraj K. Singh, K.G. Suresh, A.K. Nigam, S.K. Malik, A.A. Coelho, S. Gama, Itinerant electron metamagnetism and magnetocaloric effect in RCo2-based Laves phase compounds, J. Magn. Magn. Mater. 317 (2007) 68–79, https://doi.org/10.1016/j.jmmm.2007.04.009.
[4] B.T. Matthias, E. Corenzwit, Superconducting alkaline earth compounds, Phys. Rev. 107 (1957), https://doi.org/10.1103/PhysRev.107.1558, 1558–1558.
[5] V.B. Compton, B.T. Matthias, Laves phase compounds of rare earths and hafnium with noble metals, Acta Crystallogr. 12 (1959) 651–654, https://doi.org/10.1107/S0365110X59001918.
[6] Neel Haldolaarachchige, Quinn Gibson, Leslie M. Schoop, Huixia Luo, R.J. Cava, Characterization of the heavy metal pyrochlore lattice superconductor CaIr 2, J. Phys. Condens. Matter 27 (2015) 185701, https://doi.org/10.1088/0953-8984/27/18/185701.
[7] Hitoshi Sugawara, Hideyuki Sato, Tsuyoshi Yamazaki, Noriaki Kimura, Rikio Settai, Yoshichika Ōnuke, Superconducting properties of CeRu $_2$ single crystal, J. Phys. Soc. Jpn. 64 (1995) 4849–4855, https://doi.org/10.1143/JPSJ.64.4849.
[8] K. Young, M. Young, T. Ouchi, B. Reichman, M.A. Fetcenko, Improvement in high-rate dischargeability, activation, and low-temperature performance in multi-phase AB2 alloys by partial substitution of Zr with Y, J. Power Sources 215 (2012) 279–287, https://doi.org/10.1016/j.jpowsour.2012.05.030.
[9] X.W. Yang, T.B. Zhang, R. Hu, J.S. Li, X.Y. Xue, H.Z. Fu, Microstructure and hydrogenation thermokinetics of ZrTi0.2V1.8 alloy, Int. J. Hydrogen Energy 35 (2010) 11981–11985, https://doi.org/10.1016/j.ijhydene.2010.08.065.
[10] G. Srinivas, V. Sankaranarayanan, S. Ramaprabhu, Kinetics of hydrogen absorption in Ho1−xMmxCo2 alloys, J. Alloys Compd. 448 (2008) 159–165, https://doi.org/10.1016/j.jallcom.2006.10.064.
[11] Suklyun Hong, C.L. Fu, Hydrogen in Laves phase Zr X 2 (X = V , Cr, Mn, Fe, Co, Ni) compounds: binding energies and electronic and magnetic structure, Phys. Rev. B 66 (2002), https://doi.org/10.1103/PhysRevB.66.094109.
[12] X. Liu, K. Asano, N. Terashita, E. Akiba, Hydrogenation of C14 Laves phase alloy: CaLi2, Int. J. Hydrogen Energy 34 (2009) 1472–1475, https://doi.org/10.1016/j.ijhydene.2008.12.011.
[13] Jamil Ahmad, Hideki Maekawa, Hitoshi Takamura, Itaru Oikawa, Mariko Ando, Kuniaki Takahashi, In situ NMR study of hydrogenation/dehydrogenation of ZrCr2 and physisorbed hydrogen, J. Alloys Compd. 540 (2012) 222–227, https://doi.org/10.1016/j.jallcom.2012.06.080.
[14] Armin Von Keitz, Gerhard Sauthoff, Laves phases for high temperatures—Part II: stability and mechanical properties, Intermetallics 10 (2002) 497–510, https://doi.org/10.1016/S0966-9795(02)00025-0.
[15] D.J. Thoma, K.A. Nibur, K.C. Chen, J.C. Cooley, L.B. Dauelsberg, W.L. Hults, P.G. Kotula, The effect of alloying on the properties of (Nb,Ti)Cr2 C15 Laves phases, Mater. Sci. Eng., A 329–331 (2002) 408–415, https://doi.org/10.1016/S0921-5093(01)01614-8.
[16] J.J. Liu, W.J. Ren, Z.D. Zhang, D. Li, J. Li, X.G. Zhao, W. Liu, S.W. Or, Spin configuration and magnetostrictive properties of Laves compounds TbxDy0.7−xPr0.3(Fe0.9B0.1)1.93(0.10≤x≤0.28), J. Appl. Phys. 100 (2006), 023904, https://doi.org/10.1063/1.2219344.
[17] X.W. Nie, S.Q. Lu, K.L. Wang, Effect of mechanical alloying on the structure and properties of NbCr2 Laves phase fabricated by hot pressing, Powder Technol. 184 (2008) 333–336, https://doi.org/10.1016/j.powtec.2007.09.006.
[18] Fritz Laves, Crystal Structure and Atomic Size, American Society for Metals, 1956.
[19] Östen Rapp, Superconductivity and lattice parameters in the zirconium-molybdenum, zirconium-tungsten, hafnium-molybdenum and hafnium-tungsten alloy systems, J. Less Common Met. 21 (1970) 27–44, https://doi.org/10.1016/0022-5088(70)90162-1.
[20] Kiyoshi Inoue, Kyoji Tachikawa, Y. Iwasa, A new high-field superconductor, V $_2$ Hf $_x$ Zr 1− $_x$, appl. Phys. Lett. 18 (1971) 235–237, https://doi.org/10.1063/1.1653644.
[21] E.A. Wood, V.B. Compton, Laves-phase compounds of alkaline earths and noble metals, Acta Crystallogr. 11 (1958) 429–433, https://doi.org/10.1107/S0365110X58001134.
[22] H.M. Tütüncü, H.Y. Uzunok, Ertuğrul Karaca, E. Arslan, G.P. Srivastava, Effects of spin-orbit coupling on the electron-phonon superconductivity in the cubic Laves-phase compounds CaIr 2 and CaRh 2, Phys. Rev. B 96 (2017), https://doi.org/10.1103/PhysRevB.96.134514.
[23] Md Zahidur Rahaman, Md Atikur Rahman, Investigation of the physical properties of two Laves phase compounds HRh $_2$ (H = Ca and La): a DFT study, Int. J. Mod. Phys. B 32 (2018) 1850149, https://doi.org/10.1142/S0217979218501497.
[24] Juan Rodríguez-Carvajal, Recent advances in magnetic structure

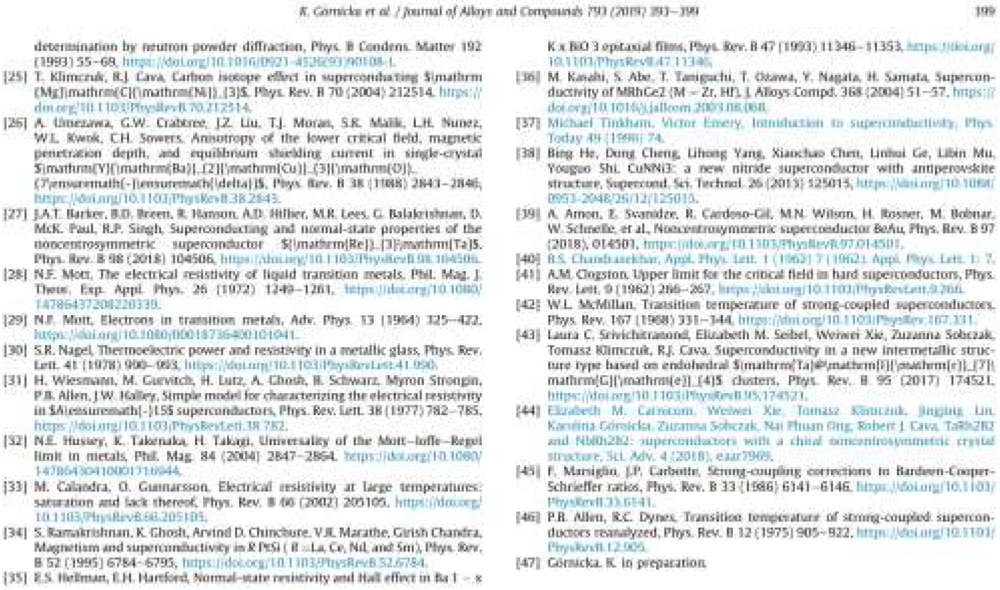

determination by neutron powder diffraction, Phys. B Condens. Matter 192 (1993) 55–68, https://doi.org/10.1016/0921-4526(93)90108-I.

[25] T. Klimczuk, R.J. Cava, Carbon isotope effect in superconducting $\mathrm{Mg}\mathrm{C}{\mathrm{Ni}}_{3}$, Phys. Rev. B 70 (2004) 212514, https://doi.org/10.1103/PhysRevB.70.212514.

[26] A. Umezawa, G.W. Crabtree, J.Z. Liu, T.J. Moran, S.K. Malik, L.H. Nunez, W.L. Kwok, C.H. Sowers, Anisotropy of the lower critical field, magnetic penetration depth, and equilibrium shielding current in single-crystal $\mathrm{Y}{\mathrm{Ba}}_{2}{\mathrm{Cu}}_{3}{\mathrm{O}}_{(7\ensuremath{-}\ensuremath{\delta})}$, Phys. Rev. B 38 (1988) 2843–2846, https://doi.org/10.1103/PhysRevB.38.2843.

[27] J.A.T. Barker, B.D. Breen, R. Hanson, A.D. Hillier, M.R. Lees, G. Balakrishnan, D. McK. Paul, R.P. Singh, Superconducting and normal-state properties of the noncentrosymmetric superconductor ${\mathrm{Re}}_{3}\mathrm{Ta}$, Phys. Rev. B 98 (2018) 104506, https://doi.org/10.1103/PhysRevB.98.104506.

[28] N.F. Mott, The electrical resistivity of liquid transition metals, Phil. Mag. J. Theor. Exp. Appl. Phys. 26 (1972) 1249–1261, https://doi.org/10.1080/14786437208220339.

[29] N.F. Mott, Electrons in transition metals, Adv. Phys. 13 (1964) 325–422, https://doi.org/10.1080/00018736400101041.

[30] S.R. Nagel, Thermoelectric power and resistivity in a metallic glass, Phys. Rev. Lett. 41 (1978) 990–993, https://doi.org/10.1103/PhysRevLett.41.990.

[31] H. Wiesmann, M. Gurvitch, H. Lutz, A. Ghosh, B. Schwarz, Myron Strongin, P.B. Allen, J.W. Halley, Simple model for characterizing the electrical resistivity in $A\ensuremath{-}15$ superconductors, Phys. Rev. Lett. 38 (1977) 782–785, https://doi.org/10.1103/PhysRevLett.38.782.

[32] N.E. Hussey, K. Takenaka, H. Takagi, Universality of the Mott–Ioffe–Regel limit in metals, Phil. Mag. 84 (2004) 2847–2864, https://doi.org/10.1080/14786430410001716944.

[33] M. Calandra, O. Gunnarsson, Electrical resistivity at large temperatures: saturation and lack thereof, Phys. Rev. B 66 (2002) 205105, https://doi.org/10.1103/PhysRevB.66.205105.

[34] S. Ramakrishnan, K. Ghosh, Arvind D. Chinchure, V.R. Marathe, Girish Chandra, Magnetism and superconductivity in *R* PtSi (*R* =La, Ce, Nd, and Sm), Phys. Rev. B 52 (1995) 6784–6795, https://doi.org/10.1103/PhysRevB.52.6784.

[35] E.S. Hellman, E.H. Hartford, Normal-state resistivity and Hall effect in Ba 1 − x K x BiO 3 epitaxial films, Phys. Rev. B 47 (1993) 11346–11353, https://doi.org/10.1103/PhysRevB.47.11346.

[36] M. Kasahi, S. Abe, T. Taniguchi, T. Ozawa, Y. Nagata, H. Samata, Superconductivity of MRhGe2 (M = Zr, Hf), J. Alloys Compd. 368 (2004) 51–57, https://doi.org/10.1016/j.jallcom.2003.08.068.

[37] Michael Tinkham, Victor Emery, Introduction to superconductivity, Phys. Today 49 (1996) 74.

[38] Bing He, Dong Cheng, Lihong Yang, Xiaochao Chen, Linhui Ge, Libin Mu, Youguo Shi, CuNNi3: a new nitride superconductor with antiperovskite structure, Supercond. Sci. Technol. 26 (2013) 125015, https://doi.org/10.1088/0953-2048/26/12/125015.

[39] A. Amon, E. Svanidze, R. Cardoso-Gil, M.N. Wilson, H. Rosner, M. Bobnar, W. Schnelle, et al., Noncentrosymmetric superconductor BeAu, Phys. Rev. B 97 (2018), 014501, https://doi.org/10.1103/PhysRevB.97.014501.

[40] B.S. Chandrasekhar, Appl. Phys. Lett. 1 (1962) 7 (1962). Appl. Phys. Lett. 1: 7.

[41] A.M. Clogston, Upper limit for the critical field in hard superconductors, Phys. Rev. Lett. 9 (1962) 266–267, https://doi.org/10.1103/PhysRevLett.9.266.

[42] W.L. McMillan, Transition temperature of strong-coupled superconductors, Phys. Rev. 167 (1968) 331–344, https://doi.org/10.1103/PhysRev.167.331.

[43] Laura C. Srivichitranond, Elizabeth M. Seibel, Weiwei Xie, Zuzanna Sobczak, Tomasz Klimczuk, R.J. Cava, Superconductivity in a new intermetallic structure type based on endohedral $\mathrm{Ta}@\mathrm{I}{\mathrm{r}}_{7}\mathrm{G}{\mathrm{e}}_{4}$ clusters, Phys. Rev. B 95 (2017) 174521, https://doi.org/10.1103/PhysRevB.95.174521.

[44] Elizabeth M. Carnicom, Weiwei Xie, Tomasz Klimczuk, Jingjing Lin, Karolina Górnicka, Zuzanna Sobczak, Nai Phuan Ong, Robert J. Cava, TaRh2B2 and NbRh2B2: superconductors with a chiral noncentrosymmetric crystal structure, Sci. Adv. 4 (2018), eaar7969.

[45] F. Marsiglio, J.P. Carbotte, Strong-coupling corrections to Bardeen-Cooper-Schrieffer ratios, Phys. Rev. B 33 (1986) 6141–6146, https://doi.org/10.1103/PhysRevB.33.6141.

[46] P.B. Allen, R.C. Dynes, Transition temperature of strong-coupled superconductors reanalyzed, Phys. Rev. B 12 (1975) 905–922, https://doi.org/10.1103/PhysRevB.12.905.

[47] Górnicka, K. in preparation.

Source material's DOI: https://doi.org/10.1088/1361-6668/aaf48f

4.4 (A4) Soft-mode enhanced type-I superconductivity in $LiPd_2Ge$

4.4.1 Cel badawczy

W bazie Materials Project można znaleźć około 30 związków typu Heuslera zawierających atom litu w pozycji 4*a*, w tym również $LiPd_2Ge$ i $LiPd_2Sn$. Jednak do 2020 roku nie opisano właściwości fizycznych wspomnianych materiałów. Sytuacja taka jest najpewniej związana z trudnościami natury technicznej ‐ większość pomiarów fizycznych wymaga próbki makroskopowej, podczas gdy badania strukturalne za pomocą dyfrakcji rentgenowskiej mogą być wykonywane na pojedynczym krysztale o rozmiarach dziesiątek mikrometrów. Ze względu na to, że istnieją zarówno $LiPd_2Ge$, jak i $LiPd_2Sn$, postawiona została pierwsza część **hipotezy 4** zakładająca, że powinien występować również związek typu Heuslera z Si tj. $LiPd_2Si$.

Co więcej, jak wspomniano w rozdziale 2.2.3, liczba elektronów walencyjnych (VEC) dla $LiPd_2X$ (X = Si, Ge, Sn) wynosi 25, co daje 6.25 elektronów na atom – wartość leżącą na początku trzeciego maksimum zależności T_c od VEC/at. zaproponowanej przez Matthiasa [33]. W związku z powyższym, druga część **hipotezy 4** postuluje występowanie stanu nadprzewodzącego w materiałach rodziny $LiPd_2X$ (X = Si, Ge, Sn).

Celem badań opisanych w publikacji A4 było opracowanie skutecznej metody syntezy faz Heuslera z Li, otrzymanie czystych fazowo próbek związków typu Heuslera $LiPd_2X$ (X = Si, Ge, Sn) oraz eksperymentalne wyznaczenie parametrów charakteryzujących stan nadprzewodzący i normalny. Badania eksperymentalne obejmowały proszkową dyfrakcję rentgenowską, pomiary elektryczne, cieplne oraz magnetyczne. Szczegółowe badania właściwości fizycznych zostały uzupełnione obliczeniami struktury elektronowej oraz fononowej (mgr inż. Gabriel Kuderowicz, dr inż. Kamil Kutorasiński, dr hab. inż. Bartłomiej Wiendlocha).

4.4.2 Opis rezultatów

Syntezę polikrystalicznych próbek $LiPd_2X$ (X = Si, Ge, Sn) przeprowadzono metodą reakcji w fazie stałej. W pracy A4 przedstawiono powtarzalną, szybką, powtarzalną metodę syntezy, która nie wymaga stosowania ampuł tantalowych lub innych. Synteza zakłada reakcję w fazie stałej wstępnie utartych proszków Pd i X, a następnie przygotowanie w komorze rękawicowej pastylki, w której fragmenty litu są oddzielone proszkiem Pd_2X. Tak przygotowana pastylka jest zawinięta w folię tantalową, aby zapobiec kontaktowi z ampułą kwarcową. Ampuła kwarcowa została następnie odpompowana i zatopiona z niewielką ilością wysokiej czystości argonu (5N). W opisanej procedurze niezwykle ważna jest nadwyżka metalu alkalicznego oraz bardzo powolne grzanie (2.5℃/h), szczególnie w niskich temperaturach, tj. w okolicy temperatury topnienia Li (180.5℃). Otrzymane za pomocą opisanej w pracy A4 metody syntezy materiały, charakteryzują się wysokim stopniem krystaliczności.

Stałe sieci krystalicznej dla $LiPd_2Ge$ i $LiPd_2Sn$ są zgodne z raportowanymi w literaturze. W publikacji A4, po raz pierwszy opisano związek $LiPd_2Si$, którego istnienie postulowane było w hipotezie 4. Stała sieci a = 5.9059(4) Å jest najmniejsza w rodzinie $LiPd_2X$, co jest konsekwencją najmniejszego w serii promienia atomowego Si.

W publikacji A4 przedstawiono szereg parametrów zarówno stanu nadprzewodzącego ($LiPd_2Ge$) jak i normalnego ($LiPd_2Si$, $LiPd_2Ge$, $LiPd_2Sn$). Powyżej temperatury 1.68 K, nadprzewodnictwo zostało potwierdzone jedynie dla $LiPd_2Ge$, jednakże rozważania teoretyczne przeprowadzone przez zespół dr. hab. Bartłomieja Wiendlochy, jednoznacznie wskazują, że nadprzewodnictwo powinno również występować dla $LiPd_2Si$ i $LiPd_2Sn$, z oszacowanymi teoretycznymi temperaturami krytycznymi wynoszącymi odpowiednio 0.76 K i 0.25 K.

Przejście ze stanu normalnego do stanu nadprzewodzącego dla $LiPd_2Ge$ zaobserwowano na temperaturowej zależności podatności magnetycznej w T_c = 1.96 K. Szczegółowa analiza wyników badań magnetycznych tj. kształt krzywych namagnesowania w funkcji przyłożonego pola magnetycznego oraz kształt pętli namagnesowania zmierzonej w T = 1.67 K wskazują, że $LiPd_2Ge$ jest nadprzewodnikiem I-rodzaju. Zostało to potwierdzone w obliczeniach przedstawionych w części teoretycznej pracy A4. Według wiedzy autorki doktoratu, $LiPd_2Ge$ jest pierwszym nadprzewodnikiem I-go rodzaju w rodzinie Heuslera i być może również pierwszym wśród trójskładnikowych związków międzymetalicznych.

Pomiary oporności elektrycznej i ciepła właściwego potwierdziły przejście do stanu nadprzewodzącego w T_c = 1.96 K. Na podstawie zależności $\rho(T)$, wyznaczona została wartość RRR ~ 14, która zdecydowanie przewyższa wartości uzyskane dla innych związków typu Heuslera ($ZrNi_2Ga$ ~ 2 [64], YPd_2Sn ~ 2.5 [31]) i może świadczyć o niskim stopniu zdefektowania materiału i/lub wysokim stopniu krystaliczności.

Niskotemperaturowe pomiary ciepła właściwego potwierdziły objętościowy charakter nadprzewodnictwa ($\Delta C/\gamma T_c$ = 1.38). Dzięki obliczeniom własności fononowych, przedstawionych w części teoretycznej, przeprowadzono szczegółową analizę ciepła właściwego w całym zakresie temperatur (1.85 – 300 K). Na wykresie krzywych dyspersji fononów występują mody akustyczne oraz dwa wyraźnie odseparowane mody optyczne. Na tej podstawie do dopasowania danych eksperymentalnych ciepła właściwego (w pełnym zakresie temperatur) zastosowano zarówno model Debye'a jak i Einsteina, przy czym liczbę modów ustalono w obu przypadkach jako 2.

Wyznaczony z zastosowaniem odwróconego wzoru McMillana parametr sprzężenia elektron-fonon, λ_{ep} = 0.53 sugeruje, że $LiPd_2Ge$ jest słabo sprzężonym nadprzewodnikiem.

Badania teoretyczne rodziny $LiPd_2X$ wskazują na występowanie tzw. *miękkich modów fononowych*, które w związkach typu Heuslera były już wcześniej obserwowane. Jakkolwiek pochodzenie *miękkich modów* nie jest w tym przypadku ustalone, to zwracamy uwagę na to, że nadprzewodnictwo jest z nimi wyraźnie skorelowane.

Warte podkreślenia jest również to, że $LiPd_2Ge$ jest pierwszym nadprzewodnikiem typu Heuslera, dla którego VEC = 25. Ponieważ dla materiałów typu Heuslera z VEC = 24, obserwowane jest występowanie przerwy energetycznej [30,33], tym samym nadprzewodnictwo w $LiPd_2Ge$ niejako domyka obszar tzw. trzeciego maksimum T_c(VEC) postulowanego przez Matthiasa.

4.4.3 Treść artykułu A4

4.4.3 Treść artykułu A4

Tytuł: Soft-mode enhanced type-I superconductivity in LiPd$_2$Ge

Autorzy: Karolina Górnicka, Gabriel Kuderowicz, Elizabeth M. Carnicom, Kamil Kutorasiński, Bartłomiej Wiendlocha, Robert J. Cava, Tomasz Klimczuk

Czasopismo: PHYSICAL REVIEW B 102, 024507 (2020)

Impact factor: 3.575 (2019/2020)

Liczba punktów ministerialnych MNiSW: 140 pkt

DOI: 10.1103/PhysRevB.102.024507

Mój udział polegał na syntezie próbek polikrystalicznych, przeprowadzeniu badań strukturalnych metodą proszkowej dyfrakcji rentgenowskiej wraz z analizą LeBaila, pomiarach właściwości magnetycznych, cieplnych oraz elektrycznych, analizie otrzymanych wyników, udziale w dyskusji uzyskanych rezultatów, wyznaczeniu parametrów charakteryzujących stan normalny i nadprzewodzący, przygotowaniu rysunków oraz tekstu manuskryptu części eksperymentalnej. Pełniłam rolę autora korespondencyjnego oraz przygotowałam odpowiedzi na recenzje.

Karolina Górnicka

mgr inż. Karolina Górnicka

***The original source: Physical Review B** 102, 024507*

PHYSICAL REVIEW B **102**, 024507 (2020)

Editors' Suggestion

Soft-mode enhanced type-I superconductivity in $LiPd_2Ge$

Karolina Górnicka,[1,*] Gabriel Kuderowicz,[2] Elizabeth M. Carnicom,[3] Kamil Kutorasiński,[2] Bartlomiej Wiendlocha,[2]
Robert J. Cava,[3] and Tomasz Klimczuk[1,†]

[1] *Faculty of Applied Physics and Mathematics and Advanced Materials Centre, Gdansk University of Technology, Narutowicza 11/12,*
80-233 Gdańsk, Poland

[2] *Faculty of Physics and Applied Computer Science, AGH University of Science and Technology, Aleja Mickiewicza 30, 30-059 Kraków, Poland*

[3] *Department of Chemistry, Princeton University, Princeton, New Jersey 08544, USA*

(Received 20 April 2020; revised 11 June 2020; accepted 16 June 2020; published 6 July 2020)

The synthesis, crystal structure, and physical properties (magnetization, resistivity, heat capacity) in combination with theoretical calculations of the electronic structure and phonon properties are reported for intermetallic compounds $LiPd_2X$ (X = Si, Ge, and Sn). LeBail refinement of powder x-ray diffraction data confirms that all compounds belong to the Heusler family (space group Fm-$3m$, No. 225). The lattice parameter increases with atomic size of X, and its value varies from $a = 5.9059(4)$ Å for $LiPd_2Si$ and $a = 6.0082(3)$ Å for $LiPd_2Ge$, to $a = 6.2644(1)$ Å for $LiPd_2Sn$. The first compound, $LiPd_2Si$, has apparently not been previously reported. All measured quantities demonstrate that $LiPd_2Ge$ exhibits superconductivity below $T_c = 1.96$ K and the normal- and superconducting-state data indicate that it is a weak-strength type-I superconductor ($C/\gamma T_c = 1.38$) with electron-phonon coupling constant $\lambda_{e-p} = (0.53 - 0.56)$. $LiPd_2Si$ and $LiPd_2Sn$ are not superconducting above 1.68 K. The experimental observations are supported by theoretical calculations which show that $LiPd_2Ge$ has the highest computed λ_{e-p} and T_c of the group. A strong softening of the acoustic phonon mode is calculated, and in the case of X = Ge and Sn, imaginary phonon frequencies were computed. The soft mode is most pronounced in the case of $LiPd_2Ge$, which suggests its correlation with superconductivity.

DOI: 10.1103/PhysRevB.102.024507

I. INTRODUCTION

Although discovered more than 100 years ago, the Heusler material classes remain an exciting and active research area. The prototype compound, $MnCu_2Al$, is a ferromagnet at room temperature though it consists of three nonmagnetic metals [1]. Nowadays, there are more than 1000 reported compounds in this family, and they reveal all kinds of physical properties: heavy fermion, shape-memory effect, thermoelectric, and ferromagnetism including half-metallic ferromagnetism. Recently a quantum critical point (QCP) and a new type of interaction between charge density wave (CDW) and superconductivity was found in $Lu(Pt_{1-x}Pd_x)_2In$ [2]. Intriguing physics has been observed in the half-Heusler compounds, e.g., band inversion [3,4] and the coexistence of magnetic ordering and superconductivity [5,6].

The Heusler and half-Heusler ternary intermetallic compounds have the chemical formula AT_2M and ATM, respectively. In the formula, A stands for rare-earth metal but it can also be Li, Be, Mg, and metals from group IV, V, and VI. T is a transition metal from group IX-XI and also Mn, Fe, Ru, Zn, and Cd, while M is an sp metal or metalloid (Sb, Bi). The compounds form in a cubic crystal structure, with the space group Fm-$3m$ (s.g. 225) for the Heusler and F-$43m$ (s.g. 216) for the half-Heusler system. An excellent description with a comparison of the crystal structures of both families, as well as a discussion concerning the chemical nomenclature can be found in Ref. [7].

Superconductivity in this family is rather uncommon. There are only about 30 reported Heusler superconductors. Their physical properties can be tentatively predicted by counting the number of valence electrons (N_{el}). For example, semiconducting behavior is expected for $N_{el} = 18$, whereas superconductivity is expected for $N_{el} = 27$ [7,8]. Interestingly, the number of valence electrons per atom $N_{el}/4 = 6.75$ electrons per atom is close to the second maximum of T_c versus the electron count observed for transition metals [9], and slightly higher than the maximum of T_c at 6.4 electrons per atom observed for $A_{0.25}B_{0.75}$ compounds with the A15 crystal structure [10].

Recently we described a Li-based Heusler superconductor, $LiGa_2Rh$ [11]. This compound is a Bardeen-Cooper-Schrieffer (BCS) superconductor with four valence electrons per atom, which is at the onset of the first superconducting dome proposed for superconducting metals [9,12] and compounds with the A15 crystal structure [10]. Motivated by finding the Li-based Heusler superconductor, we synthesized and tested several $LiPd_2X$ materials (X = Si, Ge, and Sn). In this paper we report type-I superconductivity in $LiPd_2Ge$. According to our knowledge, type-I superconductivity among Heuslers compounds has not been observed.

II. EXPERIMENTAL AND THEORETICAL DETAILS

Polycrystalline samples of $LiPd_2X$ were synthesized by a two-step solid-state reaction. The starting elements were

---

[*] karolina.gornicka@pg.edu.pl

[†] tomasz.klimczuk@pg.edu.pl

high-purity Li chunks (4N, Alfa Aesar), Pd powder (4N8, Mennica-Metale, Poland), Ge powder (4N, Alfa Aesar), Si pieces (3N, Alfa Aesar), and Sn pellets (4N, Alfa Aesar). An excess of lithium (10%) was added in order to compensate for the loss during synthesis. The following manipulations were performed in a protective Ar atmosphere in a glove box system [$p(O_2) < 0.5$ ppm]. All materials were mixed together, pressed into a pellet using a hydraulic press, placed in a tantalum crucible, and then sealed inside an Ar-filled quartz tube. The ampoule was slowly heated to 240 °C at a rate of 2.5 °C/h and then heated to 550 °C (10 °C/h), held at that temperature for 12 h, and air quenched to room temperature. The as-prepared material was reground well and once more pressed into a pellet. The samples were then enclosed inside a quartz tube and annealed at 610 °C for 3 days. No melting was observed and the resulting materials were dense and brown in color.

The chemical composition and phase purity of $LiPd_2Ge$ were measured using an FEI Quanta 250 FEG scanning electron microscope (SEM) equipped with an Apollo-X SDD energy-dispersive spectrometer (EDS). The data were analyzed using EDAX TEAM™ software. Room-temperature powder x-ray diffraction (pXRD) characterization was carried out on a Bruker D2 phaser diffractometer with Cu $K\alpha$ radiation ($\lambda = 1.5406$ Å) and a LynxEye-XE detector. The data were collected from $10^\circ - 90^\circ$ 2θ over 120 minutes of scan time. LeBail refinement of the pXRD pattern was performed to determine the lattice parameters, using the DIFFRAC.SUITE TOPAS. Temperature- and field-dependent magnetization measurements were performed in a Quantum Design Dynacool Physical Property Measurement System (PPMS) with a vibrating sample magnetometer (VSM) function. The data were collected in the temperature range of 1.68–2.1 K under various applied magnetic fields. The heat capacity was measured using the two-τ time-relaxation method in a PPMS Evercool II system in the temperature range 1.81–300 K. The sample was attached to the measuring stage using Apiezon N grease to ensure good thermal contact. The electrical resistivity measurements were performed by a conventional four-probe method using the ac transport option of the PPMS Evercool II system from 1.81 to 300 K. The electrical leads were small-diameter Pt wires attached to the polished sample using conductive silver epoxy (Epotek H20E).

Electronic structure, phonons, and the electron-phonon interaction functions were calculated using density functional theory with the plane-wave pseudopotential method as implemented in the QUANTUM ESPRESSO (QE) package [13,14]. We used the projector augmented wave pseudopotentials [15,16] and the Perdew-Burke-Ernzerhof generalized gradient approximation exchange-correlation functional [17]. Energy cutoffs for wave functions and charge densities were set to 60 and 600 Ry, respectively. A 24^3 k-point Monkhorst-Pack grid for the electronic structure and 8^3 q-point grid for the interatomic force constant calculations were employed. Both scalar-relativistic and full-relativistic [including spin-orbit coupling (SOC)] calculations of the electronic structure were done.

Firstly, $LiPd_2X$ (X = Si, Ge, Sn) unit cells were relaxed with the Broyden-Fletcher-Goldfarb-Shanno algorithm. The experimental lattice constants and the calculated ones are shown in Table I. The calculated lattice constants are slightly larger than the experimental ones, which is usually the case when using GGA functionals. The atomic positions are fixed by the symmetry, and therefore they were not changed in the relaxation. The volume relaxation was repeated with SOC included, but no important difference was found. For the relaxed structures, the electronic dispersion relations, densities of states (DOS), and Fermi surface were calculated. Using density functional perturbation theory [18], phonons and electron-phonon interaction functions (Eliashberg functions) were computed. As SOC was found to have a negligible effect on the electronic structure, phonon and electron-phonon calculations were done in a scalar-relativistic way, with an additional test of phonon frequencies calculated with SOC for a selected **q**-vector for $LiPd_2Ge$.

TABLE I. Experimental and calculated lattice constant a for the $LiPd_2X$ family.

	$LiPd_2Si$	$LiPd_2Ge$	$LiPd_2Sn$
Experimental (Å)	5.9059(4)	6.0082(3)	6.2644(1)
Calculated w/o SOC (Å)	5.9512	6.0780	6.3367
Calculated with SOC (Å)	5.9518	6.0799	6.3370

III. RESULTS OF THE EXPERIMENTAL STUDIES

The sample of $LiPd_2Ge$ was first examined using an energy dispersive spectrometer (EDS). High-resolution SEM images showed that the sample is uniform and the EDS analysis within experimental error confirmed Pd:Ge ratio near expected 2:1, consistent with the nominal composition.

The LeBail refinement of the powder x-ray diffraction pattern (Fig. S1 in the Supplemental Material (SM) [19]) for $LiPd_2Si$, $LiPd_2Ge$, and $LiPd_2Sn$ confirms that all compounds crystallize in the cubic $L2_1$ crystal structure (space group Fm-$3m$, No. 225). Lattice parameters obtained from the refinements are $a = 5.9059(4)$ Å for $LiPd_2Si$, $a = 6.0082(3)$ Å for $LiPd_2Ge$, and $a = 6.2644(1)$ Å for $LiPd_2Sn$. We have not seen reports of $LiPd_2Si$, and the cell parameter values for the other two compounds are in very good agreement with previously published data [20]. The pXRD analysis confirms the good quality of the examined samples. The difference plot (between experimental and fitted data) and the Bragg positions is also shown in Fig. S1 [19]. Additional pXRD scans were performed on a pulverized sample exposed to air for 12 h. The obtained patterns confirm stability of all compounds over that time period.

The temperature-dependent volume magnetic susceptibility, defined as $\chi = dM/dH$ where M is the magnetization and H is the applied magnetic field, for $LiPd_2Ge$ is shown in Fig. 1(a). Both zero-field-cooled (ZFC) and field-cooled (FC) data show a sharp diamagnetic transition, corresponding to the onset of superconductivity. The critical temperature, $T_c = 1.96$ K, was determined as the intersection between a line drawn at the steepest slope of the superconducting signal and the extrapolation of the normal-state magnetic susceptibility [21]. After considering the demagnetization effect of the sample by using the formula $-4\pi\chi_V = 1/(1-N)$, where

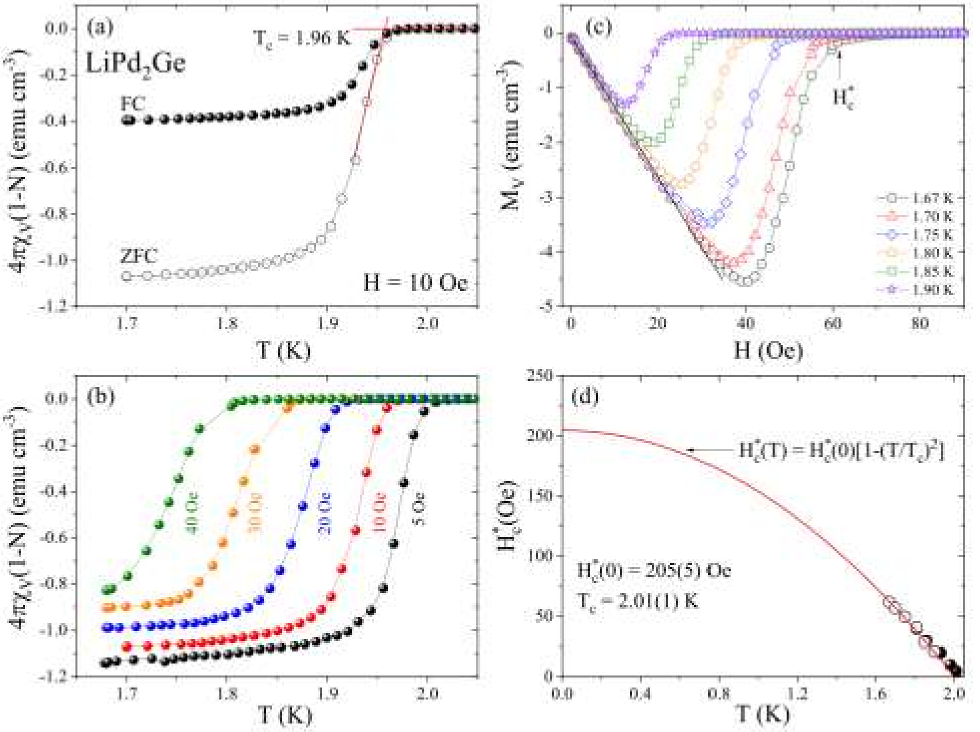

FIG. 1. Magnetic characterization of the superconductivity of LiPd$_2$Ge. (a) Zero-field-cooled (open circles) and field-cooled (full circles) temperature-dependent magnetic susceptibility data in $H = 10\,\mathrm{Oe}$. (b) The temperature-dependent magnetic susceptibility data for $5\,\mathrm{Oe} \leqslant H \leqslant 40\,\mathrm{Oe}$. (c) Field-dependent magnetization data at various temperatures. (d) Thermodynamic critical field $H_c^*(0)$ determined from $\chi_v(T)$ (full circles) and $M_V(H)$ (open circles).

$N = 0.4$ is the geometrical demagnetization factor [estimated from the $M_V(H)$ fit discussed later], the ZFC data are consistent with a 100% Meissner volume fraction, indicating bulk superconductivity in LiPd$_2$Ge. The FC diamagnetic signal at the lowest temperature is relatively strong, which might suggest that the grains are large and hence not much magnetic field is trapped at the grain boundaries. Figure 1(b) presents the ZFC data at various externally applied magnetic fields ($5\,\mathrm{Oe} \leqslant H \leqslant 40\,\mathrm{Oe}$). The application of the magnetic field suppressed the critical temperature gradually. This allows us to extract the values of the critical field H_c, represented with full circles in Fig. 1(d). The volume magnetization isotherms $M_V(H)$, taken at different temperatures below T_c, are shown in Fig. 1(c). Assuming that the initial response to a magnetic field is perfectly diamagnetic, we obtained a demagnetization factor $N = 0.4$. It is clear that the plotted curves of $M_V(H)$ show a steplike jump to zero near the critical field, indicating type-I superconductivity in LiPd$_2$Ge. The critical field value, H_c^*, was determined as the entrance to the normal state, at each temperature. The variation of H_c^* with temperature is depicted in Fig. 1(d), where full circles are obtained from the $\chi_v(T)$ analysis and open circles are data points taken from the $M_V(H)$ measurements. The solid red line gives the fit that uses temperature dependence:

$$H_c^*(T) = H_c^*(0)\left[1 - \left(\frac{T}{T_c}\right)^2\right], \tag{1}$$

where $H_c^*(0)$ is the critical field at 0 K and T_c is the superconducting critical temperature. The experimental data are well described with the above formula and a fit gives $H_c^*(0) = 205(5)\,\mathrm{Oe}$ and $T_c = 2.01(1)\,\mathrm{K}$. Taking into account the demagnetization factor derived above, the critical field value is $H_c = 342\,\mathrm{Oe}$. The full magnetization loop $M_V(H)$ measured at 1.67 K is shown in Fig. 2. The shape of the $M_V(H)$ curve—similar to other type-I superconductors, such as KBi$_2$ [22], YbSb$_2$ [23], and ScGa$_3$ and LuGa$_3$ [24]—together with relatively small critical field $H_c(0)$, implies that LiPd$_2$Ge is a type-I superconductor. This is rather surprising since type-I superconductivity is unique in the intermetallic compounds and it is unusual that LiPd$_2$Ge, being a Heusler compound, would be a type-I superconductor. It is therefore

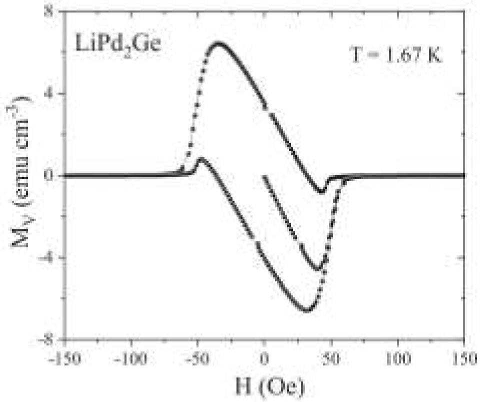

FIG. 2. Magnetization loop at $T = 1.67$ K for LiPd$_2$Ge.

important to fully characterize the superconducting state in LiPd$_2$Ge.

The main panel of Fig. 3 shows the whole temperature range of the electrical resistivity, $\rho(T)$, in zero applied magnetic field. In the normal state, the $\rho(T)$ data decrease with decreasing temperature, revealing metalliclike character ($d\rho/dT > 0$). The room-temperature resistivity is approximately 194 $\mu\Omega$ cm and the residual resistivity above the critical temperature is 14 $\mu\Omega$ cm. Hence the residual resistivity ratio RRR is $\rho(300)/\rho(3) = 14$. This value is high in comparison to those reported for full-Heusler compounds, e.g., YPd$_2$Sn ~ 2.5 [8], ZrNi$_2$Ga ~ 2 [25], or LiGa$_2$Rh ~ 1.2 [11]. As shown in the inset of Fig. 3, the electrical resistivity drops to zero at $T_c = 2.04$ K, where, for resistivity data, T_c is defined by the temperature of the 50% drop of the $\rho(T)$ data in zero magnetic field. The transition temperature is slightly higher than the critical temperature obtained from the magnetic data ($T_c = 1.96$ K). When a magnetic field is applied, the superconducting transition is quickly suppressed. For a magnetic field $H = 40$ Oe, the transition width becomes wider and the superconducting temperature is 1.85 K.

The superconducting transition was further examined through specific heat measurements. Panel (a) of Fig. 4 shows the specific heat of LiPd$_2$Ge measured from 1.81 to 300 K in zero magnetic field. At high temperatures, the experimental heat capacity $C_p(T)$ approaches the value of $3nR \approx 100\,\mathrm{J\,mol^{-1}\,K^{-1}}$ consistent with the Dulong-Petit law. Here $n = 4$ and $R = 8.31\,\mathrm{J\,mol^{-1}\,K^{-1}}$ are the number of atoms per formula unit and the ideal gas constant, respectively. The blue solid line corresponds to the whole temperature fit of a combined model: $C_p = C_{el.} + C_{\mathrm{Debye}} + C_{\mathrm{Einstein1}} + C_{\mathrm{Einstein2}}$, where $C_{el.}$ is an electronic specific heat, whereas C_{Debye} and $C_{\mathrm{Einstein1}}$ and $C_{\mathrm{Einstein2}}$ are the phonon specific heat contributions to C_p. Such a model, with two Einstein terms, is required to describe phonon contribution to the specific heat over a broad temperature range, because in the phonon spectrum of LiPd$_2X$ we observed two groups of separated, Einstein-like phonon modes (see below). Each consists of three optic modes, gathered around characteristic ω_{E1} and ω_{E2} frequencies. Thus, the contribution to the specific heat from all such modes is equal to

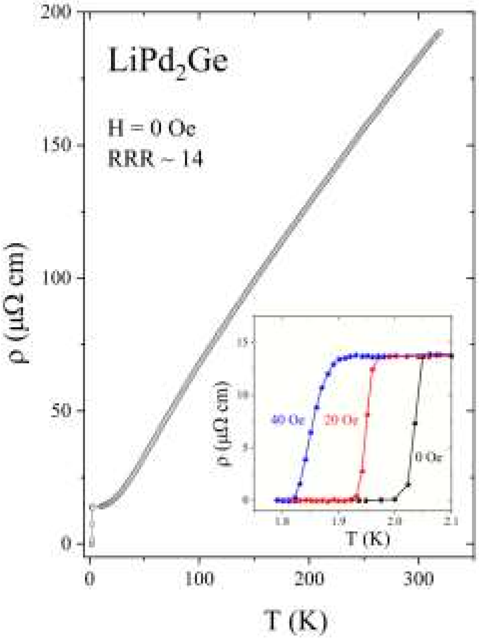

FIG. 3. The electrical resistivity of LiPd$_2$Ge versus temperature measured in zero applied magnetic field. The inset shows the expanded plot of $\rho(T)$ in the vicinity of the superconducting transition for different values of $H = 0$, 20, and 40 Oe field.

$$C_{\mathrm{Einstein}}(T) = 3R\left(\frac{\Theta_E}{T}\right)^2 \exp\left(\frac{\Theta_E}{T}\right)\left[\exp\left(\frac{\Theta_E}{T}\right) - 1\right]^{-2}, \tag{2}$$

where $\hbar\omega_E = k_B\Theta_E$. As the number of atoms in the unit cell is equal to 4, from the total number of 12 phonon modes, the contribution from the remaining six modes is described in the Debye approximation, as

$$C_{\mathrm{Debye}}(T) = 2\left\{9R\left(\frac{T}{\Theta_D}\right)^3 \int_0^{\theta_D} \frac{x^4 \exp(x)}{[\exp(x) - 1]^2} dx\right\}. \tag{3}$$

The multiplier 2 assures the correct total contribution to the specific heat from the lower-frequency part of the spectrum. In this fit we fixed the Sommerfeld parameter (γ) value, obtained from the low-temperature analysis discussed below.

The blue solid line is the fitted sum of the all phonon contributions to the specific heat. The fit is excellent and the obtained parameters are $\Theta_D = 182(1)$ K, $\Theta_{E1} = 262(1)$ K, and $\Theta_{E2} = 537(1)$ K. A similar analysis was performed for the other two compounds, LiPd$_2$Si and LiPd$_2$Sn, and the

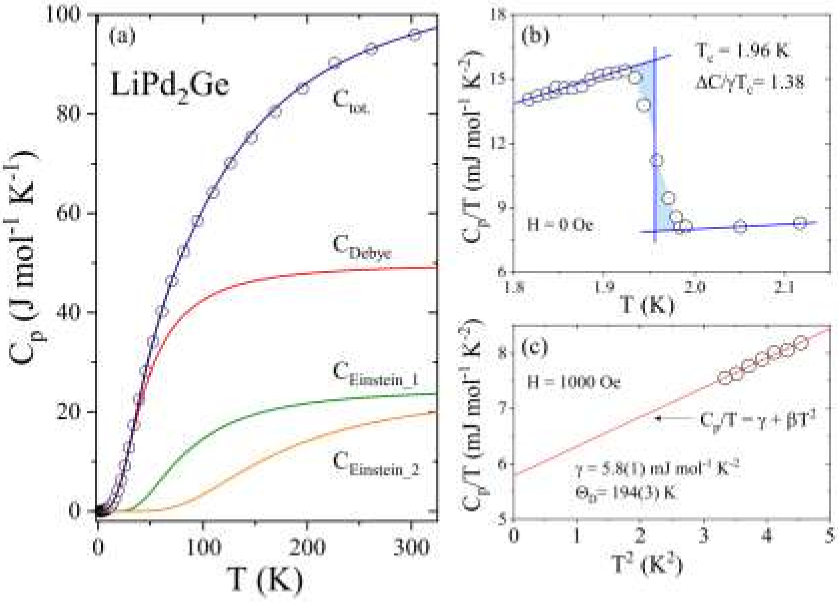

FIG. 4. Panel (a): The specific heat of $\mathrm{LiPd_2Ge}$ versus temperature in zero magnetic field with a fit to a combined model (blue solid line): $C_p = C_{el.} + C_{\mathrm{Debye}} + C_{\mathrm{Einstein1}} + C_{\mathrm{Einstein2}}$. (b) Zero-field specific heat divided by temperature (C_p/T) versus temperature. (c) C_p/T versus T^2 measured at 1000 Oe magnetic field. The red solid line represents the linear fit used to estimate the values of the electronic and phonon specific heat coefficients.

results are presented in Figs. 5 and 6. The characteristic temperatures obtained are gathered in Table II.

As shown in the expanded plot of low-temperature data collected in zero magnetic field in Fig. 4(b), a sharp jump is observed at 1.96 K, confirming the bulk nature of the superconductivity and good quality of the sample. The superconducting transition temperature ($T_c = 1.96$ K) is in good agreement with the magnetization and resistivity measurements. The specific heat jump at the critical temperature, estimated by using the equal entropy construction (blue solid

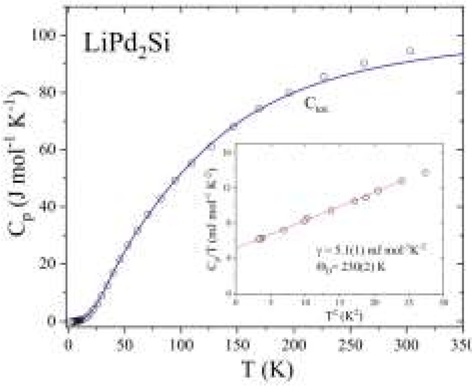

FIG. 5. Main panel: the specific heat of $\mathrm{LiPd_2Si}$ measured from 1.8 to 300 K under zero magnetic field. Inset: C_p/T data versus T^2.

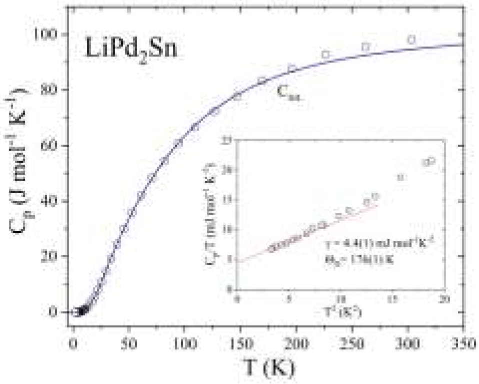

FIG. 6. Main panel: the specific heat of $\mathrm{LiPd_2Sn}$ measured from 1.8 to 300 K under zero magnetic field. Inset: C_p/T data versus T^2.

TABLE II. Characteristic temperatures derived from a combined fit to the heat capacity. The larger differences between theoretical and experimental $\Theta_{\mathrm{Einstein2}}$ are likely caused by small contribution of high-frequency phonons to specific heat up to 300 K and thermal expansion effects, important at higher temperatures.

$\mathrm{LiPd_2}X$	Θ_D (K)	$\Theta_{\mathrm{Einstein1}}$ (K)	$\Theta_{\mathrm{Einstein2}}$ (K)
Si	211(1)/230(2)[a]	398(6)/362[b]	554(9)/604[b]
Ge	182(1)/194(3)[a]	262(1)/246[b]	537(1)/549[b]
Sn	168(1)/176(1)[a]	282(5)/240[b]	440(6)/487[b]

[a] Values estimated from a low-temperature fit.

[b] Temperatures estimated from theoretical calculations as the mean phonon frequencies around Einstein-like $F(\omega)$ peaks.

lines), is found to be about $\Delta C/T_c = 7.9\,\mathrm{mJ\,mol^{-1}\,K^{-2}}$. Low-temperature $C_p(T)$ data collected under small magnetic field (up to 30 Oe) are shown in Fig. S7 in the SM [19]. The $\Delta C/T_c$ jump observed under 5 Oe measurement is slightly larger than $\Delta C/T_c$ at zero field, which might confirm type-I superconductivity proposed by field-dependent magnetization studies.

Figure 4(c) presents the heat-capacity data plotted as C_p/T versus T^2, under an applied magnetic field of $H = 1000\,\mathrm{Oe}$, which is above H_c. In the normal state the experimental data can be fitted using the formula $C_p/T = \gamma + \beta T^2$, where the first term is the electronic specific heat coefficient and the second one accounts for the lattice contribution. Fitting the data yields $\gamma = 5.8(1)\,\mathrm{mJ\,mol^{-1}\,K^{-2}}$ and $\beta = 0.531(3)\,\mathrm{mJ\,mol^{-1}\,K^{-4}}$. The Debye temperature can be then calculated via the relation

$$\Theta_D = \left(\frac{12\pi^4}{5\beta}nR\right)^{1/3}, \tag{4}$$

where $n = 2$ corresponds to our combined Debye + Einstein model, described above. In such a case, β corresponds to the Debye temperature of 194(3) K, in good agreement with the value obtained from the whole temperature range fit. If, instead of using the combined model, one follows the standard methodology (i.e., all the phonon modes are approximated using the Debye model) and takes $n = 4$ (number of atoms per formula unit) the resulting value of Θ_D is 244(3) K, which is comparable with those obtained for full-Heusler compounds, e.g., $\mathrm{LuPd_2Sn}$ ($\Theta_D = 246(2)\,\mathrm{K}$ [8]), $\mathrm{HfPd_2In}$ ($\Theta_D = 243(5)\,\mathrm{K}$ [8]), and $\mathrm{ZrPd_2In}$ ($\Theta_D = 236(5)\,\mathrm{K}$ [8]).

The insets of Figs. 5 and 6 present the heat-capacity data together with the fitting formula $C_p/T = \gamma + \beta T^2$. The extrapolation gives $\gamma = 5.1(1)\,\mathrm{mJ\,mol^{-1}\,K^{-2}}$ for $\mathrm{LiPd_2Si}$ and $\gamma = 4.4(1)\,\mathrm{mJ\,mol^{-1}\,K^{-2}}$ for $\mathrm{LiPd_2Sn}$. The calculated values of Θ_D (corresponding to the combined, Debye-Einstein model) are 230(2) K and 176(1) K for $\mathrm{LiPd_2Si}$ and $\mathrm{LiPd_2Sn}$, respectively. We do not observe any transition down to 1.81 K for either material.

Using the Sommerfeld coefficient [$\gamma = 5.8(1)\,\mathrm{mJ\,mol^{-1}\,K^{-2}}$] and the specific heat jump value at the critical temperature ($\Delta C/T_c = 7.9\,\mathrm{mJ\,mol^{-1}\,K^{-2}}$), the normalized specific heat jump was then calculated. The obtained value ($\Delta C/\gamma T_c = 1.38$) is slightly lower than the value predicted by Bardeen-Cooper-Schrieffer (BCS) theory (1.43) suggesting weak-coupling superconductivity in $\mathrm{LiPd_2Ge}$.

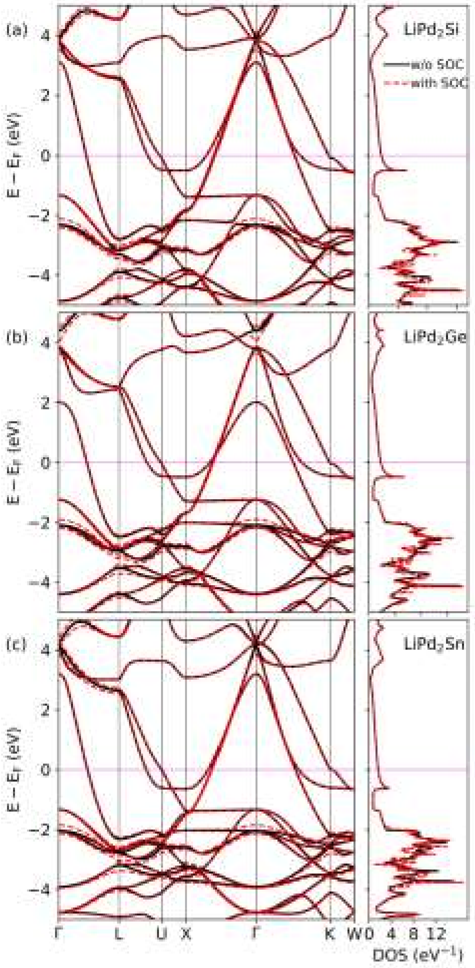

FIG. 7. Electronic structure of $\mathrm{LiPd_2}X$ calculated without SOC (black solid lines) and including SOC (red dashed lines).

The electron-phonon coupling constant λ_{e-p} can be estimated from the inverted McMillan formula, which relates the Debye temperature Θ_D and the critical temperature T_c by the formula [26]

$$\lambda_{e-p} = \frac{1.04 + \mu^* \ln(\Theta_D/1.45T_c)}{(1 - 0.62\mu^*)\ln(\Theta_D/1.45T_c) - 1.04}, \tag{5}$$

where μ^* is the repulsive screened Coulomb parameter, typically taken as $\mu^* = 0.13$ for many metal systems [27–29].

TABLE II. Characteristic temperatures derived from a combined fit to the heat capacity. The larger differences between theoretical and experimental $\Theta_{\mathrm{Einstein2}}$ are likely caused by small contribution of high-frequency phonons to specific heat up to 300 K and thermal expansion effects, important at higher temperatures.

$\mathrm{LiPd_2}X$	Θ_D (K)	$\Theta_{\mathrm{Einstein1}}$ (K)	$\Theta_{\mathrm{Einstein2}}$ (K)
Si	211(1)/230(2)[a]	398(6)/362[b]	554(9)/604[b]
Ge	182(1)/194(3)[a]	262(1)/246[b]	537(1)/549[b]
Sn	168(1)/176(1)[a]	282(5)/240[b]	440(6)/487[b]

[a] Values estimated from a low-temperature fit.

[b] Temperatures estimated from theoretical calculations as the mean phonon frequencies around Einstein-like $F(\omega)$ peaks.

lines), is found to be about $\Delta C/T_c = 7.9\,\mathrm{mJ\,mol^{-1}\,K^{-2}}$. Low-temperature $C_p(T)$ data collected under small magnetic field (up to 30 Oe) are shown in Fig. S7 in the SM [19]. The $\Delta C/T_c$ jump observed under 5 Oe measurement is slightly larger than $\Delta C/T_c$ at zero field, which might confirm type-I superconductivity proposed by field-dependent magnetization studies.

Figure 4(c) presents the heat-capacity data plotted as C_p/T versus T^2, under an applied magnetic field of $H = 1000\,\mathrm{Oe}$, which is above H_c. In the normal state the experimental data can be fitted using the formula $C_p/T = \gamma + \beta T^2$, where the first term is the electronic specific heat coefficient and the second one accounts for the lattice contribution. Fitting the data yields $\gamma = 5.8(1)\,\mathrm{mJ\,mol^{-1}\,K^{-2}}$ and $\beta = 0.531(3)\,\mathrm{mJ\,mol^{-1}\,K^{-4}}$. The Debye temperature can be then calculated via the relation

$$\Theta_D = \left(\frac{12\pi^4}{5\beta}nR\right)^{1/3}, \tag{4}$$

where $n = 2$ corresponds to our combined Debye + Einstein model, described above. In such a case, β corresponds to the Debye temperature of 194(3) K, in good agreement with the value obtained from the whole temperature range fit. If, instead of using the combined model, one follows the standard methodology (i.e., all the phonon modes are approximated using the Debye model) and takes $n = 4$ (number of atoms per formula unit) the resulting value of Θ_D is 244(3) K, which is comparable with those obtained for full-Heusler compounds, e.g., $\mathrm{LuPd_2Sn}$ ($\Theta_D = 246(2)\,\mathrm{K}$ [8]), $\mathrm{HfPd_2In}$ ($\Theta_D = 243(5)\,\mathrm{K}$ [8]), and $\mathrm{ZrPd_2In}$ ($\Theta_D = 236(5)\,\mathrm{K}$ [8]).

The insets of Figs. 5 and 6 present the heat-capacity data together with the fitting formula $C_p/T = \gamma + \beta T^2$. The extrapolation gives $\gamma = 5.1(1)\,\mathrm{mJ\,mol^{-1}\,K^{-2}}$ for $\mathrm{LiPd_2Si}$ and $\gamma = 4.4(1)\,\mathrm{mJ\,mol^{-1}\,K^{-2}}$ for $\mathrm{LiPd_2Sn}$. The calculated values of Θ_D (corresponding to the combined, Debye-Einstein model) are 230(2) K and 176(1) K for $\mathrm{LiPd_2Si}$ and $\mathrm{LiPd_2Sn}$, respectively. We do not observe any transition down to 1.81 K for either material.

Using the Sommerfeld coefficient [$\gamma = 5.8(1)$ $\mathrm{mJ\,mol^{-1}\,K^{-2}}$] and the specific heat jump value at the critical temperature ($\Delta C/T_c = 7.9\,\mathrm{mJ\,mol^{-1}\,K^{-2}}$), the normalized specific heat jump was then calculated. The obtained value ($\Delta C/\gamma T_c = 1.38$) is slightly lower than the value predicted by

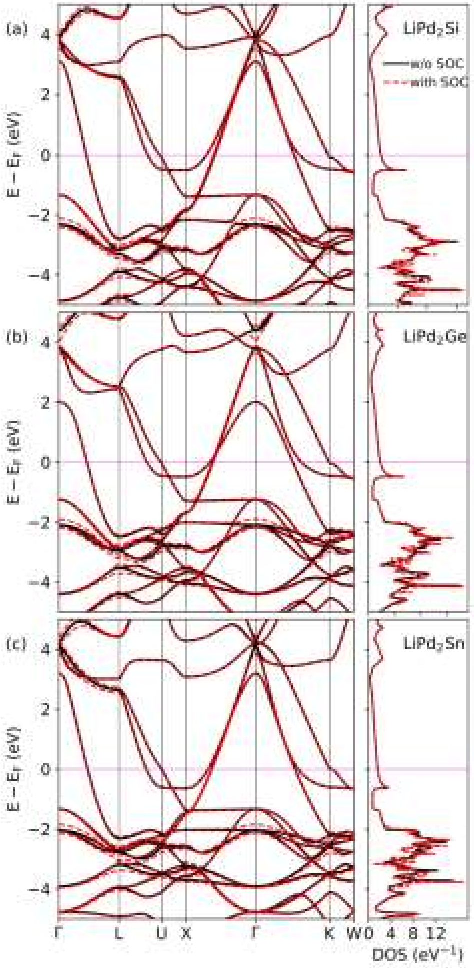

FIG. 7. Electronic structure of $\mathrm{LiPd_2}X$ calculated without SOC (black solid lines) and including SOC (red dashed lines).

Bardeen-Cooper-Schrieffer (BCS) theory (1.43) suggesting weak-coupling superconductivity in $\mathrm{LiPd_2Ge}$.

The electron-phonon coupling constant λ_{e-p} can be estimated from the inverted McMillan formula, which relates the Debye temperature Θ_D and the critical temperature T_c by the formula [26]

$$\lambda_{e-p} = \frac{1.04 + \mu^* \ln(\Theta_D/1.45T_c)}{(1 - 0.62\mu^*)\ln(\Theta_D/1.45T_c) - 1.04}, \tag{5}$$

where μ^* is the repulsive screened Coulomb parameter, typically taken as $\mu^* = 0.13$ for many metal systems [27–29].

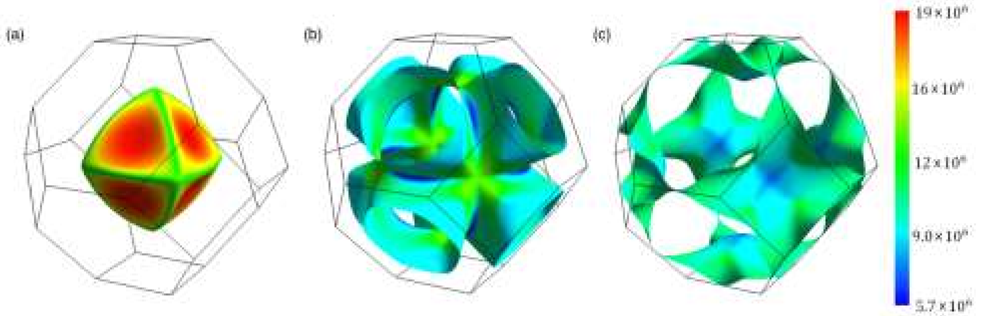

FIG. 8. Fermi surface of $LiPd_2Ge$, consisting of three sheets. Color represents the velocity of electrons (in m/s). Contribution of each sheet to the total DOS at E_F is (a) $0.25\,eV^{-1}$, (b) $0.90\,eV^{-1}$, and (c) $0.65\,eV^{-1}$.

Using $T_c = 1.96\,K$ and the Debye temperature, we obtain $\lambda_{e-p} = 0.53$ for $\Theta_D = 244\,K$ or $\lambda_{e-p} = 0.56$ for $\Theta_D = 194\,K$, which implies that $LiPd_2Ge$ is a weak-coupling superconductor.

With the electron-phonon coupling parameter λ_{e-p} and the Sommerfeld coefficient γ known, the density of states at the Fermi energy $DOS(E_F)$ can be calculated using the relation [30]

$$DOS(E_F) = \frac{3\gamma}{\pi^2 k_B^2(1+\lambda_{e-p})}, \tag{6}$$

where k_B is the Boltzmann constant. $DOS(E_F)$ is estimated to be 1.6 states eV^{-1} per formula unit (f.u.).

IV. *AB INITIO* COMPUTATIONS

A. Electronic structure

Figure 7 shows the computed electronic band structure and total density of states (DOS) calculated with and without spin-orbit coupling (SOC). The effect of SOC on the electronic structure near the Fermi energy (E_F) was found to be negligible for all three compounds. However, for some upper- and lower-lying states, band splitting, band anticrossings, and degeneracy removal due to SOC can be noticed. Three electronic bands are crossing E_F, building up three Fermi surface (FS) sheets, presented in Fig. 8 for the representative example of $LiPd_2Ge$. The other $LiPd_2X$ compounds studied, which are isostructural and isoelectronic, have very similar FS.

The total DOS and partial DOS for each atom in $LiPd_2X$ are shown in Figs. 9(a)–9(c), whereas Figs. 9(d)–9(f) display the DOS projected on atomic orbitals for $LiPd_2Ge$. States near the Fermi energy are built up mainly from Pd-4*d* and *X* atom orbitals (Si-3*p*, Ge-4*p*, and Sn-5*p*), with the smallest contribution from Li. The Fermi level is located on a decreasing slope of a local DOS maximum, associated with Pd-4*d* states, and thus doping $LiPd_2X$ with holes could be a promising strategy for increasing $DOS(E_F)$ and, potentially, T_c. Total $DOS(E_F)$, band structure value of the Sommerfeld coefficient $\gamma_{band} = \pi^2/3k_B^2 DOS(E_F)$, and the electron-phonon coupling constant λ_γ derived from the comparison of γ_{band} to the measured $\gamma = \gamma_{band}(1+\lambda_\gamma)$ are collected in Table III. In qualitative agreement with experiment, the largest $DOS(E_F)$ and γ_{band} is found for $LiPd_2Ge$ and the lowest for $LiPd_2Si$, which correlates with the presence of superconductivity, found above 1.68 K only in $LiPd_2Ge$. The computed renormalization parameters λ_γ are relatively small, 0.28, 0.37, and 0.16, for X = Si, Ge, and Sn, respectively. For the case of $LiPd_2Ge$, where $\lambda \approx 0.55$ was estimated experimentally, the underestimation is over 30%. This suggests that the computed $DOS(E_F)$ value is too large, which may be related to using the ideal Heusler crystal structure in the calculations, while site-atomic disorder is usually seen in this family [7,31]. A structural distortion may also be possible due to the unstable phonon mode (see below).

Our results for $LiPd_2Ge$, as far as the shape of the $DOS(E_F)$ curve is concerned, are similar to recently reported ones by Ayhan and Kavak Balcı [32]; however their DOS values are roughly two times smaller, with $DOS(E_F) = 0.99\,eV^{-1}$, compared to our $1.81\,eV^{-1}$. As this difference by a factor of 2 occurs for the whole DOS spectrum, we suspect that the DOS in [32] is given per spin direction. However, to double-check and independently verify our computed densities, we performed calculations by using the same full-potential linearized augmented plane-wave method (FP-LAPW) and the WIEN2K package [33] as in [32]. The calculations gave almost exactly the same electronic structure that we obtained from the pseudopotential calculations in QUANTUM ESPRESSO, and confirmed the $DOS(E_F) = 1.8\,eV^{-1}$ value.

To support our claim of the type-I superconductivity in $LiPd_2Ge$ a theoretical estimation of the Ginzburg-Landau parameter $\kappa_{GL} = \lambda_{GL}/\xi_{GL}$ has been done, where λ_{GL} and ξ_{GL} are the Ginzburg-Landau penetration depth and coherence length, respectively. First, we have to compare the BCS coherence length ξ_0 [34],

$$\xi_0 \cong 0.180\,\frac{\hbar v_F}{k_B T_c}, \tag{7}$$

with the electronic mean-free path $l_0 = v_F\tau$, to verify whether we are in the clean ($l_0 \gg \xi_0$) or dirty ($l_0 \ll \xi_0$) limit. In the above formulas, v_F is the Fermi velocity and τ is the average electronic scattering time. Values of the Fermi velocity, as shown in Fig. 8, vary between Fermi surface sheets from 5×10^6 m/s to 19×10^6 m/s, and the average $\sqrt{v_F^2} \cong 10^7$ m/s.

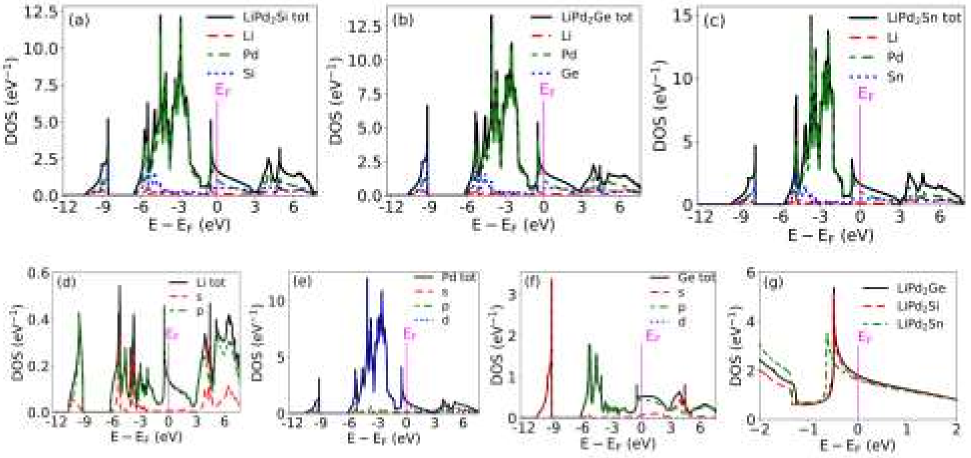

FIG. 9. The density of states (DOS) of (a) $\mathrm{LiPd_2Si}$, (b) $\mathrm{LiPd_2Ge}$, (c) $\mathrm{LiPd_2Sn}$; (d–f) partial DOS of $\mathrm{LiPd_2Ge}$; and (g) close-up of DOS near E_F for all three compounds.

This puts ξ_0 in the range 35 000–130 000 Å. To properly estimate the electronic scattering time we have calculated the electrical conductivity of $\mathrm{LiPd_2Ge}$ from the computed band structure using the Boltzmann formalism in the constant scattering time approximation, as implemented in the BOLTZTRAP code [35]. The resulting value is $\sigma/\tau = 9.5 \times 10^{21}\ \Omega^{-1}\,\mathrm{m}^{-1}\,\mathrm{s}^{-1}$. Next, taking the experimental value of the residual resistivity, measured in Fig. 3 just above transition to the superconducting state, $\rho_0 = 13.7\,\mu\Omega\,\mathrm{cm}$, we arrive at $\tau = 7.5 \times 10^{-15}$ s. Combining τ with the average Fermi velocity we get $l_0 = 750$ Å (or l_0 in the range 400–1400 Å, while using the minimum and maximum Fermi velocity from different parts of the Fermi surface), much smaller than the BCS coherence length ξ_0, estimated above. This puts our analysis to the dirty limit, where [34]

$$\kappa_{\mathrm{GL}} \simeq 0.72\frac{\lambda_L}{l_0}, \tag{8}$$

TABLE III. Calculated density of states at Fermi energy $\mathrm{DOS}(E_F)$, Sommerfeld coefficient γ_{band}, and electron-phonon coupling constant λ_γ from the band structure compared with the experimental results. λ_{expt} is calculated using the experimental T_c and the McMillan formula.

	$\mathrm{LiPd_2Si}$	$\mathrm{LiPd_2Ge}$	$\mathrm{LiPd_2Sn}$
$\mathrm{DOS}(E_F)(\mathrm{eV}^{-1})$	1.69	1.81	1.62
$\gamma_{\mathrm{band}}(\mathrm{mJ\,mol^{-1}\,K^{-2}})$	3.99	4.26	3.82
$\gamma_{\mathrm{expt}}(\mathrm{mJ\,mol^{-1}\,K^{-2}})$	5.1(1)	5.8(1)	4.4(1)
λ_{expt}	–	~0.55	–
$\lambda_\gamma = \gamma_{\mathrm{expt}}/\gamma_{\mathrm{band}} - 1$	0.28	0.37	0.16

λ_L is the zero-temperature London penetration depth, which is calculated as

$$\lambda_L^2 = 3\,\frac{1}{\mu_0 e^2 v_F^2 \mathrm{DOS}(E_F)}, \tag{9}$$

where $\mathrm{DOS}(E_F)$ is given per unit energy and volume. Calculated separately for each FS sheet $\lambda_L \cong 30 - 60$ Å, whereas the average v_F and the total $\mathrm{DOS}(E_F)$ give $\lambda_L \cong 20$ Å. The final and conservative estimate on the Ginzburg-Landau parameter is then $0.01 < \kappa_{\mathrm{GL}} < 0.1$, being considerably smaller than the critical value of $1/\sqrt{2} \cong 0.7$. Thus, $\mathrm{LiPd_2Ge}$ is indeed a type-I superconductor.

B. Phonons and the electron-phonon coupling

Figure 10 shows the computed phonon dispersion relations and phonon density of states $F(\omega)$ in $\mathrm{LiPd_2}X$. In the dispersion plots, the thick blue lines represent phonon linewidths $\gamma_{\mathbf{q}\nu}$, which are a local measure of the electron-phonon coupling, discussed below. There are four atoms in the primitive cell of $\mathrm{LiPd_2}X$, contributing to 12 phonon modes, three acoustic and nine optic. The average total and partial frequencies are collected in Table IV. The global average phonon frequency decreases with the increase of the mass of the X element, in agreement with expectations. As the partial atomic phonon DOS shows, the well-separated, Einstein-like highest-frequency optic modes are associated with Li vibrations, due to the smallest Li atomic mass ($M_{\mathrm{Li}} = 6.94$ u, $M_{\mathrm{Pd}} = 106.42$ u, $M_{\mathrm{Si}} = 28.09$ u, $M_{\mathrm{Ge}} = 72.63$ u, $M_{\mathrm{Sn}} = 118.71$ u). The average frequency of these modes also moves down when the atomic mass of the X element is changed, from ~12.3 THz (X = Si), via 11.2 THz (X = Ge), to 10 THz (X = Sn). The second group of optic modes, also with a small dispersion, is located around 7.5 THz for X = Si and 5 THz in the two remaining cases. These modes are associated mostly with Si

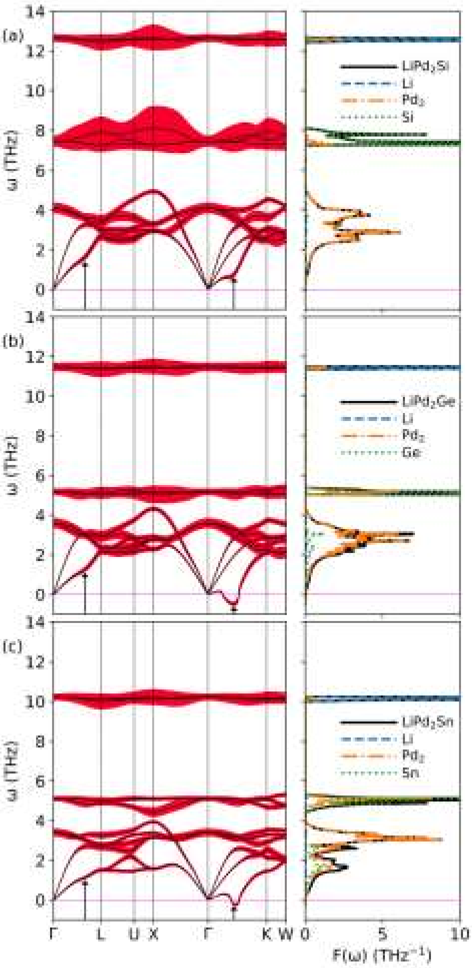

FIG. 10. Phonon dispersion relations with phonon linewidths in THz marked as thick red lines, and phonon density of states with atomic contributions. Phonon linewidths $\gamma_{\mathbf{q}\nu}$ are multiplied by 70 to improve their visibility. Arrows represent $\mathbf{q}$ vectors for which phonon anomalies occur: $\mathbf{q}_{\Gamma L} = (1/3, 1/3, 1/3)$ and $\mathbf{q}_{\Gamma K} = (1/3, 1/3, 0)$.

vibrations in LiPd$_2$Si, whereas in the two other cases they have a mixed Pd + Ge (Sn) character. A similar situation is found for the lowest part of the phonon spectrum, consisting of three acoustic and three low-frequency optic modes. For X = Si it is contributed mostly by the two Pd atoms' vibrations, whereas in the two remaining compounds, a larger contribution from Ge (Sn) is found. To verify the correctness of the calculated phonon spectra, lattice specific heat was calculated, and compared to the measured one. Results are presented in the Supplemental Material [19]. The differences, seen at higher temperatures, are most likely due to anharmonic effects (thermal expansion) and likely are responsible for the differences in the experimental and theoretical Einstein mode temperatures, as shown in Table II.

TABLE IV. Calculated average phonon frequencies, electron-phonon coupling constant, critical temperature (using $\mu^* = 0.10$), and renormalized Sommerfeld coefficient. For LiPd$_2$Ge and LiPd$_2$Sn, due to the presence of the soft mode with imaginary frequencies, for $\langle \omega_{\log}^{\alpha^2 F} \rangle$ and λ_{e-p} we give a range of values, estimated based on extrapolation of the Eliashberg function, as discussed in the Supplemental Material [19]. The soft mode, however, has negligible effect on the average ω.

LiPd$_2X$	X = Si	X = Ge	X = Sn
$\langle \omega_{\rm tot} \rangle$ (THz)	6.59	5.45	5.05
$\langle \omega_{\rm Li} \rangle$ (THz)	12.31	11.22	10.02
$\langle \omega_{\rm Pd1} \rangle$ (THz)	3.37	3.03	3.12
$\langle \omega_{\rm Pd2} \rangle$ (THz)	3.37	3.03	3.12
$\langle \omega_X \rangle$ (THz)	7.29	4.51	3.96
$\langle \omega_{\log}^{\alpha^2 F} \rangle$ (THz)	3.22	2.21–2.95	2.02 – 2.68
$\langle \omega_{\log}^{\alpha^2 F} \rangle$ (K)	155	106–142	97 – 129
λ_{e-p} (Modes 2–12)	0.30	0.33	0.26
λ_{e-p} (Total)	0.41	0.40 – 0.52	0.32 – 0.40
T_c (K) (Calc.)	0.76	0.60 – 1.50	0.11 – 0.41
T_c (K) (Expt.)	–	1.96	–

The most intriguing features of the computed phonon spectra are phonon anomalies observed in the acoustic modes in each of the studied compounds. A soft mode is detected for the transverse acoustic mode in the Γ-K direction, with a minimum frequency near $\mathbf{q}_{\Gamma K} = (1/3, 1/3, 0)$, denoted by the arrow in Fig. 10. In the case of LiPd$_2$Si, frequency is significantly lowered, whereas for X = Ge and Sn frequencies become imaginary (plotted as negative in Fig. 10). We label this mode as a "soft" one in the remaining part of the paper, although in the X = Si case frequency is positive. In addition, in the Γ-L direction at $\mathbf{q}_{\Gamma L} = (1/3, 1/3, 1/3)$ a weaker softening resembling, e.g., the Kohn anomaly in Pb [36] is seen. To rule out the possibility that the detected instability is a result of the choice of pseudopotential or insufficient q-point sampling (equivalent to insufficient number of neighboring atoms considered in calculations of interatomic force constants), we have performed test calculations for LiPd$_2$Ge with three different sets of pseudopotentials, and for all compounds, using three sizes of q-point grid: 4^3, 6^3, 8^3. The results are summarized in the Supplemental Material [19]. As far as the choice of pseudopotential is concerned, only very small differences in frequencies of higher-frequency modes were noticed (due to the slightly smaller lattice parameter), leaving the soft mode unchanged. For the q-point grid test, the 4^3 mesh was found to be too coarse, and starting from the 6^3 mesh, convergent results were obtained. Additionally, for LiPd$_2$Ge inclusion of spin-orbit coupling had no effect on either the soft mode or on the other phonon branches; these are checked in calculations for two selected q-points; see Fig. S2 [19].

Phonon anomalies are frequently observed in Heusler compounds. Among the possible reasons for such behavior we may distinguish Kohn anomalies due to Fermi surface nesting, martensitic instabilities towards modulated structures, or the formation of charge density waves [37–44]. In particular, a soft mode in the Γ-K direction at a similar wave vector $\mathbf{q}_{\Gamma K}$ was observed in several magnetic and nonmagnetic materials, including the widely studied magnetic shape-memory alloy Ni_2MnGa. Martynov and Kokorin [38], in x-ray diffraction studies, showed the presence of many thermally and stress-induced martensitic phase transitions and structure modulations. Zheludev *et al.* found soft modes in Ni_2MnGa in inelastic neutron scattering [39] and concluded that the phonon anomalies are probably caused by electron-phonon interactions. Zayak *et al.* [37] studied with *ab initio* calculations anomalous vibrations in magnetic and nonmagnetic Heusler compounds. They observed that compounds with anomalies in their phonon structure also had low-lying optical modes at Γ. Modes of the same symmetry repel each other, so they argued that these optical modes pushed acoustic modes down which softened them. Low-lying optical modes could be caused by additional covalent bonding in dominantly metallic Ni_2MnGa. Both magnetic and nonmagnetic compounds were found to have soft modes, and therefore magnetic order is not a condition for phonon anomalies in those compounds. They also pointed out that valence electron number per atom is an important quantity, because it could be used to classify stable and unstable ferromagnetic structures, where stable compounds had this ratio below 7.4. In the case of $LiPd_2X$ it is equal to 6.25, and thus it does not follow this rule. In our work we have not found any signs of phase transition in $LiPd_2X$ in the heat-capacity or resistivity measurements. It is worth noting, that in recent work on related $LiGa_2Rh$ [45], acoustic mode softening, similar to our case of $LiPd_2Si$, was detected, without imaginary frequencies.

As far as the "atomic" character of the soft mode near the minimum frequency is concerned, in all compounds it has generally equal contributions from Pd1, Pd2, and X atoms (even for $X = \mathrm{Si}$, where contribution of Si to remaining parts of the low-frequency spectrum is small). Phonon displacement patterns for the unstable mode at $\mathbf{q}_{\Gamma K} = (1/3, 1/3, 0)$ for $LiPd_2Ge$ are visualized in Fig. 11. Pd and Ge vibrate in phase with each other and out of phase with small-amplitude Li vibrations. That could indicate a tendency towards an uniform distortion of the cubic structure. As the origin of soft modes is a broad and interesting issue requiring deeper studies we leave it for future works, here pointing only to their possible connection to superconductivity.

To describe superconductivity in $LiPd_2X$ we assumed an electron-phonon pairing mechanism with the Migdal-Eliashberg theory. The electron-phonon interaction matrix elements, computed using perturbation theory in QE, allow us to calculate the phonon linewidths $\gamma_{\mathbf{q}\nu}$ (see, e.g., [46,47]), already presented in Fig. 10. Besides an enhancement of $\gamma_{\mathbf{q}\nu}$ for Si vibrations in Fig. 10(a), we do not see any specific mode or direction dependence of linewidths. Weighted by an inverse square frequency, $\gamma_{\mathbf{q}\nu}$ measures the local contribution of a phonon to the global electron-phonon coupling parameter λ_{e-p}:

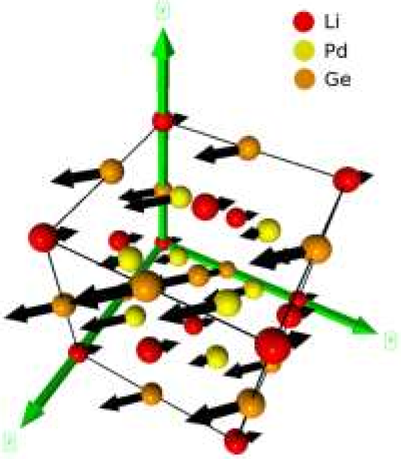

FIG. 11. Visualization of atomic vibrations with $\mathbf{q} = (1/3, 1/3, 0)$, for the first transverse acoustic mode of $LiPd_2Ge$. Red balls represent Li, orange balls in the middle of the edges and one in the middle of the cell represent Ge, and yellow balls inside the cube represent Pd. Pd and Ge vibrate in phase with each other and out of phase with Li.

$$\lambda_{e-p} = \sum_{\mathbf{q},\nu} \frac{\gamma_{\mathbf{q}\nu}}{\pi \hbar N(E_F)\omega^2_{\mathbf{q},\nu}}, \tag{10}$$

where $N(E_F)$ is the total DOS at the Fermi level. By summing over all phonon modes ν and wave vectors $\mathbf{q}$, the Eliashberg electron-phonon interaction function $\alpha^2F(\omega)$ is calculated:

$$\alpha^2F(\omega) = \frac{1}{2\pi N(E_F)} \sum_{\mathbf{q}\nu} \delta(\omega - \omega_{\mathbf{q}\nu}) \frac{\gamma_{\mathbf{q}\nu}}{\hbar\omega_{\mathbf{q}\nu}}, \tag{11}$$

which alternatively allows us to calculate λ_{e-p}:

$$\lambda_{e-p} = 2\int_0^{\omega_{\max}} \frac{\alpha^2F(\omega)}{\omega} d\omega. \tag{12}$$

The obtained $\alpha^2F(\omega)$ are plotted in Fig. 12, and, similar to $F(\omega)$, the Eliashberg functions have a three-peak structure. The phonon DOS is also plotted in the background in Fig. 12 after renormalization to the same value as the area under $\alpha^2F(\omega)$. This allows us to analyze for which frequency range Eliashberg function is enhanced. Some enhancement is seen for $LiPd_2Si$ [Fig. 12(a)] around 7.5 THz, due to large phonon linewidths, seen in Fig. 10(a). However, this effect is not very strong due to relatively high frequency of silicon vibrations, as $\alpha^2F(\omega) \propto \frac{\gamma_{\mathbf{q}\nu}}{\omega_{\mathbf{q}\nu}}$. On the other hand, in the low-frequency range we see a dominating contribution from the first "soft" mode, plotted using a dashed line in Fig. 12, which results both from the low frequency of vibrations and increased phonon linewidths at $\mathbf{q}_{\Gamma K}$. The increased $\gamma_{\mathbf{q}\nu}$ are especially

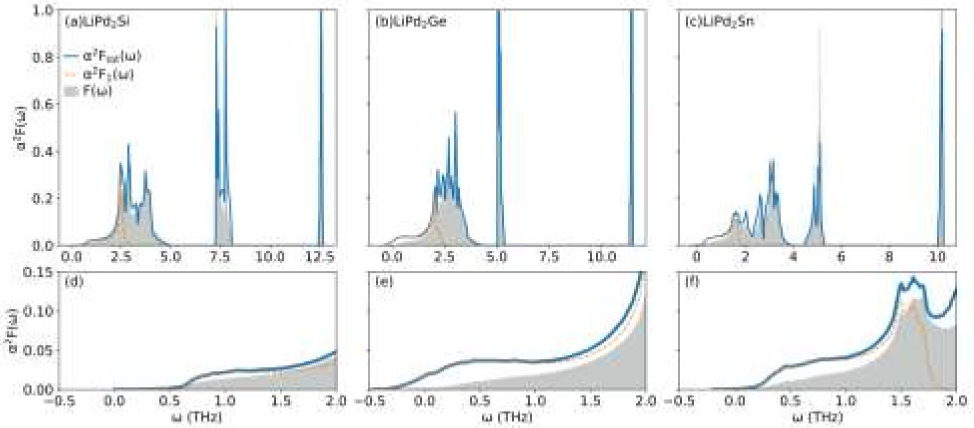

FIG. 12. Eliashberg functions for LiPd$_2X$. Orange dashed lines denote Eliashberg functions only for the first acoustic mode, whereas blue lines denote total function, summed over all 12 modes. Panels in the second row show details near zero frequency.

seen in LiPd$_2$Ge, and thus the enhancement of the Eliashberg function over the $F(\omega)$ is especially seen for this compound. Thus, superconductivity and strong soft-mode behavior are correlated in LiPd$_2X$, as the strongest electron-phonon coupling and superconductivity above 1.68 K are found for $X = \mathrm{Ge}$.

Due to the presence of imaginary frequencies, T_c and λ_{e-p} cannot be calculated accurately for LiPd$_2$Ge and LiPd$_2$Sn. Even though the contribution of the imaginary part of the spectrum, calculated as an area under the phonon DOS curve, is only 0.05% in LiPd$_2$Ge and 0.005% in LiPd$_2$Sn, the enhanced values of $\alpha^2F(\omega)$ for the soft mode and $\lambda_{e-p} \propto \frac{\gamma_{qv}}{\omega_{qv}{}^2}$ dependencies make the contribution of the low-frequency phonon modes to λ_{e-p} especially important. To be able to quantify the electron-phonon coupling strength and analyze its magnitude along the series of compounds, at first we calculated the contribution to λ_{e-p} from all the modes except the first, "soft" one. The values are shown in Table IV as λ_{e-p} (modes 2–12) and increase from 0.26 ($X = \mathrm{Sn}$), via 0.30 ($X = \mathrm{Si}$), to 0.33 ($X = \mathrm{Ge}$). The contribution from the first mode in LiPd$_2$Si is equal to 0.11, resulting in total $\lambda_{e-p} = 0.41$. The direct calculation of $\lambda_{e-p(1)}$ associated with the first mode in $X = \mathrm{Ge}$ and Sn is impossible due to the divergent behavior of $\alpha^2F(\omega)/\omega$ near $\omega = 0$. To overcome this difficulty and estimate first mode contributions, we have extrapolated $\alpha^2F(\omega)$ in two ways to set approximate upper and lower bounds for the computed $\lambda_{e-p(1)}$; the details are described in the Supplemental Material [19]. The resulting values are in the range of $\lambda_{e-p(1)} = 0.07 - 0.19$ ($X = \mathrm{Ge}$) and $\lambda_{e-p(1)} = 0.06 - 0.14$ ($X = \mathrm{Sn}$), giving the ranges of calculated total $\lambda_{e-p} = 0.40 - 0.52$ for LiPd$_2$Ge and $\lambda_{e-p} = 0.32 - 0.40$ for LiPd$_2$Sn. Within the same method, the logarithmic average frequency $\langle \omega_{\log}^{\alpha^2F} \rangle$ was calculated (see Table S-II and the Supplemental Material [19]), as it is also defined based on the Eliashberg function.

The critical temperature T_c may now be approximately computed using the Allen-Dynes [48] equation:

$$T_c = \frac{\langle \omega_{\log}^{\alpha^2F} \rangle}{1.20} \exp\left[\frac{-1.04(1+\lambda_{e-p})}{\lambda_{e-p} - \mu^*(1+0.62\lambda_{e-p})}\right], \qquad (13)$$

where $\mu^* = 0.10$, as is the case when the Allen-Dynes formula is used [48].

The results are presented in Table IV. For all compounds, the theoretical λ_{e-p} computed from the Eliashberg functions are larger than the λ_γ extracted from the electronic specific heat (see Table III). For LiPd$_2$Ge, however, it is closer to the $\lambda_{\mathrm{expt}} \approx 0.55$ estimated from the experimental T_c. The computed value of T_c, being in the range between 0.60 and 1.50 K, is visibly lower than experimental $T_c = 1.96$ K. Note that the upper value of $\langle \omega_{\log}^{\alpha^2F} \rangle = 142$ K for T_c calculations should be used in combination with the lower estimation of $\lambda_{e-p} = 0.4$, and vice versa.

For the two other studied Heuslers, where no superconductivity above 1.68 K was experimentally found, the computed T_c is lower, 0.76 K for $X = \mathrm{Si}$ and 0.26 ± 0.15 K for $X = \mathrm{Sn}$. Taking into account the inaccuracy of the electron-phonon coupling calculations due to the presence of soft modes, the qualitative agreement between theory and experiment is considered satisfactory. Calculations confirm that LiPd$_2$Ge is a weakly coupled electron-phonon superconductor, whereas LiPd$_2$Si and LiPd$_2$Sn are expected to have T_c below 1 K.

V. SUMMARY

We have optimized a solid-state reaction method to obtain polycrystalline LiPd$_2X$, where $X = \mathrm{Si}$, Ge, and Sn. LeBail analysis of the powder x-ray diffraction patterns confirm that all three compounds belong to the Heusler-type family. We have not seen reports of LiPd$_2$Si. The estimated lattice parameters for LiPd$_2$Ge and LiPd$_2$Sn are in good agreement with previous reports. Superconductivity was observed for

$LiPd_2Ge$ with $T_c = 1.96\,K$. $LiPd_2Ge$ is another example of a superconducting material in the Pd-based Heusler-type family. Interestingly it is a type-I superconductor, unique in this system, and it has the total valence electron number $N_{el.} = 25$. Theoretical calculations suggest that the two other compounds studied should also reveal superconducting behavior but with $T_c = 0.76$ and 0.25 K for $LiPd_2Si$ and $LiPd_2Sn$, respectively.

Detailed studies of the superconducting properties show that $LiPd_2Ge$ is a BCS weakly coupled superconductor with a heat-capacity anomaly $\Delta C/\gamma T_c = 1.38$ and an electron-phonon coupling constant $\lambda_{e-p} \sim 0.55$. Type-I superconductivity is rather rare in intermetallic compounds and $LiPd_2Ge$ is unusual as a Heusler compound that is a type-I superconductor.

Detailed theoretical calculations show the presence of soft modes which likely enhance electron-phonon coupling and can be responsible for the enhanced superconductivity for $LiPd_2Ge$. Studies of the soft modes will be continued.

ACKNOWLEDGMENTS

Work at GUT was supported by the National Science Centre (Poland), Grant No. 2017/27/B/ST5/03044. Work at AGH-UST was supported by the National Science Centre (Poland), Project No. 2017/26/E/ST3/00119. The synthetic work at Princeton was supported by the US Department of Energy, Division of Basic Energy Sciences, Grant No. DE-FG02-98ER45706. T.K. would like to thank Damian Brzozowski for his assistance in preparation of $LiPd_2Sn$.

---

[1] F. Heusler, W. Starck, and E. Haupt, Verh. Dtsch. Phys. Ges. **5**, 220 (1903).
[2] T. Gruner, D. Jang, Z. Huesges, R. Cardoso-Gil, G. H. Fecher, M. M. Koza, O. Stockert, A. P. Mackenzie, M. Brando, and C. Geibel, Nat. Phys. **13**, 967 (2017).
[3] S. Chadov, X. Qi, J. Kübler, G. H. Fecher, C. Felser, and S. C. Zhang, Nat Mater. **9**, 541 (2010).
[4] B. Nowak, O. Pavlosiuk, and D. Kaczorowski, J. Phys. Chem. C **119**, 2770 (2015).
[5] O. Pavlosiuk, D. Kaczorowski, X. Fabreges, A. Gukasov, and P. Wiśniewski, Sci Rep. **6**, 18797 (2016).
[6] Y. Pan, A. M. Nikitin, T. V. Bay, Y. K. Huang, C. Paulsen, B. H. Yan, and A. de Visser, EPL **104**, 27001 (2013).
[7] T. Graf, C. Felser, and S. S. P. Parkin, Prog. Solid State Chem. **39**, 1 (2011).
[8] T. Klimczuk, C. H. Wang, K. Gofryk, F. Ronning, J. Winterlik, G. H. Fecher, J.-C. Griveau, E. Colineau, C. Felser, J. D. Thompson, D. J. Safarik, and R. J. Cava, Phys. Rev. B **85**, 174505 (2012).
[9] B. T. Matthias, Phys Rev. **97**, 74 (1955).
[10] S. V. Vonsovskii, I. A. Iziumov, and E. Z. Kurmaev, *Superconductivity of Transition Metals: Their Alloys and Compounds* (Springer-Verlag, Berlin, 1982).
[11] E. M. Carnicom, W. Xie, Z. Yang, K. Górnicka, T. Kong, T. Klimczuk, and R. J. Cava, Chem Mater. **31**, 2164 (2019).
[12] B. T. Matthias, Phys Rev. **92**, 874 (1953).
[13] P. Giannozzi, S. Baroni, N. Bonini, M. Calandra, R. Car, C. Cavazzoni, D. Ceresoli, G. L. Chiarotti, M. Cococcioni, I. Dabo, A. Dal Corso, S. de Gironcoli, S. Fabris, G. Fratesi, R. Gebauer, U. Gerstmann, C. Gougoussis, A. Kokalj, M. Lazzeri, L. Martin-Samos *et al.*, J Phys.: Condens. Matter **21**, 395502 (2009).
[14] P. Giannozzi, O. Andreussi, T. Brumme, O. Bunau, M. Buongiorno Nardelli, M. Calandra, R. Car, C. Cavazzoni, D. Ceresoli, M. Cococcioni, N. Colonna, I. Carnimeo, A. Dal Corso, S. de Gironcoli, P. Delugas, R. A. DiStasio, A. Ferretti, A. Floris, G. Fratesi, G. Fugallo *et al.*, J Phys.: Condens. Matter **29**, 465901 (2017).
[15] Pseudopotentials downloaded from https://www.quantum-espresso.org/pseudopotentials: Li.pbe-s-kjpaw_psl.1.0.0.UPF; Pd.pbe-n-kjpaw_psl.1.0.0.UPF; Pd.rel-pbe-n-kjpaw_psl.1.0.0.UPF; Si.pbe-n-kjpaw_psl.1.0.0.UPF; Si.rel-pbe-n-kjpaw_psl.1.0.0.UPF; Ge.pbe-dn-kjpaw_psl.1.0.0.UPF; Ge.rel-pbe-dn-kjpaw_psl.1.0.0.UPF; Sn.pbe-dn-kjpaw_psl.1.0.0.UPF; Sn.rel-pbe-dn-kjpaw_psl.1.0.0.UPF.
[16] A. Dal Corso, Comput Mater. Sci. **95**, 337 (2014).
[17] J. P. Perdew, K. Burke, and M. Ernzerhof, Phys. Rev. Lett. **77**, 3865 (1996).
[18] S. Baroni, S. de Gironcoli, A. Dal Corso, and P. Giannozzi, Rev. Mod. Phys. **73**, 515 (2001).
[19] See Supplemental Material at http://link.aps.org/supplemental/10.1103/PhysRevB.102.024507 for more information.
[20] C.-J. Kistrup and H.-U. Schuster, Z. Anorg Allg. Chem. **410**, 113 (1974).
[21] T. Klimczuk and R. J. Cava, Phys. Rev. B **70**, 212514 (2004).
[22] S. Sun, K. Liu, and H. Lei, J. Phys.: Condens. Matter **28**, 085701 (2016).
[23] L. L. Zhao, S. Lausberg, H. Kim, M. A. Tanatar, M. Brando, R. Prozorov, and E. Morosan, Phys. Rev. B **85**, 214526 (2012).
[24] E. Svanidze and E. Morosan, Phys. Rev. B **85**, 174514 (2012).
[25] J. Winterlik, G. H. Fecher, C. Felser, M. Jourdan, K. Grube, F. Hardy, H. von Löhneysen, K. L. Holman, and R. J. Cava, Phys. Rev. B **78**, 184506 (2008).
[26] W. L. McMillan, Phys. Rev. **167**, 331 (1968).
[27] K. Górnicka, E. M. Carnicom, S. Gołąb, M. Łapiński, B. Wiendlocha, W. Xie, D. Kaczorowski, R. J. Cava, and T. Klimczuk, Supercond. Sci. Technol. **32**, 025008 (2019).
[28] K. Górnicka, R. J. Cava, and T. Klimczuk, J. Alloys Compd. **793**, 393 (2019).
[29] E. M. Carnicom, W. Xie, T. Klimczuk, J. Lin, K. Górnicka, Z. Sobczak, N. P. Ong, and R. J. Cava, Sci. Adv. **4**, eaar7969 (2018).
[30] C. Kittel, *Solid State Physics*, 4th ed. (Wiley, New York, 1966).
[31] H. C. Kandpal, V. Ksenofontov, M. Wojcik, R. Seshadri, and C. Felser, J. Phys. D: Appl. Phys. **40**, 1587 (2007).
[32] S. Ayhan and G. Kavak Balcı, Mater Res. Express **6**, 0865e9 (2019).
[33] P. Blaha, K. Schwarz, G. K. H. Madsen, D. Kvasnicka, and J. Luitz, *WIEN2K, An Augmented Plane Wave + Local Orbitals Program for Calculating Crystal Properties* (Technische Universitat Wien, Vienna, 2001).
[34] H. Bartolf, *Fluctuation Mechanisms in Superconductors* (Springer Fachmedien, Wiesebaden, Germany, 2016).

[35] G. K. H. Madsen and D. J. Singh, Comput. Phys. Commun. **175**, 67 (2006).

[36] P. Aynajian, T. Keller, L. Boeri, S. M. Shapiro, K. Habicht, and B. Keimer, Science **319**, 1509 (2008).

[37] A. T. Zayak, P. Entel, K. M. Rabe, W. A. Adeagbo, and M. Acet, Phys. Rev. B **72**, 054113 (2005).

[38] V. V. Martynov and V. V. Kokorin, J. Phys. III **2**, 739 (1992).

[39] A. Zheludev, S. M. Shapiro, P. Wochner, and L. E. Tanner, Phys. Rev. B **54**, 15045 (1996).

[40] S. Ağduk and G. Gökoğlu, J. Alloys Compd. **511**, 9 (2012).

[41] H. Kim, B. I. Min, and K. Kim, Phys. Rev. B **98**, 144305 (2018).

[42] T. Büsgen, J. Feydt, R. Hassdorf, S. Thienhaus, M. Moske, M. Boese, A. Zayak, and P. Entel, Phys. Rev. B **70**, 014111 (2004).

[43] X. Moya, L. Mañosa, A. Planes, T. Krenke, M. Acet, V. O. Garlea, T. A. Lograsso, D. L. Schlagel, and J. L. Zarestky, Phys. Rev. B **73**, 064303 (2006).

[44] S. Paul, B. Sanyal, and S. Ghosh, J. Phys.: Condens. Matter **27**, 035401 (2015).

[45] H. Y. Uzunok, E. Karaca, S. Bağcı, and H. M. Tütüncü, Solid State Commun. **311**, 113859 (2020).

[46] R. Heid, K.-P. Bohnen, I. Y. Sklyadneva, and E. V. Chulkov, Phys. Rev. B **81**, 174527 (2010).

[47] S. Gołąb and B. Wiendlocha, Phys. Rev. B **99**, 104520 (2019).

[48] P. B. Allen and R. C. Dynes, Phys. Rev. B **12**, 905 (1975).

Source material's DOI: https://doi.org/10.1103/PhysRevB.102.024507

Supplemental Material for
Soft-mode enhanced type-I superconductivity in $LiPd_2Ge$

Karolina Górnicka,[1,2] Gabriel Kuderowicz,[3] Elizabeth M. Carnicom,[4] Kamil Kutorasiński,[3]
Bartlomiej Wiendlocha,[3] Robert J. Cava[4], and Tomasz Klimczuk[1,2]

[1] *Faculty of Applied Physics and Mathematics, Gdansk University of Technology,*
ul. Narutowicza 11/12, 80-233 Gdańsk, Poland,
[2]*Advanced Materials Centre, Gdansk University of Technology,*
ul. Narutowicza 11/12, 80-233 Gdańsk, Poland,
[3] *Faculty of Physics and Applied Computer Science, AGH University of Science and Technology,*
Aleja Mickiewicza 30, 30-059 Kraków, Poland
[4] *Department of Chemistry, Princeton University, Princeton, NJ 08544, USA*

e-mail: karolina.gornicka@pg.edu.pl, tomasz.klimczuk@pg.edu.pl

Supplemental Material contains pXRD patterns for $LiPd_2X$ compounds, information on pseudopotential and **q**-grid tests for phonon calculations in $LiPd_2X$ and description of how we dealt with the soft mode to estimate the electron-phonon coupling parameter $\lambda_{e\text{-}p}$ for $LiPd_2Ge$ and $LiPd_2Sn$. Comparison of the calculated and measured lattice specific heat is also shown.

Powder x-ray diffraction

Figure S1 presents the powder x-ray diffraction pattern for $LiPd_2Si$, $LiPd_2Ge$ and $LiPd_2Sn$ together with the LeBail refinement. All compounds crystallize in the cubic *$L2_1$* crystal structure (space group *Fm-3m*, No. 225). A small amount of impurity phase (LiPd; space group *P-6m2*, No. 187) is only observed for $LiPd_2Si$.

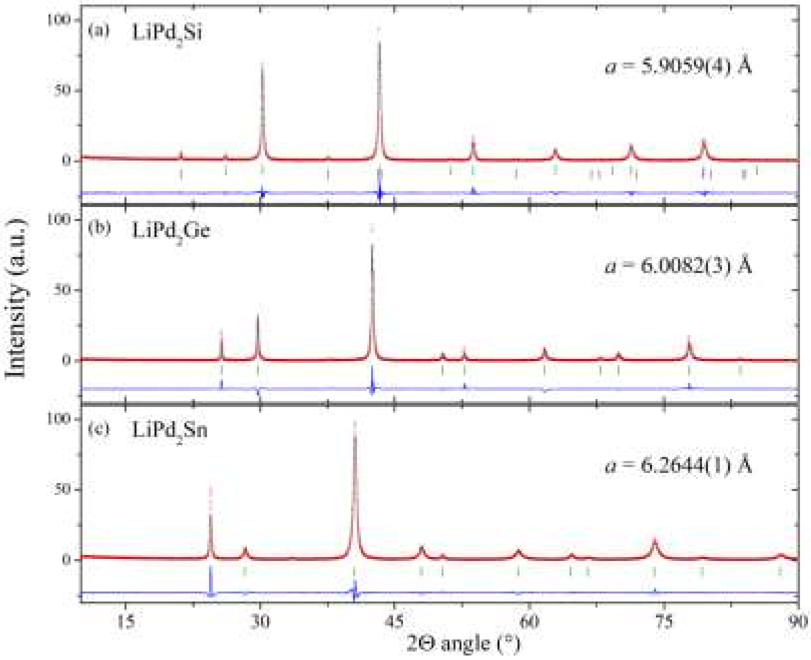

Figure S1. Powder x-ray diffraction pattern (pXRD) (red points) together with the LeBail refinement profile (black solid line) for $LiPd_2X$ (X=Si,Ge and Sn) compounds. The green and violet vertical bars indicate the expected Bragg peak positions for full Heusler (*Fm-3m*, No. 225) and LiPd impurity (*P-6m2*, No. 187).

Pseudopotentials and q-grid testing

To determine whether the appearance of the soft mode in $LiPd_2X$ is not a result of insufficient accuracy of calculations, two types of test calculations were performed: with a different sets of pseudopotentials and for different **q**-point meshes in phonon calculations, in a scalar-relativistic way. For $LiPd_2Ge$ two sets of Projector Augmented Wave (PAW) pseudopotentials (see, Ref [16] in the manuscript) with different number of valence electrons for Pd atoms were taken (labeled as pseudo1 and pseudo2, see **Table S-I**) and a set of ultrasoft pseudopotentials, labeled as pseudo3. Lattice parameter was independently relaxed for each set of pseudopotentials, and small differences are noticed in **Table S-I**. Next, phonon calculations were done for each set of pseudopotentials. In density functional perturbation theory (See Refs [13,14,18] in the manuscript) first dynamical matrices in reciprocal space are calculated on a chosen **q**-point grid and then interatomic force constants (IFC) are calculated in real space. Once IFC are calculated, by Fourier interpolation, phonon frequencies at any **q**-point are computed. For pseudopotential testing, a 8^3 q-point mesh was taken. Phonon dispersion relations in Γ-K direction, computed for $LiPd_2Ge$ using 3 sets of pseudopotentials, are shown in **Figure S2(a)**. As one can see, only small differences in frequencies are present, and larger w for pseudo2 are related to a smaller lattice parameter, with no changes to the soft mode.

Table S-I Pseudopotential files (see https://www.quantum-espresso.org/pseudopotentials), their number of valence electrons (Z_{val}) and calculated lattice parameter of $LiPd_2Ge$ for given pseudopotentials. Pseudopotentials "pseudo1" were used in further calculations.

	pseudo1	Z_{val}	pseudo2	Z_{val}	pseudo3	Z_{val}
pseudo-potentials	Li.pbe-s-kjpaw_psl.1.0.0.UPF	3	Li.pbe-s-kjpaw_psl.1.0.0.UPF	3	Li.pbe-sl-rrkjus_psl.1.0.0.UPF	3
	Pd.pbe-n-kjpaw_psl.1.0.0.UPF	10	Pd.pbe-spn-kjpaw_psl.1.0.0.UPF	18	Pd.pbe-n-rrkjus_psl.1.0.0.UPF	10
	Ge.pbe-dn-kjpaw_psl.1.0.0.UPF	14	Ge.pbe-dn-kjpaw_psl.1.0.0.UPF	14	Ge.pbe-dn-rrkjus_psl.1.0.0.UPF	14
a (Å)	6.07805		6.05619		6.08097	

Next we have tested convergence of calculations and presence of a soft-mode as a function of **q**-mesh size, using 4^3, 6^3 and 8^3 grids, which corresponds to 8, 16, and 29 inequivalent **q**-points (and dynamical matrices) to be calculated to obtain IFC matrix in real space. Additionally, frequencies in phonon dispersion plots in **Figure S2(b-d)**, obtained by Fourier interpolation from IFC, are compared with those obtained by direct, single-point calculations of phonon frequencies, done for a vector **q**=(1/4,1/4,0) [open circles in **Figure S2(b-d)**]. This **q**-vector is close to the point, where minimum of the soft mode appears at Γ-K direction. Corresponding frequencies are marked with circles in **Figure S2(b-d)**. From the figure we can see, that 4^3 **q**-point mesh is insufficient to describe soft-mode, as single-point calculations predict significantly different frequency. Also, on this mesh soft mode is predicted to appear in $LiPd_2Si$, which is not the case for denser grids. On the other hand, dispersions calculated on 6^3 and 8^3 grids do not change further and interpolated frequencies are equal to those from single-point calculations with an accuracy better than 1%. Seeing that we concluded, that 8^3 grid is sufficient.

To make sure that presence of the soft mode is not related to neglecting of the spin-orbit coupling (SOC), we have computed phonon frequencies in $LiPd_2Ge$ at **q**=(1/3,1/3,0) and **q**=(1/4,1/4,0) including SOC (full relativistic versions of pseudopotentials for Pd and Ge from the "pseudo1" set were taken). Results are marked with open squares in **Figure S2(b)** and no important changes are found.

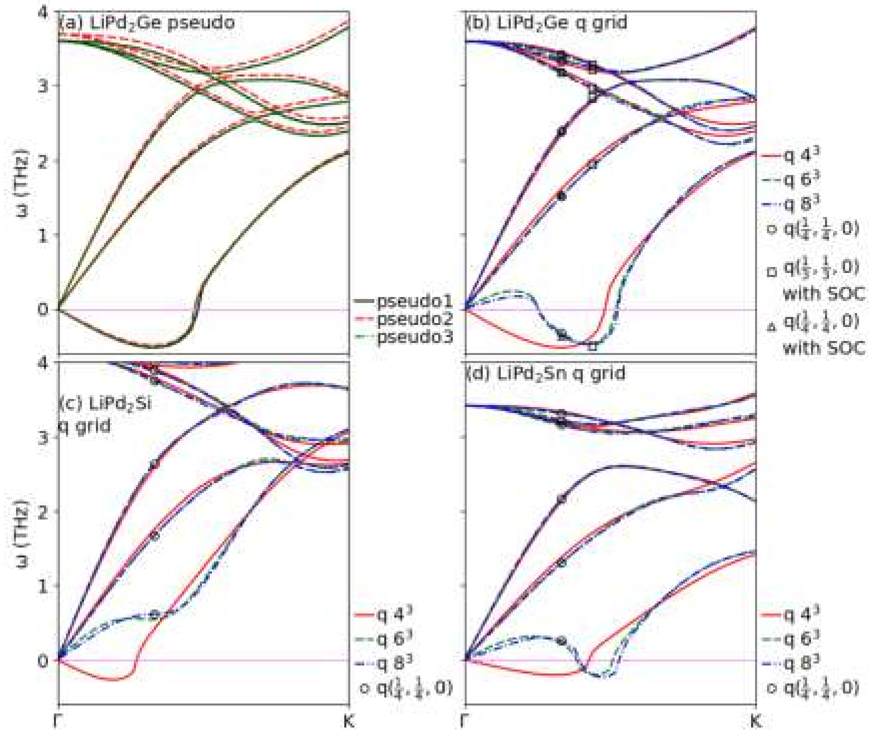

Figure S2 (a) The effect of chosen pseudopotential on phonons at Γ-K. Pseudopotentials are listed in Table SI. (b)-(d) The effect of grid sizes on phonon dispersion additionally compared with phonons calculated directly at vector **q**=(1/4,1/4,0) (open circles). For highly-symmetric, cubic $LiPd_2X$ structure grid sizes 4^3, 6^3, 8^3 correspond to 8, 16, and 29 inequivalent **q**-points (dynamical matrices) used in calculations of IFC. In panel (b) open squares and open triangles show phonon frequencies in $LiPd_2Ge$ at **q**=(1/3,1/3,0) and **q**=(1/4,1/4,0), computed including spin-orbit coupling.

Estimation of $\lambda_{e\text{-}p}$ for the soft mode

Imaginary frequencies and enhanced phonon linewidths $\gamma_{q\nu}$ of the soft mode in $LiPd_2Ge$ and $LiPd_2Sn$ lead to substantial values of Eliashberg functions $\alpha^2F(\omega)$ near $\omega = 0$. This function should quickly approach zero for $\omega \rightarrow 0$ otherwise electron-phonon coupling constant $\lambda_{e\text{-}p}$ cannot be calculated due to divergent terms appearing when using formula

$$\lambda_{e\text{-}p} = 2\int_0^{\omega_{max}} \frac{\alpha^2F(\omega)}{\omega} d\omega. \tag{1}$$

Similar problem appears in calculation of the logarithmic average frequency

$$\left\langle \omega_{log}^{\alpha^2F} \right\rangle = exp\left(\int_0^{\omega_{max}} \alpha^2F(\omega) ln(\omega) \frac{d\omega}{\omega} / \int_0^{\omega_{max}} \alpha^2F(\omega) \frac{d\omega}{\omega}\right), \tag{2}$$

which enters the Allen-Dynes formula for superconducting critical temperature T_c:

$$k_BT_c = \frac{\hbar\left\langle \omega_{log}^{\alpha^2F} \right\rangle}{1.20} exp\left(\frac{-1.04(1+\lambda)}{\lambda-\mu^*(1+0.62\lambda)}\right). \tag{3}$$

As the Eliashberg function is computed for each of the phonon modes, we can calculate the lower bound of $\lambda_{e\text{-}p}$ from the remaining 11 phonon modes and extrapolate $\alpha^2F(\omega)$ function for the first mode requiring that $\alpha^2F(\omega) \rightarrow 0$ when $\omega \rightarrow 0$. Because $LiPd_2Si$ also has a slightly softened 1st acoustic mode, however with no imaginary frequencies, we assumed that Eliashberg functions of $LiPd_2Ge$ and $LiPd_2Sn$ should behave similarly to $LiPd_2Si$. Low-frequency part of $\alpha^2F(\omega)$, coming from the 1st, 2nd and 3rd acoustic modes, is shown in **Figure S3.**

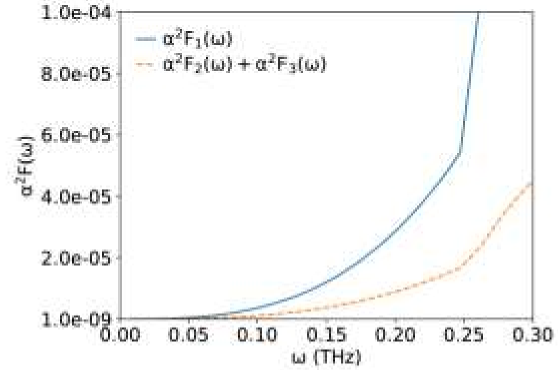

Figure S3. Partial Eliashberg functions of $LiPd_2Si$ for the first acoustic mode, $\alpha^2F_1(\omega)$, and a sum of the functions for the other two acoustic modes, $\alpha^2F_2(\omega) + \alpha^2F_3(\omega)$.

As we can see, below a characteristic frequency, equal to 0.25 THz in $LiPd_2Si$, $\alpha^2F(\omega)$ bends downwards to smoothly reach zero. Thus, for $LiPd_2Ge$ and $LiPd_2Sn$ we decided to divide

$\alpha^2F(\omega)$ function into three parts, by selecting two characteristic frequencies, ω_1 and ω_2. For $\omega > \omega_2$ we take the as-calculated $\alpha^2F_1(\omega)$.

We chose two values of ω_2, one at a slope of the first peak of the Eliashberg function, located around 2 THz in X = Ge and 1.5 THz in X = Sn, and the second at approximately 0.5 THz. For the low-frequency part for $\omega < \omega_1$ we used a sum of Eliashberg functions for the other two acoustic modes, in a similar way to what we observed for $LiPd_2Si$. In the middle part, for $\omega_1 < \omega < \omega_2$ Eliashberg function is approximated with a third order polynomial which connects the other two parts into a smooth function. By different choice of ω_1 and ω_2 (see **Table S-II** and **Figure S4**) we constructed two modified Eliashberg functions to find the lower ("modified 1") and upper ("modified 2") bounds for $\lambda_{e\text{-}p}$. For the lower bound we wanted to replace large part of the Eliashberg function of the first acoustic mode, so $\omega_1$is taken closely to ω_2. For the upper bound we chose ω_1 equal approximately 0.2 THz.

In **Figure S5** we show cumulative electron-phonon coupling constant, computed from the original (X = Si) and modified (X = Ge, Sn) Eliashberg functions. It is a convenient quantity showing contributions to $\lambda_{e\text{-}p}$ from phonon modes at different frequency ranges. It is defined as follows:

$$\lambda(\omega) = \int_0^{\omega} \frac{\alpha^2F(\omega\prime)}{\omega\prime} d\omega'. \tag{4}$$

Calculated phonon linewidths in acoustic modes are the smallest, however modes at lower frequencies contribute more to Eliashberg function and $\lambda_{e\text{-}p}$. Acoustic modes below 4 THz in $LiPd_2Ge$ and $LiPd_2Sn$ (with the largest contribution from Pd) contribute approximately 90% of total $\lambda_{e\text{-}p}$. They contribute less in $LiPd_2Si$, in approximately 80%, because upper-lying Si modes here have larger linewidths and are more strongly coupled than Ge and Sn modes.

Table S-II. Characteristic frequencies used to calculated modified Eliashberg functions, resulting electron-phonon coupling parameters $\lambda_{e\text{-}p}$ and logarithmic average frequency

	$LiPd_2Ge$				$LiPd_2Sn$			
	ω_1(THz)	ω_2(THz)	$\lambda_{e\text{-}p}$	$\left\langle \omega_{log}^{\alpha^2F} \right\rangle$ (THz)	ω_1(THz)	ω_2(THz)	$\lambda_{e\text{-}p}$	$\left\langle \omega_{log}^{\alpha^2F} \right\rangle$ (THz)
Modified 1 - lower $\lambda_{e\text{-}p}$	1.8066	1.8094	0.40	2.95	1.3119	1.3160	0.32	2.68
Modified 2 - upper $\lambda_{e\text{-}p}$	0.2027	0.4935	0.52	2.21	0.2026	0.4935	0.40	2.02

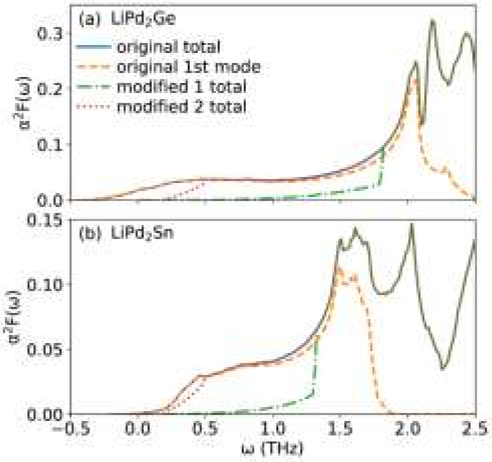

Figure S4. Original Eliashberg functions of LiPd$_2$Ge and LiPd$_2$Sn with a negative tails and modified ones used to approximate $\lambda_{\text{e-p}}$ and T_c.

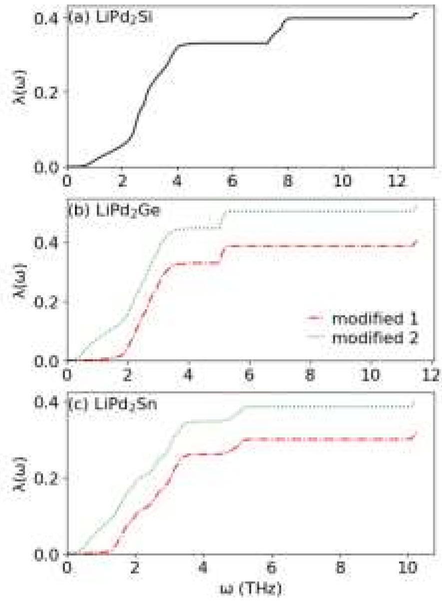

Figure S5. Cumulative electron phonon coupling constant of LiPd$_2$X.

Figure S6 shows comparison of the calculated constant-volume lattice specific heat C_v with the measured constant-pressure C_p. C_v is calculated as:

$$C_v = R\int_0^{\infty} F(\omega)\left(\frac{\hbar\omega}{k_B T}\right)^2 \frac{exp\left(\frac{\hbar\omega}{k_B T}\right)}{\left[exp\left(\frac{\hbar\omega}{k_B T}\right)-1\right]^2} d\omega, \tag{1}$$

where R is the gas constant and $F(\omega)$ is calculated phonon density of states. The calculated C_v at higher temperatures is smaller than experimental C_p, which is caused by the anharmonicity of the crystal:

$$C_p \approx C_v(1+\alpha\gamma_G T), \tag{2}$$

where γ_G is the Grüneisen parameter and α is the volume thermal expansion coefficient. Otherwise the agreement is good.

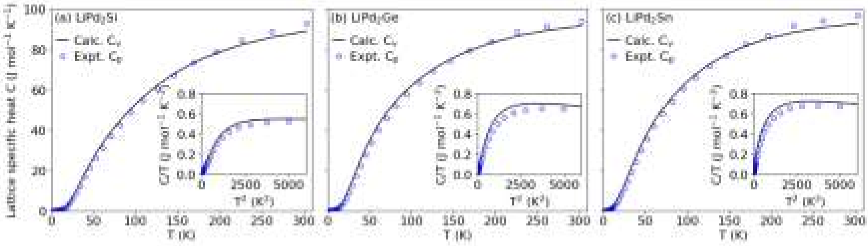

Figure S6. Calculated specific heat at constant volume and measured specific heat at constant pressure of $LiPd_2X$.

Heat capacity studies

Figure S7 presents field-dependent specific heat measurements performed in fields up to 30 Oe. The jump in specific heat at H = 5 Oe (the lowest applied H) is slightly higher than that at zero magnetic field, indicating a crossover from second- to the first-order phase transition, commonly seen in type-I superconductors.

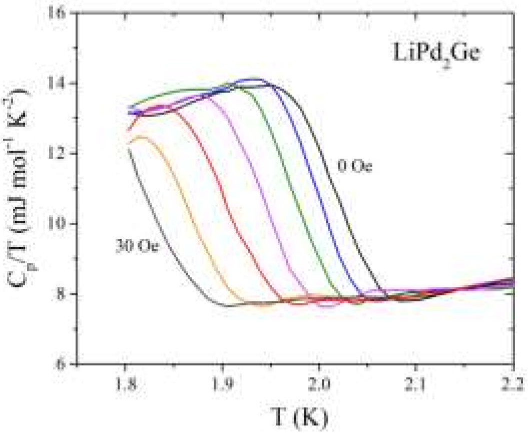

Figure S7. The dependence of the specific heat C_p on temperature in applied magnetic fields H up to 30 Oe.

Source material's DOI: https://doi.org/10.1103/PhysRevB.102.024507

4.5 (A5) Superconductivity in $LiGa_2Ir$ Heusler type compound with VEC = 16

4.5.1 Cel badawczy

Podobnie jak dla związków Heuslera opisanych w pracy A4, również dla $LiGa_2Ir$ brak jest danych eksperymentalnych nt. właściwości fizycznych, natomiast podany jest typ struktury, w którym materiał ten występuje i stała sieci krystalicznej *a*.

Jak wspomniano w rozdziale 2.2.3 liczba elektronów walencyjnych dla $LiGa_2Ir$ wynosi 16, co daje 4 elektrony na atom – wartość leżącą na początku drugiego maksimum zależności T_c od VEC/at. [33]. Postawiona **hipoteza badawcza 5** w przypadku tego projektu zakładała, że $LiGa_2Ir$ – podobnie jak jego izoelektronowy odpowiednik $LiGa_2Rh$ – będzie wykazywać zjawisko nadprzewodnictwa, z prawdopodobnie wyższą temperaturą krytyczną. Podmieniając Rh na Ir można spodziewać się silniejszego wpływu efektów relatywistycznych na strukturę elektronową oraz fononową.

Celem badań opisanych w publikacji A5 było otrzymanie czystej fazowo próbki związku typu Heuslera $LiGa_2Ir$ oraz eksperymentalne wyznaczenie parametrów charakteryzujących stan nadprzewodzący i normalny. Badania eksperymentalne obejmowały proszkową dyfrakcję rentgenowską, pomiary elektryczne, cieplne oraz magnetyczne. Szczegółowe badania właściwości fizycznych zostały uzupełnione obliczeniami struktury elektronowej oraz fononowej (mgr inż. Gabriel Kuderowicz, dr hab. inż. Bartłomiej Wiendlocha).

4.5.2 Opis rezultatów

Podobnie jak związki $LiPd_2X$, omawiany w tym rozdziale $LiGa_2Ir$ został otrzymany poprzez reakcję w fazie stałej utartego proszku prekursora $IrGa_2$ oraz kawałków litu. Zarówno ważenie jak i prasowanie pastylki wykonano w komorze rękawicowej wypełnionej argonem. Pastylka została owinięta w folię tantalową, której zadaniem była separacja od kwarcowej ampuły. Ampuła wraz z umieszczoną wewnątrz próbką została podłączona do systemu próżniowego, kilkukrotnie odpompowana i przepłukana czystym argonem (5N) i na koniec zamknięta z niewielką ilością argonu. Zastosowany program wygrzewania był taki sam jak użyty do syntezy $LiPd_2X$. Otrzymany materiał dokładnie utarto, sprasowano i ponownie wygrzewano w częściowo wypełnionej argonem ampule.

Proszkowa analiza dyfrakcyjna potwierdziła strukturę typu Heuslera dla $LiGa_2Ir$, a wyznaczona poprzez metodę LeBail'a stała sieci krystalicznej *a* = 6.0317(1) Å jest w dobrej zgodności z danymi literaturowymi [37] i tak jak oczekiwano - nieznacznie większa niż oszacowana dla izoelektronowego $LiGa_2Rh$ (*a* = 5.9997(8) Å) [39].

Przeprowadzone w pierwszej kolejności pomiary właściwości magnetycznych związku $LiGa_2Ir$ ujawniły przejście ze stanu normalnego w stan nadprzewodzący w T_c = 2.95 K, potwierdzając wysuniętą hipotezę o istnieniu izoelektronowego odpowiednika $LiGa_2Rh$ wykazującego nadprzewodnictwo. Słuszne okazało się również przepuszczenie dotyczące temperatury krytycznej – obserwowana T_c jest wyższa dla związku zawierającego Ir. Należy podkreślić, że zamiana Rh na Ir prowadziła do wzrostu temperatury krytycznej w innych izoelektronowych i izostrukturalnych związkach m.in. $SrRh_2$ vs. $SrIr_2$, $CaRh_2$ vs. $CaIr_2$ oraz IrGe vs. RhGe [65]. Efekt ten jest najpewniej związany z tym, że większa masa atomowa Ir, w porównaniu do masy atomowej Rh, prowadzi do zwiększenia parametru sprzężenia elektron – fonon, a w konsekwencji do wyższej T_c.

Pomiary namagnesowania w funkcji przyłożonego pola magnetycznego pozwoliły na sklasyfikowanie $LiGa_2Ir$ jako nadprzewodnika II-rodzaju. Oszacowana wartość dolnego pola krytycznego wynosi $H_{c1}(0)$ = 268 Oe i jest wyższa od wartości uzyskanych dla innych nadprzewodników w rodzinie Heuslerów, w tym $LiGa_2Rh$ ($H_{c1}(0)$ = 59 Oe [39]).

Badania właściwości transportowych i ciepła właściwego pozwoliły na wyznaczenie innych parametrów charakteryzujących nowy nadprzewodnik. Z niskotemperaturowych pomiarów ciepła właściwego wyznaczono T_c = 2.94 K oraz znormalizowany skok ciepła właściwego ($\Delta C/\gamma T_c$=1.40), potwierdzając objętościowy charakter nadprzewodnictwa w badanym materiale. Oszacowana wartość $\Delta C/\gamma T_c$ jest niemal identyczna z wartością oczekiwaną dla słabo sprzężonych nadprzewodników według teorii BCS ($\Delta C/\gamma T_c$ = 1.43). Parametr elektron-fonon, wyznaczony z odwróconego wzoru McMillana, wynosi λ_{ep} = 0.57, co sugeruje że $LiGa_2Ir$ jest słabo sprzężonym nadprzewodnikiem II-go rodzaju. Górne pole krytyczne ($\mu_0 H_{c2}(0)$ = 0.31(1) T) wyznaczono na podstawie analizy niskotemperaturowych pomiarów oporności elektrycznej w polu magnetycznym. Uzyskana wartość jest osiemnaście razy mniejsza od limitu Pauli'ego ($\mu_0 H^{Pauli}(0)$ =1.85 T_c = 5.4 T), co również wskazuje na słabo sprzężony nadprzewodnik. Na podstawie przeprowadzonych badań wyznaczono również: długość koherencji (ξ_{GL} = 322 Å), głębokość wnikania (λ_{GL} = 443 Å) oraz parametr Ginzburga-Landaua ($\kappa_{GL} = 1.38$). Niska wartość ostatniego parametru może sugerować, że $LiGa_2Ir$ jest na pograniczu nadprzewodnictwa I-go oraz II-go typu.

Teoretyczne obliczenia struktury elektronowej wskazują, że dominujący wkład do DOS(E) w okolicy poziomu energii Fermiego mają stany elektronowe pochodzące od elektronów 5*d* atomu Ir oraz 5*p* dwóch atomów Ga. Dla $LiGa_2Ir$ obliczenia teoretyczne nie wskazują na występowanie *miękkich modów* fononowych.

Praca A5 przedstawiona w niniejszej rozprawie doktorskiej jest wersją nieopublikowaną. W momencie składania doktoratu, akrykuł A5 znajdował się po pierwszej recenzji w Scientific Reports.

4.5.3 Treść artykułu A5

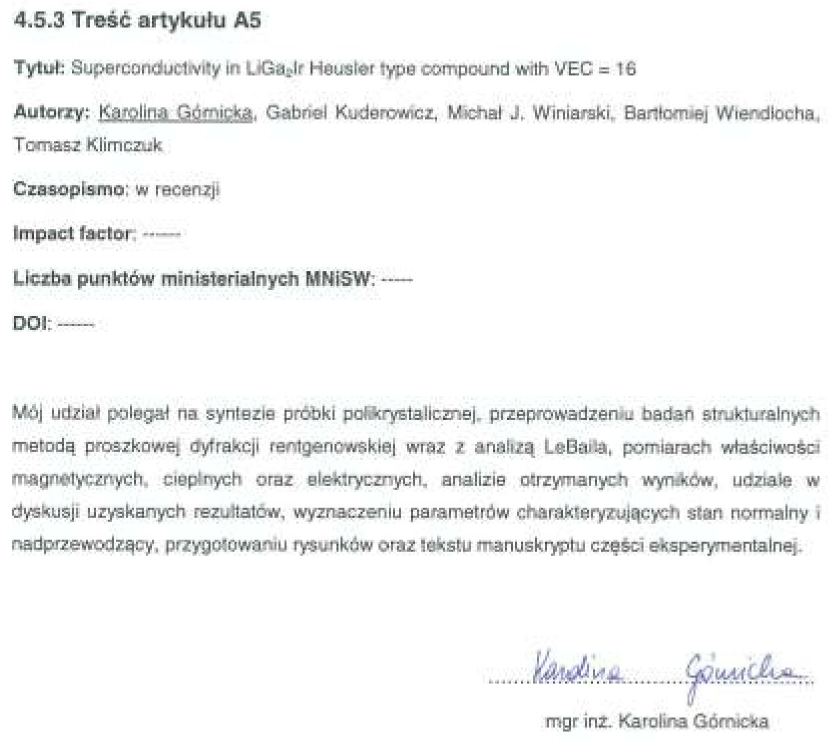

4.5.3 Treść artykułu A5

Tytuł: Superconductivity in $LiGa_2Ir$ Heusler type compound with VEC = 16

Autorzy: Karolina Górnicka, Gabriel Kuderowicz, Michał J. Winiarski, Bartłomiej Wiendlocha, Tomasz Klimczuk

Czasopismo: w recenzji

Impact factor: ------

Liczba punktów ministerialnych MNiSW: -----

DOI: ------

Mój udział polegał na syntezie próbki polikrystalicznej, przeprowadzeniu badań strukturalnych metodą proszkowej dyfrakcji rentgenowskiej wraz z analizą LeBaila, pomiarach właściwości magnetycznych, cieplnych oraz elektrycznych, analizie otrzymanych wyników, udziale w dyskusji uzyskanych rezultatów, wyznaczeniu parametrów charakteryzujących stan normalny i nadprzewodzący, przygotowaniu rysunków oraz tekstu manuskryptu części eksperymentalnej.

Karolina Górnicka

mgr inż. Karolina Górnicka

Superconductivity in $LiGa_2Ir$ Heusler type compound with VEC = 16

Karolina Górnicka[1,2], Gabriel Kuderowicz[3],Michał J. Winiarski[1,2], Bartłomiej Wiendlocha[3] and
Tomasz Klimczuk[1,2]

[1] Faculty of Applied Physics and Mathematics, Gdansk University of Technology,
ul. Narutowicza 11/12, 80-233 Gdańsk, Poland,
[2]Advanced Materials Centre, Gdansk University of Technology,
ul. Narutowicza 11/12, 80-233 Gdańsk, Poland,
[3] Faculty of Physics and Applied Computer Science, AGH University of Science and Technology,
Aleja Mickiewicza 30, 30-059 Kraków, Poland

Abstract

Polycrystalline $LiGa_2Ir$ has been prepared by a solid state reaction method. A LeBail refinement of powder x-ray diffraction data confirms a previously reported Heusler-type crystal structure (space group *Fm-3m*, No. 225) with lattice parameter a = 6.0317(1) Å. The normal and superconducting state properties were studied by magnetic susceptibility, heat capacity, and electrical resistivity techniques. A bulk superconductivity with T_c = 2.94 K was confirmed by detailed heat capacity studies. The measurements indicate that $LiGa_2Ir$ is a weak-coupling superconductor ($\lambda_{e-p} = 0.57$, $\Delta C/\gamma T_c = 1.4$) on the border between type-I and type-II superconductivity ($\kappa = 1.38$). Electronic structure, lattice dynamics, and the electron-phonon interaction are studied from first principles calculations. Ir and two Ga atoms equally contribute to the Fermi surface with a minor contribution from Li. The phonon spectrum contains separated high frequency Li modes, which are seen clearly as an Einstein-like contribution in the specific heat. The calculated electron-phonon coupling constant $\lambda_{e-p} = 0.68$ confirms the electron-phonon mechanism for the superconductivity. $LiGa_2Ir$ and recently reported isoelectronic $LiGa_2Rh$ are the only two known representatives of the Heusler superconductors with the valence electron count VEC = 16.

I. Introduction

With more than a thousand members reported in the literature, the Heusler family remains one of the most interesting and intensively studied intermetallic systems in materials science [1]. Among this class of materials we can find catalysts [2], ferromagnets [3,4], thermoelectric [5–7] and magnetocaloric materials [8]. Unwavering interest in this class of materials is also caused by the various properties and rich physics they offer, such as heavy fermion behavior [3,4,8–10], shape memory phenomena [11], magneto-optical [12] and magneto-structural [13] effects. Recently, the charge density wave and a quantum critical point were reported in $Lu(Pt_{1-x}Pd_x)_2In$ solid solution [14].

What seems to be special for Heusler compounds is that their physical properties can often be predicted just by simply counting the number of valence electrons. This valence electron count (VEC) is frequently used to classify different groups of Heuslers. For example, for VEC = 24 semimetallic behavior is expected [15] with vanishing net magnetic moment [16–22]. Adding three electrons to the system (VEC = 27) often reveals superconductivity, including the Heusler compounds containing magnetic rare earth metals, i.e. $TmPd_2Sn$ and $YbPd_2Sn$ [23]. It is worth noting that as many as 70% of known Heusler superconductors, including the T_c ~5 K record holder YPd_2Sn, have VEC 27 or 28 [24], the numbers corresponding to 6.5 and 6.75 electrons per atom – exactly at the third maximum of T_c proposed for metals by Matthias [25].

The prototype compound $MnCu_2Al$ was discovered in 1903 by Fritz Heusler and appeared to be a ferromagnet at room temperature. The crystal structure of Cu_2MnAl was first described more than 3 decades later by James Bradley [26]. The Heusler X_2YZ compounds form in a cubic space group Fm-3m (s.g. #225) with three occupied Wyckoff positions. The Y and Z atoms are usually the most and the least electronegative metals and they are located in the 4a (0, 0, 0) and 4b (½, ½, ½) sites. The X atoms occupy the 8c position (¼, ¼, ¼) and fill all the tetrahedral holes in the crystal structure. In this special crystallographic site, we can put a few transition metals from group 9, 10, and 11, as well as Li and Mg. However, there are 16 full-Heusler compounds reported with Al, Ga, and In in the 8c site and except UAl_2Cu and $MnGa_2Co$, all of them contain Li. In one of these compounds, $LiGa_2Rh$, we recently reported superconductivity [27]. In this paper, we present details of a synthesis process and superconducting properties of the isoelectronic compound – $LiGa_2Ir$. This material was obtained by an ordinary solid state reaction without using a Ta tube at rather low synthesis temperature. The observed bulk superconductivity (T_c = 2.94 K) was confirmed by the heat capacity, resistivity, and magnetic susceptibility measurements. Theoretical calculations based on Density Functional Theory (DFT) were performed to study its electronic structure, lattice dynamics, and the electron-phonon interaction and allow us to conclude on the electron-phonon mechanism of superconductivity.

II. Experimental and computational methods

The polycrystalline $LiGa_2Ir$ sample was prepared by conventional solid-state reaction. The starting elements were high-purity Li chunks (4N, Alfa Aesar), Ir powder (3N8, Mennica-Metale, Poland), and Ga pieces (3N, Alfa Aesar). First, the precursor of $IrGa_2$ taken in a 1:2 molar ratio was placed in an alumina crucible, sealed inside evacuated silica tubes, and annealed at 700℃ overnight. The as-prepared material was thoroughly ground, mixed with Li chunks with 10% excess to compensate for the loss of some Li during the synthesis, and pressed into a pellet using a hydraulic press. Complete sample preparation was performed in an argon-filled glove box system [$p(O_2) < 0.5$ ppm]. The pellet was then placed in a tantalum crucible in a sealed quartz tube under a partial atmosphere of Ar gas. The tube was heated to 240 °C at a rate of 2.5 °C/h and then heated to 550 °C (10°C/h), held at that temperature for 6 h, and air quenched to room temperature. The as-prepared material was reground well and once more pressed into a pellet. Finally, the samples were sealed in quartz tubes and annealed at 650°C for 3 days. The resulting materials formed a soft, brown pellet. The compound, although Li-containing, is stable in air over time and therefore was handled outside of the glovebox for all performed experiments.

Powder x-ray diffraction (pXRD) measurements were performed at room temperature using Cu Kα radiation (λ = 1.5406 Å) on a Bruker D2 Phaser diffractometer with a LynxEye-XE detector. Structure refinement from pXRD data was performed using the LeBail analysis method within the TOPAS code [ref]. The magnetization measurements were carried out using a Quantum Design Evercool II Physical Property Measurement System (PPMS) with a Vibrating Sample Magnetometer (VSM) function. The data were collected in the temperature range 1.95–3.2 K under various applied magnetic fields. All thermodynamic and transport measurements were also performed in a PPMS Evercool II system. The heat capacity was measured using the two-τ time-relaxation method in the temperature range 1.85-300 K. Flat, polished, circular samples of around 15 mg were fixed with Apiezon N grease on the α-Al_2O_3 measurement platform. The ac electrical resistivity measurements in a temperature range from 1.8 to 300 K were carried out using the standard four-probe method in magnetic fields up to H = 1400 Oe (μ_0H = 0.14 T). Platinum wires were attached to the surface of the bar-shaped polycrystalline samples using conductive silver epoxy (Epotek H20E). High pressure magnetization measurements were performed using a copper-beryllium bronze, VSM-compatible piston cylinder cell manufactured by HMD. Daphne 7373 oil was used as a pressure transmitting medium. A 15 mg sample was packed together with a small piece of high purity lead wire which was employed as a manometer. For calculating the actual cell pressure the pressure coefficient of the critical temperature for Pb was taken from ref. [28]. Measurements were performed at an applied field of 10 Oe in ZFC conditions.

Ab initio computations were performed for $LiGa_2Ir$ using density functional theory and Migdal-Eliashberg theory implemented in Quantum Espresso [29–31]. We calculated the electronic structure, phonons and electron-phonon interaction functions. Projector augmented wave pseudopotentials [32,33] and PBEsol exchange-correlation functional [34] were chosen. Energy cutoffs of wavefunctions and charge densities were set to 100 Ry and 1000 Ry, respectively. A 12^3 k-point Monkhorst-Pack mesh was used for self-consistent calculations, whereas the electronic density of states (DOS) and Fermi surface were calculated on 24^3 grid. Interatomic force constants were calculated on a 6^3 q-point grid which corresponds to 16 independent q-points in this cubic structure.

III. Results and discussion

A. Experimental studies

Fig.1 presents the pXRD pattern and results of the LeBail analysis for the synthesized $LiGa_2Ir$. The pXRD analysis indicates an excellent quality of the examined sample and the refinement confirms that the compound crystallizes in the cubic *L2₁* crystal structure (space group *Fm-3m*, No. 225). A difference plot (between experimental and fitted data) and the Bragg positions are also shown in Fig. 1. The refined lattice parameter a = 6.0317(1) Å is in a good agreement with the previously reported for $LiGa_2Ir$ [35,36] and slightly larger than refined for $LiGa_2Rh$ (a = 5.9997(8) Å) [27].

To characterize the superconducting transition of $LiGa_2Ir$, we have measured the temperature dependence of the volume magnetic susceptibility, defined as $\chi = M/H$ where M is the magnetization and H is the applied magnetic field, with zero-field-cooled (ZFC) and field-cooled (FC) scan modes under H = 10 Oe. As shown in the main panel of Fig.2(a), the raw data were scaled by 4π and corrected for the demagnetizing effect $-4\pi\chi_V = 1/(1-N)$, where the demagnetizing factor N is 0.58 (estimated from the $M_V(H)$ fit discussed later). A diamagnetic transition, corresponding to the onset of superconductivity, appears at T_c = 2.95 K, where the superconducting transition temperature (T_c) was estimated as the point at which the line set by the steepest slope of the superconducting signal in the zero-field cooled data set intersects with the extrapolation of the normal-state magnetic susceptibility [37]. The shielding volume fraction at 1.95 K is ~100%, showing that the sample acted as a bulk superconductor. Compared with the ZFC data, the observed FC signal is much weaker, which is typical for polycrystalline samples. In the inset of Fig.2(a), the low-field parts of the dc magnetization isotherms measured at various temperatures (from 1.9 to 2.8 K) are presented. For each temperature, the experimental data obtained in small magnetic fields were fitted using the proportionality $M_{fit} = -\alpha H$, appropriate for a full shielding effect. Assuming that the initial response to the magnetic field is perfectly diamagnetic, the demagnetization factor N = 0.58 was found. The N value is fairly consistent with the expected (theoretical) N_z value derived for a circular cylinder sample with the height to radius ratio of approx. 0.5 [38]. The value of the lower critical field H_{c1}^{*} at each temperature is defined as the point of deviation from the full Meissner effect of the data curve. Following the methodology described elsewhere [39], this point was precisely calculated. The H_{c1}^{*} values with the corresponding temperatures are shown in the main panel of Fig.2(b). At T = 1.9 K,

H^*_{c1} is 68 Oe and decreases monotonically with an increase in temperature, to 10 Oe at T = 2.8 K. The data points were analyzed with the equation:

$$H^*_{c1}(T) = H^*_{c1}(0)\left[1 - \left(\frac{T}{T_c}\right)^2\right], \tag{1}$$

where $H^*_{c1}(0)$ is the critical field at 0 K and T_c is the superconducting critical temperature. Our experimental data are well described with the above formula and the fit (red solid line) gives $H^*_{c1}(0)$ = 113(3) Oe and T_c = 3.03(3) K. Taking into account the demagnetization factor (N = 0.58) derived above, the lower critical field value is H_{c1} = 268 Oe ($H_{c1} = H^*_{c1}/(1\text{-}N)$). The value obtained is slightly larger with these reported for the other full-Heuslers compounds [24,27]. The inset in Fig.2(b) depicts the full magnetization loop versus applied magnetic field collected in the superconducting state at 1.9 K. It is evident that $LiGa_2Ir$ exhibits conventional type-II superconductivity.

Heat capacity measurements measuring the entropy changes during the superconducting transition are reliable evidence of the presence of bulk superconductivity. Fig.3(a) shows a closer view of the superconducting transition under zero magnetic field for $LiGa_2Ir$ plotted as C_p/T versus T. The sharp anomaly displayed in the specific heat data confirms bulk superconductivity and the good quality of the sample. From the graphical equal-area construction (green solid lines), which reflects conserving entropy, the estimated critical temperature is equal to 2.94 K, consistent with the value determined from magnetic susceptibility measurements. The so-determined specific heat jump at T_c is found to be about $\Delta C/T_c$ = 7.7 mJ $mol^{-1}K^{-2}$. Fig.3(b) illustrates the heat capacity data plotted as C_p/T versus T^2, under an external magnetic field of 0.15 T. In the normal state, the experimental data can be fitted using the formula $C_p/T = \gamma + \beta T^2 + \delta T^4$, where the first term is the electronic specific heat coefficient and the second and third terms are attributed to the lattice contributions to the heat capacity (the δT^5 term in the heat capacity was added after analyzing the computed phonon spectrum, discussed below). The extrapolation, represented by the red solid line, gives γ = 5.5(1) mJ $mol^{-1}K^{-2}$, β = 0.366(1) mJ $mol^{-1}K^{-4}$ and δ = 0.0052(3) mJ $mol^{-1}K^{-6}$. In a simple Debye model for the phonon contribution, the β coefficient is related to the Debye temperature Θ_D through $\Theta_D = \left(\frac{12\pi^4}{5\beta} nR\right)^{1/3}$, where R = 8.31 J $mol^{-1}K^{-1}$ and n = 4 for $LiGa_2Ir$. The resulting value of Θ_D is 277(1) K, which is significantly smaller than the Debye temperature for Rh analog $LiGa_2Rh$ (Θ_D = 320 K [27]). Using the previously derived specific heat jump at T_c and the Sommerfeld coefficient (γ = 5.5(1) mJ $mol^{-1}K^{-2}$), the ratio $\Delta C/\gamma T_c$ = 1.40 can be calculated. The calculated value is almost equal to the BCS value of 1.43, suggesting that $LiGa_2Ir$ is a weakly coupled superconductor and is close to that of $LiGa_2Rh$ ($\Delta C/\gamma T_c$ = 1.48 [27]).

With the Debye temperature available, the electron-phonon coupling constant λ_{e-p} can be estimated from the McMillan's equation [40]:

$$\lambda_{e-p} = \frac{1.04 + \mu^* \ln(\Theta_D/1.45T_c)}{(1 - 0.62\,\mu^*)\ln(\Theta_D/1.45T_c) - 1.04} \tag{2}$$

where $\mu*$ is the repulsive screened Coulomb part, usually set to $\mu* = 0.13$ for intermetallic superconductors [24,41]. Taking $T_c = 2.94$ K and $\Theta_D = 277$ K, the calculated λ_{e-p} is 0.57, implying that $LiGa_2Ir$ is weakly coupled BCS superconductor.

The main panel of Fig.4(a) presents the electrical resistivity for $LiGa_2Ir$, $\rho(T)$, as a function of temperature in the range 1.8 – 300 K without the application of an external magnetic field. In the normal state, the resistivity reveals a metallic behavior ($d\rho/dT > 0$), although the residual resistivity ratio RRR = $\rho(300K)/\rho(5K) = 2.1$ is rather small. That feature can be attributed to the polycrystalline nature of the sample investigated that probably contained many macroscopic defects. The obtained value is comparable to those reported for full-Heusler compounds [24]. The resistivity undergoes a sudden drop at 2.96 K, that perfectly agrees with the T_c obtained from magnetic and heat capacity measurements. The inset of Fig.4(a) emphasizes the low-temperature resistivity under various magnetic fields from 0 to 1400 Oe. As expected, the superconducting transition becomes slightly broader and the T_c shifts to a lower temperature as the applied magnetic field is increased. Using the criterion that the point with 50% normal state resistivity (ρ_0) is the transition temperature, we determined the upper critical field $\mu_0H_{c2}(T)$ for $LiGa_2Ir$ at various temperatures (Fig.4(b)). The solid line is a fit to the Ginzburg–Landau expression [42]:

$$\mu_0 H_{c2}(T) = \mu_0 H_{c2}(0)\frac{(1-t^2)}{(1+t^2)} \tag{3}$$

where $t = T/T_c$ and T_c is the transition temperature at zero magnetic field. Equation (3) describes the experimental data well, and yields $\mu_0H_{c2}(0) = 0.31(1)$ T. The Pauli limiting field within the BCS theory for a weak electron-phonon coupling [43,44] gives $H_{c2}^{p}(0) = 1.85\ T_c = 5.4$ T, which is eighteen times larger than estimated upper critical field value for $LiGa_2Ir$. An identical value of $\mu_0H_{c2}(0)$ has been reported for isostructural and isoelectronic $LiGa_2Rh$ superconductor [27]. Consequently, assuming that the upper critical field is purely orbital, using the GL formula $H_{c2} = \frac{\Phi_0}{2\pi\xi_{GL}^2}$ where $\Phi_0 = hc/2e$ is the flux quantum, the superconducting coherence length is calculated to be $\xi_{GL} = 322$ Å. Similarly, from the relation $H_{c1} = \frac{\Phi_0}{4\pi\lambda_{GL}^2}\ln\frac{\lambda_{GL}}{\xi_{GL}}$, a superconducting penetration depth $\lambda_{GL}(0) = 443$ Å is found for $LiGa_2Ir$. The GL parameter $\kappa_{GL} = \lambda_{GL}/\xi_{GL}$ can then be estimated as $\kappa_{GL} = 1.38 > 1/\sqrt{2}$, confirming the type-II nature of the superconductivity. Finally, the thermodynamic critical field can be obtained from κ_{GL}, H_{c1} and H_{c2} using the formula $H_{c1}H_{c2} = H_c^2 \ln \kappa_{GL}$. The resulting value of H_c is 1633 Oe ($\mu_0H_c = 0.16$ T).

With the Sommerfeld coefficient γ and the electron-phonon coupling parameter λ_{e-p} known, the non-interacting density of states at the Fermi level $N(E_F)$ can be calculated using the formula:

$$N\,(E_F) = \frac{3\gamma}{\pi^2 k_B^2\left(1+\lambda_{e-p}\right)}, \tag{4}$$

where k_B is the Boltzmann constant. For $LiGa_2Ir$, $N(E_F)$ is estimated to be 1.49 states eV^{-1} per formula unit (f.u.).

Pressure dependence of the T_c for $LiGa_2Ir$ is shown in Fig.5. $LiGa_2Ir$ shows an exceptionally low pressure coefficient compared to other Heusler compounds for which high-pressure studies were reported [24,45,46]. It is however worth noting that all of the compounds reported to date are Pd-based systems with a valence electron count of 27 per f.u. As in the case of RPd_2Z (R=Sc, Y, Tm, Yb, Lu and Z=Sn, Pb) [46] and $HfPd_2Al$ [24] the suppression of T_c by high pressure likely stems from the stiffening of the lattice, yet in the case of $LiGa_2Ir$ the effect is much weaker.

B. Theoretical calculations

First, the unit cell was relaxed with the Broyden-Fletcher-Goldfarb-Shanno algorithm starting from the experimental lattice constant. Atomic positions were fixed by the symmetry constraints of the full-Heusler structure. The relaxation was repeated including spin-orbit coupling (SOC) because the effect might be important due to the presence of a heavy Ir atom. For calculations with SOC, the scalar-relativistic pseudopotential of Ga and Ir were replaced with the full-relativistic ones. The obtained relaxed lattice constants are in a very good agreement with the experimental one, and SOC was found to have a negligible effect on the lattice constant.

Fig.6 shows the electronic dispersion relations and total DOS. Three bands cross the Fermi level forming three Fermi surface sheets visualized using XCrysDen [47] in Fig.7. SOC has a small effect on the electronic bands and DOS near the Fermi energy (E_F), however much stronger SOC effects are seen for electronic states with energies below E_F, like an anticrossing of bands in the Γ-K direction around -1.5 eV. The total and partial DOS for each atom in $LiGa_2Ir$ are shown in Fig.8. States near E_F are built mainly from Ga-4*p* and Ir-5*d* orbitals, whereas the contribution to the DOS(E_F) from Li is negligible. Interestingly, the Fermi level is located in the local minimum of the DOS(E), formed from a superposition of a decreasing DOS of Ir and increasing DOS of Ga. From the calculated DOS(E_F) values, slightly increased in the relativistic case (see Table III) , the bandstructure value of the Sommerfeld electronic specific heat coefficient is calculated, $\gamma_{band} = \frac{\pi^2}{3} k_B^2 DOS(E_F)$, and used to estimate the electron-phonon coupling parameter as $\gamma_{expt} = \gamma_{band}(1 + \lambda_\gamma)$. This results in $\lambda_\gamma = 0.48$, a slight underestimate when comparing to $\lambda_{e-p} = 0.57$ obtained from T_c using McMillan's formula.

Phonon dispersion relations $\omega(\mathbf{q})$ and phonon density of states $F(\omega)$ of $LiGa_2Ir$ with atomic contributions are shown in Fig.9. Modes associated with different atoms are well separated because of large differences in mass (M_{Li}=6.94u, M_{Ga}=69.72u, M_{Ir}=192.22u). Three optic modes of Li form an Einstein-like peak in $F(\omega)$ around 11 THz, a much higher frequency than the Ga, and Ir-dominated parts of the phonon spectrum. The acoustic part is mostly contributed by the heaviest Ir vibrations. Although SOC had a small effect on the electronic DOS(E_F), it affected phonons, slightly pushing the Ir branches towards higher frequencies and visibly lowering the Ga and Li frequencies. This is shown in Table IV, where the average phonon frequencies are collected. The global effect of SOC is a small decrease in the average frequency, from 5.77 THz to 5.75 THz.

Looking again at the phonon dispersion relations, we notice the presence of a small dip in the first acoustic branch in the Γ-K direction. Such an anomaly is frequent in Heusler compounds, and was already reported in $HfPd_2Al$ [48], $LiGa_2Rh$ [49] or $LiPd_2X$ (X = Si, Ge, Sn) [50], where in the last case it evolved into a soft mode with an imaginary frequency for X = Ge and Sn. As our ongoing investigation of the $LiPd_2Ge$ case showed [50], this may be related to the anharmonic features of the crystal potential.

The theoretical phonon spectrum allows us to analyze the lattice specific heat in more detail. The constant volume C_v is computed directly from the phonon density of states $F(\omega)$ as:

$$C_v = R\int_0^\infty F(\omega)\left(\frac{\hbar\omega}{k_BT}\right)^2 \frac{exp\left(\frac{\hbar\omega}{k_BT}\right)}{\left[exp\left(\frac{\hbar\omega}{k_BT}\right)-1\right]^2}d\omega. \tag{5}$$

The computed curve (red line) is compared to the measured constant pressure C_p data (open circles) in Fig. 10, where we notice a good overall agreement.

If one wishes to describe the heat capacity using an approximate model, a combination of Debye and Einstein terms ($C_{Debye} + C_{Einstein}$) should be considered:

$$C_{Debye}(T) = 3n_DR\left(\frac{T}{\Theta_D}\right)^3\int_0^{\frac{\Theta_D}{T}}\frac{x^4exp(x)}{[exp(x)-1]^2}dx, \tag{6}$$

$$C_{Einstein}(T) = n_ER\left(\frac{\Theta_E}{T}\right)^2 exp\left(\frac{\Theta_E}{T}\right)\left[exp\left(\frac{\Theta_E}{T}\right)-1\right]^{-2}, \tag{7}$$

where n_D and n_E are the number of phonon modes treated as Debye and Einstein type, respectively. Looking at the phonon DOS in Fig. 9 we see that the three high-frequency Li modes may be described as an Einstein term with the average frequency corresponding to about 540 K, whereas the remaining part, containing nine Ir and Ga modes, could be roughly approximated by the Debye spectrum. Hence, we assume $n_D = 9$ and $n_E = 3$ and we use only two fitting parameters: the Debye and Einstein temperatures. The fit in the temperature range 1.8 K – 200 K gave the values $\Theta_D = 242(1)$ K and $\Theta_E = 550(10)$ K. Contributions from each of these terms are shown in Fig. 10 and the combined heat capacity describes the experimental data reasonably well. Deviations are seen in the lower temperature range due to the non-Debye-like phonon spectrum, captured accurately in the direct calculation using Eq. (5). Note that the low-temperature fit, described before, yielded a larger value of $\Theta_D = 277$ K as the whole heat capacity was ascribed to the Debye-like phonon spectrum (n = 4 in eq. $\Theta_D = \left(\frac{12\pi^4}{5\beta}nR\right)^{1/3}$ corresponds to 12 phonon modes, 3 per each of the atom). Since the Einstein term in our case gives no contribution to the specific heat at low temperatures, adopting to the combined model (i.e. changing to n = 3) we get $\Theta_D = 252$ K, very close to the value obtained from the fit for the broad temperature range.

Moving on to the electron-phonon interactions, the magnitude of the electron-phonon interaction for a given phonon branch is represented in Fig. 11 by the phonon linewidth $\gamma_{\boldsymbol{q}\nu}$ which is computed from the electron-phonon interaction matrix elements $g_{\boldsymbol{q}\nu}$ as [51–53]:

$$\gamma_{\boldsymbol{q}\nu} = 2\pi\omega_{\boldsymbol{q}\nu} \sum_{ij} \int \frac{d^3k}{\Omega_{BZ}} \left| g_{\boldsymbol{q}\nu}(\boldsymbol{k}, i, j) \right|^2 \delta\left(E_{\boldsymbol{q},i} - E_F\right) \delta\left(E_{\boldsymbol{k}+\boldsymbol{q},j} - E_F\right), \tag{8}$$

where

$$g_{\boldsymbol{q}\nu}(\boldsymbol{k}, i, j) = \sum_s \left(\frac{\hbar}{2M_s\omega_{\boldsymbol{q}\nu}}\right)^{1/2} \left\langle \psi_{i,\boldsymbol{k}} \left| \frac{dV_{scf}}{d\hat{u}_{\nu,s}} \cdot \hat{e}_\nu \right| \psi_{j,\boldsymbol{k}+\boldsymbol{q}} \right\rangle. \tag{9}$$

In the formulas above, $\omega_{\boldsymbol{q}\nu}$ is the phonon frequency at the wavevector **q** for the mode ν, M_s is mass of atom s, $\psi_{i,\boldsymbol{k}}$ is an electron wavefunction for a given band i and wavevector $\boldsymbol{k}$, $\hat{e}_\nu$ is a phonon polarization vector and $\frac{dV_{scf}}{d\hat{u}_{\nu,s}}$ is a change of the electronic potential due to a displacement of the atom s in the direction u.

The strongest electron-phonon interactions, seen as the largest phonon linewidths, are associated with the optic modes of Ga near 5 THz and the Einstein-like Li branch around 11 THz. Next, the electron-phonon interaction function $\alpha^2F(\omega)$ (Eliashberg function) is calculated by summing the contributions from each of the phonon branches, weighted by their inverse frequency:

$$\alpha^2F(\omega) = \frac{1}{2\pi N(E_F)} \sum_{\boldsymbol{q}\nu} \delta\left(\omega - \omega_{\boldsymbol{q}\nu}\right) \frac{\gamma_{\boldsymbol{q}\nu}}{\hbar\omega_{\boldsymbol{q}\nu}}. \tag{10}$$

$\alpha^2F(\omega)$ is plotted in Fig. 11 and has three peaks associated with enhanced electron-phonon interactions: at 1.78 THz, 5.22 THz, and 11.49 THz . The first peak is associated with acoustic Ir vibrations, having moderate phonon linewidths but low frequencies, effectively increasing the Eliashberg function. The second and third maxima are associated with the above-mentioned Ga and Li branches. Comparing $\alpha^2F(\omega)$ with the phonon DOS function F(ω) (see also Fig. 11) we see, that the Eliashberg function is enhanced over the phonon DOS at lower frequencies, and as a consequence the height of all three $\alpha^2F(\omega)$ maxima become comparable.

The overall electron-phonon coupling parameter λ is calculated from the Eliashberg function:

$$\lambda = 2\int_0^{\omega_{max}} \frac{\alpha^2F(\omega)}{\omega} d\omega, \tag{11}$$

and reaches λ = 0.68, slightly lowered by the spin-orbit coupling from the scalar-relativistic value of 0.70 (see Table IV). The frequency distribution of λ:

$$\lambda(\omega) = 2\int_0^{\omega} \frac{\alpha^2F(\omega\prime)}{\omega\prime} d\omega' \tag{12}$$

is plotted in Fig. 12 and the mode contribution from all 12 phonon branches is displayed in Table V. The acoustic phonons contribute in approximately 72% to the electron-phonon coupling constant, therefore, Ir vibrations are the most important factor in the superconductivity of $LiGa_2Ir$.

The superconducting critical temperature T_c is calculated using the Allen-Dynes formula [54]:

$$T_c = \frac{\left\langle \omega_{log}^{\alpha^2 F} \right\rangle}{1.20} \exp\left[\frac{-1.04(1+\lambda)}{\lambda-\mu^*(1+0.62\lambda)}\right], \qquad (13)$$

where

$$\left\langle \omega_{log}^{\alpha^2 F} \right\rangle = exp\left(\int_0^{\omega_{max}} \alpha^2 F(\omega) ln(\omega) \frac{d\omega}{\omega} / \int_0^{\omega_{max}} \alpha^2 F(\omega) \frac{d\omega}{\omega}\right). \qquad (14)$$

Taking the standard value of the Coulomb screening parameter μ^*=0.13, the calculated value T_c = 2.85 K is in a very good agreement with the experimental value of 2.95 K. The experimental T_c is exactly reproduced using an only slightly smaller μ^* = 0.121. The spin-orbit coupling has a small effect on the calculated critical temperature, slightly decreasing its value to T_c = 2.69 K. The agreement between calculations and experiment clearly confirms that superconductivity in $LiGa_2Ir$ is mediated by phonons.

To investigate exceptionally low decrease of T_c with pressure we have calculated electronic structure and lattice dynamics under the pressure of 1 GPa. All further calculations were done including SOC. The lattice constant relaxed under 1 GPa is a = 6.0021 Å. Electronic structure was almost unchanged, with only slight decrease of DOS(E_F) by 0.016 eV^{-1} (see Tab. III). Moreover, only small changes were induced by the pressure in the phonon dispersion relations and in the electron-phonon coupling. Small effect of the lattice stiffening under the external pressure is observed in phonon dispersion relations shown in Fig. 13, where Ga and Li modes moved towards higher frequencies, but modes of heaviest Ir changed only slightly. The small dip in the acoustic mode at Γ-K was not affected either. Average phonon frequencies, electron-phonon coupling constant and critical temperature are collected in Tab. IV. Assuming the same value of mu*, which reproduces the experimental Tc under ambient pressure, the obtained change of T_c is equal -0.048 K/GPa, which is in excellent agreement with the experiment.

To understand why the effect of pressure on T_c is so weak in $LiGa_2Ir$, comparing to other Heusler compounds, we have to compare the values of characteristic parameters which determine the response of superconductor to external pressure. In our analysis we will compare $LiGa_2Ir$ to $MgPd_2Sb$, for which we have recently found much stronger response to pressure: -0.23 K/GPa [45]. The most important parameter which determines the change of T_c with respect to pressure is the variation of the electron-phonon coupling constant λ, which in the case of $LiGa_2Ir$ drops from 0.6754 to 0.6708 at p = 1 GPa. On the other hand, in $MgPd_2Sb$ the change is stronger as λ decreases from 0.611 to 0.582. As $\lambda \propto \frac{\gamma_{qv}}{\omega_{qv}{}^2}$ (see equations 6-9) is composed of two factors, the frequency-independent electronic contribution expressed by phonon linewidths $\gamma_{\boldsymbol{qv}}$ and the phonon frequency $\omega_{\boldsymbol{qv}}$, we may analyze what is the origin of such differences. To do so, we calculate the first moment of Eliashberg function [40]:

$$I = \int_0^{\omega_{max}} \omega \, \alpha^2 F(\omega) \, d\omega. \tag{15}$$

This quantity is frequency-independent because:

$$\begin{aligned} I &= \frac{1}{2\pi\hbar N(E_F)} \int_0^{\omega_{max}} d\omega \sum_{\boldsymbol{q}\nu} \delta(\omega - \omega_{\boldsymbol{q}\nu}) \gamma_{\boldsymbol{q}\nu} = \\ &= \frac{1}{2\pi\hbar N(E_F)} \int_0^{\omega_{max}} d\omega \sum_{\boldsymbol{q}\nu} \delta(\omega - \omega_{\boldsymbol{q}\nu}) \sum_s \frac{1}{2M_s} \times \\ &\times \int \frac{d^3k}{\Omega_{BZ}} \left| \left\langle \psi_{i,\boldsymbol{k+q}} \right| \frac{dV_{scf}}{d\hat{u}_{\nu s}} \cdot \hat{e}_{\nu s} \left| \psi_{j,\boldsymbol{k}} \right\rangle \right|^2 \delta(E_{\boldsymbol{k},i} - E_F) \delta(E_{\boldsymbol{k+q},j} - E_F). \end{aligned} \tag{16}$$

At 0 and 1 GPa the first moment of Eliashberg function is equal respectively: 4.144 THz^2, 4.217 THz^2 in LiGa$_2$Ir and 1.869 THz^2, 1.890 THz^2 in MgPd$_2$Sb. Thus the changes in I are +1.8% in LiGa$_2$Ir and + 1.12% in MgPd$_2$Sb. As far as the electronic part of λ is concerned, stronger increase in the electronic contribution in the case of LiGa$_2$Ir is found.

Much larger difference is found in the change of the "average square phonon frequency" defined as

$$< \omega^2 >= \int_0^{\omega_{max}} \omega \alpha^2 F(\omega) d\omega \; / \left(\int_0^{\omega_{max}} \frac{\alpha^2 F(\omega)}{\omega} d\omega \right) \tag{17}$$

With such definition $\lambda = 2I / < \omega^2 >$ and in the case of a weak frequency dependent electron-phonon interaction $< \omega^2 >$ is close to similar quantity determined from the pure phonon DOS [40]. For LiGa$_2$Ir we get 12.273 THz^2 (0 GPa) and 12.574 THz^2 (1 GPa), i.e. 2.4% increase. On the other hand, for MgPd$_2$Sb we have 6.116 THz^2 (0 GPa) and 6.491 THz^2 (1 GPa), which is 6.13% increase. When analogical quantities are computed from the pure phonon DOS, the increases are 2.6% for LiGa$_2$Ir and 5.5% for MgPd$_2$Sb, confirming the trend. Thus, the effect of lattice stiffening takes over the increase in electronic contribution to electron-phonon coupling constant in both materials, explaining the decrease of λ with pressure. The much weaker effect on λ in LiGa$_2$Ir is explained by stronger increase in the electronic contribution (parameter I) accompanied by the smaller increase in the average square phonon frequency, while compared to MgPd$_2$Sb.

Two other global parameters are important in determining the pressure evolution of T$_c$. In the McMillan or Allen-Dynes formulas for T$_c$ we have $T_c \propto \omega_c$, with ω_c being the characteristic phonon frequency ($\langle \omega_{log}^{\alpha^2 F} \rangle$ in the Allen-Dynes formula and Θ_D in McMillan formula). The evolution of the exponential part of T$_c$ equation is governed by the evolution of λ, discussed above, thus we should also take a look on how the multiplicator in T$_c$ formula is affected by pressure. The more intuitive picture is provided by the McMillan formula, thus calculating the pressure derivative of Debye temperature we get:

$$\frac{\partial \ln \Theta_D}{\partial dp} = \frac{1}{B} \frac{\partial \ln \Theta_D}{\partial \ln V} = \frac{\gamma_G}{B}, \tag{18}$$

γ_G is the average Grüneisen parameter:

$$\gamma_G = -\frac{d\ln < \omega >}{d\ln V} \approx \frac{d\ln \Theta_D}{d\ln V}, \tag{19}$$

and B is the bulk modulus defined by the approximate pressure-volume relation $v = v_0 \exp(-P/B)$ which holds in the small pressure ranges where the variation in bulk modulus with pressure can be neglected. In our case we fitted this relation in the pressure range 0-5 GPa obtaining B = 151(2) GPa (see Fig. 14(b)) for $LiGa_2Ir$ and 118(2) GPa in $MgPd_2Sb$, whereas the average Grüneisen parameter is 1.9 in $LiGa_2Ir$ compared to 2.7 in $MgPd_2Sb$. The larger B, along with the smaller γ_G additionally lower the pressure dependence of T_c in $LiGa_2Ir$, compared to $MgPd_2Sb$ and other Heusler compounds.

To complete the analysis of bulk modulus for $LiGa_2Ir$ we have fitted p(V) relation using the Birch-Murnaghan equation of state [55]:

$$p(V) = 3B_0 f(1+2f)^{5/2}\left[1 + \tfrac{3}{2}(B_0' - 4)f\right], \tag{20}$$

where

$$f = \tfrac{1}{2}\left[\left(\tfrac{V_0}{V}\right)^{2/3} - 1\right]. \tag{21}$$

Pressure volume relation was obtained by relaxing cells up to 20 GPa with a 1 GPa step, whereby the starting lattice constant was the one calculated at p=0 GPa. Fitted equation of state and fit parameters with standard deviations are shown in Fig. 14(a). Bulk modulus B_0 equal 139 GPa is quite high and confirms $LiGa_2Ir$ resistance to pressure. Similarly calculated value for $MgPd_2Sb$ is 106 GPa, confirming the difference between the two compounds.

IV. Summary and conclusions

Most of the known Heusler-type superconductors have the valence electron number VEC = 27 or 28. $LiGa_2Ir$ is the second known superconductor in this family with VEC below 24, for which the semimetallic behavior is usually observed.

We have made high-quality polycrystalline $LiGa_2Ir$ using a solid state reaction method. $LiGa_2Ir$ forms in a full-Heusler crystal structure type with a refined lattice parameter a = 6.0317(1) Å, in agreement with that reported by Czybulka, et al. in ref. [35,36]. The heat capacity, electrical resistivity, and magnetic susceptibility confirm the bulk superconductivity with T_c = 2.94 K. Analysis of our data shows that $LiGa_2Ir$ is a weak-coupling superconductor ($\lambda_{e\text{-}p}$= 0.57 from the McMillan formula, $\Delta C/\gamma T_c$ = 1.4) on the border between type-I and type-II superconductivity (κ = 1.38). Theoretical calculations show that 5d states of Ir and 4p states of Ga equally contribute to the Fermi surface, which consists of three sheets. Although the compound contains heavy Ir, the spin-orbit coupling does not modify the electronic structure near the Fermi level, with the influence only visible for the deeper-lying electronic states. In the phonon spectrum we may distinguish three groups of modes, lined up according to the atomic mass: high-frequency Einstein-like optic Li vibrations, a medium-frequency group of mostly Ga optic modes and a low-frequency acoustic Ir part. The calculations of the Eliashberg function gave λ_{e-p}= 0.68 with the dominating contribution from the heaviest iridium. SOC slightly lowers the coupling constant, as the scalar-relativistic value is λ_{e-p}= 0.70. The computed superconducting critical temperature agrees very well with the measurements, confirming the phonon mechanism of superconductivity.

Comparing the superconducting properties of $LiGa_2Ir$ and $LiGa_2Rh$ (see Table I) we see that $LiGa_2Ir$ is another Ir-based superconductor with a T_c higher than that observed for the isostructural and isoelectronic compound containing Rh. The other examples are $SrRh_2$ vs. $SrIr_2$, $CaRh_2$ vs. $CaIr_2$, IrGe vs. RhGe [56]. This is caused by the larger electron-phonon coupling constants λ_{e-p} originating from the larger mass of Ir versus Rh. The heavier atom oscillates with lower frequency, thus the inverse proportionality of $\lambda_{e\text{-}p} \propto \frac{\gamma_{qv}}{\omega_{qv}{}^2}$ enhances λ_{e-p} if in both compounds the frequency-independent phonon linewidths γ_{qv} are similar.

The weak pressure dependence of T_c in $LiGa_2Ir$ originates from the large bulk modulus, relatively small Grüneisen parameter and compensating increase of the electronic contribution to the electron-phonon coupling constant.

Future studies and experimental effort to find other Heusler superconductors with the valence electron number 16 < VEC < 24 will be important in this regard.

Acknowledgments

Work at Gdansk Tech. was supported by the National Science Centre (Poland), grant number: UMO-2017/27/B/ST5/03044. Work at AGH-UST was supported by the National Science Centre (Poland), Project No. 2017/26/E/ST3/00119 and by an allocation of the computational time by PL-GRID infrastructure.

Table I. Experimental superconducting parameters of $LiGa_2T$ where T = Ir and Rh.

Parameter	**Unit**	**$LiGa_2Ir$**	**$LiGa_2Rh$**
T_c	K	2.94	2.4
$\mu_0H_{c1}(0)$	mT	26.8	5.9
$\mu_0H_{c2}(0)$	T	0.31	0.31
μ_0H^{Pauli}	T	5.4	4.4
ξ_{GL}	Å	322	326
λ_{GL}	Å	443	2342
κ_{GL}	---	1.38	7.2
γ	mJ mol^{-1} K^{-2}	5.5	4.73
$\Delta C_p/\gamma T_c$	---	1.40	1.48
λ_{e-p}	---	0.57	0.52
Θ_D	K	277	320

Table II. Calculated and experimental lattice constant of $LiGa_2Ir$.

	Experiment	w/o SOC	with SOC
a (Å)	6.0317(1)	6.0161	6.0164

Table III. Calculated DOS(E_F), γ_{band} and λ_γ of $LiGa_2Ir$ compared with experimental results obtained from electronic heat and McMillan formula.

	p=0 GPa		p=1 GPa
	w/o SOC	with SOC	with SOC
DOS(E_F) (eV^{-1})	1.545	1.574	1.558
γ_{band} (mJ mol^{-1} K^{-2})	3.64	3.71	3.67
γ_{expt} (mJ mol^{-1} K^{-2})	5.5(1)		-
λ_γ	0.51	0.48	0.50
λ_{expt}	0.57		-

Table IV. Calculated average phonon frequencies, electron-phonon coupling constant and superconducting transition temperature from Allen-Dynes formula.

	p=0 GPa		p=1 GPa
	w/o SOC	with SOC	with SOC
$\langle\omega\rangle$ (THz)	5.77	5.74	5.82
$\langle\omega_{Li}\rangle$ (THz)	11.11	11.08	11.20
$\langle\omega_{Ga}\rangle$ (THz)	4.70	4.58	4.65
$\langle\omega_{Ir}\rangle$ (THz)	2.67	2.73	2.78
$\langle\omega_{log}^{\alpha^2F}\rangle$ (THz)	2.22	2.34	2.35
$\langle\omega_{log}^{\alpha^2F}\rangle$ (K)	106.64	112.31	112.69
λ	0.7010	0.6754	0.6708
$T_{c,calc}$ (K) (μ^*=0.13)	2.85	2.69	2.64
$T_{c,calc}$ (K) (μ^*=0.121)	3.1053	2.9442	2.8963
$T_{c,expt}$ (K)	2.95		-

Table V. Electron-phonon coupling constant contributions from the 12 phonon modes.

	λ_{tot}	λ_1	λ_2	λ_3	λ_4	λ_5	λ_6	λ_7	λ_8	λ_9	λ_{10}	λ_{11}	λ_{12}
w/o SOC	0.7010	0.2679	0.1588	0.0905	0.0283	0.0291	0.0253	0.0260	0.0235	0.0304	0.0089	0.0058	0.0065
with SOC	0.6754	0.2430	0.1506	0.0873	0.0310	0.0313	0.0271	0.0269	0.0253	0.0324	0.0080	0.0056	0.0067

Figures:

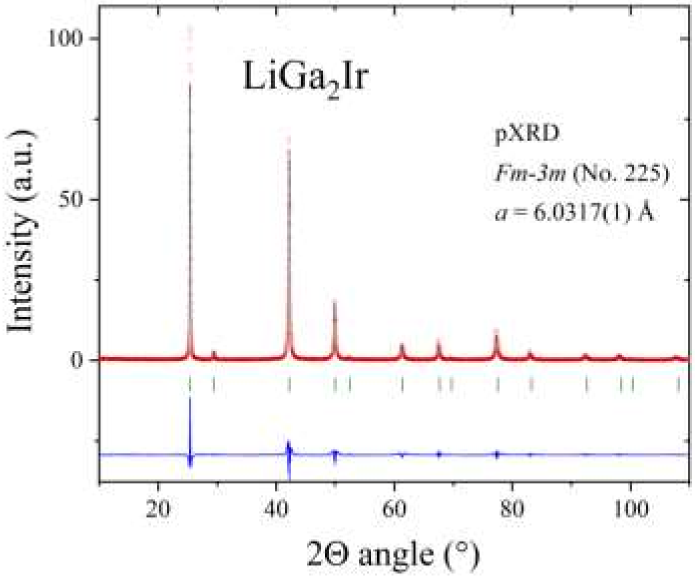

Fig.1. Powder X-ray diffraction pattern of LiGa$_2$Ir (red points) together with the LeBail refinement profile (black solid line). The blue curve is the difference between experimental and model results. The green vertical bars indicate the expected Bragg peak positions (space group *Fm-3m*).

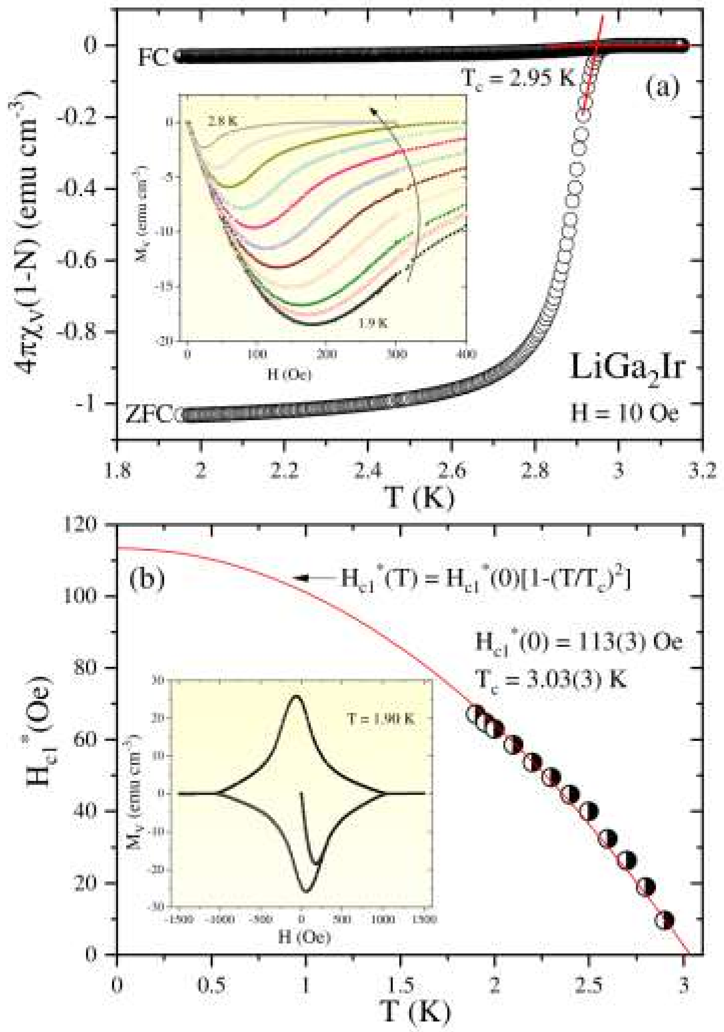

Fig.2.(a) Temperature dependences of the zero-field-cooled (ZFC) and field-cooled (FC) volume magnetic susceptibility measured in a magnetic field of 10 Oe. The red straight lines illustrate derivation of the critical temperature. Inset: the field-dependent magnetization curves $M_V(H)$ for $LiGa_2Ir$ taken at different temperatures. (b) The temperature dependence of the lower critical fields determined from Mv(H). Inset: Magnetization loop at T = 1.90 K.

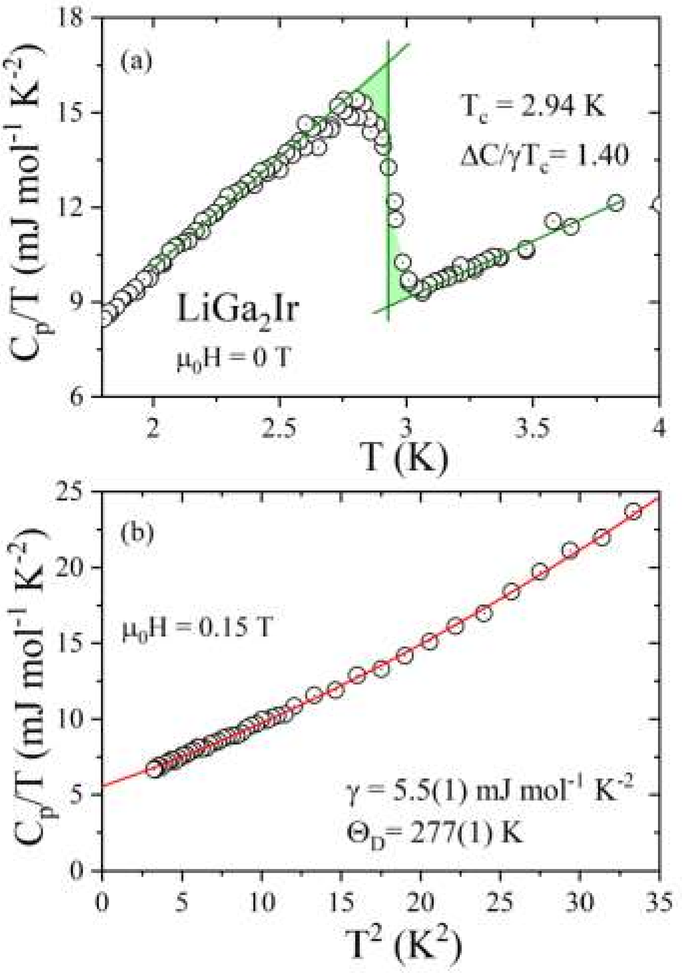

Fig.3. (a) Specific heat divided by temperature (C_p/T) vs. temperature of $LaGa_2Ir$ measured in zero magnetic field in the vicinity of the superconducting phase transition. (b) C_p/T vs. T^2 measured at 0.15 T magnetic field. The red straight line represents the Debye fit discussed in the main text.

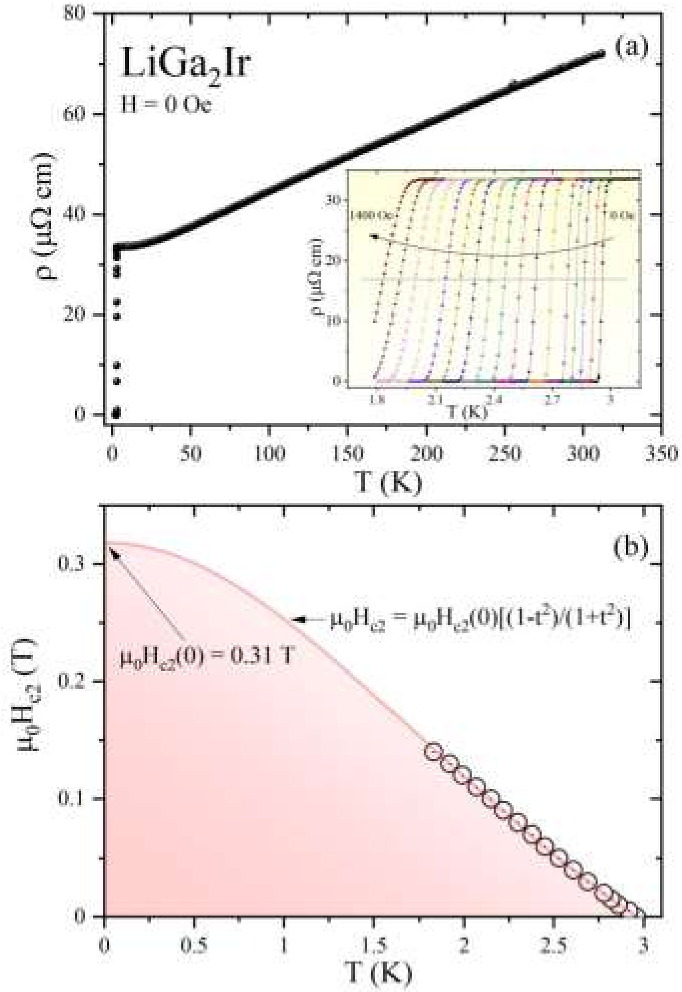

Fig.4. (a) The temperature dependent resistivity for LaGa$_2$Ir over a wide temperature range measured in zero applied magnetic field. Inset: the low- temperature resistivity data taken in several different magnetic fields. (b) The temperature dependence of the upper critical field of LiGa$_2$Ir, determined from electrical resistivity measurements.

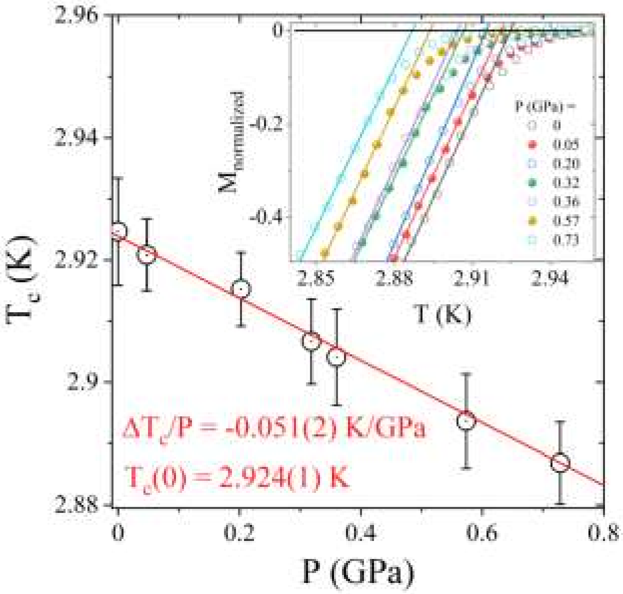

Fig.5. Pressure dependence of the T_c for $LiGa_2Ir$. T_c was taken as the temperature where the extrapolation of the steepest slope of the normalized magnetization versus temperature curves intersects the extrapolation of the normal state magnetization (inset).

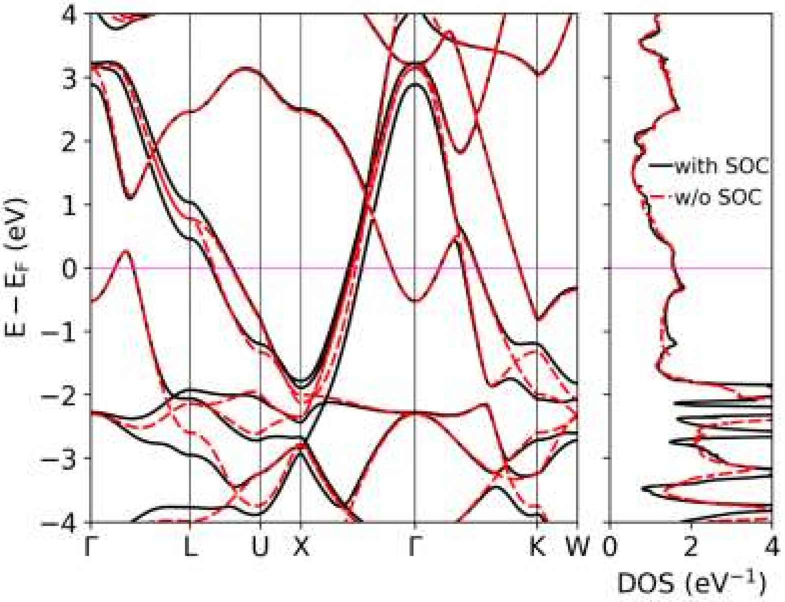

Fig.6. Electronic dispersion relation and total DOS of $LiGa_2Ir$ calculated with and without SOC.

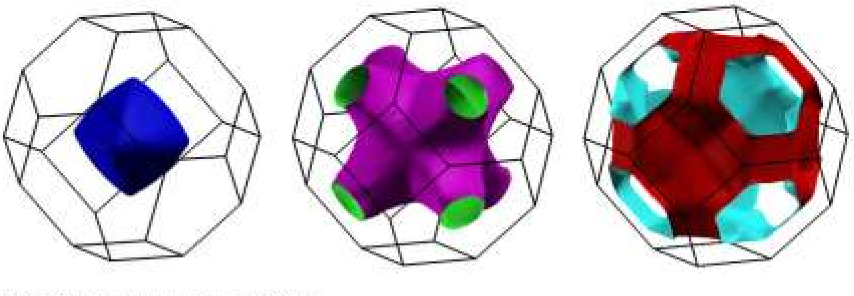

Fig.7. Fermi surface sheets of $LiGa_2Ir$.

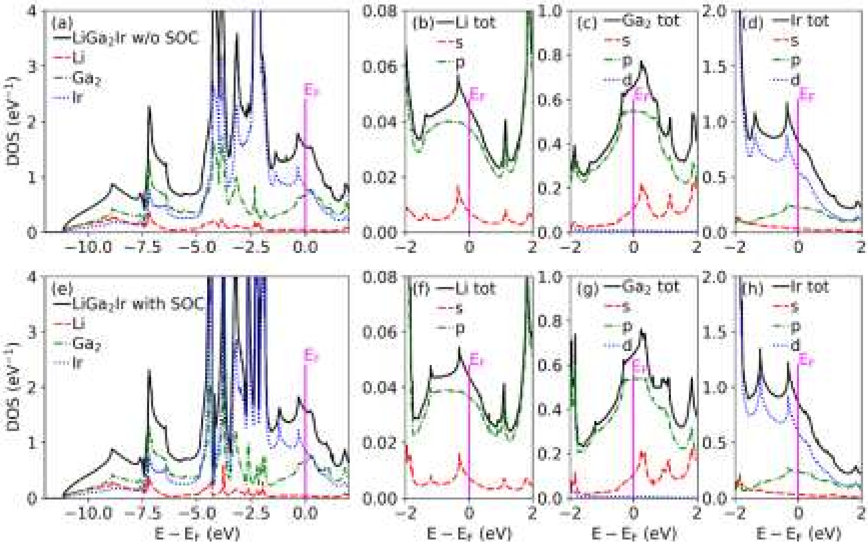

Fig.8. Total and partial DOS of $LiGa_2Ir$ calculated without SOC (a-d) and with SOC (e-h).

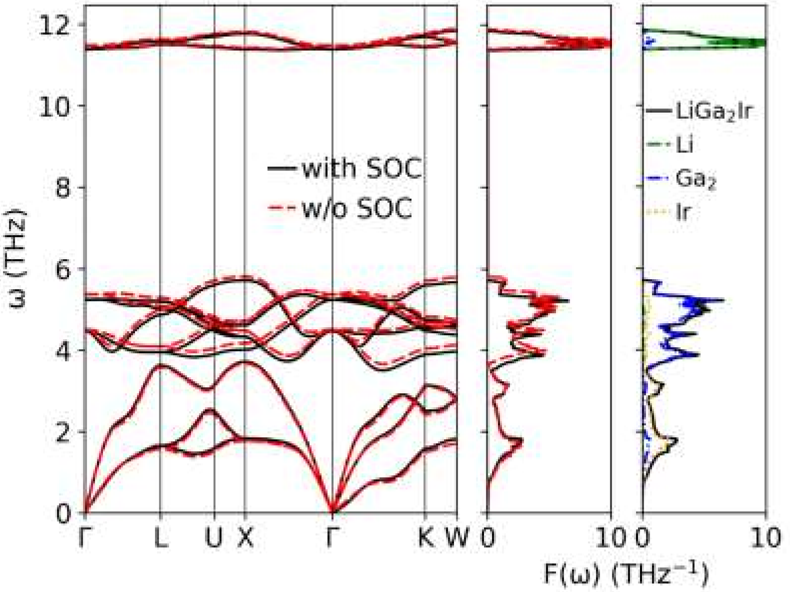

Fig.9. Phonon dispersion relation and density of states of $LiGa_2Ir$ calculated with and without SOC.

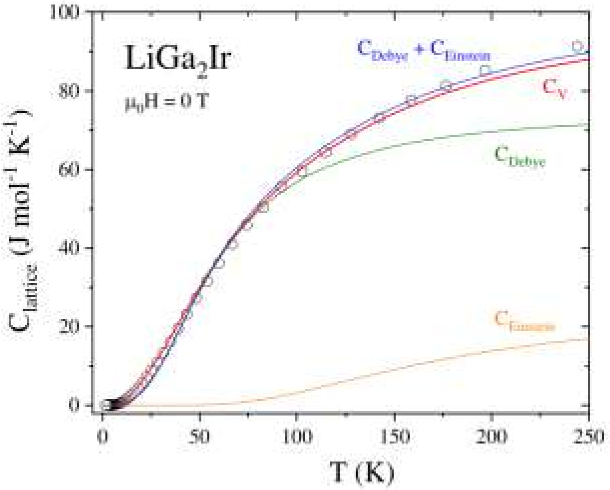

Fig.10. Zero magnetic field, lattice heat capacity data of LiGa$_2$Ir versus temperature T for 1.8 K < T < 250 K. The red line shows constant volume C$_v$, computed directly from the phonon density of states F(ω). The blue solid line represents the fitted sum of the contributions from the Debye (green) and the Einstein (orange) heat capacity contributions.

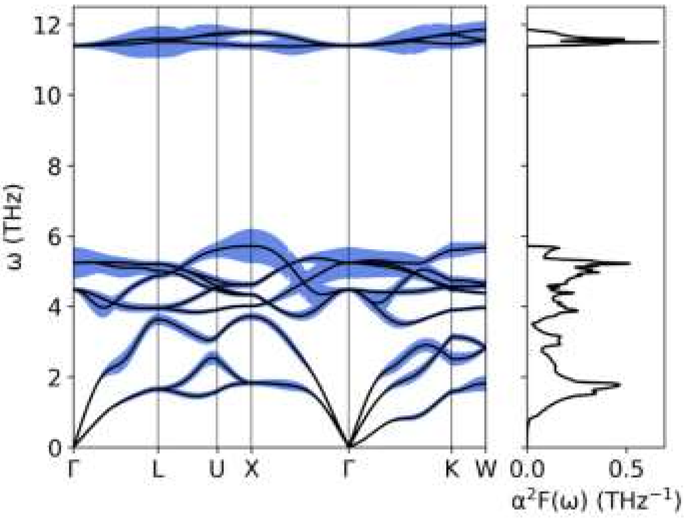

Fig.11. Phonon dispersion relation and function of LiGa$_2$Ir calculated with SOC. Blue filling is proportional to phonon linewidth (multiplied 50 times to make it visible).

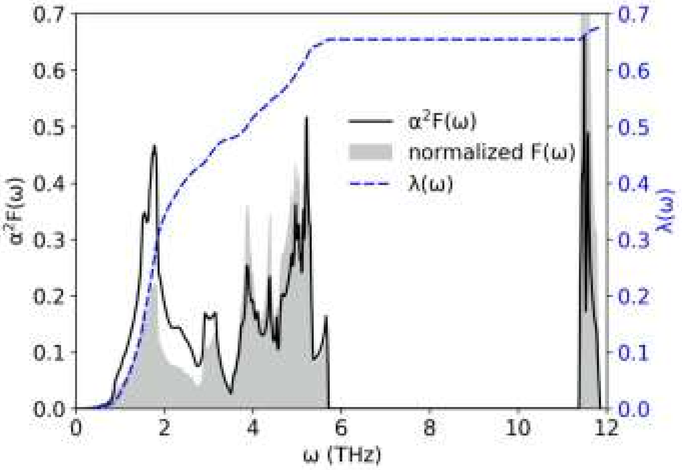

Fig.12. Eliashberg function (solid line) of $LiGa_2Ir$ and cumulative electron-phonon coupling constant (dashed line) calculated with SOC. Phonon density of states, marked with gray filling, was normalized to have the same integral as Eliashberg function.

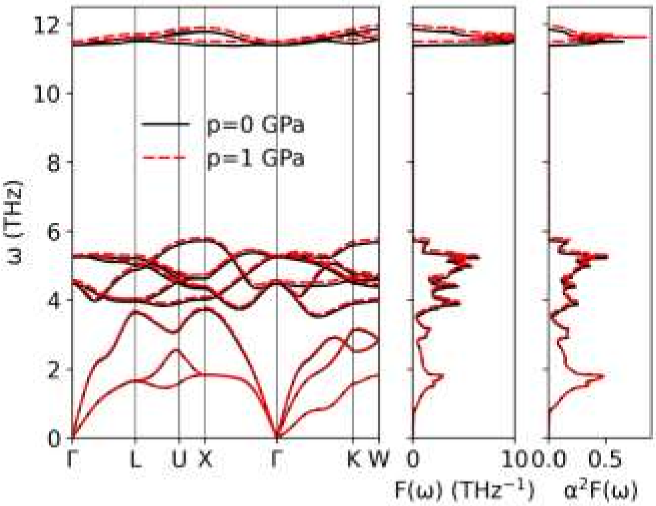

Fig.13. Phonon dispersion relation, phonon density of states and Eliashberg function of $LiGa_2Ir$ under 1 GPa.

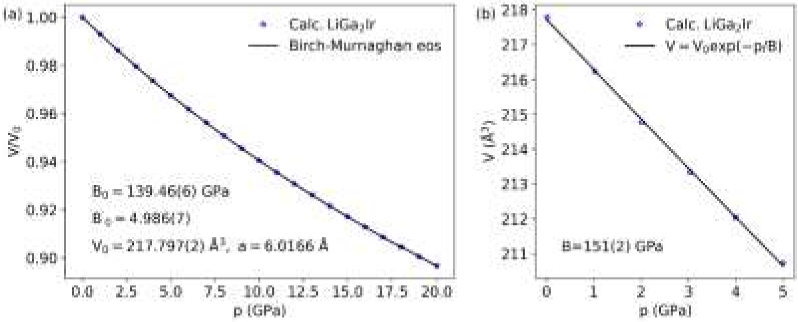

Tab.14. (a) Birch-Murnaghan equation of state fitted to calculated cell volumes of $LiGa_2Ir$ under pressures and (b) approximate pressure-volume relation in 0-5 GPa range.

Bibliography:

[1] A. S. Gzyl, A. O. Oliynyk, and A. Mar, *Half-Heusler Structures with Full-Heusler Counterparts: Machine-Learning Predictions and Experimental Validation*, Cryst. Growth Des. **20**, 6469 (2020).

[2] T. Kojima, S. Kameoka, and A.-P. Tsai, *The Emergence of Heusler Alloy Catalysts*, Sci. Technol. Adv. Mater. **20**, 445 (2019).

[3] C. J. Palmstrøm, *Heusler Compounds and Spintronics*, Prog. Cryst. Growth Charact. Mater. **62**, 371 (2016).

[4] C. Felser, L. Wollmann, S. Chadov, G. H. Fecher, and S. S. P. Parkin, *Basics and Prospective of Magnetic Heusler Compounds*, APL Mater. **3**, 041518 (2015).

[5] J.-W. G. Bos and R. A. Downie, *Half-Heusler Thermoelectrics: A Complex Class of Materials*, J. Phys. Condens. Matter **26**, 433201 (2014).

[6] W. G. Zeier, J. Schmitt, G. Hautier, U. Aydemir, Z. M. Gibbs, C. Felser, and G. J. Snyder, *Engineering Half-Heusler Thermoelectric Materials Using Zintl Chemistry*, Nat. Rev. Mater. **1**, (2016).

[7] S. J. Poon, *Half Heusler Compounds: Promising Materials for Mid-to-High Temperature Thermoelectric Conversion*, J. Phys. Appl. Phys. **52**, 493001 (2019).

[8] A. Planes, L. Mañosa, and M. Acet, *Magnetocaloric Effect and Its Relation to Shape-Memory Properties in Ferromagnetic Heusler Alloys*, J. Phys. Condens. Matter **21**, 233201 (2009).

[9] B. Yan and A. de Visser, *Half-Heusler Topological Insulators*, MRS Bull. **39**, 859 (2014).

[10] K. Manna, Y. Sun, L. Muechler, J. Kübler, and C. Felser, *Heusler, Weyl and Berry*, Nat. Rev. Mater. **3**, 244 (2018).

[11] M. Acet and E. F. Wassermann, *Magnetic Interactions in Ni-Mn-Based Magnetic Shape-Memory Heusler Alloys*, Adv. Eng. Mater. **14**, 523 (2012).

[12] P. G. van Engen, K. H. J. Buschow, R. Jongebreur, and M. Erman, *PtMnSb, a Material with Very High Magneto-optical Kerr Effect*, Appl. Phys. Lett. **42**, 202 (1983).

[13] R. Kainuma, Y. Imano, W. Ito, Y. Sutou, H. Morito, S. Okamoto, O. Kitakami, K. Oikawa, A. Fujita, T. Kanomata, and K. Ishida, *Magnetic-Field-Induced Shape Recovery by Reverse Phase Transformation*, Nature **439**, 957 (2006).

[14] T. Gruner, D. Jang, Z. Huesges, R. Cardoso-Gil, G. H. Fecher, M. M. Koza, O. Stockert, A. P. Mackenzie, M. Brando, and C. Geibel, *Charge Density Wave Quantum Critical Point with Strong Enhancement of Superconductivity*, Nat. Phys. **13**, 967 (2017).

[15] C. N. Kuo, H. W. Lee, C.-M. Wei, Y. H. Lin, Y. K. Kuo, and C. S. Lue, *Ru 2 NbGa : A Heusler-Type Compound with Semimetallic Characteristics*, Phys. Rev. B **94**, (2016).

[16] Y. Nishino, M. Kato, S. Asano, K. Soda, M. Hayasaki, and U. Mizutani, *Semiconductorlike Behavior of Electrical Resistivity in Heusler-Type Fe 2 VAl Compound*, Phys. Rev. Lett. **79**, 1909 (1997).

[17] C. S. Lue, J. H. Ross, C. F. Chang, and H. D. Yang, *Field-Dependent Specific Heat in Fe 2 VAl and the Question of Possible 3 d Heavy Fermion Behavior*, Phys. Rev. B **60**, R13941 (1999).

[18] C. S. Lue, Y. Li, J. H. Ross, and G. M. Irwin, *NMR and Mössbauer Study of Spin Dynamics and Electronic Structure of Fe 2 + x V 1 − x Al and Fe 2 VGa*, Phys. Rev. B **67**, (2003).

[19] A. Ślebarski and J. Goraus, *Electronic Structure and Thermodynamic Properties of Fe 2 VGa*, Phys. Rev. B **80**, (2009).

[20] C. S. Lue, J. H. Ross, K. D. D. Rathnayaka, D. G. Naugle, S. Y. Wu, and W.-H. Li, *Superparamagnetism and Magnetic Defects in Fe $_2$ VAl and Fe $_2$ VGa*, J. Phys. Condens. Matter **13**, 1585 (2001).

[21] A. Ślebarski, M. B. Maple, E. J. Freeman, C. Sirvent, D. Tworuszka, M. Orzechowska, A. Wrona, A. Jezierski, S. Chiuzbaian, and M. Neumann, *Weak Ferromagnetism Induced by Atomic Disorder in Fe 2 TiSn*, Phys. Rev. B **62**, 3296 (2000).

[22] A. Ślebarski, J. Deniszczyk, W. Borgieł, A. Jezierski, M. Swatek, A. Winiarska, M. B. Maple, and W. M. Yuhasz, *Electronic Structure and Thermodynamic Properties of the Heusler Alloys Fe 2 Ti 1 − x V x Sn*, Phys. Rev. B **69**, (2004).

[23] C. L. Seaman, N. R. Dilley, M. C. de Andrade, J. Herrmann, M. B. Maple, and Z. Fisk, *Superconductivity and Magnetism in the Heusler Alloys* M *Pd 2 Pb (* M *=rare Earth, Th, and U)*, Phys. Rev. B **53**, 2651 (1996).

[24] T. Klimczuk, C. H. Wang, K. Gofryk, F. Ronning, J. Winterlik, G. H. Fecher, J.-C. Griveau, E. Colineau, C. Felser, J. D. Thompson, D. J. Safarik, and R. J. Cava, *Superconductivity in the Heusler Family of Intermetallics*, Phys. Rev. B **85**, 174505 (2012).

[25] B. T. Matthias, *Chapter V Superconductivity in the Periodic System*, in *Progress in Low Temperature Physics*, Vol. 2 (Elsevier, 1957), pp. 138–150.

[26] A. J. Bradley and J. W. Rodgers, *The Crystal Structure of the Heusler Alloys*, Proc. R. Soc. Lond. Ser. Contain. Pap. Math. Phys. Character **144**, 340 (1934).

[27] E. M. Carnicom, W. Xie, Z. Yang, K. Górnicka, T. Kong, T. Klimczuk, and R. J. Cava, *Importance of Specific Heat Characterization When Reporting New Superconductors: An Example of Superconductivity in LiGa $_2$ Rh*, Chem. Mater. **31**, 2164 (2019).

[28] M. J. Clark and T. F. Smith, *Pressure Dependence of T c for Lead*, J. Low Temp. Phys. **32**, 495 (1978).

[29] P. Giannozzi, S. Baroni, N. Bonini, M. Calandra, R. Car, C. Cavazzoni, D. Ceresoli, G. L. Chiarotti, M. Cococcioni, I. Dabo, A. Dal Corso, S. de Gironcoli, S. Fabris, G. Fratesi, R. Gebauer, U. Gerstmann, C. Gougoussis, A. Kokalj, M. Lazzeri, L. Martin-Samos, N. Marzari, F. Mauri, R. Mazzarello, S. Paolini, A. Pasquarello, L. Paulatto, C. Sbraccia, S. Scandolo, G. Sclauzero, A. P. Seitsonen, A. Smogunov, P. Umari, and R. M. Wentzcovitch, *QUANTUM ESPRESSO: A Modular and Open-Source Software Project for Quantum Simulations of Materials*, J. Phys. Condens. Matter **21**, 395502 (2009).

[30] P. Giannozzi, O. Andreussi, T. Brumme, O. Bunau, M. Buongiorno Nardelli, M. Calandra, R. Car, C. Cavazzoni, D. Ceresoli, M. Cococcioni, N. Colonna, I. Carnimeo, A. Dal Corso, S. de Gironcoli, P. Delugas, R. A. DiStasio, A. Ferretti, A. Floris, G. Fratesi, G. Fugallo, R. Gebauer, U. Gerstmann, F. Giustino, T. Gorni, J. Jia, M. Kawamura, H.-Y. Ko, A. Kokalj, E. Küçükbenli, M. Lazzeri, M. Marsili, N. Marzari, F. Mauri, N. L. Nguyen, H.-V. Nguyen, A. Otero-de-la-Roza, L. Paulatto, S. Poncé, D. Rocca, R. Sabatini, B. Santra, M. Schlipf, A. P. Seitsonen, A. Smogunov, I. Timrov, T. Thonhauser, P. Umari, N. Vast, X. Wu, and S. Baroni, *Advanced Capabilities for Materials Modelling with Quantum ESPRESSO*, J. Phys. Condens. Matter **29**, 465901 (2017).

[31] P. Giannozzi, O. Baseggio, P. Bonfà, D. Brunato, R. Car, I. Carnimeo, C. Cavazzoni, S. de Gironcoli, P. Delugas, F. Ferrari Ruffino, A. Ferretti, N. Marzari, I. Timrov, A. Urru, and S. Baroni, *Q UANTUM ESPRESSO toward the Exascale*, J. Chem. Phys. **152**, 154105 (2020).

[32] A. Dal Corso, *Pseudopotentials Periodic Table: From H to Pu*, Comput. Mater. Sci. **95**, 337 (2014).

[33] *Pseudopotentials Downloaded from Https://Www.Quantum-Espresso.Org/Pseudopotentials : Li.Pbe-s-Kjpaw_psl.1.0.0.UPF, Pd.Pbe-n-Kjpaw_psl.1.0.0.UPF, Pd.Rel-Pbe-n-Kjpaw_psl.1.0.0.UPF, Si.Pbe-n-Kjpaw_psl.1.0.0.UPF, Si.Rel-Pbe-n-Kjpaw_psl.1.0.0.UPF, Ge.Pbe-Dn-Kjpaw_psl.1.0.0.UPF,*

Ge.Rel-Pbe-Dn-Kjpaw_psl.1.0.0.UPF, Sn.Pbe-Dn-Kjpaw_psl.1.0.0.UPF, Sn.Rel-Pbe-Dn-Kjpaw_psl.1.0.0.UPF.

[34] J. P. Perdew, A. Ruzsinszky, G. I. Csonka, O. A. Vydrov, G. E. Scuseria, L. A. Constantin, X. Zhou, and K. Burke, *Restoring the Density-Gradient Expansion for Exchange in Solids and Surfaces*, Phys. Rev. Lett. **100**, (2008).

[35] A. Czybulka, A. Petersen, and H.-U. Schuster, *Lithium-platinmetall-Al(Ga, In)-legierungen: Neue farbige ternäre intermetallische phasen*, J. Common Met. **161**, 303 (1990).

[36] L. Drews-Nicolai and G. Hohlneicher, *Electronic Structure Calculations for the Ternary Intermetallic Compounds A2MX and AMX2 (A=Li; M=Rh, Pd, Ir, Pt; X=Al, Ga, In) Using Density-Functional Theory*, J. Alloys Compd. **316**, 1 (2001).

[37] T. Klimczuk and R. J. Cava, *Carbon Isotope Effect in Superconducting Mg C Ni 3*, Phys. Rev. B **70**, 212514 (2004).

[38] M. Sato and Y. Ishii, *Simple and Approximate Expressions of Demagnetizing Factors of Uniformly Magnetized Rectangular Rod and Cylinder*, J. Appl. Phys. **66**, 983 (1989).

[39] K. Górnicka, D. Das, S. Gutowska, B. Wiendlocha, M. J. Winiarski, T. Klimczuk, and D. Kaczorowski, *Iridium 5 d -Electron Driven Superconductivity in ThI r 3*, Phys. Rev. B **100**, (2019).

[40] W. L. McMillan, *Transition Temperature of Strong-Coupled Superconductors*, Phys. Rev. **167**, 331 (1968).

[41] K. Górnicka, R. J. Cava, and T. Klimczuk, *The Electronic Characterization of the Cubic Laves-Phase Superconductor CaRh2*, J. Alloys Compd. **793**, 393 (2019).

[42] M. Tinkham, *Introduction to Superconductivity* (Courier Corporation, 1996).

[43] A. M. Clogston, *Upper Limit for the Critical Field in Hard Superconductors*, Phys. Rev. Lett. **9**, 266 (1962).

[44] B. S. Chandrasekhar, *A Note on the Maximum Critical Field of High-field Superconductors*, Appl. Phys. Lett. **1**, 7 (1962).

[45] M. J. Winiarski and et al., *MgPd2Sb - the Fist Mg-Based Heusler-Type Superconductor*, Submitted (n.d.).

[46] M. J. Johnson and R. N. Shelton, *Pressure Effects on the Superconductivity of Ternary Rare Earth Palladium Heusler Alloys*, Solid State Commun. **52**, 839 (1984).

[47] A. Kokalj, *XCrySDen—a New Program for Displaying Crystalline Structures and Electron Densities*, J. Mol. Graph. Model. **17**, 176 (1999).

[48] B. Wiendlocha, M. J. Winiarski, M. Muras, C. Zvoriste-Walters, J.-C. Griveau, S. Heathman, M. Gazda, and T. Klimczuk, *Pressure Effects on the Superconductivity of the Hf Pd 2 Al Heusler Compound: Experimental and Theoretical Study*, Phys. Rev. B **91**, (2015).

[49] H. Y. Uzunok, E. Karaca, S. Bağcı, and H. M. Tütüncü, *Physical Properties and Superconductivity of Heusler Compound LiGa 2 Rh: A First-Principles Calculation*, Solid State Commun. **311**, 113859 (2020).

[50] K. Górnicka, G. Kuderowicz, E. M. Carnicom, K. Kutorasiński, B. Wiendlocha, R. J. Cava, and T. Klimczuk, *Soft-Mode Enhanced Type-I Superconductivity in LiP d 2 Ge*, Phys. Rev. B **102**, (2020).

[51] M. Wierzbowska, S. de Gironcoli, and P. Giannozzi, *Origins of Low- and High-Pressure Discontinuities of T_{c} in Niobium*, ArXivcond-Mat0504077 (2006).

[52] R. Heid, K.-P. Bohnen, I. Y. Sklyadneva, and E. V. Chulkov, *Effect of Spin-Orbit Coupling on the Electron-Phonon Interaction of the Superconductors Pb and Tl*, Phys. Rev. B **81**, 174527 (2010).

[53] S. Gołąb and B. Wiendlocha, *Electron-Phonon Superconductivity in CaBi 2 and the Role of Spin-Orbit Interaction*, Phys. Rev. B **99**, 104520 (2019).

[54] P. B. Allen and R. C. Dynes, *Transition Temperature of Strong-Coupled Superconductors Reanalyzed*, Phys. Rev. B **12**, 905 (1975).

[55] F. Birch, *Finite Elastic Strain of Cubic Crystals*, Phys. Rev. **71**, 809 (1947).

[56] D. Hirai, M. N. Ali, and R. J. Cava, *Strong Electron–Phonon Coupling Superconductivity Induced by a Low-Lying Phonon in IrGe*, J. Phys. Soc. Jpn. **82**, 124701 (2013).

4.6 (A6) Superconductivity on a Bi Square Net in LiBi

4.6.1 Cel badawczy

Motywacją do przeprowadzenia badań, których wyniki zawarte zostały w pracy (A6), był brak szczegółowych danych eksperymentalnych nt. właściwości fizycznych nadprzewodnika LiBi, który zawiera najlżejszy i najcięższy nieradioaktywny metal. Analizując strukturę tetragonalną, w której krystalizuje LiBi, można zauważyć kwadratowe sieci Bi odseparowane od siebie płaszczyznami Li. Na tej podstawie została wysunięta **hipoteza 6** zakładająca, że za nadprzewodnictwo w LiBi odpowiadają głównie kwadratowe sieci Bi. Ponadto, mając na uwadze kształt krzywych M(H) dla izoelektronowego odpowiednika NaBi [43] założono, że LiBi będzie nadprzewodnikiem I-go rodzaju.

Celem badań opisanych w publikacji A6 było otrzymanie monokryształu LiBi metodą wzrostu z fazy ciekłej, wyznaczenie parametrów charakteryzujących stan nadprzewodzący i normalny, a także szczegółowy opis struktury krystalicznej (dr inż. Michał Winiarski). Badania eksperymentalne obejmowały proszkową dyfrakcję rentgenowską, pomiary cieplne oraz magnetyczne. Badania właściwości fizycznych zostały uzupełnione szczegółowymi obliczeniami struktury elektronowej i fononowej (mgr inż. Sylwia Gutowska, dr hab. inż. Bartłomiej Wiendlocha).

4.6.2 Opis rezultatów

Kryształy LiBi zostały otrzymane metodą wzrostu z fazy ciekłej. Wszystkie czynności związane z otrzymaniem materiału zostały przeprowadzone w komorze rękawicowej wypełnionej Ar. Pierwiastki Li oraz Bi, naważone w odpowiednim stosunku (1:2), zostały umieszczone w tyglu niobowym przykrytym watą kwarcową. Całość została zamknięta w ampule kwarcowej z niewielką ilością wysokiej czystości argonu (5N). Tak przygotowaną ampułę grzano (100℃/h) do temperatury 500℃. Po 6 godzinach rozpoczęto proces powolnego chłodzenia (5℃/h) do temperatury 270℃, po czym odwirowano nadmiar Bi, uzyskując błyszczące kryształy LiBi w kształcie płytek.

Badania strukturalne potwierdziły, że LiBi krystalizuje w strukturze tetragonalnej (*P4/mmm* No. 123), którą można rozważać jako wariant regularnej struktury *Pm-3m* wydłużonej wzdłuż osi *z*. Z powodu tego zniekształcenia, LiBi można rozpatrywać jako związek o quasi-dwuwymiarowym charakterze struktury elektronowej, co uwidacznia się w kształcie powierzchni Fermiego oraz rozkładzie gęstości ładunku, gdzie metaliczne warstwy Bi odseparowane są płaszczyznami Li.

Pomiary podatności magnetycznej w niskich temperaturach potwierdziły występowanie nadprzewodnictwa w T_c = 2.38 K. Pełna pętla namagnesowania, wykonana w T = 1.7 K, a także kształt krzywych namagnesowania w funkcji przyłożonego pola magnetycznego *M(H)* wskazują, że LiBi jest nadprzewodnikiem I-rodzaju. Wyznaczona wartość pola krytycznego wynosi $H_c(0)$ = 157(2) Oe. Pole to jest niższe niż szacowane dla NaBi (250 Oe) [43], przy czym należy zwrócić uwagę, że autorzy ref. [43] najpewniej błędnie interpretowali typ występującego w NaBi nadprzewodnictwa.

Objętościowy charakter nadprzewodnictwa został potwierdzony w pomiarach ciepła właściwego. Oszacowany znormalizowany skok ciepła właściwego wynosi $\Delta C/\gamma T_c = 1.49$ i jest nieznacznie wyższy od wartości BCS ($\Delta C/\gamma T_c = 1.43$). Potwierdzeniem nadprzewodnictwa I-go rodzaju są również wyniki nisko-polowych pomiarów cieplnych. Skok ciepła właściwego w najmniejszym przyłożonym polu ($H = 10$ Oe) jest nieznacznie wyższy i ostrzejszy od $\Delta C/T$ w zerowym polu. Takie zachowanie jest związane z tym, że w nadprzewodnikach I-go typu, indukowane polem magnetycznym przejście fazowe jest przejściem pierwszego rodzaju [2]. Parametr sprzężenia elektron-fonon, wyliczony ze wzoru McMillana, wynosi λ_{ep}=0.66 co wskazuje na słabo sprzężony charakter nadprzewodnictwa w LiBi.

Obliczenia teoretyczne wskazują, że stany elektronowe w pobliżu energii Fermiego, są w zdecydowanym stopniu związane z atomami bizmutu. Na tej podstawie można przyjąć, że za nadprzewodnictwo w LiBi odpowiada kwadratowa sieć Bi, co stanowiło hipotezę badawczą 6. Co więcej, obliczenia pokazały, że stosunkowo silne sprzężenie elektron-fonon jest związane nie tylko z modami akustycznymi (drgania atomów bizmutu), ale także z modami optycznymi (drgania atomów litu). Te ostatnie powodują nieznacznie większą, w porównaniu do NaBi, temperaturę krytyczną dla LiBi.

4.6.3 Treść artykułu A6

4.6.3 Treść artykułu A6

Tytuł: Superconductivity on a Bi Square Net in LiBi

Autorzy: Karolina Górnicka, Sylwia Gutowska, Michał J. Winiarski, Bartłomiej Wiendlocha, Weiwei Xie, Robert J. Cava, Tomasz Klimczuk

Czasopismo: Chemistry of materials 2020, 32, 3150–3159

Impact factor: 9.567 (2019)

Liczba punktów ministerialnych MNiSW: 200 pkt

DOI: 10.1021/acs.chemmater.0c00179

Mój udział polegał na syntezie próbki monokrystalicznej, przeprowadzeniu badań strukturalnych metodą proszkowej dyfrakcji rentgenowskiej wraz z analizą LeBaila, pomiarach właściwości magnetycznych oraz cieplnych, analizie otrzymanych wyników, udziale w dyskusji uzyskanych rezultatów, wyznaczeniu parametrów charakteryzujących stan normalny i nadprzewodzący, przygotowaniu rysunków oraz tekstu manuskryptu w części eksperymentalnej. Brałam udział w przygotowaniu odpowiedzi na recenzje.

Karolina Górnicka

mgr inż. Karolina Górnicka

The original source: Chem. Mater. *2020, 32, 7, 3150–3159*

Further permissions related to the material excerpted should be directed to the ACS.

CHEMISTRY OF MATERIALS

pubs.acs.org/cm Article

Superconductivity on a Bi Square Net in LiBi

Karolina Górnicka, Sylwia Gutowska, Michał J. Winiarski, Bartłomiej Wiendlocha, Weiwei Xie, R. J. Cava, and Tomasz Klimczuk*

Cite This: *Chem. Mater.* 2020, 32, 3150−3159

Read Online

ACCESS | Metrics & More | Article Recommendations | Supporting Information

ABSTRACT: We present the crystallographic analysis, superconducting characterization and theoretical modeling of LiBi, that contains the lightest and the heaviest nonradioactive metal. The compound crystallizes in a tetragonal (CuAu-type) crystal structure with Bi square nets separated by Li planes (parameters $a = 3.3636(1)$ Å and $c = 4.2459(2)$ Å, $c/a = 1.26$). Superconducting state was studied in detail by magnetic susceptibility and heat capacity measurements. The results reveal that LiBi is a moderately coupled type-I superconductor ($\lambda_{e-p} = 0.66$) with $T_c = 2.48$ K and a thermodynamic critical field $H_c(0) = 157$ Oe. Theoretical studies show that bismuth square net is responsible for superconductivity in this compound, but the coupling between the Li planes and Bi planes makes a significant contribution to the superconductivity.

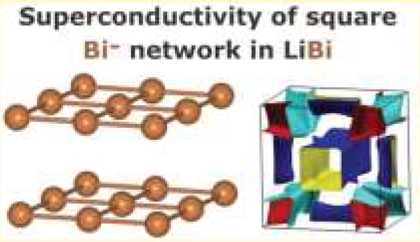

INTRODUCTION

The two-dimensional electronic structures of square nets are an important current topic in materials physics.[1,2] A net of this geometry is present in high temperature copper and iron based superconductors and is responsible for their high temperature transition to the superconducting state. In addition, compounds with a Bi square net are of great current interest due to their importance in topological physics and are extensively studied by both theorists and experimentalists.

Bismuth is the heaviest nonradioactive element, and is widely used in solid state laboratories around the world. In contrast to its neighbors in the periodic table (Pb and Po), Bi is nontoxic and can be treated as nonradioactive (though it actually has a half-life 1.9 × 10^{19} years,[3] a billion times longer than the age of the universe). What is special about Bi from our perspective is its electronic configuration in charge-transfer-based compounds, it can commonly be present as a cation, that is, as Bi^{3+} ($6s^2 6p^0$) or Bi^{5+} ($6s^0 6p^0$), or an anion, that is, as Bi^{3-} ($6s^2 6p^6$). Formal oxidation states of −1 and −2 are also observed, often forming a square net in compounds that reveal novel electronic behavior, such as superconductivity. Superconductivity in layered compounds with Bi square nets has been reported for $CeNi_{0.8}Bi_2$,[4] $LaPd_{1-x}Bi_2$,[5] $SrMnBi_2$,[6] Y_2O_2Bi,[7] and $CaBi_2$.[8]

The elemental antipode to bismuth in the periodic table, the first and lightest metal known is lithium. Found in the upper left corner of the periodic table with a single valence electron, Li is a highly a reactive metal, with a strong tendency to donate electrons. Lithium-based compounds are often unstable in air and hence frequently require special attention during synthesis and characterization. Reacting the lightest and the heaviest metals together in a 1:1 ratio, one gets the LiBi binary compound. Surprisingly, it does not form in the CsCl structure type, common for many intermetallic compounds.[9] Instead it forms in a tetragonal (CuAu-type) crystal structure with $c/a = 1.26$.[10] For the next metal down the alkali column in the periodic table, Na, the analogous NaBi compound also forms in the same basic structure, although the distortion is larger, with $c/a = 1.39$.[11] Proceeding further down the column, KBi crystallizes in a more complex structure, featuring infinite Bi−Bi spirals, closely resembling the Te−Te chains observed in elemental tellurium.[12]

LiBi has previously been reported as a superconductor, but except for T_c and its pressure derivative[13] and the Li isotope effect,[14] no more information concerning its normal and superconducting states is available. Here we describe our experimental and theoretical studies of LiBi. We show that LiBi is a type-I superconductor and that the superconductivity is purely driven by electrons on the formally Bi^{2-} square net. The relevance of the structural distortion of LiBi from ideal cubic to observed tetragonal symmetry to the superconductivity is proposed.

Received: January 15, 2020
Revised: March 15, 2020
Published: March 16, 2020

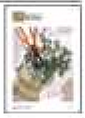

ACS Publications

[illegible]
Chem. Mater. 2020, 32, 3150−3159

RESULTS AND DISCUSSION

Single crystals of LiBi were grown by the flux method, using a Bi flux. The obtained crystals show plate-like shape and metallic luster. The typical SEM image of the as-grown LiBi single crystal is presented in Figure 1 in the Supporting Information (SI). The purity and crystallographic structure of crushed crystals was tested by powder X-ray diffraction (see SI). All the Bragg lines can be indexed to the tetragonal crystal structure of LiBi, with centrosymmetric space group *P4/mmm* (No. 123), plus elemental Bi (remaining flux or decomposition product) present as impurity. The sharpness of diffraction peaks reflects the good crystallinity of the sample. A LeBail fit to the diffraction pattern yields the lattice parameters a = 3.3636(1) Å and c = 4.2459(2) Å, in good agreement with the previously reported values.[10] Additional pXRD scans were performed on a pulverized sample exposed to air for 2 and 12 h. Although the patterns showed that the LiBi phase is stable after 2 h in air, the compound completely decomposes after the longer time period, with only Bi reflections observed.

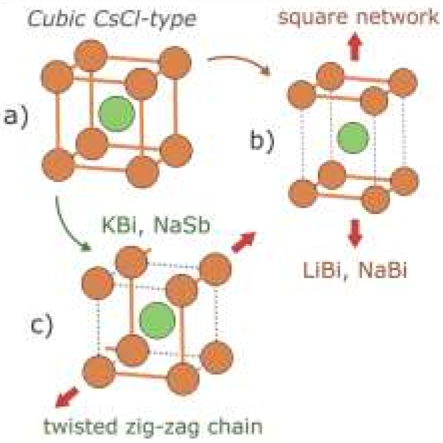

Figure 1. In the hypothetical cubic CsCl-type LiBi, each Bi atom forms six close contacts with neighboring Bi. As discussed in the manuscript, the structure is unstable toward a distortion either to a variant featuring planar Bi square networks (seen in room-temperature structures of LiBi and NaBi) (b) or a twisted zigzag chain arrangement (c) found, e.g., in KBi and NaSb, which also resemble chains found in elemental tellurium. Both (b) and (c) variants can be derived from the cubic parent by selectively breaking 2 or 4 bonds at each Bi site, respectively.

Low-temperature α-LiBi has a tetragonal CuAu-type crystal structure[15,16] which can be viewed as variant of the cubic *Pm-3m* CsCl-type structure elongated along the *z* axis (see Figure 1(a)). Such a structure is difficult to understand in the simple framework of dense packing of hard spheres, which should lead to a CsCl- or NaCl-type structure. Moreover, in the isoelectronic compounds such as KBi, NaSb, and LiAs, one-dimensional spirals of pnictogen atoms are found instead of the square network. The occurrence of these spirals can be understood in the framework of the Zintl−Klemm concept: with a single electron transfer from K, Bi acquires a formal electron configuration of Bi^- [Xe] $6s^2$ $6p^4$ and becomes isoelectronic with chalcogens which, in case of heavier members (Se, Te), feature infinite 1D chains similar to the ones observed in KBi, as well as in NaSb and LiAs. These chains can be derived from a simple cubic arrangement of pnictogen atoms by a distortion that breaks four of the six bonds between nearest-neighbors. From the viewpoint of the VSEPR theory these 1D spirals suggest the presence of two sp^3 lone pairs on each Bi^-, resulting in a bent-linear geometry of each (Bi−Bi−Bi) unit (the local coordination of Bi^- is distorted tetrahedral due to lone pair repulsion being stronger than the tendency to form bonding pairs).

Having the same electron count as KBi, LiBi (and isostructural NaBi) should also form these spiral chains and become semiconducting. Instead, we observe perfect square framework of Bi^-, which results from breaking only two of the six possible bonds, leaving a four-connected network. As pointed out by Papoian and Hoffmann,[2] a square network with ns^2 np^4 species (as Sb^- or Bi^-) is unstable toward at least three types of distortion, one of them being the formation of zigzag chains. Nesper suggested that the structure of LiBi is stabilized by relativistic effects, namely (a) the contraction of s orbitals,[2,17] which reduces the s-p overlap and leaves only p valence orbitals available for bonding (note that good s-p overlap is necessary to produce sp^3 hybrid atomic orbitals and a locally tetrahedral coordination), and (b) the spin−orbit splitting of triply degenerate p orbitals into nondegenerate $p_{1/2}$ and doubly degenerate $p_{3/2}$, the former being significantly lower in energy. With six electrons per Bi, this results in s and $p_{1/2}$ bands being completely filled, leaving two electrons for two $p_{3/2}$ orbitals that available for forming Bi−Bi bonds.

From the viewpoint of our electronic structure calculations, presented in the last part of the paper, this stabilization of the square Bi network can be at least partially attributed to the effects of spin−orbit coupling that strongly affects the shape of Fermi surface (FS), weakening the possible FS nesting. Such an effect was previously postulated to be responsible for stabilization of the simple cubic structure of Po with respect to the trigonal structure of the isoelectronic elemental Te.[18] On the other hand, Tremel and Hoffman[1] have shown that in case of the isoelectronic compounds $EuSb_2$ and $YbSb_2$ the stabilization of the Sb square network in the latter stems from the small contribution of trivalent Yb in contrast to the purely divalent character of Eu in the former. This also implies that the effect is caused by a stronger covalent character of Yb−Sb bonding, in agreement with the electronegativity differences (Eu: 1.01 vs Yb 1.06). The same reasoning can be applied to the LiBi-NaBi-KBi and NaBi-NaSb-NaAs series, as K is more electropositive than both Li and Na, whereas both Sb and As are more electronegative than Bi, resulting in a more "ionic" bonding, leading to a Peierls distortion, formation of spiral pnictogen polyanions, and opening of the band gap, in agreement with the Zintl picture.

A high-temperature β- phase has been reported for LiBi, but its structure has not been established due to its very narrow temperature stability range.[15] From simple entropic reasoning, one may expect that the β−α transformation on cooling is a symmetry-breaking transition, and the likely higher-symmetry variant of the CuAu-type structure is a cubic CsCl-type lattice with a simple cubic arrangement of Bi atoms. The related LiPb compound is known to undergo a symmetry breaking transition around 200 °C from CsCl-type cubic structure to a trigonally distorted (elongated along the (111) axis) $R\bar{3}m$

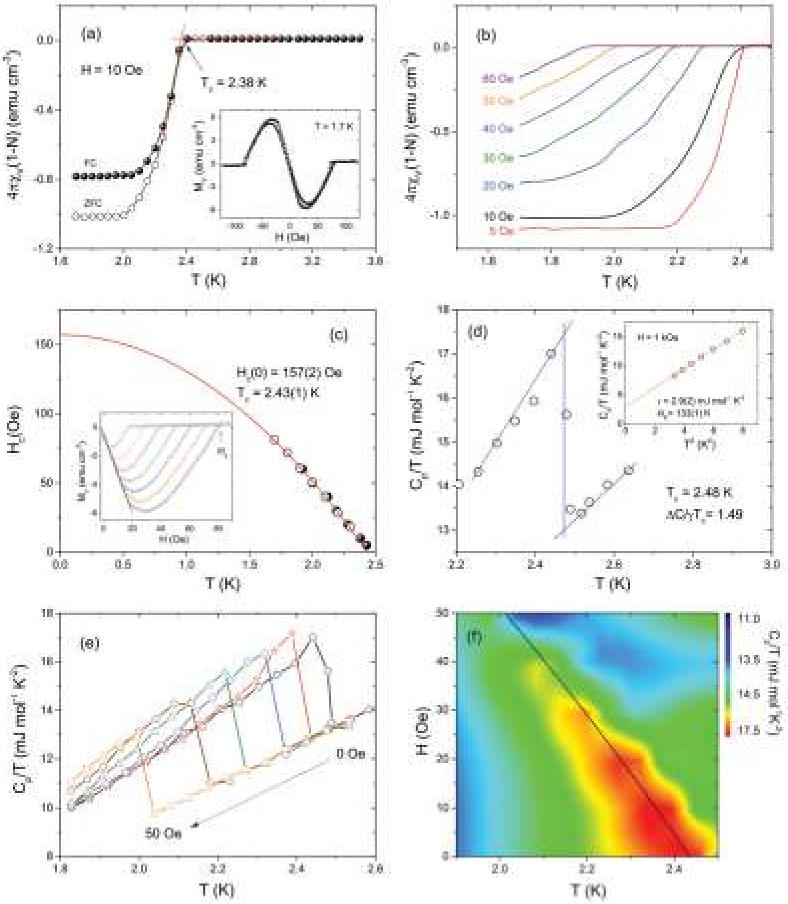

Figure 2. (a) The main panel shows zero-field-cooled (ZFC) and field-cooled (FC) temperature-dependent volume magnetic susceptibility $\chi_V(T)$ measurements performed under a small applied magnetic field of 10 Oe. The inset presents a full magnetization loop measured at T = 1.7 K. (b) The temperature-dependent volume magnetic susceptibility in several different magnetic fields. (c) Main panel: The temperature variation of the thermodynamic critical field (H_c). Inset: volume magnetization, M_V, vs applied field at various temperatures from 1.7 to 2.3 K. (d) The specific heat anomaly in zero magnetic field at low temperatures with T_c = 2.48 K. Inset: C_p/T vs T^2 measured at 1 kOe. A red solid line represents a linear fit used to estimate the values of electronic and phonon specific heat coefficients. (e) The dependence of the specific heat C_p on temperature in applied magnetic fields H up to 50 Oe. (f) Map of the specific heat of LiBi as a function of temperature and applied magnetic field.

structure.[15,16,19] LiPb has one valence electron less than LiBi, and one can expect that the bonding will be stronger as the population of antibonding states is lower. In fact the Pb−Pb distance is of the order of 3.60 Å in both high- and low-temperature phase,[16,19] shorter than the average value $\frac{2a+c}{3}$ = 3.66 Å in α-LiBi.

As was proposed earlier for SrSnP and NbRuB,[20,21] a superconducting transition is one of the possible ways (besides a structural distortion or a magnetic transition) of reducing the total energy of an electronic system, which is larger when the valence electrons are in antibonding orbitals. The superconducting state for LiBi was initially characterized via measurements of its magnetic properties. The temperature-dependent volume magnetic susceptibility χ_V(T) in a small applied field of 10 Oe is shown in Figure 2(a). Both zero-field-cooled (open circles) and field-cooled (full circles) data show a sharp diamagnetic transition at T_c = 2.38 K, reflecting the

Table 1. Estimated and calculated parameters of LiBi and NaBi.[26]

		calculations				experiment	
parameter	unit	LiBi w/o SOC	LiBi w. SOC	NaBi w.SOC	Li*Bi	LiBi	NaBi
DOS(E_F)	eV^{-1}/f.u.	0.68	0.67	0.61		0.74	0.88
γ	mJ mol^{-1} K^{-2}	1.59	1.59	1.53		2.90	3.4
$\lambda_{e-p} = \gamma_{expt}/\gamma_{calc} - 1$		0.82	0.82	1.36			
λ_{e-p}(α^2F/McMillan)		0.61[a]	0.66[a]	0.62[a]	0.66[a]	0.66[b]	0.62[b]
ω_{log}	K	90.2	86.4	71.5	87.3		
T_c (α^2F, μ = 0.11)	K	2.06	2.48	1.67	2.51	2.48	2.15
T_c (α^2F, μ = 0.13)	K	1.63	2.03	1.33	2.05		
Θ_D	K					133	140
$\Delta C_p/\gamma T_c$						1.49	0.78

[a]From the computed Eliashberg function α^2F. [b]From the inverted McMillan formula.

occurrence of superconductivity in this material. The superconducting critical temperature, T_c, is conservatively estimated as being the intersection between the line obtained by extrapolation of the normal-state magnetic susceptibility to lower temperatures and the steepest slope line of the diamagnetic superconducting signal. The estimated value of T_c = 2.38 K is in very good agreement with the value reported previously by Sambongi.[14] After taking into account the demagnetization effect of the sample by using the formula $-4\pi\chi_V = 1/(1 - N)$, where N = 0.75 is the demagnetization factor (obtained from the M(H) fit discussed next), the superconducting volume fraction estimated from the zero-field-cooled dc susceptibility is close to 100%, a signature of the bulk superconductivity in LiBi. The relatively small difference between the FC and ZFC magnetic susceptibility is due to the character of the tested sample, for which flux pinning is weak. A full magnetization loop measured at T = 1.7 K is shown in the inset of Figure 2(a). The M(H) curve initially shows a linear dependence on the magnetic field, and then drops to zero near the critical field. This is a characteristic feature of type-I superconductors, such as YSb_2,[22] KBi_2,[23] $ScGa_3$, $LuGa_3$,[24] and $ReAl_6$.[25] The broadening of the M(H) data from a pure sawtooth is likely a consequence of demagnetization effects.

Figure 2(b) shows the temperature-dependent volume magnetic susceptibility in several different magnetic fields, H = 5, 10, 20, 30, 40, 50, and 60 Oe. With increasing H, the width of the superconducting transition increases slightly and T_c systematically shifts to lower temperature. Defining the critical temperature as the onset of diamagnetic ZFC susceptibility for each field, the values obtained were then used to determine the thermodynamic critical field H_c (see the main panel of Figure 2(c)). The inset in Figure 2(c) presents the low-field parts of the dc magnetization isotherms measured at various temperatures (from 1.7 to 2.3 K). Assuming that the initial response to magnetic field is perfectly diamagnetic, the demagnetization factor N = 0.75 was found, consistent with the sample's shape used in the magnetic measurements. The critical fields were extracted for each temperature as being where the material enters the normal state. Using these data, the temperature variation of the thermodynamic critical field is shown in the main panel of Figure 2(c). The data points shown as full circles are extracted from the $\chi_V(T)$ analysis and the open circles are obtained from the $M_V(H)$ measurements. The data points thus obtained were analyzed with the following formula:

$$H_c(T) = H_c(0)\left|1 - \left(\frac{T}{T_c}\right)^2\right| \quad (1)$$

where $H_c(0)$ is the critical field at 0 K and T_c is the superconducting critical temperature. The fit (solid red line) is very good and yields T_c = 2.43(1) K and $H_c(0)$ = 157(2) Oe. The critical temperature obtained from this analysis is very close to the T_c obtained from the magnetic susceptibility measurements.

Further information on the superconducting transition of LiBi can be gained from specific-heat measurements. The results of low-temperature heat capacity measurements are shown in Figure 2(d). The zero-field data of LiBi are plotted as C_p/T versus T. The bulk superconductivity in LiBi is manifested by the pronounced anomaly in the specific heat data. From the graphical equal-area construction (blue solid lines), which reflects the expected entropy balance between the normal and the superconducting states at the superconducting phase transition, the estimated critical temperature is equal to 2.48 K, consistent with the value determined from magnetic susceptibility measurements. The specific heat jump at T_c is found to be $\Delta C/T_c$ = 4.3 mJ mol^{-1}K^{-2}.

The inset in Figure 2(d) presents the variation in C_p/T with T^2 at under magnetic field of 1 kOe, which is above H_c; thus the material is in its nonsuperconducting state. The specific heat data provide an extrapolation of the normal-state behavior to $T \to 0$ and allow the determination of the Sommerfeld coefficient γ from the equation $C_p/T = \gamma + \beta T^2$, where the second term is the phonon contribution to the specific heat. The fit, represented by the red solid line, gives γ = 2.9(2) mJ mol^{-1}K^{-2} and β = 1.64(4) mJ mol^{-1}K^{-4}. Furthermore, the Debye temperature Θ_D can be determined using the simple Debye model:

$$\Theta_D = \left(\frac{12\pi^4}{5\beta}nR\right)^{1/3} \quad (2)$$

where R = 8.31 J mol^{-1}K^{-1} and n = 2 for LiBi. Using β = 1.64(4) mJ mol^{-1}K^{-4}, the calculated Debye temperature is 133(1) K, comparable with Θ_D = 140 K reported for NaBi.[26] With the estimated Debye temperature Θ_D in hand, the electron−phonon coupling constant, λ_{e-p}, can be then estimated from McMillan's theory[27] as

$$\lambda_{e-p} = \frac{1.04 + \mu^{*}\ln(\Theta_D/1.45T_c)}{(1 - 0.62\mu^{*})\ln(\Theta_D/1.45T_c) - 1.04} \quad (3)$$

https://dx.doi.org/10.1021/acs.chemmater.0c00179
Chem. Mater. 2020, 32, 3150−3159

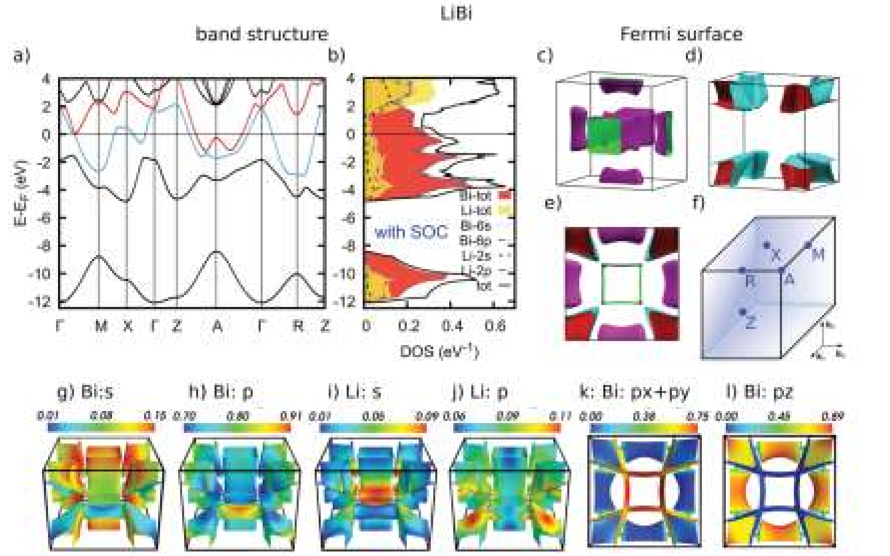

Figure 3. Electronic structure of LiBi in terms of (a) band structure, (b) DOS (with partial DOS coming from atoms and from orbitals marked as a filled curve and colored lines respectively), and (c−e) the Fermi surface calculated with SOC. Brillouin zone (f) is also attached. Atomic orbital character of the Fermi surface of LiBi calculated with SOC are presented in panels g−j calculated with SOC, while the projections into the nonrelativistic p_x, p_y, and p_z basis (calculated without SOC), are presented in panels k,l. The p states of Bismuth are crucial in the electronic structure of LiBi around the Fermi level and are only slightly hybridized with s states.

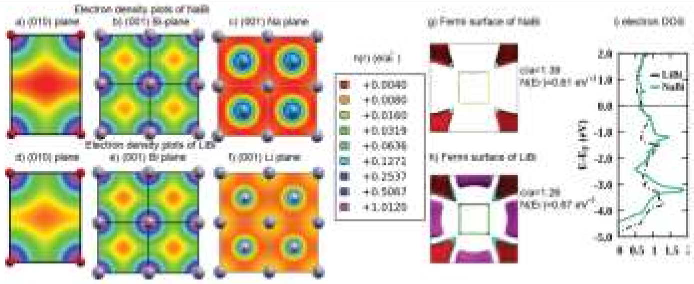

Figure 4. Comparison of LiBi and NaBi compounds in terms of (a−f) electron density, (g−h) Fermi surface, and (i) electron DOS. Due to smaller distortion in LiBi, Bismuth planes and Li atoms are less separated, which contributes to the stronger electron−phonon coupling and T_c, comparing to NaBi.

where, μ^* is the repulsive screened Coulomb parameter, usually taken as $\mu^* = 0.13$ for intermetallic superconductors.[28−30] Taking $T_c = 2.48$ K and $\Theta_D = 133$ K, the calculated λ_{e-p} is 0.66, implying that LiBi is weakly or moderately coupled BCS superconductor.

Using the Sommerfeld coefficient $\gamma = 2.9(2)$ mJ mol^{-1}K^{-2} and the value of the specific heat jump at T_c ($\Delta C/T_c = 4.3$ mJ mol^{-1}K^{-2}), the ratio $\Delta C/\gamma T_c$ can be calculated. The normalized specific heat jump is equal to 1.49, which is near to the expected value of 1.43 for a weakly coupled BCS superconductor.

As shown in Figure 2(e), field-dependent specific heat measurements were performed in fields up to 50 Oe. As expected, the jump in specific heat at $H = 10$ Oe (the lowest applied H) is higher and sharper than that at zero magnetic field, indicating a crossover from second- to the first-order phase transition, commonly seen in type-I superconductors.[23,31,32] The panel of Figure 2(f) presents a map of the specific heat of LiBi as a function of temperature and applied magnetic field (up to 50 Oe) in the vicinity of the superconducting transition. The black solid fit line to eq 1 is shown in a main panel of Figure 2(c) and confirms the complementarity of both experimental methods employed. This is the borderline between normal and superconducting states. The estimated superconducting and normal state parameters of LiBi are gathered in Table 1. Our analysis suggests weak-coupling type - I superconductivity for LiBi.

We now discuss the electronic structure of LiBi and compare it to NaBi. Figure 3 presents the calculated electronic band structure of LiBi in terms of its dispersion relations, DOS and Fermi surface. Spin−orbit coupling (SOC) is included in calculations. Additionally, Figures 3(g−j) show the atomic orbital character of the Fermi surface calculated as a projection of the wave function onto atomic wave functions. The split of the Bi *p*-orbital into $p_x + p_y$ and p_z shown at Figure 3(k,l) is calculated without SOC, as such designations correspond to a nonrelativistic basis. In Figure 4 the charge density plot, the Fermi surface and the DOS are presented and compared to the same characteristics of NaBi. As the charge density plots (see Figure 4(a)) show, due to the distortion from the cubic to the tetragonal structure along the [001] axis, the bismuth atoms in both materials form metallic layers that are separated from each other. This is reflected in the shape of Fermi surface as well as in the filling of the *p* orbitals, as shown below.

Atomic Bi has 6*p* and 6*s* orbitals occupied by three and two valence electrons respectively, for a total of five, while in the case of the alkali Li, one electron occupies an *s*-orbital and the *p*-orbital is empty. This gives six electrons per f.u. for the LiBi crystal. Bi is more electronegative than Li, thus we expect the transfer of the electron from the *s*-orbital of Li to Bi. This is reflected quantitatively in the calculations. The Bader analysis, performed with help of Critic2 software,[33] indeed indicates that 0.85*e* of charge is transferred from the Li atom to the Bi atom in LiBi. As shown in Figure 3(a), in the energy range from −12 to −8 eV below E_F there is a semicore hybridized *sp* band dominated by the 6*s* state of Bi with the contribution of 2*p* states of Li. The main valence band block spans the range between −5 eV and E_F, and consists of one completely filled and two partially filled bands. Figure 3(b) shows these bands to be dominated by the 6*p* states of Bi hybridized with the 2*s* and 2*p* states of Li.

The resulting Fermi surface consists of two pieces, as is shown in Figure 3(c,d). Figure 3(e) presents the [001] view of the Fermi surface. The hole-like band, marked in Figure 3(a) with the blue line, is connected with the first piece of Fermi surface (Figure 3(c)), which consists of pockets centered at the X point and the cuboid-like part. The electron-like band, marked with the red line in Figure 3(a), is connected to second piece of FS (Figure 3(d)), consisting of pockets centered at the A-points. The cuboid-like part of Fermi surface is open in the k_z direction, which is a signature of the quasi-two-dimensional character for this sheet. As shown in Figure 3(g−l), parts of the Fermi surface parallel to the [001] axis, including the cuboid-like part, come from the p_x and p_y states of Bi hybridized with the *s*-states of Li and Bi, while the parts in the (001) plane have p_z character hybridized with the *p*-states of Li. This stands in agreement with the charge density plots, which show bismuth layers to be metallic and separated from each other. These calculations show that the square Bi planes have a *k*-space signature.

The results of scalar-relativistic calculations (*i.e.*, neglecting SOC) are shown in the SI. Comparison with relativistic results shows that SOC strongly modifies electronic structure of LiBi, as expected for a Bicontaining compound. This influence, however, is not in the vicinity of the Fermi level. Thus, the calculations ignoring the SOC and including the SOC lead to almost the same Fermi surface shape and DOS (E_F) values (0.68 eV^{-1} versus 0.67 eV^{-1}, see Table 1).

There are many similarities between the electronic structures of LiBi and NaBi,[26,34] which superconducts at a T_c = 2.15 K. The electronic structures of these compounds are compared in Figure 4. The DOS at E_F (our calculated values are 0.61 eV^{-1}/f.u for NaBi and 0.67 eV^{-1}/f.u for LiBi) and the electron−phonon coupling parameters are similar. The differences are as follows. First of all, the structural distortion along the [001] direction is bigger in case of NaBi (c/a = 1.39) than in LiBi (c/a = 1.26). This fact is reflected in the charge density plots, where the Bismuth layers are more separated from each other (see Figure 4(a)) than in LiBi (see Figure 4(d)). Because of that, the pockets around X point found in the Fermi surface (see Figure 4(h)) of LiBi disappear in NaBi (see Figure 4(g)), which is reflected in a slightly smaller value of DOS at Fermi level in NaBi (Figure 4(i)). Moreover, the charge density in the plane of sodium (Figure 4(c)) is smaller than in the plane of lithium (Figure 4(f)), while atomic plane of bismuth is metallic-like in both cases (Figure 4(b,e)), thus it cannot be an effect of a slightly bigger lattice parameter in the case of NaBi (a = 3.41 Å) in comparison to LiBi (a = 3.37 Å), it may rather be a consequence of the smaller electronegativity of sodium. Thus, the electrons may be more intensively transferred to bismuth in the case of NaBi than in LiBi. Thus, there is a lower electronic density around sodium than around lithium, which is important for the electron−phonon coupling, as discussed below.

Besides superconductivity, topological surface states have been suggested to exist in NaBi.[34] The analysis of the topological properties in ref 34 has been performed using the Z2 invariant, however, which is not well-defined in a three-dimensional metallic case where no band gap is present. In the current material, therefore, due to the absence of a band gap in any of the planes in the Brillouin zone, even weak topological insulating properties are not expected.

Our calculated phonon dispersion relations, with phonon line widths $\gamma_{q\nu}$ marked at each wave vector q and phonon branch ν, the density of states $F(\omega)$ decomposed into atomic contributions, and the Eliashberg electron−phonon coupling function $\alpha^2F(\omega)$, decomposed over phonon modes, are shown in Figure 5. As there are two atoms in the unit cell of LiBi, six phonon branches, three acoustic and three optic, are seen. Due

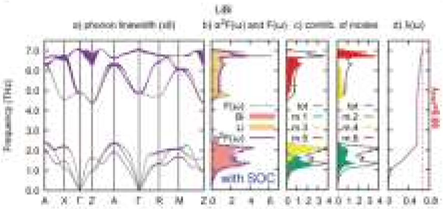

Figure 5. Phonons and electron−phonon coupling of LiBi shown in terms of (a) phonon dispersion relation with phonon line width marked as a fatband, (b) phonon DOS decomposed into atomic contribution marked as a filled curve and Eliashberg function $\alpha^2F(\omega)$ normalized to phonon dos, (c) partial $\alpha^2F_n(\omega)$ where n runs over phonon modes and (d) the cumulative electron−phonon coupling constant λ_{e-ph}.

to the huge mass difference ($m_{Bi} \simeq 30m_{Li}$), the low-frequency part arises mostly from Bi and the optic part from Li vibrations. These two groups of phonon modes are well separated: the acoustic part has calculated frequencies in the range from 0 to 2.5 THz, while the optic modes are found between 4.5 and 7 THz. Both these ranges, as well as the gap between them, are much bigger than in the case of NaBi[34] (0 to 2 THz for the acoustic and 2.25 to 5 THz for the optic modes, respectively). Our computational results for NaBi are presented in the SI.

The increase of Li frequencies with respect to Na frequencies is in agreement with a simple diatomic chain model. Having the chain of two types of atoms: Bi plus Li or Na, one gets the optical frequencies at gamma equal to $\omega_{LiBi} = 2C(m_{Li} + m_{Bi})/(m_{Li}m_{Bi}) = 0.54C$ (C is a constant) in case of LiBi and $\omega_{NaBi} = 0.31C$ in case of NaBi. Its ratio is equal to $\omega_{LiBi}/\omega_{NaBi} = 1.74$. Calculations performed in this work and in ref 34 show the frequency of two (degenerate at gamma) lower optical modes to be $\omega_{LiBi} = 4.89$ THz and $\omega_{NaBi} = 2.79$ THz, which gives the ratio of $\omega_{LiBi}/\omega_{NaBi} = 1.75$ in excellent agreement with the chain model.

These two described optical branches have a considerable dispersion, while the highest optical branch is rather narrow and well-separated from the other branches. As shown in the SI, the fourth and fifth phonons with wave vector $\mathbf{q} = (0,0,0.5)$ (point Z in the Brillouin zone) are associated with the displacement of Li atoms along the [110] direction. The same holds for phonons at the Γ and A points in the Brillouin zone. Since the unit cell is shorter along the [100] and [010] axes in comparison to the [001] axis, in the (001) plane the Li atoms are much closer to each other than in the [001] direction and the Bi−Li and Li−Li distances are nearly equal. This can explain the agreement with predictions of the chain model as well as the considerable dispersion of these two branches. On the other hand, the sixth phonon mode is associated with vibration of atoms along the [001] direction, where the lattice parameter is larger and the atoms are more separated, making the highest phonon mode an Einstein-like less dispersive one.

As far as the electron−phonon interaction is concerned, the largest phonon line width $\gamma_{\mathbf{q}\nu}$ (corresponding to the strongest coupling, see ref 35) is observed for the above-mentioned highest frequency optical mode at the Z point. Here both the phonon propagation vector and Li atomic displacement are along the z-axis. This vibration will strongly affect the Bi−Li bonding, and thus a strong effect on the corresponding electronic states is expected. Especially, this may strongly influence the p_z orbitals of Bi, which are essential for the tetragonal distortion of the crystal structure of this compound.

Large phonon line widths contribute to the Eliashberg function $\alpha^2F(\omega)$, which is defined as a sum over all the phonons:

$$\alpha^2F(\omega) = \frac{1}{2\pi N(E_F)} \sum_{\mathbf{q}\nu} \delta(\omega - \omega_{\mathbf{q}\nu}) \frac{\gamma_{\mathbf{q}\nu}}{\hbar\omega_{\mathbf{q}\nu}} \tag{4}$$

and which is used to calculate the electron−phonon coupling constant $\lambda_{e-p} = 2\int_0^{\omega_{max}} \frac{\alpha^2F(\omega)}{\omega} d\omega$. However, as one can see $\lambda_{e-p} \propto \frac{\gamma_{\mathbf{q}\nu}}{\omega_{\mathbf{q}\nu}^2}$, due to this large phonon line width the contribution from this high-frequency branch is important. A total $\lambda_{e-p} = 0.66$ parameter is computed from the Eliashberg coupling function and its frequency distribution, as shown in Figure 5. The acoustic part of the phonon spectrum, dominated by Bi vibrations, contributes about 85% to the total λ_{e-p}, leaving 15% (0.1 in absolute value) for the optic branches.

The Allen-Dynes formula[36]

$$T_c = \frac{\omega_{log}}{1.20} \exp\left[\frac{-1.04(1 + \lambda_{e-p})}{\lambda_{e-p} - \mu^*(1 + 0.62\lambda_{e-p})}\right] \tag{5}$$

is next used to compute the superconducting critical temperature value. As shown in Table 1, $\lambda_{e-p} = 0.66$ results in an experimental value of $T_c = 2.48$ K, when the Coulomb pseudopotential parameter is set to $\mu^* = 0.11$, which confirms that superconductivity in LiBi is accurately described within the electron−phonon mechanism. The calculated value of λ_{e-p} is slightly smaller than extracted from the experimental Sommerfeld parameter with the help of calculated DOS(E_F) value, which is $\lambda_{e-p} = 0.82$ but both values correspond to intermediate coupling regime.

As far as the spin−orbit coupling (SOC) effects are concerned (see SI), in the scalar-relativistic calculations λ_{e-p} is smaller in about 8%, which is caused by the shift of the highest phonon mode to higher frequencies. Thus, in the present case, SOC weakly enhances the electron−phonon interaction strength, in contrast to the recently studied $CaBi_2$ superconductor.[37]

Comparing now the coupling strengths in LiBi and NaBi (see SI for the figures), both λ_{e-p} (0.66 and 0.62 for LiBi and NaBi, respectively) and T_c (2.48 and 2.15 K, respectively) are higher in the case of LiBi. It may seem surprising that the strong hardening in the phonon spectrum of LiBi, resulting in much larger phonon frequency range (0−7.5 THz for LiBi and 0−4.5 THz for NaBi) does not result in the opposite trend, as $\lambda_{e-p} \propto \frac{\gamma_{\mathbf{q}\nu}}{\omega_{\mathbf{q}\nu}^2}$. In fact, though, this is caused by substantial differences in the Eliashberg function. While in the acoustic part of the spectrum $\alpha^2F(\omega)$ does not differ much between the NaBi and LiBi cases, giving similar (and even slightly larger for NaBi) contribution to the total λ_{e-p} ($\lambda_{e-p}^{acoustic} = 0.56$ in LiBi, $\lambda_{e-p}^{acoustic} = 0.58$ in NaBi), the contribution from the optical branches, especially from the first one, is 2.5 times larger ($\lambda_{e-p}^{optic} = 0.10$ in LiBi, $\lambda_{e-p}^{optic} = 0.04$ in NaBi).

As shown in the SI for the Z-point, where the phonon line widths are the largest in both compounds, the first two degenerate optical modes in LiBi are associated with transverse phonons, where Li atom vibrates in the xy Li−Li plane, while the third one is a longitudal mode along z, where Li vibrates perpendicular to xy Li planes and toward the planes of Bi atoms. In NaBi the same atomic displacements are found. As discussed before, due to the smaller c/a ratio of LiBi and larger electron density around Li, when compared to the Na case, the Li atoms' vibrations couple more effectively to Bismuth electronic states. This gives an additional, though nominally less-expected contribution of the light atom vibrations to the total λ_{e-p} in LiBi compared to NaBi.

In both cases of LiBi and NaBi, the theoretical (calculated from Eliashberg coupling function) and experimental (calculated from McMillan equation) values of λ_{e-p} agree with each other (both equal to 0.66 for LiBi and 0.62 for NaBi), while the values estimated as a renormalization factor of the electronic heat capacity seem to be overestimated (0.82 for LiBi and 1.36 for NaBi). We consider λ_{e-p} obtained from the Eliashberg function and T_c as a more accurate one, and the larger discrepancy observed for NaBi is likely related to inaccuracy of γ value due to a very difficult measurement process in ref 26.

In the previous report on superconductivity in LiBi[14] the Li isotope effect was studied. Replacing natural abundance Li (m_{Li} = 6.94 u) with Li^6 was found to increase the critical temperature by about 0.02 K. This can be used to additionally verify our calculations, the isotope effect experiments were simulated by the appropriate change in the atomic mass of Li, with the results shown in Table 1. The computed critical temperature increased by 0.026 K and taking into account the small absolute values of those increases, the agreement is considered as very good, validating our theoretical results.

■ CONCLUSIONS

In summary, we have grown single crystals of LiBi, which contains the lightest and the heaviest nonradioactive metallic elements together. This compound forms in a tetragonal (CuAu-type) crystal structure with Bi square planes separated by Li planes. The distortion from an ideal cubic CsCl structure, yielding c/a = 1.26, is rather large. Due to this distortion, which we argue is driven by the lower energy of a structure that reduces the degeneracy of the p_z orbitals from the p_x and p_y orbitals of Bi, a quasi-two-dimensional character of the electronic structure is seen in both Fermi surface shape and charge density distribution, where metallic Bismuth layers are separated by Lithium planes.

Detailed experimental and theoretical studies of the superconducting and normal state parameters for LiBi are presented. We find LiBi to be a moderately coupled type-I superconductor with T_c = 2.48 K and a critical field $H_c(0)$ = 157 Oe. Our calculations show that the electron−phonon coupling is strongest for the acoustic phonons (Bi vibrations), with, importantly, an additional (15% of the total λ_{e-p}) contribution from Li modes, which is responsible for the larger T_c of LiBi, compared to NaBi. As Bismuth atoms provide majority of both the electronic states at the Fermi surface and phonons for the electron−phonon coupling, we conclude that the Bi square net is responsible for superconductivity of LiBi, but that the coupling between the light element planes and the heavy element planes makes a significant contribution to the superconductivity. As this compound is electronically dominated by Bi square planes with partly filled p orbitals separated by the lightest possible metallic element Li, it offers a unique opportunity to study the superconductivity of Bi square planes using various spectroscopic methods, thus studies like ARPES should be of future interest.

■ MATERIALS AND METHODS

Single crystals of LiBi were grown by the flux method, using Bi flux. Elemental Li pieces (99.9%, Alfa Aesar) and Bi shot (99.99%, Alfa Aesar) in an atomic ratio 1:2 were packed in a niobium crucible, covered with a plug of quartz wool and sealed inside a silica tube under a partial pressure of Ar. Complete sample preparation was performed in an Ar-filled glovebox without exposing the Li metal to air. The ampule was heated to 500 °C at a rate of 100 °C/h and kept at that temperature for 6 h. After cooling at a rate of 5 °C/h to 270 °C, shiny crystals were separated by decanting the excess of Bi flux using a centrifuge.

The crystal structure of the sample was determined by the LeBail refinement of room-temperature powder X-ray diffraction (pXRD) data for crushed single crystals collected on a Bruker D8 Advance Eco diffractometer with Cu Kα radiation and LynxEye-XE detector. The LeBail refinement of the pXRD pattern was performed using the code TOPAS. Magnetic properties were measured using a Quantum Design Dynacool Physical Property Measurement System (PPMS) with a vibrating sample magnetometer (VSM) system in the temperature range of 1.7−3.5 K under various applied magnetic fields. The temperature dependencies of the zero-field-cooled (ZFC) and field-cooled (FC) magnetic susceptibility (defined as dM/dH, where M is the magnetization and H is the applied field strength) were measured in an external magnetic field up to 60 Oe. Furthermore, the magnetic field dependencies of the magnetization were measured at various temperatures in the superconducting state. The heat capacity measurements were carried out using the two-τ time- relaxation method in a PPMS Evercool II system. The data were collected between 1.9 and 300 K at 0 Oe and in magnetic fields up to 50 Oe. The crystal of LiBi was mounted to the measuring stage using Apiezon N grease to ensure good thermal contact.

The electronic band structure was calculated with help of pseudopotential and plane wave method implemented in Quantum Espresso.[57] Ultrasoft pseudopotentials have been chosen,[58] along with the Perdew−Burke−Ernzerhof[59] scheme for exchange-correlation effects. For lithium the scalar-relativistic pseudopotential has been used, while for bismuth, the fully relativistic pseudopotential has been chosen because relativistic effects, including spin−orbit coupling (SOC), may be essential for such a heavy element.

The phonons and electron−phonon coupling are calculated with help of density functional perturbation theory (DFPT) as implemented in Quantum Espresso. Phonons were calculated on the mesh of 6 × 6 × 6 q points on the basis of the band structure calculated on the mesh of 18 × 18 × 18 k points. Electron−phonon coupling was obtained on the basis of the phonons, and the band structure calculated on a mesh of 36 × 36 × 36 k points.

■ ASSOCIATED CONTENT

Supporting Information

The Supporting Information is available free of charge at https://pubs.acs.org/doi/10.1021/acs.chemmater.0c00179.

> Powder X-ray diffraction pattern of LiBi; the SEM image of LiBi single crystal; structure of KBi featuring Bi spiral chains; electronic structure of LiBi calculated in scalar- and fully relativistic way; phonon structure and electron−phonon coupling in NaBi; the phonon displacement patterns of the six phonon modes for q = (0,0,0.5) of LiBi (PDF)

■ AUTHOR INFORMATION

Corresponding Author

Tomasz Klimczuk − *Faculty of Applied Physics and Mathematics and Advanced Materials Centre, Gdansk University of Technology, 80-233 Gdańsk, Poland*; orcid.org/0000-0002-7089-4631; Email: tomasz.klimczuk@pg.edu.pl

Authors

Karolina Górnicka − *Faculty of Applied Physics and Mathematics and Advanced Materials Centre, Gdansk University of Technology, 80-233 Gdańsk, Poland*
Sylwia Gutowska − *Faculty of Physics and Applied Computer Science, AGH University of Science and Technology, 30-059 Kraków, Poland*
Michal J. Winiarski − *Faculty of Applied Physics and Mathematics and Advanced Materials Centre, Gdansk University of Technology, 80-233 Gdańsk, Poland*; orcid.org/0000-0001-9083-8066
Bartlomiej Wiendlocha − *Faculty of Physics and Applied Computer Science, AGH University of Science and Technology, 30-059 Kraków, Poland*

Weiwei Xie − *Department of Chemistry, Louisiana State University, Baton Rouge, Louisiana 70803, United States;* orcid.org/0000-0002-5500-8195

R. J. Cava − *Department of Chemistry, Princeton University, Princeton, New Jersey 08544, United States*

Complete contact information is available at:
https://pubs.acs.org/10.1021/acs.chemmater.0c00179

Notes

The authors declare no competing financial interest.

■ ACKNOWLEDGMENTS

The research performed at the Gdansk University of Technology was supported by the National Science Centre (Poland) grant (UMO-2017/27/B/ST5/03044). The synthesis and magnetic properties measurements performed at Princeton were supported by the Department of Energy, Division of Basic Energy Sciences, grant DEFG02-98ER45706. W.X. is supported by the Beckman Young Investigator (BYI) Program. The research performed at the AGH-UST was supported by the National Science Center (Poland), Project No. 2017/26/E/ST3/00119. S.G. was partly supported by the EU Project POWR.03.02.00-00-I004/16.

■ REFERENCES

(1) Tremel, W.; Hoffmann, R. Square Nets of Main-Group Elements in Solid-State Materials. *J. Am. Chem. Soc.* **1987**, *109* (1), 124−140.

(2) A. Papoian, G.; Hoffmann, R. Hypervalent Bonding in One, Two, and Three Dimensions: Extending the Zintl-Klemm Concept to Nonclassical Electron-Rich Networks. *Angew. Chem., Int. Ed.* **2000**, *39* (14), 2408−2448.

(3) de Marcillac, P.; Coron, N.; Dambier, G.; Leblanc, J.; Moalic, J.-P. Experimental Detection of α-Particles from the Radioactive Decay of Natural Bismuth. *Nature* **2003**, *422* (6934), 876−878.

(4) Mizoguchi, H.; Matsuishi, S.; Hirano, M.; Tachibana, M.; Takayama-Muromachi, E.; Kawaji, H.; Hosono, H. Coexistence of Light and Heavy Carriers Associated with Superconductivity and Antiferromagnetism in CeNi 0.8 Bi 2 with a Bi Square Net. *Phys. Rev. Lett.* **2011**, *106* (5). DOI: 10.1103/PhysRevLett.106.057002.

(5) Han, F.; Malliakas, C. D.; Stoumpos, C. C.; Sturza, M.; Claus, H.; Chung, D. Y.; Kanatzidis, M. G. Superconductivity and Strong Intrinsic Defects in LaPd 1 − x Bi 2. *Phys. Rev. B: Condens. Matter Mater. Phys.* **2013**, *88* (14). DOI: 10.1103/PhysRevB.88.144511.

(6) Park, J.; Lee, G.; Wolff-Fabris, F.; Koh, Y. Y.; Eom, M. J.; Kim, Y. K.; Farhan, M. A.; Jo, Y. J.; Kim, C.; Shim, J. H.; et al. Anisotropic Dirac Fermions in a Bi Square Net of SrMnBi 2. *Phys. Rev. Lett.* **2011**, *107* (12). DOI: 10.1103/PhysRevLett.107.126402.

(7) Sei, R.; Kitani, S.; Fukumura, T.; Kawaji, H.; Hasegawa, T. Two-Dimensional Superconductivity Emerged at Monatomic Bi $^{2-}$ Square Net in Layered Y $_2$ O $_2$ Bi via Oxygen Incorporation. *J. Am. Chem. Soc.* **2016**, *138* (35), 11085−11088.

(8) Winiarski, M. J.; Wiendlocha, B.; Gołąb, S.; Kushwaha, S. K.; Wiśniewski, P.; Kaczorowski, D.; Thompson, J. D.; Cava, R. J.; Klimczuk, T. Superconductivity in CaBi $_2$. *Phys. Chem. Chem. Phys.* **2016**, *18* (31), 21737−21745.

(9) Dshemuchadse, J.; Steurer, W. Some Statistics on Intermetallic Compounds. *Inorg. Chem.* **2015**, *54* (3), 1120−1128.

(10) Zintl, E.; Brauer, G. Konstitution Der Lithium-Wismut-Legierungen: 14. Mitteilung Über Metalle u. Legierungen. *Z. Für Elektrochem. Angew. Phys. Chem.* **1935**, *41* (5), 297−303.

(11) Zintl, E.; Dullenkopf, W. Metals and Alloys. III. Polyantimonides, Polybismuthides and Their Transformation into Alloys.; *Z. Phys. Chem.*, **1932**; Vol. *16*. DOI: 10.1515/zpch-1932-1615.

(12) Emmerling, F.; Längin, N.; Petri, D.; Kroeker, M.; Röhr, C. Alkalimetallbismutide ABi und ABi2 (A= K, Rb, Cs)— Synthesen, Kristallstrukturen, Eigenschaften. *Z. Anorg. Allg. Chem.* **2004**, *630* (1), 171−178.

(13) Alekseevskii, N. E.; Brandt, N. B.; Kostina, T. I. Superconductivity of Binary Alloys of Bismuth; 233-63; *Izv. Akad. Nauk SSSR Ser. Fiz*, 1952; Vol. *16*.

(14) Sambongi, T. Superconductivity of LiBi. *J. Phys. Soc. Jpn.* **1971**, 30 (1), 294−294.

(15) Massalski, T. B. Binary Alloy Phase Diagrams. *ASM Int.* **1992**, 3, 2874.

(16) Xu, Y.; Yamazaki, M.; Villars, P. Inorganic Materials Database for Exploring the Nature of Material. *Jpn. J. Appl. Phys.* **2011**, *50* (11), 11RH02.

(17) Nesper, R. Structure and Chemical Bonding in Zintl-Phases Containing Lithium. *Prog. Solid State Chem.* **1990**, *20* (1), 1−45.

(18) Min, B. I.; Shim, J. H.; Park, M. S.; Kim, K.; Kwon, S. K.; Youn, S. J. Origin of the Stabilized Simple-Cubic Structure in Polonium: Spin-Orbit Interaction versus Peierls Instability. *Phys. Rev. B: Condens. Matter Mater. Phys.* **2006**, 73 (13), 132102.

(19) Zalkin, A.; Ramsey, W. J. Intermetallic Compounds between Lithium and Lead. IV. The Crystal Structure of Li $_{22}$ Pb $_5$. *J. Phys. Chem.* **1958**, *62* (6), 689−693.

(20) Xie, W.; Luo, H.; Baroudi, K.; Krizan, J. W.; Phelan, B. F.; Cava, R. J. Fragment-Based Design of NbRuB as a New Metal-Rich Boride Superconductor. *Chem. Mater.* **2015**, *27* (4), 1149−1152.

(21) Gui, X.; Sobczak, Z.; Chang, T.-R.; Xu, X.; Huang, A.; Jia, S.; Jeng, H.-T.; Klimczuk, T.; Xie, W. Superconducting SrSnP with Strong Sn−P Antibonding Interaction: Is the Sn Atom Single or Mixed Valent? *Chem. Mater.* **2018**, *30* (17), 6005−6013.

(22) Zhao, L. L.; Lausberg, S.; Kim, H.; Tanatar, M. A.; Brando, M.; Prozorov, R.; Morosan, E. Type-I Superconductivity in YbSb$_2$ Single Crystals. *Phys. Rev. B: Condens. Matter Mater. Phys.* **2012**, *85* (21). DOI: 10.1103/PhysRevB.85.214526.

(23) Sun, S.; Liu, K.; Lei, H. Type-I Superconductivity in KBi$_2$ single Crystals. *J. Phys.: Condens. Matter* **2016**, *28* (8), 085701.

(24) Svanidze, E.; Morosan, E. Type-I Superconductivity in ScGa$_3$ and LuGa$_3$ Single Crystals. *Phys. Rev. B: Condens. Matter Mater. Phys.* **2012**, *85* (17), 174514.

(25) Peets, D. C.; Cheng, E.; Ying, T.; Kriener, M.; Shen, X.; Li, S.; Feng, D. Type-I Superconductivity in Al 6 Re. *Phys. Rev. B: Condens. Matter Mater. Phys.* **2019**, *99* (14). DOI: 10.1103/PhysRevB.99.144519.

(26) Kushwaha, S. K.; Krizan, J. W.; Xiong, J.; Klimczuk, T.; Gibson, Q. D.; Liang, T.; Ong, N. P.; Cava, R. J. Superconducting Properties and Electronic Structure of NaBi. *J. Phys.: Condens. Matter* **2014**, *26* (21), 212201.

(27) McMillan, W. L. Transition Temperature of Strong-Coupled Superconductors. *Phys. Rev.* **1968**, *167* (2), 331−344.

(28) Barker, J. A. T.; Breen, B. D.; Hanson, R.; Hillier, A. D.; Lees, M. R.; Balakrishnan, G.; Paul, D. M.; Singh, R. P. Superconducting and Normal-State Properties of the Noncentrosymmetric Superconductor `${\mathrm{Re}}_{3}\mathrm{Ta}$`. *Phys. Rev. B: Condens. Matter Mater. Phys.* **2018**, 98 (10), 104506.

(29) Amon, A.; Svanidze, E.; Cardoso-Gil, R.; Wilson, M. N.; Rosner, H.; Bobnar, M.; Schnelle, W.; Lynn, J. W.; Gumeniuk, R.; Hennig, C.; et al. Noncentrosymmetric Superconductor BeAu. *Phys. Rev. B: Condens. Matter Mater. Phys.* **2018**, 97 (1), 014501.

(30) Górnicka, K.; Cava, R. J.; Klimczuk, T. The Electronic Characterization of the Cubic Laves-Phase Superconductor CaRh2. *J. Alloys Compd.* **2019**, 793, 393−399.

(31) Singh, Y.; Niazi, A.; Vannette, M. D.; Prozorov, R.; Johnston, D. C. Superconducting and Normal-State Properties of the Layered Boride Os B 2. *Phys. Rev. B: Condens. Matter Mater. Phys.* **2007**, 76 (21). DOI: 10.1103/PhysRevB.76.214510.

(32) Singh, J.; Jayaraj, A.; Srivastava, D.; Gayen, S.; Thamizhavel, A.; Singh, Y. Possible Multigap Type-I Superconductivity in the Layered Boride RuB 2. *Phys. Rev. B: Condens. Matter Mater. Phys.* **2018**, 97 (5). DOI: 10.1103/PhysRevB.97.054506.

(33) Otero-de-la-Roza, A.; Johnson, E. R.; Luaña, V. Critic2: A Program for Real-Space Analysis of Quantum Chemical Interactions in Solids. *Comput. Phys. Commun.* **2014**, *185* (3), 1007−1018.

(34) Li, R.; Cheng, X.; Xie, Q.; Sun, Y.; Li, D.; Li, Y.; Chen, X.-Q. Topological Metal of NaBi with Ultralow Lattice Thermal Conductivity and Electron-Phonon Superconductivity. *Sci. Rep.* **2015**, *5* (1). DOI: 10.1038/srep08446.

(35) Gołąb, S.; Wiendlocha, B. Electron-Phonon Superconductivity in CaBi 2 and the Role of Spin-Orbit Interaction. *Phys. Rev. B: Condens. Matter Mater. Phys.* **2019**, *99* (10). DOI: 10.1103/PhysRevB.99.104520.

(36) Allen, P. B.; Dynes, R. C. Transition Temperature of Strong-Coupled Superconductors Reanalyzed. *Phys. Rev. B* **1975**, *12* (3), 905−922.

(37) Giannozzi, P.; Baroni, S.; Bonini, N.; Calandra, M.; Car, R.; Cavazzoni, C.; Ceresoli, D.; Chiarotti, G. L.; Cococcioni, M.; Dabo, I.; et al. QUANTUM ESPRESSO: A Modular and Open-Source Software Project for Quantum Simulations of Materials. *J. Phys.: Condens. Matter* **2009**, *21* (39), 395502.

(38) Dal Corso, A. Pseudopotentials Periodic Table: From H to Pu. *Comput. Mater. Sci.* **2014**, *95*, 337−350.

(39) Perdew, J. P.; Burke, K.; Ernzerhof, M. Generalized Gradient Approximation Made Simple. *Phys. Rev. Lett.* **1996**, *77* (18), 3865−3868.

Source material's DOI: https://pubs.acs.org/doi/abs/10.1021/acs.chemmater.0c00179

Supplemental Material

Superconductivity on a Bi square net in LiBi

Karolina Górnicka[1,2], Sylwia Gutowska[3], Michał J. Winiarski[1,2],
Bartlomiej Wiendlocha[3], Weiwei Xie[4], R. J. Cava[5] and Tomasz Klimczuk[1,2]

[1] Faculty of Applied Physics and Mathematics, Gdansk University of Technology,
ul. Narutowicza 11/12, 80-233 Gdańsk, Poland,
[2] Advanced Materials Centre, Gdansk University of Technology,
ul. Narutowicza 11/12, 80-233 Gdańsk, Poland,
[3] Faculty of Physics and Applied Computer Science, AGH University of Science and Technology,
Aleja Mickiewicza 30, 30-059 Kraków, Poland
[4] Department of Chemistry, Louisiana State University, Baton Rouge LA 70803
[5] Department of Chemistry, Princeton University, Princeton, NJ 08544, USA

Powder x-ray diffraction

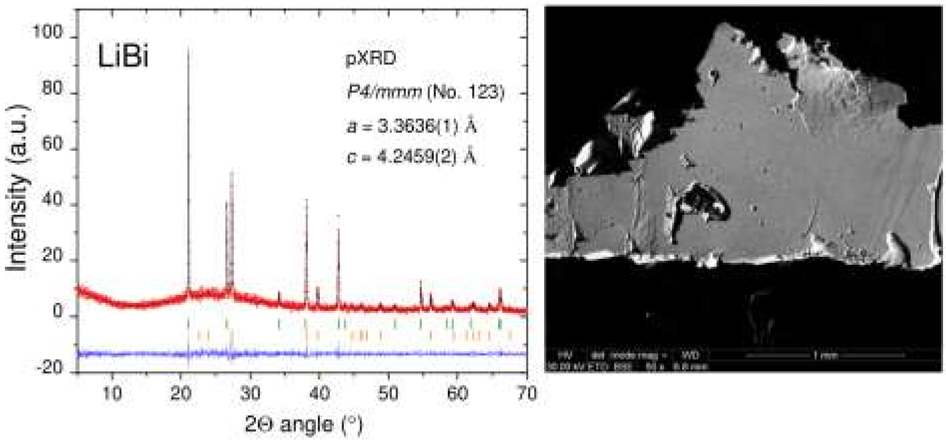

Figure 1SI. Left: Powder X-ray diffraction pattern of LiBi (red points) together with the LeBail refinement profile (black solid line). The green and orange vertical bars indicate the expected Bragg peak positions for LiBi and elemental Bi, respectively. The blue curve is the difference between experimental and model results. **Right**: The SEM image of LiBi single crystal.

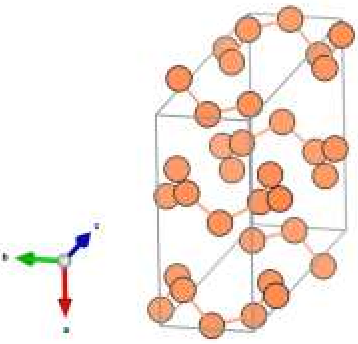

Figure 2. Structure of KBi featuring Bi spiral chains. K atoms were omitted for clarity.

The influence of spin-orbit coupling (SOC) on the electronic structure of LiBi

Here we analyze the influence of the SOC by comparing the electronic structure of LiBi calculated without and with SOC, both shown in Fig.3. and, in the smaller energy range in Fig. 4.

The main valence band (MVB) consists of three bands and starts -4.5 eV below the Fermi level. SOC significantly changes MVB, bands are separated and several peaks in DOS appear. The reason is that in the scalar-relativistic case one can observe many band crossings, marked with arrows in Fig. 4. As a consequence, the scalar-relativistic DOS of MVB has essentially only one peak placed at the energy, where the lowest two bands are crossing each other. When SOC is included, the bands are repulsed (band anticrossing) such that the gap appears between them at these particular points of the Brillouin zone. Due to appearance of the local band extrema, individual peaks in DOS appear, thus there are three peaks instead of a one. The bands, however, especially the highest two of them, are still well-dispersed and their energy ranges are not separated from each other.

Quite surprisingly, this significant change in the band structure almost does not affect the Fermi surface, as shown in Fig. 3. The only change is in the second piece of the Fermi surface, where the gap in [110] direction is opened when SOC is included. It is connected with the anticrossing of bands in ΓM direction of the Brillouin zone, shown in Fig. 4. As a consequence, the DOS (Fig. 4.) is almost unchanged around the Fermi level. The value of DOS is equal $N(E_F) = 0.674\ eV^{-1}$ and $N(E_F) = 0.676\ eV^{-1}$ in the scalar- and fully-relativistic case, respectively.

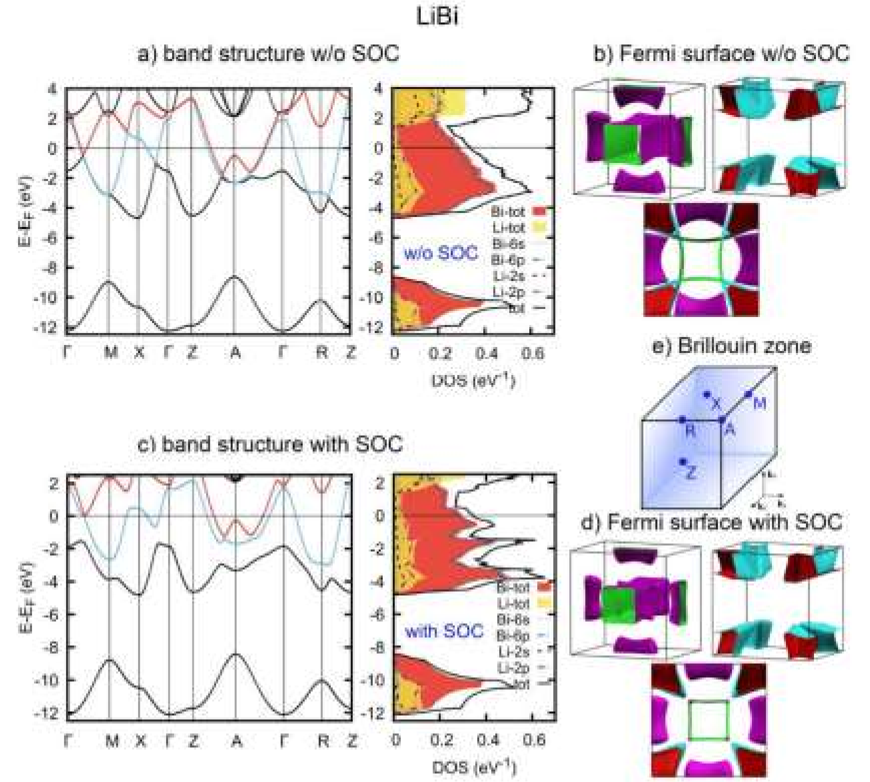

Figure 3. Electronic structure of LiBi calculated in scalar- (a-b) and fully-relativistic (c-d) way in terms of band structure and DOS (a, c) as well as the Fermi surface (b, d).

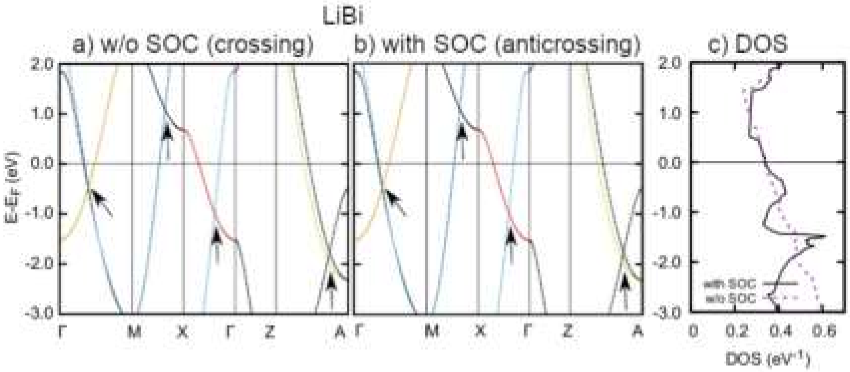

Figure 4. Zoomed picture of the band structure of LiBi calculated in the scalar- (a) and fully-relativistic (b) way, and the DOS calculated in both ways (c).

LiBi *versus* NaBi: phonons and the electron-phonon coupling

Fig. 5 shows phonon dispersion relations, phonon linewidths, phonon DOS and Eliashberg function for NaBi. The phonon structures of LiBi and NaBi are much different. The phonon frequency range in NaBi is from 0 to 5 THz, while in the case of LiBi up to 7 THz. It is not surprising, as Sodium is simply heavier than Lithium. In the acoustic part of the spectrum, up to 2.5 THz in LiBi, three peaks in phonon DOS are formed, while in the case of NaBi there is one peak contributed from all acoustic phonons and the frequency range is squeezed up to 2 THz. This change of the acoustic phonons, contributed by Bismuth atoms, can be associated with the change of the crystal and electronic structure. As described in manuscript, the crystal structure of NaBi is more distorted (c/a=1.39) than LiBi (c/a=1.26), hence the highest phonon mode, which involves out-of-plane Bi vibrations (see below), is less dispersive in the case on NaBi, than in LiBi.

The optical phonons, contributed by Li / Na atoms, spread the frequency range from 4.5 THz to 7 THz in case of LiBi and are from 2.5 THz to 5 THz in the case of NaBi. As discussed in the manuscript, in spite of this drastic lowering of frequency, the electron-phonon constants, generally proportional to $\lambda_{e-p} \propto \frac{1}{\omega^2}$, is lower in NaBi ($\lambda_{e-p} = 0.62$) than in the case of LiBi ($\lambda_{e-p} = 0.66$), due to enhanced contribution of the optical mode in the latter system.

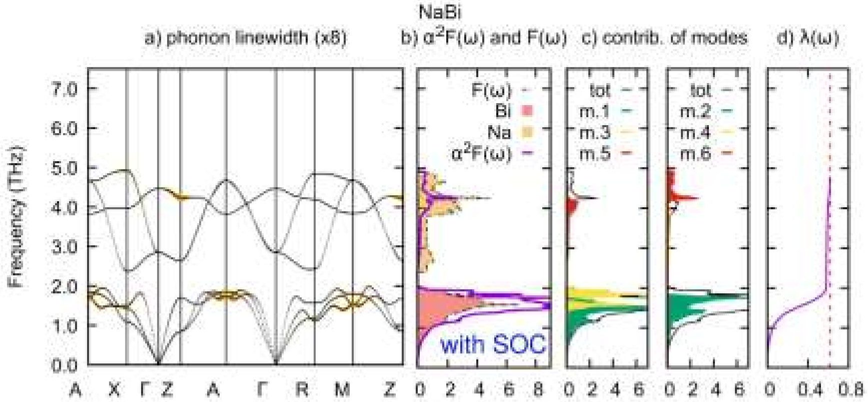

Figure 5. Phonon structure and electron-phonon coupling in NaBi in terms of (a) phonon dispersion relation with phonon linewidth marked as "fatbands" (b) phonon DOS and Eliasherg function, (c) contribution of the modes do the Eliashberg function, (d) frequency distribution of λ. The figure should be compared with fig. 5 of the manuscript, where these properties of LiBi are shown.

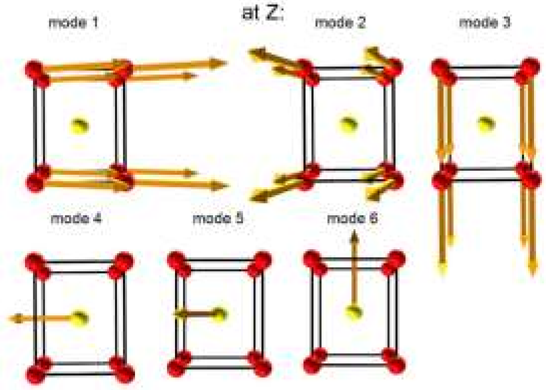

Figure 6. The phonon displacement patterns of the six phonon modes for **q**=(0,0,0.5) (Z point in the Brillouin zone) of LiBi (not in the scale). We can distinguish two transverse acoustic in-plane Bi modes (1 & 2), one longitudal acoustic Bi mode (3), two transverse optical in-plane Li modes (4 & 5) and one longitudal optical Li mode (6). The sixth mode, which has the biggest phonon linewidth, is along the direction where the unit cell is distorted.

Source material's DOI: https://pubs.acs.org/doi/abs/10.1021/acs.chemmater.0c00179

4.7 (A7) $NbIr_2B_2$ and $TaIr_2B_2$ – New Low Symmetry Noncentrosymmetric Superconductors with Strong Spin–Orbit Coupling

4.7.1 Cel badawczy

Nośnikami prądu elektrycznego w nadprzewodnikach są tzw. pary Coopera. Teoria Bardeena-Coopera-Schriefera (BCS) zakłada, że nośniki tworzące parę Coopera charakteryzują się przeciwnie skierowanymi spinami (stan singletowy). Zewnętrzne pole magnetyczne, o wartość powyżej limitu Pauli'ego (H_c^{Pauli}), powoduje przeorientowanie jednego ze spinów, co w konsekwencji prowadzi do rozerwania pary Coopera i zaniku nadprzewodnictwa. Rozważania teoretyczne wskazują, że w układach niecentrosymetrycznych, w których dodatkowo występuje silne sprzężenie spin-orbita (SOC), możliwe jest mieszanie symetrii par Coopera. Oznacza to, że obok składowej singletowej występować będzie również składowa trypletowa, a dla takiej limit Pauli'ego nie ma zastosowania, a co za tym idzie drugie pole krytyczne może przewyższać H_c^{Pauli}.

Odkrycie dwóch nadprzewodników $(Nb,Ta)Rh_2B_2$ było motywacją do postawienia **hipotezy badawczej 7** zakładającej, że istnieją izoelektronowe odpowiedniki potrójnych związków $(Nb,Ta)Rh_2B_2$ z irydem, które również wykazują właściwości nadprzewodzące.

Otrzymanie borków irydowo-niobowych i irydowo-tantalowych było możliwe dzięki gruntownej eksploracji potrójnych diagramów fazowych Nb/Ta-Ir-B. Silny sygnał diamagnetyczny świadczący o występowaniu nadprzewodnictwa z T_c około 7 K (dla układu z Nb) był bezpośrednią motywacją aby przygotować blisko kilkadziesiąt próbek o różnej stechiometrii, które były syntetyzowane w różnych temperaturach w piecu wysoko-próżniowym.

Celem badań opisanych w publikacji A7 było otrzymanie czystych fazowo próbek związków $\{Nb,Ta\}Ir_2B_2$, opis struktury krystalicznej (dr Xin Gui, prof. Weiwei Xie, prof. Robert J. Cava) oraz eksperymentalne wyznaczenie parametrów charakteryzujących stan nadprzewodzący i normalny. Badania eksperymentalne obejmowały proszkową dyfrakcję rentgenowską, analizę strukturalną za pomocą czterokołowego dyfraktometru rentgenowskiego, pomiary elektryczne, cieplne oraz magnetyczne. Szczegółowe badania właściwości fizycznych zostały uzupełnione obliczeniami struktury elektronowej (dr hab. inż. Bartłomiej Wiendlocha).

4.7.2 Opis rezultatów

Jednym z wyzwań podczas badań związków $NbIr_2B_2$ oraz $TaIr_2B_2$ było rozwiązanie struktury krystalicznej, co bezpośrednio wiąże się z tym, że struktura tego typu nie była w literaturze opisana. Otrzymany materiał, o znanym składzie nominalnym, był badany za pomocą techniki dyfrakcji na monokryształach. W kolejnym kroku, proponowany model struktury krystalicznej był weryfikowany poprzez analizę LeBaile'a i Rietvielda proszkowych dyfraktogramów rentgenowskich, a także wyniki analizy EDX. Ostatecznie ustalono, że $NbIr_2B_2$ oraz $TaIr_2B_2$ krystalizują w nowej, jednoskośnej, niecentrosymetrycznej strukturze krystalicznej (*Cc* No.9). Warto wspomnieć, że nadprzewodniki bardzo rzadko występują w strukturze jednoskośnej.

Izoelektronowe związki nadprzewodnikowe: $NbRh_2B_2$ i $TaRh_2B_2$ krystalizują w trygonalnej strukturze, wykazującej chiralność. W obu typach struktur krystalicznych cechą wspólną są dimery atomów boru, które oddalone są od siebie o ok. 1.7Å. Występuje jednak różnica ułożeń dimerów, tak że dla związków na bazie Rh obserwuje się dwa (X, Y), podczas gdy dla związków na bazie Ir trzy (X, Y, Z) charakterystyczne sposoby ułożenia dimerów boru.

Drugim wyzwaniem było opracowanie powtarzalnej metody syntezy, tj. ustalenie optymalnego nominalnego składu pierwiastkowego, temperatury i czasu wygrzewania. Czynnikami, które zdecydowały o sukcesie syntezy nowych związków były odpowiednio dobrana: nadwyżka boru, a także temperatura wygrzewanie próbek (1100℃). Proces prowadzony był w warunkach wysokiej oraz dynamicznej próżni ($p = 10^{-6}$ Torr).

Niskotemperaturowe badania podatności magnetycznej, ujawniły przejście ze stanu normalnego w stan nadprzewodzący w $T_c = 7.16$ K dla $NbIr_2B_2$ oraz $T_c = 5.07$ K dla $TaIr_2B_2$. Są to temperatury tylko nieznacznie niższe od podanych dla $NbRh_2B_2$ i $TaRh_2B_2$. Dalsze pomiary magnetyczne tj. namagnesowanie w funkcji zewnętrznego pola magnetycznego, pozwoliły na sklasyfikowanie $NbIr_2B_2$ i $TaIr_2B_2$ jako nadprzewodników II-go rodzaju. Oszacowana wartość dolnego pola krytycznego wyniosła $\mu_0H_{c1}(0) = 13.0$ mT dla $NbIr_2B_2$ oraz $\mu_0H_{c1}(0) = 6.0$ mT dla analogu z Ta.

Pomiary ciepła właściwego potwierdziły objętościowe nadprzewodnictwo w obu związkach. Wyznaczony znormalizowany skok ciepła właściwego $(\Delta C/\gamma T_c)$ wynosi 2.94 oraz 1.44 odpowiednio dla $NbIr_2B_2$ oraz $TaIr_2B_2$. Skok dla związku z Nb ponad dwukrotnie przewyższa wartość wynikającą z teorii BCS ($\Delta C/\gamma T_c = 1.43$) co sugeruje, że za nadprzewodnictwo odpowiadają silnie sprzężone nośniki ładunków. Powyższy wniosek znajduje potwierdzenie w uzyskanej wartości parametru sprzężenia elektron-fonon $\lambda_{ep} = 0.74$ ($NbIr_2B_2$) oraz $\lambda_{ep} = 0.70$ ($TaIr_2B_2$).

W następnej kolejności wykonano pomiary oporu elektrycznego. W przypadku związku $NbIr_2B_2$ oporność właściwa maleje wraz z obniżaniem temperatury, natomiast dla analogu z Ta obserwowany jest wzrost krzywej $\rho(T)$. Takie zachowanie najpewniej spowodowane jest słabą lokalizacją nośników ładunku na skutek występującego nieporządku struktury krystalicznej. W niskich temperaturach (poniżej T_c) zaobserwowano spadek oporności do zera, świadczący o przejściu obu związków do stanu nadprzewodzącego. Przyłożenie pola magnetycznego skutkuje przesunięciem temperatury przejścia w stronę niższych wartości. Wyznaczona wartość górnego pola krytycznego wynosi $\mu_0H_{c2}(0) = 16.3(2)$ T dla $NbIr_2B_2$ oraz $\mu_0H_{c2}(0) = 14.7(1)$ T dla $TaIr_2B_2$. W przypadku obu nadprzewodników $\mu_0H_{c2}(0)$ przekracza limit Pauli'ego ($\mu_0H^{Pauli} = 1.85T_c$), który wynosi 13.3(1) T dla związku z Nb oraz 9.5(1) T dla analogu z Ta. Uzyskane wyniki mogą świadczyć o niekonwencjonalnym charakterze nadprzewodnictwa w badanych związkach.

4.7.3 Treść artykułu A7

4.7.3 Treść artykułu A7

Tytuł: $NbIr_2B_2$ and $TaIr_2B_2$ – New Low Symmetry Noncentrosymmetric Superconductors with Strong Spin–Orbit Coupling

Autorzy: Karolina Górnicka, Xin Gui, Bartłomiej Wiendlocha, Loi T. Nguyen, Weiwei Xie, Robert J. Cava, Tomasz Klimczuk

Czasopismo: Advanced Functional Materials 2021, *31*, 2007960

Impact factor: 16.836 (2019)

Liczba punktów ministerialnych MNiSW: 200 pkt

DOI: 10.1002/adfm.202007960

Mój udział polegał na syntezie próbek polikrystalicznych metodą syntezy w fazie stałej, przeprowadzeniu badania metodą proszkowej dyfrakcji rentgenowskiej wraz z analizą Rietvelda, pomiarach i analizie wyników właściwości magnetycznych, elektrycznych oraz cieplnych, udziale w dyskusji uzyskanych rezultatów, wyznaczeniu parametrów charakteryzujących stan normalny i nadprzewodzący, przygotowaniu rysunków oraz tekstu manuskryptu w części eksperymentalnej. Brałam udział w przygotowaniu odpowiedzi na recenzje.

Karolina Górnicka

mgr inż. Karolina Górnicka

The original source: Adv. Funct. Mater. *2021, 31, 2007960*

FULL PAPER

ADVANCED FUNCTIONAL MATERIALS
www.afm-journal.de

$NbIr_2B_2$ and $TaIr_2B_2$ – New Low Symmetry Noncentrosymmetric Superconductors with Strong Spin–Orbit Coupling

*Karolina Górnicka, Xin Gui, Bartlomiej Wiendlocha, Loi T. Nguyen, Weiwei Xie, Robert J. Cava, and Tomasz Klimczuk**

Superconductivity was first observed more than a century ago, but the search for new superconducting materials remains a challenge. The Cooper pairs in superconductors are ideal embodiments of quantum entanglement. Thus, novel superconductors can be critical for both learning about electronic systems in condensed matter and for possible application in future quantum technologies. Here two previously unreported materials, $NbIr_2B_2$ and $TaIr_2B_2$, are presented with superconducting transitions at 7.2 and 5.2 K, respectively. They display a unique noncentrosymmetric crystal structure, and for both compounds the magnetic field that destroys the superconductivity at 0 K exceeds one of the fundamental characteristics of conventional superconductors (the "Pauli limit"), suggesting that the superconductivity may be unconventional. Supporting this experimentally based deduction, first-principle calculations show a spin-split Fermi surface due to the presence of strong spin–orbit coupling. These materials may thus provide an excellent platform for the study of unconventional superconductivity in intermetallic compounds.

1. Introduction

Superconducting compounds continue to challenge our ideas about how to understand the behavior of electronic materials. Across the many superconductors known, there are two fundamental parameters of most general interest: the temperature below which the superconducting state occurs (T_c) and the critical magnetic field required to fully suppress the superconductivity (H_{c2}). The second parameter, which is crucial from the practical point of view, must, at 0 K in a conventional picture, be below the so called "Pauli limit" ($\mu_0 H_{c2}(0) = 1.85 T_c$), which is derived from a simple relation assuming that the Zeeman energy splitting must be lower than the superconducting energy gap.[1] This is not necessarily the case for superconductors that lack a center of symmetry (NCS), however. The absence of inversion symmetry, when present in systems together with spin orbit coupling (SOC), introduces an antisymmetric spin–orbit coupling (ASOC)[2,3] term into the description of the electronic system that leads to a splitting of electronic bands. As a result, a mixture of singlet and triplet pairing can be observed[2,4–6] and the upper critical field can potentially be larger than predicted by the Pauli relation. For this reason, NCS superconductors are of significant interest.[1,7–15]

Here we describe two previously unreported compounds, $NbIr_2B_2$ and $TaIr_2B_2$, the first known ternary compounds in the Nb–Ir–B and Ta–Ir–B chemical systems. They form in an unreported, low symmetry *Cc* noncentrosymmetric crystal structure. Magnetization, heat capacity and resistivity measurements confirm presence of superconductivity with T_c's = 7.2 and 5.1 K. The estimated upper critical fields $\mu_0 H_{c2}(0) = 16.3$ and 14.7 T respectively, significantly exceed the Pauli limit (which for $NbIr_2B_2$ is 13.3 T and for $TaIr_2B_2$ is 9.5 T). Our electronic band structure calculations show that the Fermi surface is mostly formed by Ir-5*d* orbitals and is split by strong SOC. The theoretical results support a multigap scenario for $NbIr_2B_2$—which we speculate to be present based on the analysis of the heat capacity data in the superconducting state of that material.

2. Results and Discussion

2.1. Crystal Structure

$NbIr_2B_2$ adopts a previously unreported structure type in the space group *Cc* (no. 9), determined by single crystal X-ray

---

K. Górnicka, Prof. T. Klimczuk
Faculty of Applied Physics and Mathematics
Gdansk University of Technology
ul. Narutowicza 11/12, Gdańsk 80–233, Poland
E-mail: tomasz.klimczuk@pg.edu.pl
K. Górnicka, Prof. T. Klimczuk
Advanced Materials Centre
Gdansk University of Technology
ul. Narutowicza 11/12, Gdańsk 80–233, Poland
Dr. X. Gui, L. T. Nguyen, Prof. R. J. Cava
Department of Chemistry
Princeton University
Princeton, NJ 08540, USA
Dr. B. Wiendlocha
Faculty of Physics and Applied Computer Science
AGH University of Science and Technology
Aleja Mickiewicza 30, Kraków 30–059, Poland
Prof. W. Xie
Department of Chemistry and Chemical Biology
Rutgers University
Piscataway, NJ 08854, USA

The ORCID identification number(s) for the author(s) of this article can be found under https://doi.org/10.1002/adfm.202007960.

DOI: 10.1002/adfm.202007960

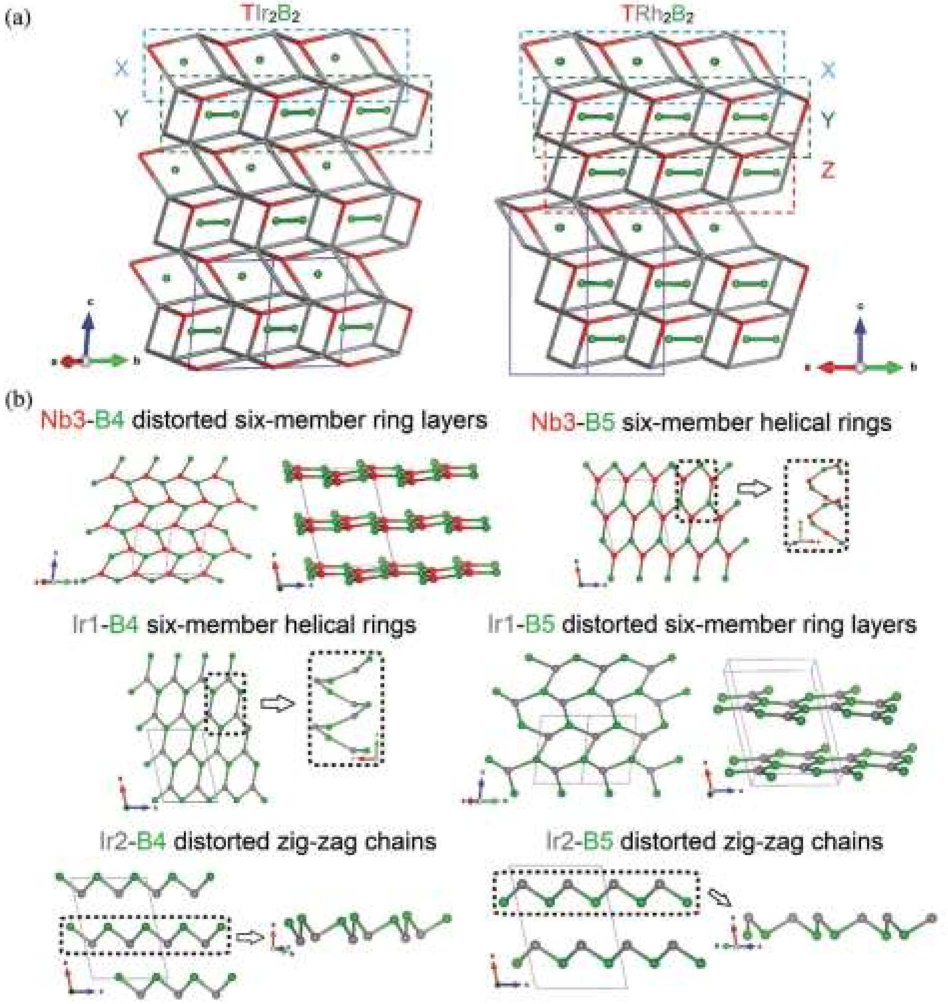

Figure 1. a) The structural comparison between TIr_2B_2 and TRh_2B_2 with emphasis on the stacking pattern difference. b) The coordination environments of the Boron atoms in TIr_2B_2.

diffraction (see Table S1 in the Supporting Information), shown in **Figure** 1a. Details of the crystal structure, i.e., atomic coordinates and anisotropic thermal displacements are provided in Tables S2 and S3 in the Supporting Information, respectively. The single crystal structure determination shows that Boron dimers occupy the voids in the five edge-sharing Nb@Ir_4 polyhedra (see Figure 1a). $NbIr_2B_2$ and $TaIr_2B_2$ are isoelectronic to noncentrosymmetric superconductors $NbRh_2B_2$ and $TaRh_2B_2$, which are found in the chiral space group $P3_1$, instead of the current monoclinic space group.[9] TT'_2B_2 (T = Nb and Ta; T' = Rh and Ir) share common structural features, as shown in Figure 1a. Two repeating units are present in TIr_2B_2, labelled as X and Y. There is a third type of repeating unit, marked as Z, found in TRh_2B_2. Note that the difference between Y and Z is that the B dimers are not aligned in parallel. Therefore, TIr_2B_2 can be interpreted as a stacking system with a pattern of XYXYXY while TRh_2B_2 stacks as XYZXYZXYZ. The difference between Ir and Rh atoms plays an important role in determining that the stability of the repeating unit Z. Figure 1b shows coordination of two distinct boron sites (B4 and B5) in $NbIr_2B_2$ to different atoms (Nb3, Ir1, and Ir2). One can find that Nb3-B4 and Ir1-B5 construct edge-shared distorted six-member ring layers while Nb3-B5 and Ir1-B4 build up six-member helical rings. In these four frameworks, boron atoms are three coordinated to Nb3/Ir1 atoms. While turning to the other Ir site, marked as Ir2, boron atoms become two-coordinated with Ir atoms and construct quasi-1D distorted Ir-B zig-zag chains.

We also performed powder X-ray diffraction (pXRD) on powderized $NbIr_2B_2$ and $TaIr_2B_2$. Rietveld refinements of the pXRD diffraction patterns (Figure S1, Supporting Information) confirm that both compounds crystallize in the same monoclinic, noncentrosymmetric structure and show that replacement of the 4*d* element Nb by the 5*d* element Ta causes a small decrease (≈0.5%) of the unit cell volume.

The energy dispersive X-ray spectroscopy (EDS) analysis of these materials reveals that the Nb(Ta):Ir ratio, 1:2, is consistent with the nominal composition ($Nb(Ta)Ir_2B_2$), confirming the refined structural model (for the Nb(Ta) and Ir, the B content is not quantitatively determined by this method).

2.2. Superconducting Properties

The superconductivity in $NbIr_2B_2$ and $TaIr_2B_2$ is revealed through the magnetic measurements shown in **Figure 2**a–d. Figure 2a,b present the temperature dependence of the volume dc magnetic susceptibility $\chi_V(T)$ with a clear transition to the superconducting state. Superconducting critical temperature determined from the magnetic susceptibility is estimated as the point at which the line set by the steepest slope of the superconducting signal in the zero-field cooled data set intersects with the extrapolation of the normal-state magnetic susceptibility to lower temperatures.[16] The critical temperature is estimated to be $T_c = 7.2$ K and $T_c = 5.1$ K for $NbIr_2B_2$ and $TaIr_2B_2$, respectively. Correcting the dc susceptibility data for the demagnetization factor (derived from $M(\mu_0 H)$ studies as it is described in the Supporting Information), $N = 0.49$ for the Nb variant and $N = 0.55$ for the Ta variant, the ZFC measurements are consistent with 100% Meissner volume fraction. The N values are fairly consistent with the expected (theoretical) N_z value derived for a circular cylinder sample with the height to radius ratio of approx. 0.5 (see ref. [17]). Compared with the ZFC data, the observed FC signal is much weaker, which is typical for polycrystalline samples.

Discussing the characterization of the superconductors in more detail, the magnetization versus applied magnetic field $M(\mu_0 H)$ curves over a range of temperatures below the superconducting critical temperature are shown in the inset of Figure 2c,d. The first deviation from linearity from the initial slope is taken as the basis to determine the value of the lower critical field ($\mu_0 H_{c1}^*$) in these type-II superconductors. In order to precisely calculate this point, and also obtain a

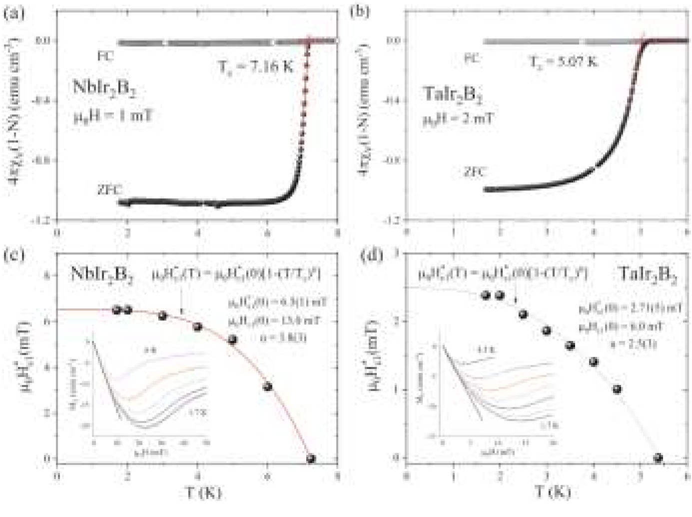

Figure 2. Temperature dependences of the zero-field-cooled (ZFC) and field-cooled (FC) volume magnetic susceptibility measured in a magnetic field of a) 1 mT for $NbIr_2B_2$ and b) 2mT for $TaIr_2B_2$. The temperature dependence of the lower critical fields for c) $NbIr_2B_2$ and d) $TaIr_2B_2$. The inset shows the field-dependent magnetization curves $M_V(\mu_0 H)$ taken at different temperatures.

demagnetization factor N, we follow the methodology described in the Supporting Information and in the literature.[12,18] The resulting estimated values of $\mu_0H^*_{c1}$ are depicted in the main panel of Figure 2c,d. An additional point for $H = 0$ is the zero field transition temperature taken from the resistivity measurement. The data points are modeled using the expression

$$\mu_0 H^*_{c1}(T) = \mu_0 H^*_{c1}(0)\left[1-\left(\frac{T}{T_c}\right)^n\right] \tag{1}$$

where $\mu_0H^*_{c1}(0)$ is the lower critical field at 0 K and T_c is the superconducting critical temperature. A typical $\mu_0H_{c1}(T)$ relation has parabolic character ($n = 2$) although there is no fundamental significance of the parabolic shape.[19] Our experimental data are well described with the above formula and the fit (red solid line) yields $n = 3.8(3)$, $T_c = 7.23(5)$ K and $\mu_0H^*_{c1}(0) = 6.5(1)$ mT for the Nb variant, and $n = 2.5(3)$, $T_c = 5.41(6)$ K and $\mu_0H^*_{c1}(0) = 2.71(5)$ mT for the Ta variant. Taking into account the demagnetization factor N for each sample, the lower critical field (μ_0H_{c1}) at 0 K was calculated from the formula

$$\mu_0 H_{c1}(0) = \mu_0 H^*_{c1}(0)/(1-N) \tag{2}$$

The obtained values are $\mu_0H_{c1}(0) = 13.0$ mT for $NbIr_2B_2$ and $\mu_0H_{c1}(0) = 6.0$ mT for $TaIr_2B_2$.

The low-temperature heat capacity measurements were performed to confirm the bulk nature of the superconductivity and in order to obtain important superconducting parameters, i.e., the normalized specific heat jump ($\Delta C/\gamma T_c$) and electron–phonon coupling constant (λ_{e-p}). The results are shown in **Figure 3**a–c. A pronounced, large anomaly in the zero-field C_p/T data confirms the bulk nature of the superconductivity

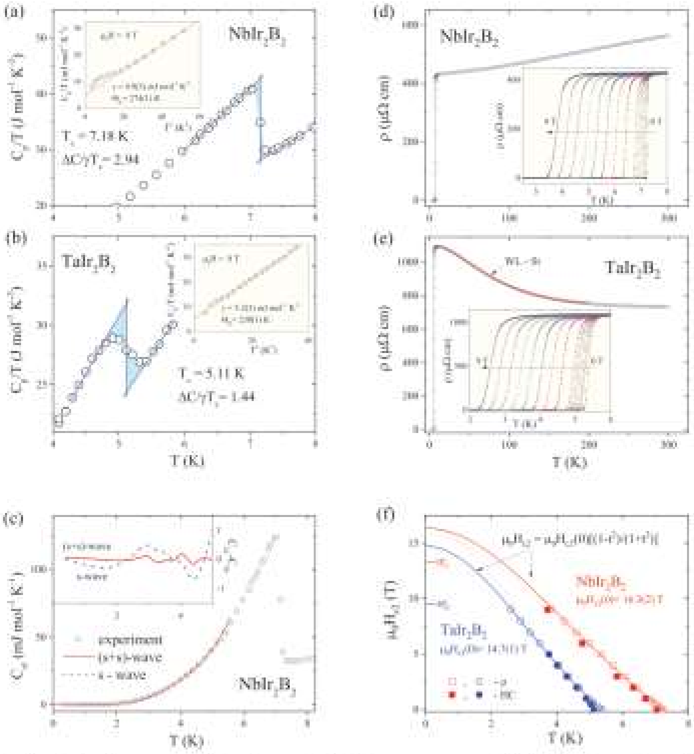

Figure 3. Further characterization of the superconductors. The specific heat jump in zero magnetic field at low temperatures with a) $T_c = 7.18$ K for $NbIr_2B_2$ and b) $T_c = 5.11$ K for $TaIr_2B_2$. Inset: C_p/T versus T^2 measured in 8 T field (in the normal state) fitted to $C_p/T = \gamma + \beta T^2$. c) Temperature-dependent electronic specific heat C_{el} for $NbIr_2B_2$ with a fit of a single gap isotropic s-wave model (blue dashed line) and an isotropic two-gap (s+s)-wave model (red solid line) to the data. The temperature dependence of the electrical resistivity of d) $NbIr_2B_2$ and e) $TaIr_2B_2$ measured in zero magnetic field. The inset shows the low temperature resistivity data taken in several different magnetic fields. f) Temperature dependence of the upper critical field, determined from the electrical resistivity (open points) and heat capacity (full points) data.

for both compounds. From the equal entropy construction (blue solid lines) one finds the critical temperature $T_c = 7.18$ K for the Nb-based compound (Figure 3a) and $T_c = 5.11$ K for the Ta-based compound (Figure 3b). The variations of C_p/T with T^2 at lower temperature and under 8 T magnetic field are presented in the insets of Figure 3a,b. The normal state specific-heat data can be fitted using the equation $C_p/T = \gamma + \beta T^2$, where the first and second terms are attributed to the electronic and lattice contributions to C_p, respectively. The extrapolation gives $\gamma = 4.9(3)$ mJ mol^{-1} K^{-2} and $\beta = 0.470(7)$ mJ mol^{-1} K^{-4} for $NbIr_2B_2$ and $\gamma = 5.2(3)$ mJ mol^{-1} K^{-2} and $\beta = 0.80(1)$ mJ mol^{-1} K^{-4} for $TaIr_2B_2$. Having calculated the Sommerfeld coefficient (γ) and the specific heat jump ($\Delta C/T_c$) at T_c, another important superconducting parameter can be obtained. The normalized specific heat jump ($\Delta C/\gamma T_c$) is equal 2.94 and 1.44 for $NbIr_2B_2$ and $TaIr_2B_2$, respectively. In the case of Nb variant compound, the calculated value (2.94) is much larger than the expected value of 1.43 for the Bardeen–Cooper–Schrieffer (BCS) weak coupling limit and suggests that strongly coupled electrons are involved in the superconductivity in this compound. Such a large value of $\Delta C/\gamma T_c$ was reported for Mo_3Al_2C (2.14),[20] W_3Al_2C (2.7),[7] KOs_2O_6 (2.87),[21] $Rh_{17}S_{15}$ (2.0),[22] or IrGe (3.04).[23]

In the next step, the Debye temperature Θ_D was calculated using the relation

$$\Theta_D = \left(\frac{12\pi^4}{5\beta} nR\right)^{1/3} \tag{3}$$

where $R = 8.31$ J mol^{-1} K^{-1} is a gas constant, $n = 5$ is the number of atoms per formula unit. The values of Θ_D were estimated to be 274(1) K for $NbIr_2B_2$ and 230(1) K for $TaIr_2B_2$. Having the calculated Debye temperature Θ_D, the electron–phonon constant λ_{e-p}, a dimensionless number that describes the coupling between the electron and the phonon, can be calculated from the inverted McMillan formula[24]

$$\lambda_{e-p} = \frac{1.04 + \mu^* \ln(\Theta_D / 1.45T_c)}{(1 - 0.62\mu^*)\ln(\Theta_D / 1.45T_c) - 1.04} \tag{4}$$

where μ^* is the Coulomb pseudopotential parameter having typical material specific values in the range $0.1 \leq \mu^* \leq 0.15$, where 0.13 is typically used for intermetallic superconductors.[9,25–27] The constant $\lambda_{e-p} = 0.74$ for $NbIr_2B_2$ and $\lambda_{e-p} = 0.70$ for $TaIr_2B_2$, suggesting that both compounds are moderately or strongly coupled superconductors.

The temperature dependence of the electronic specific heat (C_{el}) below T_c for $NbIr_2B_2$ is shown in Figure 3c. The C_{el} was then analyzed by fitting the data with a single gap isotropic *s*-wave model and an isotropic two-gap (*s*+*s*)-wave model. Both fits were done below 5 K, which is about 0.7 T_c and the expected by BCS theory value energy gap is $2\Delta_0 = 3.52k_BT_c = 2.17$ meV. An *s*-wave single gap BCS model (blue dashed line) gives $2\Delta_0 = 2.70(6)$ meV. A better fit was obtained assuming a multigap (*s*+*s*) scenario with $2\Delta_{01} = 2.32(5)$ meV and $2\Delta_{02} = 9.1(12)$ meV, represented by a red line. The dashed and solid lines in the inset represent the difference between the experiment and a single and double *s*-wave gap model, respectively. For a gap with nodes, theory predicts power-law dependence, which does not work here; the fits are shown in Figure S3 (Supporting Information) of the Supporting Information. More experiments that shed light on the gap symmetry are required. For example, multigap superconductivity, probed by the μSR technique, has been reported for isoelectronic but not isostructural $TaRh_2B_2$.[28]

The last experimental technique used for characterization of the new superconductors was temperature dependent resistivity with the results shown in the main panel of Figure 3d for $NbIr_2B_2$ and Figure 3e for $TaIr_2B_2$. $NbIr_2B_2$ behaves like a poor metal, with a shallow negative gradient for the resistivity upon cooling from room temperature. The residual resistivity ratio (RRR), $\rho_{300}/\rho_{10} = 1.3$, is small, which can be attributed to the polycrystalline nature of the sample contained grain boundaries and macroscopic defects. In the case of Ta variant, one observes an increase in $\rho(T)$ as the temperature was decreased. Comparing ρ (300 K) and ρ (10 K), resistivity increases about 50%. This behavior could be due to a weak localization (WL) of charge carriers due to disorder. The experimental data were fitted with the function[29,30] $\rho(T) = [1/(\sigma_0 + \alpha T^{p/2})] + \beta T$, where $\sigma_0 = 1/\rho_0$ is the residual conductivity, p is related to the temperature dependence of the inelastic scattering time and the second term describes the high temperature part. The experimental data are very well described with this model ($R^2 = 0.9996$), yielding the fit parameters $\sigma_0 = 9.02(1) \times 10^{-4}$ μΩ^{-1} cm^{-1}, $\alpha = 6.5(2) \times 10^{-6}$ μΩ^{-1} cm^{-1} K$^{-p/2}$, $p = 2.92(2)$ and $\beta = 1.71(2)$ μΩ cm K^{-1}.

At low temperatures the electrical resistivity drops sharply to zero at $T_c = 7.24$ K for $NbIr_2B_2$ and at $T_c = 5.38$ K for $TaIr_2B_2$, where T_c is defined as the midpoint of the transition. The slightly higher superconducting temperature value obtained in the resistivity measurement is likely due to the influence of surface superconductivity emerging in each cross-sectional area of the sample. The effect of applying a magnetic field on T_c is shown in the insets of Figure 3d,e. As expected, the transition becomes broader, and T_c shifts to lower temperature, as the applied field is increased. It should be noted that a transition to a zero-resistance state was obtained even at 9 T and above 3 K for $NbIr_2B_2$ or 2 K for $TaIr_2B_2$, indicating a large upper critical field.

Using the midpoint resistivity, the upper critical field (μ_0H_{c2}) for both compounds, plotted as a function of temperature, is illustrated in Figure 3f. For $TaIr_2B_2$ one observes a small concave-upwards curvature curve of μ_0H_{c2} versus T. Such behavior is a typical feature observed for conventional superconductors with an anisotropic Fermi surface, and has been observed in multigap superconductors, as well as in unconventional superconductors.[22] The solid line, presented in Figure 3f, is a fit to the Ginzburg–Landau expression

$$\mu_0H_{c2}(T) = \mu_0H_{c2}(0)\frac{(1-t^2)}{(1+t^2)} \tag{5}$$

where $t = T/T_c$ and T_c is the transition temperature at zero magnetic field. Our experimental data fit Equation (5) fairly well. The obtained values of $\mu_0H_{c2}(0)$ are: 16.3(2) T and 14.7(1) T for $NbIr_2B_2$ and $TaIr_2B_2$, respectively. According to the BCS theory, the Pauli-limiting field can be obtained from $\mu_0H_{c2}^{P}(0) = 1.85T_c$, which for $NbIr_2B_2$ gives $\mu_0H_{c2}^{P}(0) = 13.3(1)$

T and $\mu_0H_{c2}^{P}(0) = 9.5(1)$ T for $TaIr_2B_2$. The experimentally estimated $\mu_0H_{c2}(0)$ values obtained for the current materials are roughly 20% and 50% larger than the $\mu_0H_{c2}^{P}$, and hence suggest that the materials may exhibit non-BCS superconductivity. The critical temperatures extracted from the anomaly in $C_p(T)$ at the superconducting transition are also added to Figure 3f (filled circles and squares). The thermodynamic data were fitted with Equation (5) (dashed line), yielding $\mu_0H_{c2}(0) = 15.8(1)$ T for Nb variant and $\mu_0H_{c2}(0) = 16.5(2)$ T for Ta variant. Table S7 (Supporting Information) gathers $\mu_0H_{c2}(0)$ values obtained from GL and WHH models. In all cases the $\mu_0H_{c2}(0)$ exceeds the Pauli-limiting field.

Consequently, the characteristic Ginzburg–Landau coherence length, ξ_{GL}, can be obtained using the relation

$$\mu_0H_{c2}(0) = \frac{\Phi_0}{2\pi\xi_{GL}^2} \tag{6}$$

where $\Phi_0 = hc/2e$ is the quantum flux, and μ_0H_{c2} were taken from the GL fit to the resistivity data. This way, the value of ξ_{GL} was estimated to be 45 Å for $NbIr_2B_2$ and 47 Å for $TaIr_2B_2$. In the next step, the Ginzburg–Landau penetration depth $\lambda_{GL}(0)$ can be calculated from the relation

$$\mu_0H_{c1}(0) = \frac{\Phi_0}{4\pi\lambda_{GL}^2}\ln\frac{\lambda_{GL}}{\xi_{GL}} \tag{7}$$

The value is found to be $\lambda_{GL}(0) = 2230$ Å for Nb variant and $\lambda_{GL}(0) = 3420$ Å for Ta variant. From the equation $\kappa_{GL} = \lambda_{GL}/\xi_{GL}$, the Ginzburg–Landau parameter κ_{GL} is about 50 for $NbIr_2B_2$ and 72 for $TaIr_2B_2$ and therefore, it is clear that each superconducting material is a type-II superconductor ($\kappa_{GL} > 1/\sqrt{2}$). Finally, the thermodynamic critical field can be obtained from κ_{GL}, H_{c1}, and H_{c2} using the formula

$$H_{c1}H_{c2} = H_c^2 \ln\kappa_{GL} \tag{8}$$

yielding $\mu_0H_c = 232$ mT for $NbIr_2B_2$ and $\mu_0H_c = 144$ mT for $TaIr_2B_2$. All the superconducting and normal state parameters of $NbIr_2B_2$ and $TaIr_2B_2$ are gathered in **Table 1**.

Table 1. Superconducting parameters of TIr_2B_2 where T = Nb and Ta.

Parameter	Unit	$NbIr_2B_2$	$TaIr_2B_2$
T_c	K	7.18	5.11
$\mu_0H_{c1}(0)$	mT	13.0	6.0
$\mu_0H_{c2}(0)$	T	16.3	14.7
μ_0H^{Pauli}	T	13.3	9.5
ξ_{GL}	Å	45	47
λ_{GL}	Å	2230	3420
κ_{GL}	–	50	72
γ	mJ mol^{-1} K^{-2}	4.9	5.2
$\Delta C_p/\gamma T_c$	–	2.94	1.44
λ_{e-p}	–	0.74	0.70
Θ_D	K	274	230

2.3. Electronic Band Structure

To get an insight into the electronic structure of our compounds, density functional theory (DFT) calculations were performed. **Figure 4** shows the computed electronic bands E(k) and densities of states (DOS), whereas Fermi surface is displayed in **Figure 5**. As seen from the atomic character of DOS near E_F, the Fermi surface will be mainly formed from Nb-4d (Ta-5d) and Ir-5d orbitals, and due to larger atomic population, contribution from Ir is larger. Figure 4a,c shows that two bands are crossing E_F in a scalar-relativistic case, and due to combination of spin–orbit coupling and lack of inversion symmetry, bands are split. The value of energy band splitting (E_{ASOC}) is strongly k-dependent and ranges from 25 to 250 meV, as large as is seen in $CePt_3Si$ or Li_2Pt_3B[15] (≈200 meV) and larger than in $LaNiC_2$,[11,12] (≈40 meV), where nonunitary triplet pairing has been proposed.[11] Generally, systems with large E_{ASOC} are promising to look at for singlet-triplet mixing.[15] SOC has a negligible effect on the DOS(E_F) in $NbIr_2B_2$, but, for $TaIr_2B_2$, the relativistic value is reduced by about 20% due to a shift in the DOS peak position. This is correlated with the smaller T_c in this compound, which additionally enhances the ratio of E_{ASOC} to k_BT_c, the most fundamental superconducting parameter correlated with the presence of an unconventional pairing symmetry.[11]

In Figure 4e–g the band structure is projected on the spin directions, showing the mixed spin character.

Figure 5 shows the calculated Fermi surface (FS) and FS cross-sections for $NbIr_2B_2$ (Figure 5a–j) and $TaIr_2B_2$ (Figure 5k–u). Spin–orbit coupling not only splits each FS sheet into two pieces, but also the topology of the Fermi surface is strongly affected. Especially the second FS sheet, shown in Figure 5b,l, is visibly modified after introducing SOC, see Figure 5d,f and Figure 5n,p for Nb analog and Ta analog, respectively. The reason for such a strong modification of the FS is seen in the bandstructure plots in Figure 4a–c. Due to SOC the highest band (among those which cross E_F) is shifted towards higher energy and the number of points where this band crosses E_F is reduced, leading to a smaller area of this FS sheet. FS cross-sections, shown in Figure 5g–j,r–u, additionally visualize the Fermi surface mismatch and observation, that SOC effect on FS in the studied materials is more than splitting of the Fermi surface into a set of similar parallel sheets.

Returning to the densities of states, the computed band structure DOS(E_F) values (with SOC included) are equal to 2.14 eV^{-1} (Nb analog) and 2.06 eV^{-1} (Ta analog), which result in the band values of the Sommerfeld electronic specific heat parameter $\gamma_{band} = 5.05$ mJ mol^{-1} K^{-2} for $NbIr_2B_2$ and $\gamma_{band} = 4.85$ mJ mol^{-1} K^{-2} for $TaIr_2B_2$. The experimental values are equal to 4.9 and 5.2 mJ mol^{-1} K^{-2}, respectively, which leads to a puzzling situation, since almost equal "bare" bandstructure and experimental γ values leave no room for the electron-phonon renormalization factor, where $\gamma = \gamma_{band}(1 + \lambda_{e-p})$. The λ_{e-p}, estimated from the critical temperature via the McMillan formula is about 0.7 in both materials, thus we expect either a smaller γ_{band} values, of the order of 3 mJ mol^{-1} K^{-2} for both compounds, or about 70% larger than the measured γ values. As the accuracy of the measured γ is certainly much better than 10%, other explanations must be considered. As we have shown in Figure 4b–d

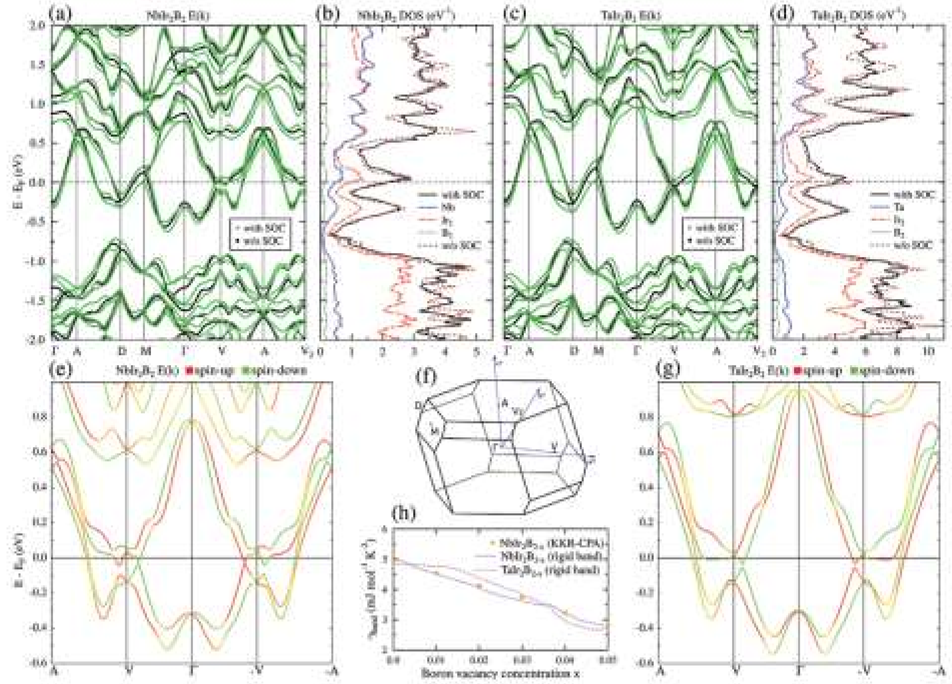

Figure 4. Calculated electronic structures of the superconductors. a,c) Electronic dispersion relations $E(k)$, computed with and without spin–orbit coupling, band splitting due to SOC is clearly visible; b,d) densities of states (DOS); e,g) zoom of $E(k)$ where spin character of each band is marked with color. Bands have a mixed, spin "up" – "down" character. In calculations monoclinic b-axis was chosen as a magnetization direction. Our compounds are nonmagnetic materials, the time reversal symmetry is preserved thus in spin-split bands $E(k) = E(-k)$ degeneracy is kept; however, spin direction is flipped, when k is changed to $-k$; f) the Brillouin zone; h) evolution of the computed value of the Sommerfeld parameter γ_{band} with the boron vacancy concentration x in (Nb,Ta)Ir$_2$B$_{2-x}$. KKR-CPA calculations were performed for NbIr$_2$B$_{2-x}$ for $x = 0$, 0.01, 0.02, 0.03, 0.04, and 0.05, and perfectly follow the rigid band model prediction, where E_F is shifted in the stoichiometric $x = 0$ DOS according to the reduced number of electrons in the system.

in both compounds E_F is located at the steep DOS slope. If we assume that the studied samples are slightly electron-deficient, e.g., due to the formation of boron vacancies, we may explain the discrepancy in the γ values, as in such situation E_F will move to the lower energies, considerably decreasing DOS(E_F) values. Quantitatively this analysis is shown in Figure 4h. Boron vacancies are expected to rigidly shift E_F downwards, with each vacancy delivering three holes to the system, as boron is a trivalent element. To reach $\gamma_{band} = 3$ mJ mol^{-1} K^{-2} it is sufficient to assume having at most 2.5% of boron deficiency (i.e., (Nb,Ta)Ir$_2$B$_{1.95}$). To cross-check the computed γ_{band} values and verify the assumption of rigid-band-like behavior in the boron-deficient system, additional calculations were done for NbIr$_2$B$_{2-x}$. We used the Korringa–Kohn–Rostoker method, and the presence of boron vacancies was explicitly taken into account using the coherent potential approximation.[54,55] KKR-CPA calculations confirmed that boron vacancy rigidly shifts Fermi level position leading to the decrease in DOS(E_F) value, see Figure S4 in the Supporting Information. As shown in Figure 4h the $x = 0$ value of γ_{band} obtained from KKR-CPA perfectly agrees with the one obtained using FP-LAPW. Thus, the observed discrepancy in the Sommerfeld parameter values suggests that a small amount of B vacancies are present in the system.

Such a small boron deficiency (2.5%) is certainly not possible to detect by EDS or pXRD technique. It is worth noting that for the MgCNi$_3$ superconductor, a powder neutron diffraction analysis reveals that the carbon occupancy is 0.978(8), though 25% excess of carbon has been used in the synthesis.[16] Hence, similar situation might occur in preparation of (Nb,Ta)Ir$_2$B$_2$.

If we accept the hypothesis, that E_F in the studied materials is rigidly shifted to lower energies, the required shift to match the experimental and renormalized calculated Sommerfeld parameter is equal to 85 meV (NbIr$_2$B$_2$) and 73 meV (TaIr$_2$B$_2$). In such a case the contribution of the first two FS sheets (Figure 5c,e,m,o) to the total Fermi surface will increase, limiting the role of the third (Figure 5d,n) and especially the fourth (Figure 5f,p) one in electronic structure of the materials. The asymmetry between the last two FS sheets will also be

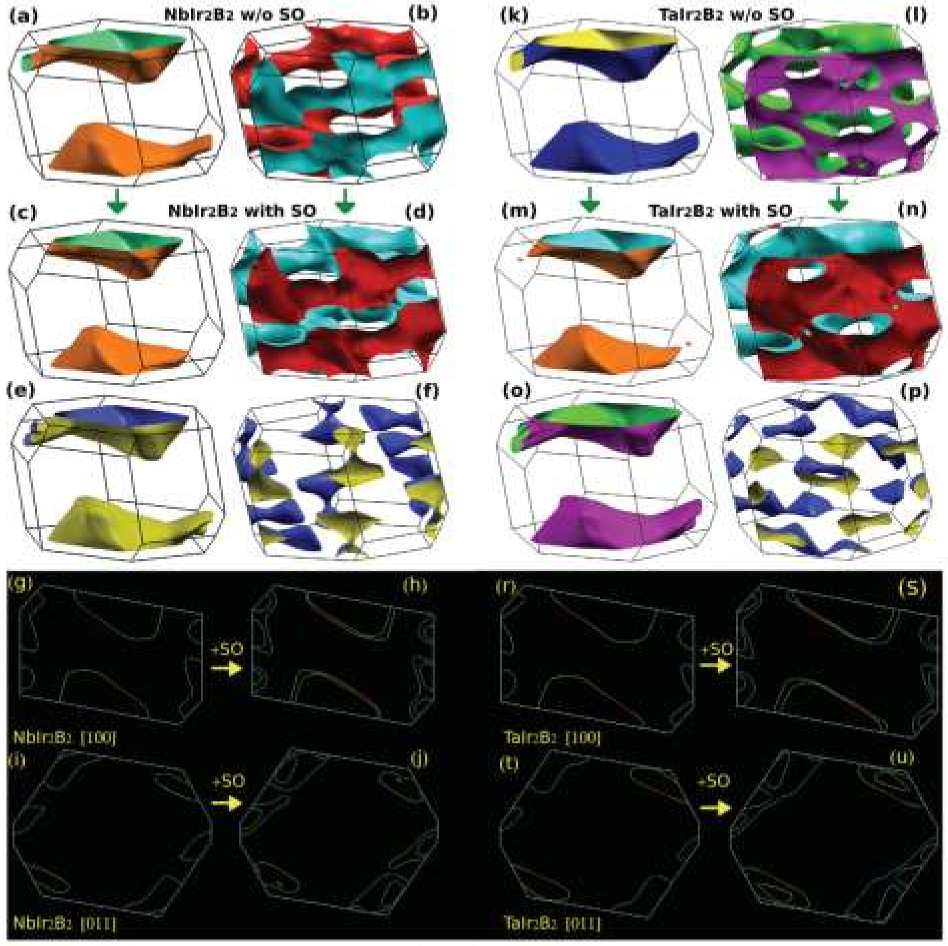

Figure 5. Impact of spin–orbit (SO) interaction on the Fermi surface (FS) of $NbIr_2B_2$ and $TaIr_2B_2$. In both compounds, two FS sheets [panels (a,b) and (k,l)] are split into four sheets [panels (c–f) and (m–p)]. FS splitting is well visible on FS cross sections, shown in panels (g–j) and (r–u) for $NbIr_2B_2$ and $TaIr_2B_2$, respectively.

larger. The presence of two dominating FS sheets fits in with the hypothesis of two superconducting gaps. Additional Fermi surface plots for the shifted E_F are presented in Figures S5 and S6 in the Supporting Information.

3. Conclusions

The first rule proposed by Matthias and Hulm for superconductors was: "high symmetry is good, cubic symmetry is best."[37] History, through the copper oxide and iron pnictide superconductors, has taught us that this is not generally the case, but this rule can still be imagined to hold for conventional intermetallic superconductors. The two intermetallic compounds reported here, which display a previously unreported noncentrosymmetric low symmetry crystal structures appear to violate that rule. The new compounds are type-II superconductors with T_c = 7.2 and 5.1 K for $NbIr_2B_2$ and $TaIr_2B_2$. Unlike the well-known boron-based superconductor MgB_2[38] and heavy-fermion superconductor $YbAlB_4$[39] where boron atoms form isolated layers, i.e., honeycomb layer for MgB_2 and edge-shared five-member ring with seven-member ring for $YbAlB_4$, the boron dimers present in noncentrosymmetric TT'_2B_2 superconductors may lead to a novel design rule for boron-based superconductors.

The most important common characteristic of both families of noncentrosymmetric TT'_2B_2 superconductors is their large value of the upper critical field. For the current materials, the estimated upper critical fields are $\mu_0H_{c2} = 16.3$ and 14.7 T, both of which exceed their so-called Pauli limits. Analysis of heat capacity data in the superconducting state for $NbIr_2B_2$ suggests a possible 2 gap (s+s) pairing symmetry function. In noncentrosymmetric compounds, the degree of admixture of spin-singlet and spin-triplet states in the superconductor depends on the strength of the spin orbit coupling. $NbIr_2B_2$ $TaIr_2B_2$ therefore appear to form a good family for investing the impact of atomic make up on the degree of spin orbit coupling at the Fermi surface and its effect on superconductivity.

4. Experimental Section

The starting materials for the synthesis of $NbIr_2B_2$ and $TaIr_2B_2$ were elemental niobium (3N, 200 mesh, Sigma-Aldrich), tantalum (3N, 100 mesh, Alfa Aesar), iridium (4N, Mennica – Metale, Poland) and boron (submicron particles, Callery Chemical). Powders of Nb/Ta, Ir and B were weighed out in a 1:2:2.33 ratio, ground thoroughly using a mortar and pestle and pressed into a pellet using a hydraulic press. The samples (≈200 mg) were then wrapped in tantalum foil, placed in an alumina crucible and heat treated at 1100 °C for 13 h under high vacuum (10^{-6} torr). Mass loss during the synthesis was negligible.

Multiple crystals (of size ≈30 × 30 × 30 μm^3) were measured at 300 K to get precise structural information. A Bruker Apex II diffractometer equipped with Mo radiation ($\lambda_{K\alpha} = 0.71073$ Å) was employed at room temperature. The small crystals were stuck to a Kapton loop with glycerol. Ten different detector positions were chosen to take the diffraction intensity measurements with an exposure time of 20 s per frame and a scanned 2θ width of 0.3°. Direct methods and full-matrix least-squares on F^2 within the SHELXTL package were employed to solve the structure.[40] Lorentz and polarization effects were modeled by the SAINT program, and numerical absorption corrections were accomplished with *XPREP*, which is based on face-index modeling.[41] Powder X-ray diffraction analysis on well-ground powder of a portion of samples was carried out on a Bruker D8 Advance Eco diffractometer with Cu $K\alpha$ radiation and a LynxEye-XE detector. Having the crystallographic data of new compounds, Rietveld refinement of this data was performed by employing the software Topas. The Nb:Ir or Ta:Ir ratio was examined using a FEI Quanta 250 FEG scanning electron microscope (SEM) equipped with an Apollo-X SDD EDS. The data were collected for 300 s and analyzed using the EDAX TEAM software.

Magnetization and magnetic susceptibility measurements were performed using a Physical Property Measurement System (Quantum Design PPMS) with a vibrating sample magnetometer (VSM) in the temperature range of 1.7–8.0 K under various applied magnetic fields. Both specific heat and electrical resistivity were measured in the temperature range between 300 and 1.85 K, in magnetic fields up to 9 T in the PPMS. The lower temperature heat capacity of $NbIr_2B_2$ was measured in a Dynacool Physical Property Measurement System equipped with a ^3He attachment. The resistivity was determined using a standard four-probe technique, with four 37-μm-diameter platinum wire leads spark-welded to the flat polished sample surface. Specific-heat measurements were performed using the two-τ time-relaxation method. The sample was attached to the measuring platform by a small amount of Apiezon N. The addendum heat capacity was measured in a separate run without a sample and was subtracted from the data.

The electronic structure was calculated using the full-potential linearized augmented plane wave method (FP-LAPW) implemented in the WIEN2k package,[42] using the Perdew–Burke–Ernzerhof generalized gradient approximation[43] (PBE-GGA) for the exchange-correlation potential. Calculations were done using the experimental lattice parameters, and for both the experimental and computed (relaxed) atomic positions, however the relaxation process does not lead to any visible changes in the calculated electronic band structure. Calculations were done in a scalar-relativistic (spin–orbit interaction is neglected) and relativistic (spin–orbit interaction included) way. Fermi surface plots and FS cross-sections were prepared using XCrysDen[44] and FermiSurfer[45] software. To simulate the effect of boron vacancies on the DOS(E_F), the Korringa–Kohn–Rostoker method with the coherent potential approximation[34,35] was applied.

Supporting Information

Supporting Information is available from the Wiley Online Library or from the author.

Acknowledgements

The work at GUT was supported by the National Science Centre (Poland), grant number: UMO-2017/27/B/ST5/03044. W.X. was supported by Beckman Young Investigator Program and NSF-DMR-1944965. Work at AGH was supported by the National Science Centre (Poland), project No. 2017/26/E/ST3/00119. The synthetic work at Princeton was supported by the US Department of Energy, Basic Energy Sciences, grant DE-FG02-98ER45706.

Conflict of Interest

The authors declare no conflict of interest.

Keywords

crystal structure, noncentrosymmetric superconductors, spin–orbit coupling

Received: September 18, 2020

[1] M. Tinkham, *Introduction to Superconductivity*, Courier Corporation, North Chelmsford, MA, USA **1996**.
[2] L. P. Gor'kov, E. I. Rashba, *Phys. Rev. Lett.* **2001**, *87*, 037004.
[3] D. Singh, K. P. Sajilesh, J. A. T. Barker, D. M. Paul, A. D. Hillier, R. P. Singh, *Phys. Rev. B* **2018**, *97*, 100505.
[4] E. Bauer, G. Hilscher, H. Michor, C. Paul, E. W. Scheidt, A. Gribanov, Y. Seropegin, H. Noël, M. Sigrist, P. Rogl, *Phys. Rev. Lett.* **2004**, *92*, 027003.
[5] P. A. Frigeri, D. F. Agterberg, A. Koga, M. Sigrist, *Phys. Rev. Lett.* **2004**, *93*, 099903.
[6] E. Bauer, M. Sigrist, *Non-Centrosymmetric Superconductor: Introduction and Overview*, Springer-Verlag, Heidelberg **2012**.
[7] T. P. Ying, Y. P. Qi, H. Hosono, *Phys. Rev. B* **2019**, *100*, 094522.
[8] K. P. Sajilesh, D. Singh, P. K. Biswas, G. B. G. Stenning, A. D. Hillier, R. P. Singh, *Phys. Rev. Mater.* **2019**, *3*, 104802.
[9] E. M. Carnicom, W. Xie, T. Klimczuk, J. Lin, K. Górnicka, Z. Sobczak, N. P. Ong, R. J. Cava, *Sci. Adv.* **2018**, *4*, eaar7969.

[10] A. Amon, E. Svanidze, R. Cardoso-Gil, M. N. Wilson, H. Rosner, M. Bobnar, W. Schnelle, J. W. Lynn, R. Gumeniuk, C. Hennig, G. M. Luke, H. Borrmann, A. Leithe-Jasper, Y. Grin, *Phys. Rev B* **2018**, *97*, 014501.

[11] Y. Qi, Z. Xiao, J. Guo, H. Lei, T. Kamiya, H. Hosono, *Europhys. Lett.* **2018**, *121*, 57001.

[12] J. A. T. Barker, B. D. Breen, R. Hanson, A. D. Hillier, M. R. Lees, G. Balakrishnan, D. M. Paul, R. P. Singh, *Phys. Rev. B* **2018**, *98*, 104506.

[13] A. Ptok, K. Domieracki, K. J. Kapcia, J. Łażewski, P. T. Jochym, M. Sternik, P. Piekarz, D. Kaczorowski, *Phys. Rev. B* **2019**, *100*, 165130.

[14] I. Bonalde, H. Kim, R. Prozorov, C. Rojas, P. Rogl, E. Bauer, *Phys. Rev. B* **2011**, *84*, 134506.

[15] M. Smidman, M. B. Salamon, H. Q. Yuan, D. F. Agterberg, *Rep. Prog. Phys.* **2017**, *80*, 036501.

[16] T. Klimczuk, R. J. Cava, *Phys. Rev. B* **2004**, *70*, 212514.

[17] M. Sato, Y. Ishii, *J. Appl. Phys.* **1989**, *66*, 983.

[18] A. Umezawa, G. W. Crabtree, J. Z. Liu, T. J. Moran, S. K. Malik, L. H. Nunez, W. L. Kwok, C. H. Sowers, *Phys. Rev. B* **1988**, *38*, 2843.

[19] A. C. Rose-Innes, E. H. Rhoderick, *Introduction to Superconductivity*, Pergamon Place Plc, Oxford **1978**.

[20] E. Bauer, G. Rogl, X.-Q. Chen, R. T. Khan, H. Michor, G. Hilscher, E. Royanian, K. Kumagai, D. Z. Li, Y. Y. Li, R. Podloucky, P. Rogl, *Phys. Rev. B* **2010**, *82*, 064511.

[21] Z. Hiroi, S. Yonezawa, Y. Nagao, J. Yamaura, *Phys. Rev. B* **2007**, *76*, 014523.

[22] H. R. Naren, A. Thamizhavel, A. K. Nigam, S. Ramakrishnan, *Phys. Rev. Lett.* **2008**, *100*, 026404.

[23] D. Hirai, M. N. Ali, R. J. Cava, *J. Phys. Soc. Jpn.* **2013**, *82*, 124701.

[24] W. L. McMillan, *Phys. Rev.* **1968**, *167*, 331.

[25] K. Górnicka, E. M. Carnicom, S. Gołąb, M. Łapiński, B. Wiendlocha, W. Xie, D. Kaczorowski, R. J. Cava, T. Klimczuk, *Supercond. Sci. Technol.* **2019**, *32*, 025008.

[26] V. Y. Verchenko, A. A. Tsirlin, A. O. Zubtsovskiy, A. V. Shevelkov, *Phys. Rev. B* **2016**, *93*, 064501.

[27] D. Singh, A. D. Hillier, A. Thamizhavel, R. P. Singh, *Phys. Rev. B* **2016**, *94*, 054515.

[28] D. A. Mayoh, A. D. Hillier, K. Götze, D. M. Paul, G. Balakrishnan, M. R. Lees, *Phys. Rev. B* **2018**, *98*, 014502.

[29] P. A. Lee, T. V. Ramakrishnan, *Rev. Mod. Phys.* **1985**, *57*, 287.

[30] D. Vollhardt, P. Wolfle, *Electronic Phase Transitions*, Elsevier Science Publishers B.V, Amsterdam, Netherlands **1992**.

[31] G. Csire, B. Újfalussy, J. F. Annett, *Eur. Phys. J. B* **2018**, *91*, e2018.

[32] B. Wiendlocha, R. Szczęśniak, A. P. Durajski, M. Muras, *Phys. Rev. B* **2016**, *94*, 134517.

[33] L. Jiao, J. L. Zhang, Y. Chen, Z. F. Weng, Y. M. Shao, J. Y. Feng, X. Lu, B. Joshi, A. Thamizhavel, S. Ramakrishnan, H. Q. Yuan, *Phys. Rev. B* **2014**, *89*, 060507.

[34] H. Ebert, D. Ködderitzsch, J. Minár, *Rep. Prog. Phys.* **2011**, *74*, 096501.

[35] H. Ebert, The Munich SPR-KKR package, version 7.7.3, https://www.ebert.cup.uni-muenchen.de/index.php/en/software-en/13-sprkkr (accessed: September 2020).

[36] T. Amos, Q. Huang, J. Lynn, T. He, R. Cava, *Solid State Commun.* **2002**, *121*, 73.

[37] K. Conder, *Supercond. Sci. Technol.* **2016**, *29*, 080502.

[38] J. Nagamatsu, N. Nakagawa, T. Muranaka, Y. Zenitani, J. Akimitsu, *Nature* **2001**, *410*, 63.

[39] S. Nakatsuji, K. Kuga, Y. Machida, T. Tayama, T. Sakakibara, Y. Karaki, H. Ishimoto, S. Yonezawa, Y. Maeno, E. Pearson, G. G. Lonzarich, L. Balicas, H. Lee, Z. Fisk, *Nat. Phys.* **2008**, *4*, 603.

[40] G. M. Sheldrick, *Acta Crystallogr., Sect. A: Found. Crystallogr.* **2008**, *64*, 112.

[41] G. M. Sheldrick, *XPREP*, University of Gottingen, Gottingen, Germany **2001**.

[42] P. Blaha, K. Schwarz, G. K. H. Madsen, D. Kvasnicka, J. Luitz, R. Laskowski, F. Tran, L. D. Marks, *WIEN2K, An Augmented Plane Wave + Local Orbitals Program for Calculating Crystal Properties* (Ed: K. Schwarz), Techn. Universitat Wien, Austria **2018**.

[43] J. P. Perdew, K. Burke, M. Emzerhof, *Phys. Rev. Lett.* **1996**, *77*, 3865.

[44] A. Kokalj, *Comput. Mater. Sci.* **2003**, *28*, 155.

[45] M. Kawamura, *Comput. Phys. Commun.* **2019**, *239*, 197.

Source material's DOI: https://doi.org/10.1002/adfm.202007960

ADVANCED
FUNCTIONAL
MATERIALS

Supporting Information

for *Adv. Funct. Mater.*, DOI: 10.1002/adfm.202007960

$NbIr_2B_2$ and $TaIr_2B_2$ – New Low Symmetry Noncentrosymmetric Superconductors with Strong Spin–Orbit Coupling

*Karolina Górnicka, Xin Gui, Bartlomiej Wiendlocha, Loi T. Nguyen, Weiwei Xie, Robert J. Cava, and Tomasz Klimczuk**

Supplementary Material

$NbIr_2B_2$ and $TaIr_2B_2$ – new low symmetry noncentrosymmetric superconductors with strong spin orbit coupling

Karolina Górnicka[1,2], Xin Gui[3], Bartlomiej Wiendlocha[4], Loi T. Nguyen[3],
Weiwei Xie[5], Robert J. Cava[3] and Tomasz Klimczuk[1,2,*]

[1] *Faculty of Applied Physics and Mathematics, Gdansk University of Technology,*
ul. Narutowicza 11/12, 80-233 Gdańsk, Poland, e-mail: karolina.gornicka@pg.edu.pl
[2]*Advanced Materials Centre, Gdansk University of Technology,*
ul. Narutowicza 11/12, 80-233 Gdańsk, Poland,
[3] *Department of Chemistry, Princeton University, New Jersey NJ 08540*
[4] *Faculty of Physics and Applied Computer Science, AGH University of Science and Technology,*
Aleja Mickiewicza 30, 30-059 Kraków, Poland
[5] *Department of Chemistry and Chemical Biology, Rutgers University, Piscataway, NJ 08854, USA*

* Tomasz Klimczuk, e-mail: tomasz.klimczuk@pg.edu.pl

SM-1. Single-crystal X-ray diffraction studies

To determine the crystal structure of the new Nb-Ir-B phase, we carried out a single-crystal X-ray diffraction structure refinement at room temperature. A summary of the crystallographic data from the structure refinement, and the atomic coordinates, can be found in Tables S1 and S2 respectively. The anisotropic thermal displacements are gathered in Table S3. Since this method tests a micrometer size crystal, we also performed the powder X-ray (pXRD) diffraction for the samples used for physical properties characterization.

Table S1. Single crystal refinement for $NbIr_2B_2$ at 300 (2) K.

Refined Formula	$NbIr_2B_2$
F.W. (g/mol)	498.93
Space group; Z	Cc; 4
a (Å)	8.1586 (5)
b (Å)	4.7746 (3)
c (Å)	6.0067 (3)
β (°)	102.256 (3)
V (Å^3)	228.65 (2)
Extinction Coefficient	0.0029 (2)
θ range (deg)	4.977-34.982
R_σ	0.0563
hkl range	$-13 \leq h \leq 12$ $-7 \leq k \leq 7$ $-9 \leq l \leq 9$
No. reflections; R_{int}	3557; 0.0435
No. independent reflections	991
No. parameters	48
R_1: ωR_2 (I>2σ(I))	0.0254; 0.0433
Goodness of fit	0.885
Diffraction peak and hole (e$^-$/ Å^3)	2.359; -1.957
Absolute structure parameter	0.04 (2)

Table S2. Atomic coordinates and equivalent isotropic displacement parameters of $NbIr_2B_2$ system. (U_{eq} is defined as one-third of the trace of the orthogonalized U_{ij} tensor (Å^2))

Atom	Wyck.	Occ.	*x*	*y*	*z*	U_{eq}
Ir1	4*a*	1	0.1945 (2)	0.6125 (2)	0.1898 (2)	0.0073 (2)
Ir2	4*a*	1	0.3463 (1)	0.1101 (2)	0.0965 (2)	0.0075 (2)
Nb3	4*a*	1	0.0000 (2)	0.1115 (4)	0.0000 (3)	0.0062 (3)
B4	4*a*	1	0.018 (3)	0.370 (5)	0.355 (4)	0.013 (4)
B5	4*a*	1	0.198 (3)	0.195 (5)	0.354 (4)	0.011 (4)

Table S3. Anisotropic thermal displacements from $NbIr_2B_2$.

Atom	U11	U22	U33	U23	U13	U12
Ir1	0.0061 (3)	0.0058 (3)	0.0095 (4)	0.0028 (7)	0.0007 (3)	-0.0010 (7)
Ir2	0.0051 (3)	0.0056 (3)	0.0118 (3)	0.0017 (7)	0.0018 (2)	-0.0012 (7)
Nb3	0.0053 (6)	0.0054 (7)	0.0078 (7)	0.0025 (9)	0.0010 (5)	-0.0006 (9)
B4	0.019 (10)	0.011 (10)	0.011 (10)	0.006 (8)	0.005 (7)	0.007 (8)
B5	0.008 (8)	0.011 (9)	0.011 (10)	0.004 (7)	-0.002 (7)	0.006 (7)

The DFT-relaxed atomic positions for $NbIr_2B_2$ and $TaIr_2B_2$, see Table S4, do not differ much and are close to the X-ray structure determined refined values.

Table S4. Relaxed atomic positions of $NbIr_2B_2$ and $TaIr_2B_2$

	$NbIr_2B_2$			$TaIr_2B_2$		
Atom	*x*	*y*	*z*	*x*	*y*	*z*
Ir1	0.19449	0.61362	0.18833	0.19558	0.61521	0.18927
Ir2	0.34681	0.11110	0.09665	0.34726	0.11356	0.09658
Nb/Ta	0.00119	0.11202	0.00172	0.00087	0.11280	0.00147
B1	0.01434	0.37095	0.35286	0.01348	0.36993	0.35199
B2	0.19995	0.19284	0.35576	0.19963	0.19194	0.35603

Table S5. Selected interatomic distances for $NbIr_2B_2$.

Atom1	Atom2	Distance (Å)
B1	B2	1.69 (4)
Nb	Ir1	2.953 (2) / 2.962 (2) / 2.997 (2)
Nb	Ir2	2.761 (2) / 2.815 (2) / 2.819 (3)
Ir1	Ir2	2.777 (1) / 2.791 (1) / 2.810 (1)

Selected interatomic distances in $NbIr_2B_2$ are listed in Table S5. Based on the differences in atomic radius, Nb-Ir and Ir-Ir bond lengths are comparable to what are present in previously reported superconducting Nb/$TaRh_2B_2$[1]. Turning to the B-B distance, in the rhodium materials it is 1.77(7) Å between two boron atoms in each boron dimer. In our case their separation is1.69(4) Å which is slightly smaller but still in the standard deviation range. The short B-B distance in the boron dimers may result from the increasing of atomic radii from Rh to Ir, which furthermore compresses the space for boron dimers in between Nb@Ir9 polyhedra. Moreover, considering the quality of our single crystal diffraction results where the highest diffraction peak (2.359 $e^-/Å^3$) and deepest diffraction hole (-1.957 $e^-/Å^3$) are 1.24 Å from Nb and 0.76 Å from Ir2, respectively, and the Flack parameter is 0.04(2) with small standard deviation, the noncentrosymmetric model in *Cc* space group is highly likely correct. Besides, the powder XRD pattern measured for both compounds are fitted well with the refined crystal structure with no missing peaks which also supports that the model is correct.

SM-2. Powder X-ray diffraction analysis (pXRD)

The pXRD patterns with the Rietveld refinement are shown in Figure S1(a) and Figure S1(b) for $NbIr_2B_2$ and $TaIr_2B_2$, respectively. The pXRD data were analyzed by the Rietveld method with the starting model obtained by a single-crystal refinement. The quantities of impurity phases are as follows: TaB_2 (3.5% wt.) and $TaIr_3$ (2.5% wt.) for $TaIr_2B_2$ and NbB_2 (4.8% wt.) for $NbIr_2B_2$. An additional impurity phase is SiO_2, which is often present if a boron reach, very hard sample is ground in an agate mortar[2]. The refined lattice and structural parameters (Table S6) are in good agreement with those obtained by the single-crystal X-ray diffraction method.

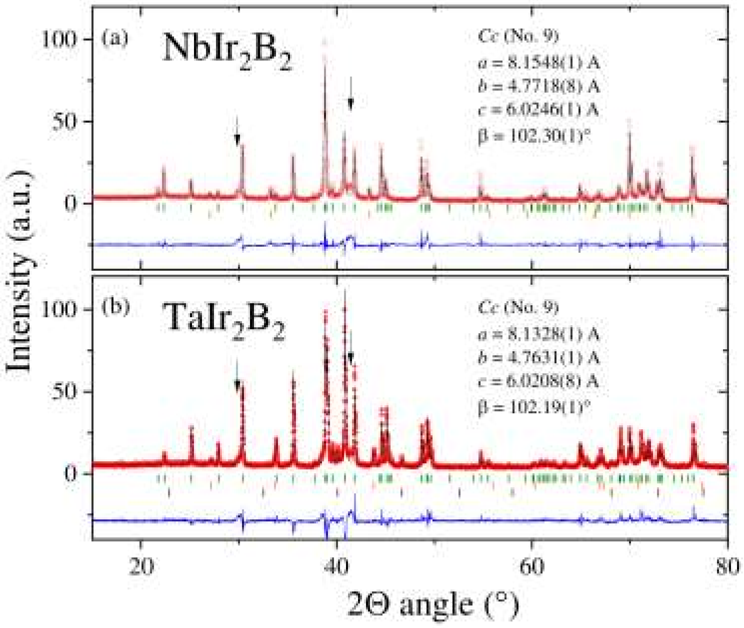

Figure S1. Powder x-ray diffraction pattern (pXRD) (red points) together with the Rietveld refinement profile (black solid line) for NbIr$_2$B$_2$ (upper panel) and TaIr$_2$B$_2$ (lower panel). The green, orange and violet vertical bars indicate the expected Bragg peak positions for (Nb/Ta)Ir$_2$B$_2$ (*Cc* (no. 9)), (Nb/Ta)B$_2$ impurity (*P6/mmm* (no. 191)) and TaIr$_3$ impurity (*Pm-3m* (no. 221)), respectively. Arrows indicate the broad reflections coming from SiO$_2$ (mortar and pestle). The blue curve is the difference between experimental and model results.

Table S6. Refined structural parameters for $NbIr_2B_2$ and $TaIr_2B_2$ obtained from the powder refinements. Background-corrected Rietveld refinement reliability factors: profile residual R_p = 12.4%, weighted profile residual R_{WP} = 16.4%, expected residual R_{exp} = 7.6%, GOF = 2.2 for the Nb analog and R_p = 9.3%, R_{WP} = 12.1%, R_{exp} = 7.0%, GOF = 1.7 for the Ta analog.

	$NbIr_2B_2$			$TaIr_2B_2$		
Atom	*x*	*y*	*z*	*x*	*y*	*z*
Ir1	0.22826	0.60475	0.19022	0.19682	0.61293	0.19139
Ir2	0.35654	0.10757	0.10100	0.34676	0.11346	0.09765
Nb/Ta	0.00108	0.11337	0.00142	0.00087	0.11285	0.00147
B1	0.01434	0.37095	0.35286	0.01348	0.36993	0.35199
B2	0.19995	0.19284	0.35576	0.19963	0.19194	0.35603

SM-3. Estimate of the physical properties for $NbIr_2B_2$ and $TaIr_2B_2$

In order to determine the lower critical field ($\mu_0 H^*_{c1}(0)$), the magnetization was measured as a function of magnetic field at several temperatures below the superconducting transition temperature T_c. For each temperature, the experimental data obtained in small magnetic fields were fitted using the proportionality $M_{fit} = -pH$, appropriate for a full shielding state. Comparing the value of a prefactor p derived from the isotherm taken at T = 1.7 K with the ideal diamagnetism quantified as $-1/4\pi$, the demagnetization factor N = 0.49 for the Nb variant and N = 0.55 for the Ta variant was estimated. Those values are fairly consistent with the expected (theoretical) N_z value derived for a circular cylinder sample with the height to radius ratio of approx. 0.5 (see ref.[3]). The low-field linear fit to the magnetization data (M_{fit}) was used to construct the $M_V - M_{fit}$ plot. In the next step, the values of the lower critical field $\mu_0 H_{c1}^*(T)$ were extracted as is shown in Figure S2. Note that the black dashed lines $\Delta M = M_V - M_{fit} = 0.2$ emu cm^{-3} ($NbIr_2B_2$) and 0.1 emu cm^{-3} ($TaIr_2B_2$) were chosen carefully and they are as small as possible (ΔM is less than 2% of the magnetization value M for applied field of H_{c1}^* obtained at T = 1.7 K, for each compound). The resulting values of $\mu_0 H^*_{c1}$

estimated in this manner are depicted in the main panel of Figure 2(c) and Figure 2(d). An additional point for H = 0 is a zero field transition temperature taken from the resistivity measurement.

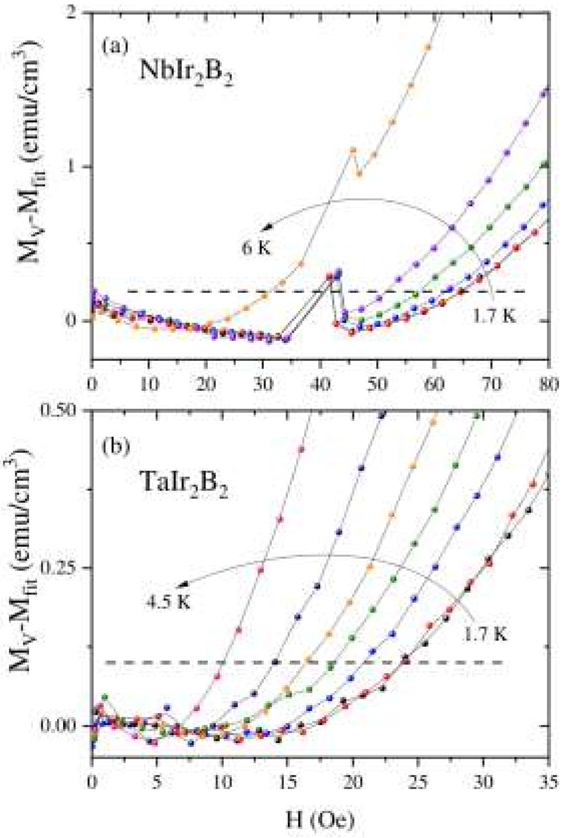

Figure S2. The field dependence of the difference between volume magnetization M_v and M_{fit} at various temperatures below T_c. The dashed line is a line used for obtaining $\mu_0H_{c1}^*$ at each temperature. An anomaly seen for H –40 Oe (part (a)) is possibly caused by a superconducting vortex avalanche effect.

The temperature dependence of the electronic specific heat (C_{el}) below T_c for $NbIr_2B_2$ is shown in Figure S3 (a) and (b). $C_{el.}$ was calculated by subtracting the phonon contribution (C_{ph}) from the total specific heat C_p. The C_{el} was then analyzed by fitting the data with a single gap isotropic *s*-wave model and an isotropic two-gap (*s*+*s*)-wave model (panel (a)), and power-law model ($C_{el.} \propto T^3$) expected for point nodes (panel (b)). All fits were done below 5K, which is about $0.7T_c$. An *s*-wave single gap BCS model (blue dashed line) gives $2\Delta_0$ = 2.70(6) meV, with a coefficient of determination $R^2 = 0.9991$. The expected by BCS theory value is $2\Delta_0 = 3.52k_BT_c$ = 2.17 meV. A better fit ($R^2 = 0.99992$) was obtained assuming a multigap (*s*+*s*) scenario with $2\Delta_{01}$ = 2.32(5) meV and $2\Delta_{02}$ = 9.1(12) meV, represented by a red line. A solid and dash line in an inset represent difference between experiment and a single and double *s*-wave gap model, respectively. For a gap with nodes, theory predicts power-law dependence, with n = 2 or 3 for line or point nodes, respectively. A green line in a panel (b) is a $C_{el.} \propto T^3$ fit, and its low quality does not support a point nodes scenario for $NbIr_2B_2$. A better fit ($R^2 = 0.9988$), but still worse than obtained for the gap models, was obtained for $C_{el.} \propto T^n$ and a refined n value is 3.65(2), which is close to n = 3.3 reported for W_3Al_2C[4]. The difference between experiment and power-law models are shown in an inset. Note that the scale here is twice larger comparing to an inset in an upper panel.

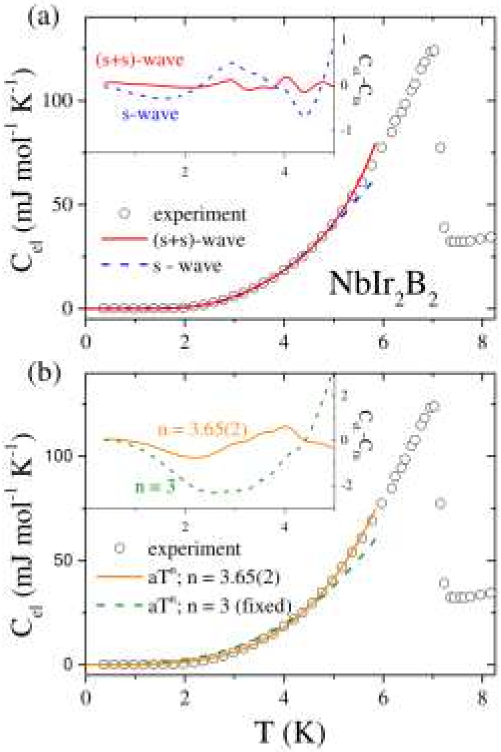

Figure S3. Temperature-dependent electronic specific heat $C_{el.}$ for $NbIr_2B_2$. (a) a fit of a single gap isotropic *s*-wave model (blue dashed line) and an isotropic two-gap (*s+s*)-wave model (red solid line) to the data. (b) a fit of a power-law model ($C_{el.} \propto T^3$) to the data.

The last experimental technique used for characterization of the new superconductors was temperature dependent resistivity. $NbIr_2B_2$ behaves like a poor metal, with a shallow negative gradient for the resistivity upon cooling from room temperature. The residual resistivity ratio (RRR), ρ_{300}/ρ_{10} = 1.3, is small, which can be attributed to the polycrystalline nature of the sample contained grain boundaries and macroscopic defects. In the case of Ta variant, one observes an increase in ρ(T) as the temperature was decreased. Comparing ρ(300 K) and ρ(10 K), resistivity increases about 50%. A non-metallic behavior is likely caused by disorder scattering and the charge carrier localization effect. At low temperatures the electrical resistivity drops sharply to zero at T_c = 7.24 K for $NbIr_2B_2$ and at T_c = 5.38 K for $TaIr_2B_2$. Superconducting critical temperature T_c is defined by the temperature of the 50% drop of the ρ(T) data in zero magnetic field. The slightly higher superconducting temperature value obtained in the resistivity measurement is likely due to the influence of surface superconductivity emerging in each cross-sectional area of the sample. The effect of applying a magnetic field on T_c is shown in the inset of Figure 3(d) for Nb analog and Figure 3(e) for Ta analog. As expected, the transition becomes broader, and T_c shifts to lower temperature as the applied field was increased. It should be noted that a transition to a zero-resistance state was obtained even at 9 T and above 3 K for $NbIr_2B_2$ or 2 K for $TaIr_2B_2$, indicating a large upper critical field.

To estimate the upper critical field at 0 K, $\mu_0H_{c2}(0)$, we fit the data shown in Figure 3(f) to the Ginzburg-Landau (GL) expression

$$\mu_0 H_{c2}(T) = \mu_0 H_{c2}(0)\frac{(1-t^2)}{(1+t^2)} \tag{1}$$

where t = T/T_c and T_c is the transition temperature at zero magnetic field. The fit of the resistivity data is represented by a solid line and the obtained values of $\mu_0H_{c2}(0)$ are: 16.3(2) T and 14.7(1) T for $NbIr_2B_2$ and $TaIr_2B_2$, respectively. For the thermodynamic data the values of the upper critical fields are $\mu_0H_{c2}(0)$ = 15.8(1) T for Nb variant and $\mu_0H_{c2}(0)$ = 16.5(2) T for Ta variant (the dashed line). Furthermore, a conservative evaluation of the upper critical fields at 0 K was performed using the Werthamer-Helfand-Hohenberg (WHH) approximation in the dirty limit[5,6]:

$$\mu_0 H_{c2}(0) = -AT_c \frac{d\mu_0 H_{c2}}{dT}\bigg|_{T=T_c} \tag{2}$$

where A is the purity factor given by 0.693 for the dirty limit. Table S7 presents the expected $\mu_0H_{c2}(0)$ value obtained from WHH and GL models.

Table S7. The upper critical field $\mu_0H_{c2}(0)$ estimated from WHH and GL models.

$\mu_0Hc_2(0)$	Unit	$NbIr_2B_2$	$TaIr_2B_2$
WHH $_{\text{resistivity}}$	T	13.3(2)	11.6(1)
GL $_{\text{resistivity}}$	T	16.3(2)	14.7(1)
WHH $_{\text{heat capacity}}$	T	14.2(2)	12.8(1)
GL $_{\text{heat capacity}}$	T	15.8(1)	16.5(2)
$\mu_0H_{c2}^{p}(0)$	T	13.3(1)	9.5(1)

SM-4. Electronic structure calculations

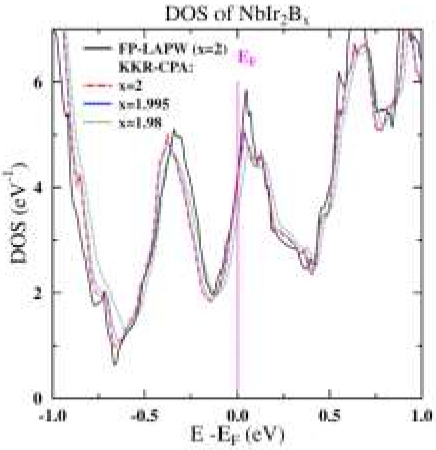

Figure S4. Evolution of DOS near the Fermi level in $NbIr_2B_x$ as a function of boron concentration, obtained using the KKR-CPA method. For the stoichiometric composition (x = 2) KKR-CPA DOS very well agrees with the FP-LAPW result.

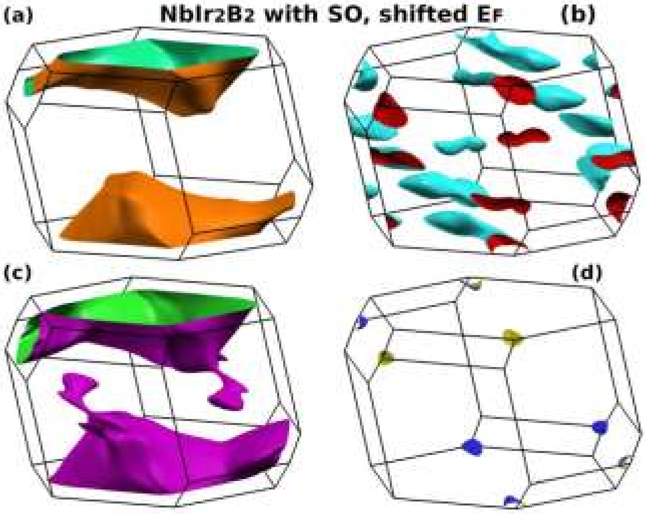

Figure S5. Fermi surface of NbIr$_2$B$_2$ calculated with spin-orbit coupling, for the shifted Fermi energy, so as the experimental and renormalized calculated Sommerfeld parameters match. E$_F$ shift, comparing to Fig. 5 is equal to -84 meV. The contribution from the third and fourth FS sheet (panels b,d) is considerably reduced, as compared to Fig. 5 (d,f).

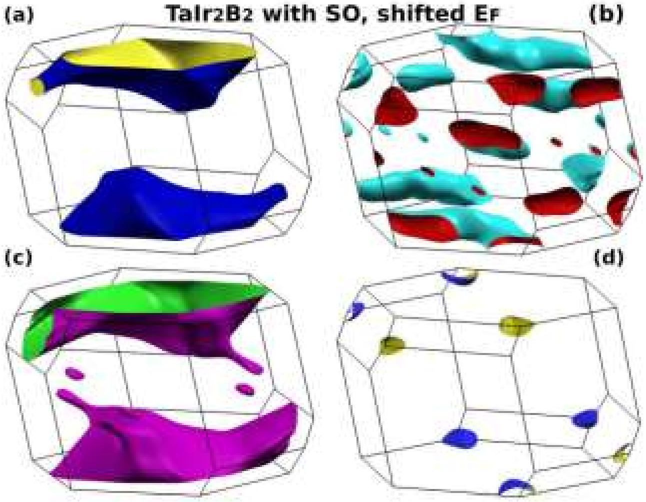

Figure S6. Fermi surface of $TaIr_2B_2$ calculated with spin-orbit coupling, for the shifted Fermi energy, so as the experimental and renormalized calculated Sommerfeld parameters match. E_F shift, comparing to Fig. 5 is equal to -73 meV. The contribution from the third and fourth FS sheet (panels b,d) is considerably reduced, as compared to Fig. 5 (n,p).

References

[1] E. M. Carnicom, W. Xie, T. Klimczuk, J. Lin, K. Górnicka, Z. Sobczak, N. P. Ong, R. J. Cava, *Science Advances* **2018**, *4*, eaar7969.
[2] E. M. Carnicom, J. Strychalska-Nowak, P. Wiśniewski, D. Kaczorowski, W. Xie, T. Klimczuk, R. J. Cava, *Superconductor Science and Technology* **2018**, *31*, 115005.
[3] M. Sato, Y. Ishii, *Journal of Applied Physics* **1989**, *66*, 983.
[4] T. P. Ying, Y. P. Qi, H. Hosono, *Physical Review B* **2019**, *100*, 094522.
[5] N. R. Werthamer, E. Helfand, P. C. Hohenberg, *Phys. Rev.* **1966**, *147*, 295.
[6] E. Helfand, N. R. Werthamer, *Phys. Rev.* **1966**, *147*, 288.

Source material's DOI: https://doi.org/10.1002/adfm.202007960

5. Podsumowanie

W doktoracie przedstawiono wyniki badań związanych z poszukiwaniem nowych, bądź opisem częściowo znanych, nadprzewodników międzymetalicznych. Opisane w 7 publikacjach (1 w recenzji) wyniki można podsumować poprzez modną obecnie klasyfikację, w której brane są pod uwagę istniejące informacje na temat badanego związku.

W przypadku $CeIr_3$, $CaRh_2$ i LiBi dostępne były informacje na temat struktury krystalicznej, a także podana była temperatura przejścia do stanu nadprzewodnictwa. Otrzymane próbki polikrystaliczne ($CeIr_3$, $ThIr_3$, $CaRh_2$) i monokrystaliczne (LiBi) charakteryzowały się bardzo dobrą jakością i pozwoliły na określenie najważniejszych parametrów stanu nadprzewodzącego, w tym typu nadprzewodnictwa (pierwszego lub drugiego rodzaju). Dla wymienionych wyżej czterech nadprzewodników zastosowane podejście można określić jako znane / znane (known / known).

Dla międzymetalicznego związku $ThIr_3$ literatura naukowa podawała jedynie temperaturę obserwowanego przejścia do stanu nadprzewodzącego. Wszelkie inne informacje, w tym również na temat struktury krystalicznej, pozostawały nieznane. Tym samym zastosowane podejście można określić jako nieznane / znane (unknown / known).

Dla badanych związków typu Heuslera, $LiGa_2Ir$ oraz $LiPd_2Ge$, prowadzone badania można określić jako znane / nieznane (known / unknown). W obu przypadkach w literaturze opisana była struktura krystaliczna, nie podane były jednak informacje dotyczące właściwości fizycznych. W publikacjach A4 oraz A5 przedstawione zostały szczegóły powtarzalnej i stosunkowo prostej metody syntezy opierającej się na reakcji w fazie stałej. Metoda pozwala na uzyskanie objętościowych, polikrystalicznych próbek związków typu Heuslera na bazie litu, które poddano badaniom właściwości fizycznych. Nadprzewodnictwo dla $LiGa_2Ir$ było w pewnym sensie oczekiwane. $LiGa_2Ir$ jest drugim, obok $LiGa_2Rh$, nadprzewodnikiem typu Heuslera, dla którego liczba elektronów walencyjnych (VEC) jest równa 16 i znajduje się poniżej granicznej wartości VEC = 24. Warto w tym miejscu nadmienić, ze dla VEC = 24 obserwuje się odejście od metalicznego zachowania.

Drugi z opisanych w pracy doktorskiej nadprzewodników typu Heuslera, $LiPd_2Ge$, podobnie jak niemal wszystkie nadprzewodniki tej rodziny znajduje się powyżej granicznej wartości VEC. Jest to pierwszy opisany nadprzewodnik Heuslera z VEC = 25. Pomiary podatności magnetycznej wskazują, że $LiPd_2Ge$ jest nadprzewodnikiem pierwszego rodzaju. Jest to z całą pewnością pierwszy znany przypadek nadprzewodnictwa pierwszego rodzaju w rodzinie nadprzewodników typu Heuslera i prawdopodobnie pierwszy wśród trójskładnikowych związków międzymetalicznych. Kolejna intrygująca obserwacja jest związana z występowaniem tzw. miękkich modów fononowych, które najpewniej prowadzą do *wzmocnienia* zjawiska nadprzewodnictwa.

Wreszcie dla ostatnich dwóch nadprzewodników opisanych w doktoracie, sklasyfikowane podejście to tzw. nieznane / nieznane (unknown / unknown). Projekt polegał na poszukiwaniu nieznanych związków, w niezbadanym dotąd układzie potrójnym Nb–Ir–B. Sukces projektu był możliwy dzięki opracowanej metodzie syntezy z zastosowaniem wysokotemperaturowego pieca komorowego w warunkach wysokiej i dynamicznej próżni. Równolegle prowadzone były badania krystalograficzne, które pozwoliły na określenie nowego typu struktury (*Cc* No.9), w którym brak jest środka symetrii. Ważną właściwością obu nadprzewodników jest również bardzo wysoka wartość górnego pola krytycznego przewyższająca limit Pauli'ego. W konsekwencji materiały mogą charakteryzować się niekonwencjonalnym typem nadprzewodnictwa.

Projekty będące podstawą rozprawy doktorskiej, łączy zjawisko nadprzewodnictwa w materiałach międzymetalicznych. Dla wszystkich 8 nadprzewodników, opisano sposób syntezy materiałów, badania strukturalne i właściwości fizyczne. Obliczenia struktury elektronowej, a w niektórych przypadkach również fononowej, przeprowadzone przez grupę dr. hab. Bartłomieja Wiendlochy, pozwoliły na pełniejszy opis badanych związków. Wykonane badania pozwoliły na potwierdzenie stawianych hipotez, ale jednocześnie zostawiły nowe, intrygujące pytania, w tym między innymi: dlaczego obserwowane w $LiPd_2Ge$ nadprzewodnictwo jest pierwszego rodzaju? Czy dla $LiPd_2Si$ i $LiPd_2Sn$ będzie występować, sugerowane przez obliczenia teoretyczne, nadprzewodnictwo poniżej 1.8 K? Czy istnieją inne nadprzewodniki typu Heuslera, dla których VEC jest niższe niż 24, i dla których T_c będzie tworzyć tzw. drugie maksimum T_c(VEC) proponowane przez Matthiasa? Czy można wytworzyć roztwory stałe $Nb(Ir_{1-x}Rh_x)_2B_2$ i jak zmieniać się będą właściwości nadprzewodnikowe?

Prace eksperymentalne prowadzone na Politechnice Gdańskiej, ale także na Princeton University (NJ, USA) i Louisiana State University (LA, USA) były finansowane w ramach Diamentowego Grantu Ministerstwa Nauki i Szkolnictwa Wyższego, a także OPUS-14 Narodowego Centrum Nauki.

6. Oświadczenia

POLITECHNIKA
GDAŃSKA

WYDZIAŁ FIZYKI TECHNICZNEJ
I MATEMATYKI STOSOWANEJ

Gdańsk, 02.06.2021 r.

Dotyczy: oświadczenie o wkładzie Pani mgr inż. Karoliny Górnickiej w przygotowanie publikacji stanowiących podstawę rozprawy doktorskiej

We wszystkich niżej wymienionych publikacjach występuję w roli autora korespondencyjnego i poświadczam wkład Doktorantki zgodny z opisem.

Tomasz Klimczuk

Prof. dr hab. inż. Tomasz Klimczuk
promotor rozprawy
Pani mgr inż. Karoliny Górnickiej

1. Tytuł publikacji wraz z jej danymi bibliograficznymi:

$CeIr_3$: superconductivity in a phase based on tetragonally close packed clusters; Supercond. Sci. Technol. 32 (2019) 025008 (13pp)

Opis merytorycznego wkładu doktorantki w/w publikację:

Udział doktorantki polegał na syntezie próbki polikrystalicznej, przeprowadzeniu badań strukturalnych metodą proszkowej dyfrakcji rentgenowskiej wraz z analizą LeBaila otrzymanego dyfraktogramu, pomiarach właściwości magnetycznych, cieplnych, elektrycznych wraz z analizą wyników, udziale w dyskusji otrzymanych rezultatów, wyznaczeniu parametrów charakteryzujących stan normalny i nadprzewodzący, przygotowaniu rysunków oraz tekstu manuskryptu w części eksperymentalnej obejmującej wyniki wyżej wymienionych pomiarów. Doktorantka pełniła rolę autora korespondencyjnego oraz brała udział w przygotowaniu odpowiedzi na recenzje. Doktorantka kierowała również projektem naukowym (Diamentowy Grant, MNiSW) obejmującym badania opisane w pracy.

POLITECHNIKA GDAŃSKA
ul. G. Narutowicza 11/12
80-233 Gdańsk

tel. +48 58 348 6611
e-mail: tomasz.klimczuk@pg.edu.pl
www.mif.pg.gda.pl/homepages/tomek

2. Tytuł publikacji wraz z jej danymi bibliograficznymi:

Iridium 5d-electron driven superconductivity in ThIr$_3$; PHYSICAL REVIEW B 100, 214514 (2019)

Opis merytorycznego wkładu doktorantki w/w publikację:

Udział doktorantki polegał na przeprowadzeniu badań strukturalnych metodą proszkowej dyfrakcji rentgenowskiej, częściowych pomiarach właściwości magnetycznych, cieplnych oraz elektrycznych, analizie otrzymanych wyników, udziale w dyskusji uzyskanych rezultatów, wyznaczeniu parametrów charakteryzujących stan normalny i nadprzewodzący, przygotowaniu rysunków oraz wybranych fragmentów tekstu manuskryptu w części eksperymentalnej. Doktorantka brała udział w przygotowaniu odpowiedzi na recenzje. Doktorantka kierowała również projektem naukowym (Diamentowy Grant, MNiSW) obejmującym badania opisane w pracy.

3. Tytuł publikacji wraz z jej danymi bibliograficznymi:

The electronic characterization of the cubic Laves-phase superconductor CaRh$_2$; Journal of Alloys and Compounds 793 (2019) 393-399

Opis merytorycznego wkładu doktorantki w/w publikację:

Udział doktorantki polegał na syntezie próbki polikrystalicznej, przeprowadzeniu badań strukturalnych metodą proszkowej dyfrakcji rentgenowskiej wraz z analizą LeBaila otrzymanego dyfraktogramu, pomiarach właściwości magnetycznych, cieplnych, elektrycznych wraz z analizą wyników, udziale w dyskusji otrzymanych rezultatów, wyznaczeniu parametrów charakteryzujących stan normalny i nadprzewodzący, przygotowaniu rysunków oraz tekstu manuskryptu. Doktorantka pełniła rolę autora korespondencyjnego oraz brała udział przygotowaniu odpowiedzi na recenzje.

4. Tytuł publikacji wraz z jej danymi bibliograficznymi:

Soft-mode enhanced type-I superconductivity in LiPd$_2$Ge; PHYSICAL REVIEW B 102, 024507 (2020)

Opis merytorycznego wkładu doktorantki w/w publikację:

Udział doktorantki polegał na syntezie próbek polikrystalicznych, przeprowadzeniu badań strukturalnych metodą proszkowej dyfrakcji rentgenowskiej wraz z analizą LeBaila, pomiarach właściwości magnetycznych, cieplnych oraz elektrycznych, analizie otrzymanych wyników, udziale w dyskusji uzyskanych rezultatów, wyznaczeniu parametrów charakteryzujących stan normalny i nadprzewodzący, przygotowaniu rysunków oraz tekstu manuskryptu w części eksperymentalnej. Doktorantka pełniła rolę autora korespondencyjnego oraz brała udział w przygotowaniu odpowiedzi na recenzje.

5. Tytuł publikacji wraz z jej danymi bibliograficznymi:

Superconductivity in $LiGa_2Ir$ Heusler type compound with VEC = 16

Opis merytorycznego wkładu doktorantki w/w publikację:

Udział doktorantki polegał na syntezie próbki polikrystalicznej, przeprowadzeniu badań strukturalnych metodą proszkowej dyfrakcji rentgenowskiej wraz z analizą LeBaila, pomiarach właściwości magnetycznych, cieplnych oraz elektrycznych, analizie otrzymanych wyników, udziale w dyskusji uzyskanych rezultatów, wyznaczeniu parametrów charakteryzujących stan normalny i nadprzewodzący, przygotowaniu rysunków oraz tekstu manuskryptu w części eksperymentalnej

6. Tytuł publikacji wraz z jej danymi bibliograficznymi:

Superconductivity on a Bi Square Net in LiBi; Chemistry of materials 2020, 32, 3150–3159

Opis merytorycznego wkładu doktorantki w/w publikację:

Udział doktorantki polegał na syntezie próbki monokrystalicznej, przeprowadzeniu badań strukturalnych metodą proszkowej dyfrakcji rentgenowskiej wraz z analizą LeBaila, pomiarach właściwości magnetycznych oraz cieplnych, analizie otrzymanych wyników, udziale w dyskusji uzyskanych rezultatów, wyznaczeniu parametrów charakteryzujących stan normalny i nadprzewodzący, przygotowaniu rysunków oraz tekstu manuskryptu w części eksperymentalnej. Doktorantka brała udział przygotowaniu odpowiedzi na recenzje.

7. Tytuł publikacji wraz z jej danymi bibliograficznymi:

New Low Symmetry Noncentrosymmetric Superconductors with Strong Spin–Orbit Coupling; Adv. Funct. Mater. 2021, 31, 2007960

Opis merytorycznego wkładu doktorantki w/w publikację:

Udział doktorantki polegał syntezie próbek polikrystalicznych metodą syntezy w fazie stałej, przeprowadzeniu badania metodą proszkowej dyfrakcji rentgenowskiej wraz z analizą Rietvelda, pomiarach i analizie wyników właściwości magnetycznych, elektrycznych oraz cieplnych. Doktorantka odpowiadała za przygotowanie wykresów, rysunków w części eksperymentalnej i fragmentów tekstu dotyczących syntezy, właściwości magnetycznych, cieplnych oraz elektrycznych.

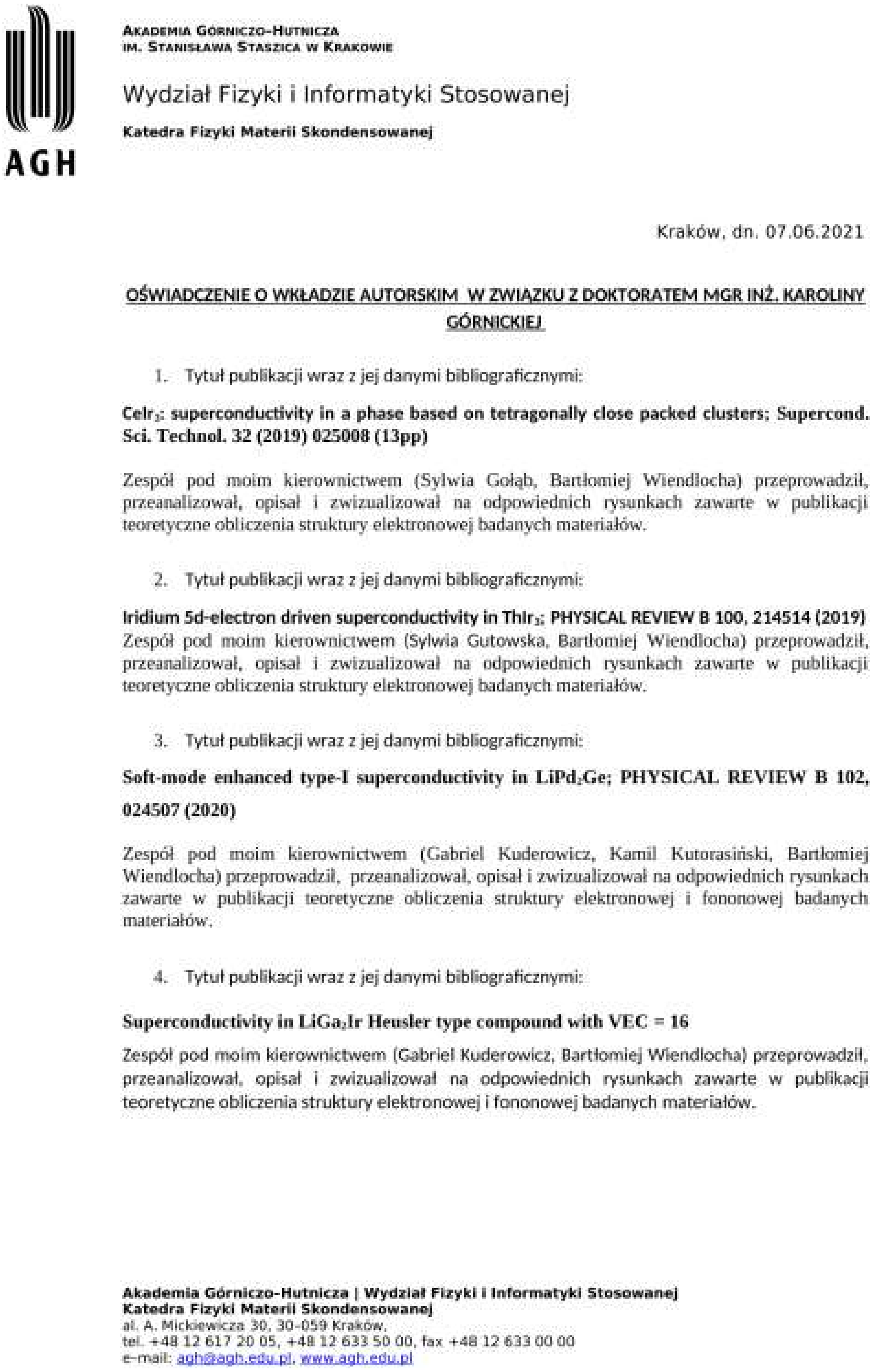

AKADEMIA GÓRNICZO-HUTNICZA
IM. STANISŁAWA STASZICA W KRAKOWIE

Wydział Fizyki i Informatyki Stosowanej

Katedra Fizyki Materii Skondensowanej

Kraków, dn. 07.06.2021

OŚWIADCZENIE O WKŁADZIE AUTORSKIM W ZWIĄZKU Z DOKTORATEM MGR INŻ. KAROLINY GÓRNICKIEJ

1. Tytuł publikacji wraz z jej danymi bibliograficznymi:

CeIr$_3$: superconductivity in a phase based on tetragonally close packed clusters; Supercond. Sci. Technol. 32 (2019) 025008 (13pp)

Zespół pod moim kierownictwem (Sylwia Gołąb, Bartłomiej Wiendlocha) przeprowadził, przeanalizował, opisał i zwizualizował na odpowiednich rysunkach zawarte w publikacji teoretyczne obliczenia struktury elektronowej badanych materiałów.

2. Tytuł publikacji wraz z jej danymi bibliograficznymi:

Iridium 5d-electron driven superconductivity in ThIr$_3$; PHYSICAL REVIEW B 100, 214514 (2019)

Zespół pod moim kierownictwem (Sylwia Gutowska, Bartłomiej Wiendlocha) przeprowadził, przeanalizował, opisał i zwizualizował na odpowiednich rysunkach zawarte w publikacji teoretyczne obliczenia struktury elektronowej badanych materiałów.

3. Tytuł publikacji wraz z jej danymi bibliograficznymi:

Soft-mode enhanced type-I superconductivity in LiPd$_2$Ge; PHYSICAL REVIEW B 102, 024507 (2020)

Zespół pod moim kierownictwem (Gabriel Kuderowicz, Kamil Kutorasiński, Bartłomiej Wiendlocha) przeprowadził, przeanalizował, opisał i zwizualizował na odpowiednich rysunkach zawarte w publikacji teoretyczne obliczenia struktury elektronowej i fononowej badanych materiałów.

4. Tytuł publikacji wraz z jej danymi bibliograficznymi:

Superconductivity in LiGa$_2$Ir Heusler type compound with VEC = 16

Zespół pod moim kierownictwem (Gabriel Kuderowicz, Bartłomiej Wiendlocha) przeprowadził, przeanalizował, opisał i zwizualizował na odpowiednich rysunkach zawarte w publikacji teoretyczne obliczenia struktury elektronowej i fononowej badanych materiałów.

Akademia Górniczo-Hutnicza | Wydział Fizyki i Informatyki Stosowanej
Katedra Fizyki Materii Skondensowanej
al. A. Mickiewicza 30, 30-059 Kraków,
tel. +48 12 617 20 05, +48 12 633 50 00, fax +48 12 633 00 00
e-mail: agh@agh.edu.pl, www.agh.edu.pl

5. Tytuł publikacji wraz z jej danymi bibliograficznymi:

Superconductivity on a Bi Square Net in LiBi; Chemistry of materials 2020, 32, 3150−3159

Zespół pod moim kierownictwem (Sylwia Gutowska, Bartłomiej Wiendlocha) przeprowadził, przeanalizował, opisał i zwizualizował na odpowiednich rysunkach zawarte w publikacji teoretyczne obliczenia struktury elektronowej i fononowej badanych materiałów.

6. Tytuł publikacji wraz z jej danymi bibliograficznymi:

New Low Symmetry Noncentrosymmetric Superconductors with Strong Spin–Orbit Coupling; Adv. Funct. Mater. 2021, 31, 2007960

Przeprowadziłem przeanalizowałem, opisałem i zwizualizowałem na odpowiednich rysunkach zawarte w publikacji teoretyczne obliczenia struktury elektronowej badanych materiałów.

BWendlocha

dr hab. inż. Bartłomiej Wiendlocha
wiendlocha@fis.agh.edu.pl

OŚWIADCZENIE O WKŁADZIE DOKTORANTKI MGR INŻ. KAROLINY GÓRNICKIEJ W NIŻEJ WYMIENIONE PUBLIKACJE:

1. Tytuł publikacji wraz z jej danymi bibliograficznymi:

$\mathrm{CeIr_3}$: superconductivity in a phase based on tetragonally close packed clusters; Supercond. Sci. Technol. 32 (2019) 025008 (13pp)

Opis merytorycznego wkładu doktorantki w/w publikację:

Udział doktorantki polegał na syntezie próbki polikrystalicznej, przeprowadzeniu badań strukturalnych metodą proszkowej dyfrakcji rentgenowskiej wraz z analizą LeBaila otrzymanego dyfraktogramu, pomiarach właściwości magnetycznych, cieplnych, elektrycznych wraz z analizą wyników, udziale w dyskusji otrzymanych rezultatów, wyznaczeniu parametrów charakteryzujących stan normalny i nadprzewodzący, przygotowaniu rysunków oraz tekstu manuskryptu w części eksperymentalnej obejmującej wyniki wyżej wymienionych pomiarów. Doktorantka pełniła rolę autora korespondencyjnego oraz brała udział w przygotowaniu odpowiedzi na recenzje. Doktorantka kierowała również projektem naukowym (Diamentowy Grant, MNiSW) obejmującym badania opisane w pracy.

2. Tytuł publikacji wraz z jej danymi bibliograficznymi:

Iridium 5d-electron driven superconductivity in $\mathrm{ThIr_3}$; PHYSICAL REVIEW B 100, 214514 (2019)

Opis merytorycznego wkładu doktorantki w/w publikację:

Udział doktorantki polegał na przeprowadzeniu badań strukturalnych metodą proszkowej dyfrakcji rentgenowskiej, częściowych pomiarach właściwości magnetycznych, cieplnych oraz elektrycznych, analizie otrzymanych wyników, udziale w dyskusji uzyskanych rezultatów, wyznaczeniu parametrów charakteryzujących stan normalny i nadprzewodzący, przygotowaniu rysunków oraz wybranych fragmentów tekstu manuskryptu w części eksperymentalnej. Doktorantka brała udział w przygotowaniu odpowiedzi na recenzje. Doktorantka kierowała również projektem naukowym (Diamentowy Grant, MNiSW) obejmującym badania opisane w pracy.

D. Kaczorowski

prof. dr hab. Dariusz Kaczorowski

7. Lista osiągnięć naukowych doktorantki

Projekty:

1. Kierownik projektu Nadprzewodnictwo i magnetyzm w nowych związkach podwójnych R-Rh i R-Ir (R-ziemia rzadka) finansowanego w ramach programu Ministerstwa Nauki i Szkolnictwa Wyższego „Diamentowy Grant” (nr projektu 0205/DIA/2017/46, okres realizacji: 29.08.2017 – 28.08.2020);

2. Kierownik projektu Nadprzewodnictwo w związkach Lavesa na bazie metali ziem alkalicznych finansowanego w ramach programu Narodowego Centrum Nauki PRELUDIUM-17 (nr projektu UMO-2019/33/N/ST5/01496, okres realizacji: 29.01.2020 – 28.01.2023).

Publikacje naukowe:

1. MJ. Winiarski, G. Kuderowicz, **K. Górnicka,** LS. Litzbarski, K. Stolecka, B. Wiendlocha, RJ. Cava, T. Klimczuk: MgPd2Sb: : A Mg-based Heusler-type superconductor; Phys. Rev. B 103, 214501 (140 pkt);
2. Catherine Witteveen, **Karolina Górnicka**, Johan Chang, Martin Månsson, Tomasz Klimczuk, Fabian O von Rohr: Polytypism and superconductivity in the NbS2 system; Dalton Trans., 2021, 50, 3216-3223 (140 pkt);
3. **K. Górnicka**, X. Gui, B. Wiendlocha, L.T. Nguyen, W. Xie, R.J. Cava, T. Klimczuk: NbIr2B2 and TaIr2B2 – New Low Symmetry Noncentrosymmetric Superconductors with Strong Spin-Orbit Coupling; Advanced Functional Materials 2021, 31, 2007960 (200 pkt);
4. Shu Guo, Ruidan Zhong, **Karolina Górnicka**, Tomasz Klimczuk, RJ Cava: Crystal Growth, Structure, and Magnetism of the 2D Spin 1/2 Triangular Lattice Material Rb3Yb(PO4)2, Chemistry of Materials 2020 DOI: 10.1021/acs.chemmater.0c03850 (200 pkt);
5. Justyna Ignaczak, Yevgeniy Naumovich, **Karolina Górnicka**, Jan Jamroz, Wojciech Wróbel, Jakub Karczewski, Ming Chen, Piotr Jasiński, Sebastian Molin: Preparation and characterisation of iron substituted Mn1. 7Cu1. 3-xFexO4 spinel oxides (x= 0, 0.1, 0.3, 0.5); Journal of the European Ceramic Society Volume 40, Issue 15, December 2020, 5920-5929 (140 pkt);
6. Makarova I., Ryl J., Sun Z., Kurilo I., **Górnicka K**., Laatikainen M., Repo E.: One-step recovery of REE oxalates in electro-leaching of spent NdFeB magnets; Separation and Purification Technology -Vol. 251, (2020), s.117362, (140 pkt);
7. Nasser Y Mostafa, Mohsen M Qhtani, Saad H Alotaibi, Zaki I Zaki, Sarah Alharthi, Mateusz Cieslik, **Karolina Gornicka**, Jacek Ryl, Rabah Boukherroub, Mohammed A Amin: Cathodic activation of synthesized highly defective monoclinic hydroxyl-functionalized ZrO2 nanoparticles for efficient electrochemical production of hydrogen in alkaline media; International Journal of Energy Research - 2020;1–15., (100 pkt)

8. **Górnicka K**., Kuderowicz G., Carnicom E., Kutorasiński K., Wiendlocha B., Cava R., Klimczuk T.: Soft-mode enhanced type-I superconductivity in LiPd2Ge; PHYSICAL REVIEW B -Vol. 102,iss. 2 (2020), s.1-13, (140 pkt)

9. Lankauf K., Cysewska K., Karczewski J., Mielewczyk-Gryń A., **Górnicka K**., Cempura G., Chen M., Jasiński P., Molin S.: MnxCo3-xO4 spinel oxides as efficient oxygen evolution reaction catalysts in alkaline media; INTERNATIONAL JOURNAL OF HYDROGEN ENERGY -Vol. 45,iss. 29 (2020), s.14867-14879, (140 pkt)

10. Gui X., **Górnicka K**., Chen Q., Zhou H., Klimczuk T., Xie W.: Superconductivity in Metal-Rich Chalcogenide Ta2Se// INORGANIC CHEMISTRY -Vol. 59,iss. 9 (2020), s.5798-5802, (140 pkt)

11. **Górnicka K**., Gutowska S., Winiarski M., Wiendlocha B., Xie W., Cava R., Klimczuk T.: Superconductivity on a Bi Square Net in LiBi; CHEMISTRY OF MATERIALS -Vol. 32,iss. 7 (2020), s.3150-3159, (200 pkt)

12. Iga Szpunar, Sebastian Wachowski, Tadeusz Miruszewski, Kacper Dzierzgowski, **Karolina Górnicka**, Tomasz Klimczuk, Magnus Helgerud Sørby, María Balaguer, José M Serra, Ragnar Strandbakke, Maria Gazda, Aleksandra Mielewczyk-Gryń: Electric and magnetic properties of Lanthanum Barium Cobaltite; Journal of the American Ceramic Society 2020;103:1809–1818 (100 pkt)

13. **Górnicka K**., Das D., Gutowska S., Wiendlocha B., Winiarski M., Klimczuk T., Kaczorowski D.: Iridium 5d -electron driven superconductivity in ThIr3; PHYSICAL REVIEW B -Vol. 100,iss. 21 (2019), s.214514, (140 pkt)

14. Jasiewicz K., Wiendlocha B., **Górnicka K**., Gofryk K., Gazda M., Klimczuk T., Tobola J.: Pressure effects on the electronic structure and superconductivity of (TaNb)0.67(HfZrTi)0.33 high entropy alloy; PHYSICAL REVIEW B -Vol. 100,iss. 18 (2019), s.184503; (140 pkt)

15. Marshall M., **Górnicka K**., Mudiyanselage R., Klimczuk T., Xie W.: New Tetragonal ReGa5(M) (M = Sn, Pb, Bi) Single Crystals Grown from Delicate Electrons Changing; Crystals -Vol. 9,iss. 10 (2019), s.527, (70 pkt)

16. M. A. Mezni, M. Alsawat, T. Kumeria, M. R. Das, S. Alzahly, A. Aldalbahi, **K. Górnicka**, J. Ryl, M. A. Amin, T. Altalhi, „Enhanced hydrogen evolution reaction on highly stable titania-supported PdO and Eu2O3 nanocomposites in a strong alkaline solution"; International Journal of Energy Research 43 (10), 5367-5383 (100 pkt)

17. **K. Górnicka**, R. J. Cava, T. Klimczuk, „The electronic characterization of the cubic Laves-phase superconductor CaRh2"; Journal of Alloys and Compounds 793 (2019) 393e399 (100 pkt)

18. B. Kamecki, T. Miruszewski, **K. Górnicka**, T. Klimczuk, J. Karczewski, „Characterization methods of nickel nano-particles obtained by the ex-solution process on the surface of Pr, Ni-doped SrTiO3 perovskite ceramics"; SN Applied Sciences (2019) 1:322

19. E. M. Carnicom, W. Xie, Z. Yang, **K. Górnicka**, T. Kong, T. Klimczuk, R. J. Cava, „Importance of Specific Heat Characterization when Reporting New Superconductors: An Example of Superconductivity in LiGa2Rh"; Chemistry of Materials 2019, 31, 2164−2173 (200 pkt)

20. **K. Górnicka,** W. Xie, E.M. Carnicom, R. J. Cava, T. Klimczuk, „Synthesis and physical properties of the 10.6 K ferromagnet NdIr3"; Physical Review B 99, 104430 (2019) (140 pkt)

21. **K. Górnicka**, E. M. Carnicom, S. Gołąb, M. Łapiński, B. Wiendlocha, W. Xie, D. Kaczorowski, R. J. Cava, T. Klimczuk, „ CeIr3: Superconductivity in a phase based on Tetragonally Close

Packed (TCP) clusters"; Superconductor Science and Technology 32 (2019) 025008 (13pp) (100 pkt)

22. **K. Górnicka**, K.K. Kolincio, T. Klimczuk; Spin-glass behavior in a binary Pr3Ir intermetallic compound; Intermetallics 100, 63-69 (100 pkt)

23. EM Carnicom, **K Górnicka,** T Klimczuk, RJ Cava: The homometallic warwickite V2OBO3; Journal of Solid State Chemistry 265, 319-325 (70 pkt);

24. T Kong, **K Górnicka**, S Gołąb, B Wiendlocha, T Klimczuk, RJ Cava: A family of Pb-based superconductors with variable cubic to hexagonal packing; Journal of the Physical Society of Japan 87 (7), 074711 (70 pkt)

25. Elizabeth M Carnicom, Weiwei Xie, Tomasz Klimczuk, Jingjing Lin, **Karolina Górnicka**, Zuzanna Sobczak, Nai Phuan Ong, Robert J Cava: TaRh2B2 and NbRh2B2: Superconductors with a chiral noncentrosymmetric crystal structure; Science advances 4 (5), eaar7969 (200 pkt);

26. KK Kolincio, **K Górnicka**, MJ Winiarski, J Strychalska-Nowak, T Klimczuk: Field-induced suppression of charge density wave in GdNiC2; Physical Review B 94 (19), 195149 (140 pkt)

8. Bibliografia

[1] S. Blundell, *Superconductivity: A Very Short Introduction* (Oxford University Press, Oxford ; New York, 2009).

[2] A. Szewczyk, A. Wiśniewski, R. Puźniak, and H. Szymczak, *Magnetyzm i Nadprzewodnictwo*, 1st ed. (Wydawnictwo Naukowe PWN, Warszawa, 2012).

[3] J. Sosnowski, *Fizykalne Problemy Zastosowań Nadprzewodników Wysokotemperaturowych w Elektro-Energetyce*, Przegląd Elektrotechniczny **90**, (2014).

[4] P. Kroupka, *Nadprzewodnictwo – Krótki Przewodnik. Historia, Teoria, Zastosowania*, https://iviter.pl/artykuly/nadprzewodnictwo-krotki-przewodnik-historia-teoria-zastosowania/.

[5] E. Bauer and M. Sigrist, *Non-Centrosymmetric Superconductor:Introduction and Overview* (Springer-Verlag, Heidelberg, 2012).

[6] M. Smidman, M. B. Salamon, H. Q. Yuan, and D. F. Agterberg, *Superconductivity and Spin–Orbit Coupling in Non-Centrosymmetric Materials: A Review*, Rep. Prog. Phys. **80**, 036501 (2017).

[7] D. Singh, A. D. Hillier, A. Thamizhavel, and R. P. Singh, *Superconducting Properties of the Noncentrosymmetric Superconductor Re 6 Hf*, Phys. Rev. B **94**, (2016).

[8] A. C. Rose-Innes and E. H. Rhoderick, *Introduction to Superconductivity* (Pergamon Place plc, 1978).

[9] C. Kittel, *Solid State Physics*, 4th edition (Wiley, New York, 1966).

[10] A. Sukiennicki and A. Zagórski, *Fizyka Ciała Stałego*, **II** (Wydawnictwo Naukowo-Techniczne, 1984).

[11] W. Meissner and R. Oschenfeld, *Ein Neuer Effekt Bei Eintritt Der Supraleitfähigkeit.*, Naturwissenschaften **22**, 787 (1933).

[12] *Meissner effect*, https://en.wikipedia.org/wiki/Meissner_effect.

[13] A. A. Abrikosov, *On the Magnetic Properties of Superconductors of the Second Group.*, Sov Phys JETP 1174 (1957).

[14] F. London and H. London, *The Electromagnetic Equations of the Supraconductor*, Proc. R. Soc. Lond. Ser. - Math. Phys. Sci. **149**, 71 (1935).

[15] V. L. Ginzburg and L. D. Landau, *On the Theory of Superconductivity*, in *On Superconductivity and Superfluidity* (Springer Berlin Heidelberg, Berlin, Heidelberg, 2009), pp. 113–137.

[16] J. Bardeen, L. N. Cooper, and J. R. Schrieffer, *Theory of Superconductivity*, Phys. Rev. **108**, 1175 (1957).

[17] J. Bardeen, L. N. Cooper, and J. R. Schrieffer, *Microscopic Theory of Superconductivity*, Phys. Rev. **106**, 162 (1957).

[18] M. Tinkham, *Introduction to Superconductivity* (Courier Corporation, 1996).

[19] W. L. McMillan, *Transition Temperature of Strong-Coupled Superconductors*, Phys. Rev. **167**, 331 (1968).

[20] T. H. Geballe, B. T. Matthias, V. B. Compton, E. Corenzwit, G. W. Hull, and L. D. Longinotti, *Superconductivity in Binary Alloy Systems of the Rare Earths and of Thorium with Pt-Group Metals*, Phys. Rev. **137**, A119 (1965).

[21] DMITRIEVA, N. V., *Melting Diagram and Thermodynamic Properties of Certain Intermetallic Compounds of the Ir-Ce System*, Akad Nauk Ukr. SSR Metallofiz. **49**, 109 (1973).

[22] O. Sologub, P. Salamakha, A. P. Gonçalves, H. Ipser, and M. Almeida, *Crystal Structure of the CeIr3 Compound*, J. Alloys Compd. **373**, L5 (2004).

[23] H. Kleykamp, *Thermodynamische untersuchungen in den systemen Thorium-Osmium und Thorium-Iridium*, J. Common Met. **63**, P25 (1979).

[24] Y. J. Sato, A. Nakamura, Y. Shimizu, A. Maurya, Y. Homma, D. Li, F. Honda, and D. Aoki, *Superconducting Properties of CeIr$_3$ Single Crystal*, J. Phys. Soc. Jpn. **87**, 053704 (2018).

[25] B. T. Matthias and E. Corenzwit, *Superconducting Alkaline Earth Compounds*, Phys. Rev. **107**, 1558 (1957).

[26] E. A. Wood and V. B. Compton, *Laves-Phase Compounds of Alkaline Earths and Noble Metals*, Acta Crystallogr. **11**, 429 (1958).

[27] N. Haldolaarachchige, Q. Gibson, L. M. Schoop, H. Luo, and R. J. Cava, *Characterization of the Heavy Metal Pyrochlore Lattice Superconductor CaIr 2*, J. Phys. Condens. Matter **27**, 185701 (2015).

[28] H. M. Tütüncü, H. Y. Uzunok, E. Karaca, E. Arslan, and G. P. Srivastava, *Effects of Spin-Orbit Coupling on the Electron-Phonon Superconductivity in the Cubic Laves-Phase Compounds CaIr 2 and CaRh 2*, Phys. Rev. B **96**, (2017).

[29] C. J. Palmstrøm, *Heusler Compounds and Spintronics*, Prog. Cryst. Growth Charact. Mater. **62**, 371 (2016).

[30] T. Graf, C. Felser, and S. S. P. Parkin, *Simple Rules for the Understanding of Heusler Compounds*, Prog. Solid State Chem. **39**, 1 (2011).

[31] T. Klimczuk, C. H. Wang, K. Gofryk, F. Ronning, J. Winterlik, G. H. Fecher, J.-C. Griveau, E. Colineau, C. Felser, J. D. Thompson, D. J. Safarik, and R. J. Cava, *Superconductivity in the Heusler Family of Intermetallics*, Phys. Rev. B **85**, 174505 (2012).

[32] M. J. Winiarski, G. Kuderowicz, K. Górnicka, L. S. Litzbarski, K. Stolecka, B. Wiendlocha, R. J. Cava, and T. Klimczuk, *Mg Pd 2 Sb : A Mg-Based Heusler-Type Superconductor*, Phys. Rev. B **103**, (2021).

[33] B. T. Matthias, *Chapter V Superconductivity in the Periodic System*, in *Progress in Low Temperature Physics*, Vol. 2 (Elsevier, 1957), pp. 138–150.

[34] S. V. Vonsovskiĭ, I. A. Iziumov, and Ė. Z. Kurmaev, *Superconductivity of Transition Metals: Their Alloys and Compounds* (Springer-Verlag, Berlin ; New York, 1982).

[35] C.-J. Kistrup and H.-U. Schuster, *Neue tern�re Phasen von Platinmetallen mit Lithium und Elementen der 4. Hauptgruppe*, Z. F�r Anorg. Allg. Chem. **410**, 113 (1974).

[36] S. Ayhan and G. Kavak Balcı, Ab-Initio *Calculations: Structural, Electronic and Elastic Properties of LiX $_2$ Ge (X: Rh, Cu, Ni, Pd) Heusler Compounds*, Mater. Res. Express **6**, 0865e9 (2019).

[37] A. Czybulka, A. Petersen, and H.-U. Schuster, *Lithium-platinmetall-Al(Ga, In)-legierungen: Neue farbige ternäre intermetallische phasen*, J. Common Met. **161**, 303 (1990).

[38] L. Drews-Nicolai and G. Hohlneicher, *Electronic Structure Calculations for the Ternary Intermetallic Compounds A2MX and AMX2 (A=Li; M=Rh, Pd, Ir, Pt; X=Al, Ga, In) Using Density-Functional Theory*, J. Alloys Compd. **316**, 1 (2001).

[39] E. M. Carnicom, W. Xie, Z. Yang, K. Górnicka, T. Kong, T. Klimczuk, and R. J. Cava, *Importance of Specific Heat Characterization When Reporting New Superconductors: An Example of Superconductivity in LiGa $_2$ Rh*, Chem. Mater. **31**, 2164 (2019).

[40] E. Zintl and G. Brauer, *Konstitution Der Lithium-Wismut-Legierungen: 14. Mitteilung Über Metalle u. Legierungen*, Z. Für Elektrochem. Angew. Phys. Chem. **41**, 297 (1935).

[41] N. E. Alekseevskii, N. B. Brandt, and T. I. Kostina, *Superconductivity of Binary Alloys of Bismuth*, Vol. 16 (Izv. Akad. Nauk SSSR Ser. Fiz, 1952).

[42] T. Sambongi, *Superconductivity of LiBi*, J. Phys. Soc. Jpn. **30**, 294 (1971).

[43] S. K. Kushwaha, J. W. Krizan, J. Xiong, T. Klimczuk, Q. D. Gibson, T. Liang, N. P. Ong, and R. J. Cava, *Superconducting Properties and Electronic Structure of NaBi*, J. Phys. Condens. Matter **26**, 212201 (2014).

[44] E. M. Carnicom, W. Xie, T. Klimczuk, J. Lin, K. Górnicka, Z. Sobczak, N. P. Ong, and R. J. Cava, *TaRh2B2 and NbRh2B2: Superconductors with a Chiral Noncentrosymmetric Crystal Structure*, Sci. Adv. **4**, eaar7969 (2018).

[45] E. Bauer, G. Hilscher, H. Michor, C. Paul, E. W. Scheidt, A. Gribanov, Y. Seropegin, H. Noël, M. Sigrist, and P. Rogl, *Heavy Fermion Superconductivity and Magnetic Order in Noncentrosymmetric C e P t 3 S I*, Phys. Rev. Lett. **92**, 027003 (2004).

[46] D. A. Mayoh, A. D. Hillier, K. Götze, D. M. Paul, G. Balakrishnan, and M. R. Lees, *Multigap Superconductivity in Chiral Noncentrosymmetric TaRh 2 B 2*, Phys. Rev. B **98**, 014502 (2018).

[47] S. S. Saxena, P. Agarwal, K. Ahilan, F. M. Grosche, R. K. W. Haselwimmer, M. J. Steiner, E. Pugh, I. R. Walker, S. R. Julian, P. Monthoux, G. G. Lonzarich, A. Huxley, I. Sheikin, D. Braithwaite, and J. Flouquet, *Superconductivity on the Border of Itinerant-Electron Ferromagnetism in UGe2*, Nature **406**, 587 (2000).

[48] T. Akazawa, H. Hidaka, T. Fujiwara, T. C. Kobayashi, E. Yamamoto, Y. Haga, R. Settai, and Y. nuki, *Pressure-Induced Superconductivity in Ferromagnetic UIr without Inversion Symmetry*, J. Phys. Condens. Matter **16**, L29 (2004).

[49] D. Aoki, A. Huxley, E. Ressouche, D. Braithwaite, J. Flouquet, J.-P. Brison, E. Lhotel, and C. Paulsen, *Coexistence of Superconductivity and Ferromagnetism in URhGe*, Nature **413**, 613 (2001).

[50] N. T. Huy, A. Gasparini, D. E. de Nijs, Y. Huang, J. C. P. Klaasse, T. Gortenmulder, A. de Visser, A. Hamann, T. Görlach, and H. v. Löhneysen, *Superconductivity on the Border of Weak Itinerant Ferromagnetism in UCoGe*, Phys. Rev. Lett. **99**, (2007).

[51] I. R. Walker, F. M. Grosche, D. M. Freye, and G. G. Lonzarich, *The Normal and Superconducting States of CeIn3 near the Border of Antiferromagnetic Order*, Phys. C Supercond. **282**–**287**, 303 (1997).

[52] N. Haldolaarachchige, L. Schoop, M. A. Khan, W. Huang, H. Ji, Kalani Hettiarachchilage, and D. P. Young, *Ir d -Band Derived Superconductivity in the Lanthanum-Iridium System LaIr 3*, J. Phys. Condens. Matter **29**, 475602 (2017).

[53] F. Laves, *Kristallographie der Legierungen*, Naturwissenschaften **27**, 65 (1939).

[54] F. Laves, *Crystal Structure and Atomic Size*, Am. Soc. Met. (1956).

[55] J. B. Friauf, *The Crystal Structure of Magnesium Di-Zincide*, Phys. Rev. **29**, 34 (1927).

[56] B. M. Klein, W. E. Pickett, D. A. Papaconstantopoulos, and L. L. Boyer, *Electronic Structure, Superconductivity, and Magnetism in the C 15 Compounds Zr V 2 , Zr Fe 2 , and Zr Co 2*, Phys. Rev. B **27**, 6721 (1983).

[57] X.-Q. Chen, W. Wolf, R. Podloucky, and P. Rogl, Ab Initio *Study of Structural, Magnetic, Vibrational, and Thermodynamic Properties of the Laves-Phase Compound Hf Mn 2*, Phys. Rev. B **76**, (2007).

[58] E. Gratz and A. S. Markosyan, *Physical Properties of RCo $_2$ Laves Phases*, J. Phys. Condens. Matter **13**, R385 (2001).

[59] F. Stein, M. Palm, and G. Sauthoff, *Structure and Stability of Laves Phases Part II—Structure Type Variations in Binary and Ternary Systems*, Intermetallics **13**, 1056 (2005).

[60] A. E. Clark, *Magnetic and Magnetoelastic Properties of Highly Magnetostrictive Rare Earth-Iron Laves Phase Compounds*, in *MAGNETISM AND MAGNETIC MATERIALS — 1973: Nineteenth Annual Conference* (ASCE, Boston, Massachusetts, 1974), pp. 1015–1029.

[61] G. Srinivas, V. Sankaranarayanan, and S. Ramaprabhu, *Kinetics of Hydrogen Absorption in Ho1−xMmxCo2 Alloys*, J. Alloys Compd. **448**, 159 (2008).

[62] H. Sugawara, H. Sato, T. Yamazaki, N. Kimura, R. Settai, and Y. Ōnuke, *Superconducting Properties of CeRu2 Single Crystal*, J. Phys. Soc. Jpn. **64**, 4849 (1995).

[63] P. B. Allen and R. C. Dynes, *Transition Temperature of Strong-Coupled Superconductors Reanalyzed*, Phys. Rev. B **12**, 905 (1975).

[64] J. Winterlik, G. H. Fecher, C. Felser, M. Jourdan, K. Grube, F. Hardy, H. von Löhneysen, K. L. Holman, and R. J. Cava, *Ni-Based Superconductor: Heusler Compound ZrNi 2 Ga*, Phys. Rev. B **78**, 184506 (2008).

[65] D. Hirai, M. N. Ali, and R. J. Cava, *Strong Electron–Phonon Coupling Superconductivity Induced by a Low-Lying Phonon in IrGe*, J. Phys. Soc. Jpn. **82**, 124701 (2013).